University of Bath

PHD

Active Valve & Pump Technology: Modelling and Control of Variable-Speed Trim Transfer Pump in Aircraft Fuel Systems

Boyd, Lewis

Award date:
2008

Awarding institution:
University of Bath

Link to publication

General rights
Copyright and moral rights for the publications made accessible in the public portal are retained by the authors and/or other copyright owners and it is a condition of accessing publications that users recognise and abide by the legal requirements associated with these rights.

- Users may download and print one copy of any publication from the public portal for the purpose of private study or research.
- You may not further distribute the material or use it for any profit-making activity or commercial gain
- You may freely distribute the URL identifying the publication in the public portal ?

Take down policy
If you believe that this document breaches copyright please contact us providing details, and we will remove access to the work immediately and investigate your claim.

Download date: 22. May. 2019

ACTIVE VALVE & PUMP TECHNOLOGY: MODELLING AND CONTROL OF VARIABLE-SPEED TRIM TRANSFER PUMPS IN AIRCRAFT FUEL SYSTEMS

Submitted by Lewis John Boyd
for the degree of
Doctor of Philosophy
of the University of Bath
Department of Mechanical Engineering
September 2008

COPYRIGHT

Attention is drawn to the fact that copyright of this thesis rests with its author. This copy of the thesis has been supplied on condition that anyone who consults it is understood to recognise that its copyright rests with its author and no information derived from it may be published without the prior written consent of the author.

This thesis may be made available for consultation within the University library and may be photocopied or lent to other libraries for the purposes of consultation.

Abstract

The current generation of Airbus long-range civil transport aircraft actively control the centre of gravity of the aircraft by adjusting the fuel distribution between the horizontal tail surface and the forward tanks in order to minimise cruise drag. Here, it is proposed that the current on-off control method could be replaced by a variable flow rate, provided by a variable speed centrifugal pump. The impacts of this at the aircraft level in terms of cruise fuel burn reduction, valve operation cycle reduction and power consumption are investigated here using an extension to an existing fuel system simulation package and a generic aircraft fuel system definition. It is shown that using such a control system reduces fuel burn and the number of valve cycles, which could translate into a reduction in operating costs. The benefit of changing the controller to use tailplane trim angle directly rather than inferred centre of gravity position is assessed, and is shown to further reduce the fuel burn. It is suggested that such centre of gravity could provide significant benefits over the existing method.

Steady-state and dynamic models of centrifugal pumps, AC induction drives and typical aircraft fuel system pipework components are developed. These are validated against experimental data from a test rig of a representative system. Test rig simulation results are shown to agree well with those from experimentation. A new secondary noise source is developed for the dynamic analysis of the centrifugal pump, and a new acoustic experimental method is developed for the prediction of fluid inductance in pipework components. The results are compared against an existing CFD based method and show good agreement. The new method represents a much simpler experimental means of determining the effects of fluid inertia than the existing secondary source method. It is demonstrated that the dynamic behaviour of the centrifugal pump is, as expected, insignificant when considering systems containing long pipes, and that steady-state pump models are sufficient for analysing their behaviour.

The pump models are generalised by non-dimensionalisation, in order to maximise their

applicability to analysis of aircraft fuel systems. They are applied to a generic aircraft fuel system simulation, in order to model the behaviour of the system during a trim transfer. This is used to demonstrate the application of the proposed variable flow rate trim control system. The results of these simulations agree well with those used to demonstrate the benefits of the control system at the aircraft level. Concepts of system health monitoring tools are discussed with reference to the system simulations.

Acknowledgements

I would like to extend my acknowledgements to both Airbus UK and Parker Aerospace for their funding and support.

My most sincere thanks go to my supervisors, Prof. Kevin Edge, Dr. Derek Tilley and Dr. Nigel Johnston, for their expert advice, and to the support staff Andrew Galloway, Jo Wankowski, Vijay Rajput and Colin Brain.

Thanks to my colleagues on the Active Valve and Pump Technology project: Andy Roberts, Michail Soumelidis and Greg Skawinski, and also to Andrew Collett, with his help and input on the acoustic measurement of inertance work.

Finally, I would like to thank my wife Hazel. Her love and support were invaluable.

Contents

List of Figures

List of Tables

Nomenclature

The following nomenclature is used throughout the thesis:

A	lift equation coefficient, pipe cross-sectional area
a	speed of sound
B	lift equation coefficient, fluid bulk modulus
b	blade passage width
C	drag equation coefficient, capacitance
C_D	drag coefficient
C_L	lift coefficient
C_{mo}	aircraft pitching moment
c	chord length
$\bar{c}$	MAC length
D	drag, drag equation coefficient
d	drag coefficients, impeller outer blade diameter, pipe diameter
E	Young's modulus
F	secondary source coefficient, intermediate variable in dynamic motor analysis
f	frequency (Hz)
G	secondary source coefficient
g	acceleration due to gravity
h	ratio of tailplane to wing reference area
i	current
j	$\sqrt{-1}$
J	inertia

L	lift,
	lapse rate,
	inertance
l	pipe length
M_{cr}	cruise Mach number
m	mass
n	number of phases,
	angular speed (rev/min)
P	power,
	pressure
p	pressure,
	number of poles
Q	flow rate
q	flow rate
R	specific gas constant,
	resistance
R_e	Reynolds number
r	fuel burn rate,
	impeller radius at flow outlet
S_{ref}	wing reference area
s	wing span,
	slip factor
T	thrust,
	temperature,
	torque
t	time,
	pipe wall thickness
U	velocity
V	voltage
V_r	rotate speed
v	volume
X	orthogonal axis,
	reactance
x	distance aft of datum
Y	orthogonal axis
Z	impedance

α coefficients of pump pressure-flow non-dimensional characteristic,
angle of attack
β tailplane angle of attack
χ centre of gravity as a percentage of MAC
ϵ aircraft attitude angle,
relative roughness
Poisson's ratio,
error in centre of gravity position
η efficiency
γ glide slope angle,
adiabatic index,
wave propogation coefficient,
coefficients of pump torque-hydraulic power non-dimensional characteristic,
magnetic flux
ν kinematic viscosity
ω frequency (rad/s),
ϕ non-dimensional flow rate
ψ non-dimensional pressure
ρ wave reflection/termintaion coefficient,
fluid density
τ non-dimensional torque
θ angular displacement

Subscripts:

0	pipe characteristic
a	aircraft
cg	centre of gravity
eff	effective
m	magnetising
r	rotor
s	source,
	stator
T	termination
t	tail
w	wing

Acronyms:

AC	Alternating Current
AFBN	Airbus Fluid Borne Noise (software)
AMPEC	Aircraft Mission Performance Estimation Code (software)
AVPT	Active Valve and Pump Technology
BITE	Built-In Test Equipment
BSP	British Standard Pipe
CAD	Computer Aided Design
CFD	Computational Fluid Dynamics
DC	Direct Current
EAS	Equivalent Airspeed
FBN	Fluid Borne Noise
FRA	Frequency Response Analyser
GUI	Graphical User Interface
ICA	Initial Cruise Altitude
ISA	International Standard Atmosphere
MAC	Mean Aerodynamic Chord
MTOW	Maximum Take-Off Weight
PRPT	Piezo-Resistive Pressure Transducer
PWM	Pulse Wave Modulation
SA	Spectrum Analyser
SGPT	Strain Gauge Pressure Transducer
THS	Trimmable Horizontal Stabiliser

Chapter 1

Introduction

1.1 Current Fuel System Description

The current generation of mid- to long-range civil airliners rely on a complex system of tanks, valves, pumps and pipes to both store fuel and deliver fuel to the engines. The tanks are normally located in the wings, horizontal tailplane and below the passenger cabin in the main fuselage. In the wings, they help provide bending moment relief to the wings during take-off, and in the horizontal tailplane the fuel is used to control the position of the centre of gravity and hence the longitudinal stability of the aircraft. Each of the tanks must be interconnected with pipes for refuel on the ground, transfer of fuel between tanks during flight and cross-feed in the event of engine failure to provide system redundancy. Motor operated ball valves are commonly used to control the flow and isolate tanks. During fuel transfer operations, centrifugal pumps act as a source of flow and at other times are operated to scavenge and mix any water in the tanks.

For the purposes of describing a generic near-future aircraft fuel system, consider a wide-body long range airliner such as that shown in figure 1.1. The positions of the tanks are indicated.

Consider the fuel system for such a twin engine aircraft, the tank and pipe layout of which is shown diagrammatically in figure 1.2. This simplified system, whose exact definition is given in chapter 7, consists of a single tank in each wing, a centre tank in the main fuselage and a trim tank in the horizontal stabiliser. Each wing tank also

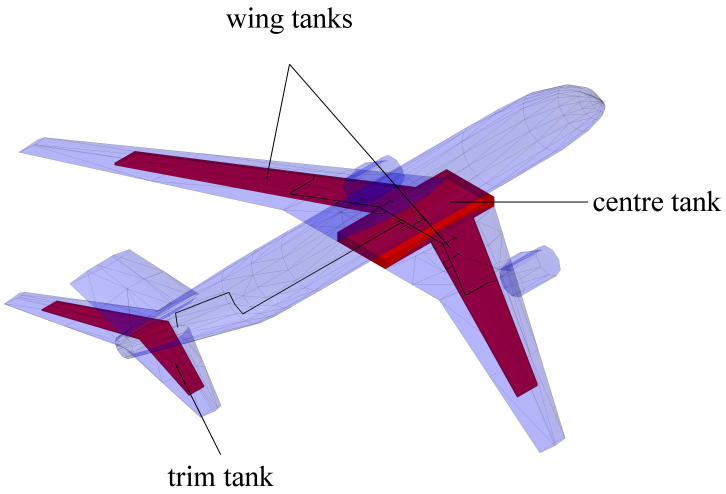

Figure 1.1: generic near-future, wide-body, twin engine civil jet transport aircraft

contains a smaller collector cell for each engine which is maintained full throughout the flight in order to provide a constant flow of fuel to the engine even during negative-g manoeuvres. Fuel transfer between the wing and centre tanks occurs along the refuel/transfer gallery using the pumps either in the wings or the centre tank. Fuel transfer between the trim tank and the centre tank occurs along the trim gallery using either the pumps in the trim tank or the centre tank. The forward cross-feed gallery exists for emergency cases, where either engine can be fed from the wing tank on the other side of the aircraft. The refuel/transfer gallery is also used for refuel of the aircraft on the ground.

The weight of the fuel in the wings will counteract the bending moment due to lift, and is beneficial in all stages of the flight. Therefore, the wing tanks are primarily used for fuel reserves storage, and are the last tanks to be used in flight. Here, the wing tanks consist of a single section, although in actual fact the wing tank is usually made up of several distinct tanks allowing better distribution of fuel along the length of the wing for bending moment relief and to provide protection against fuel loss through tank failure.

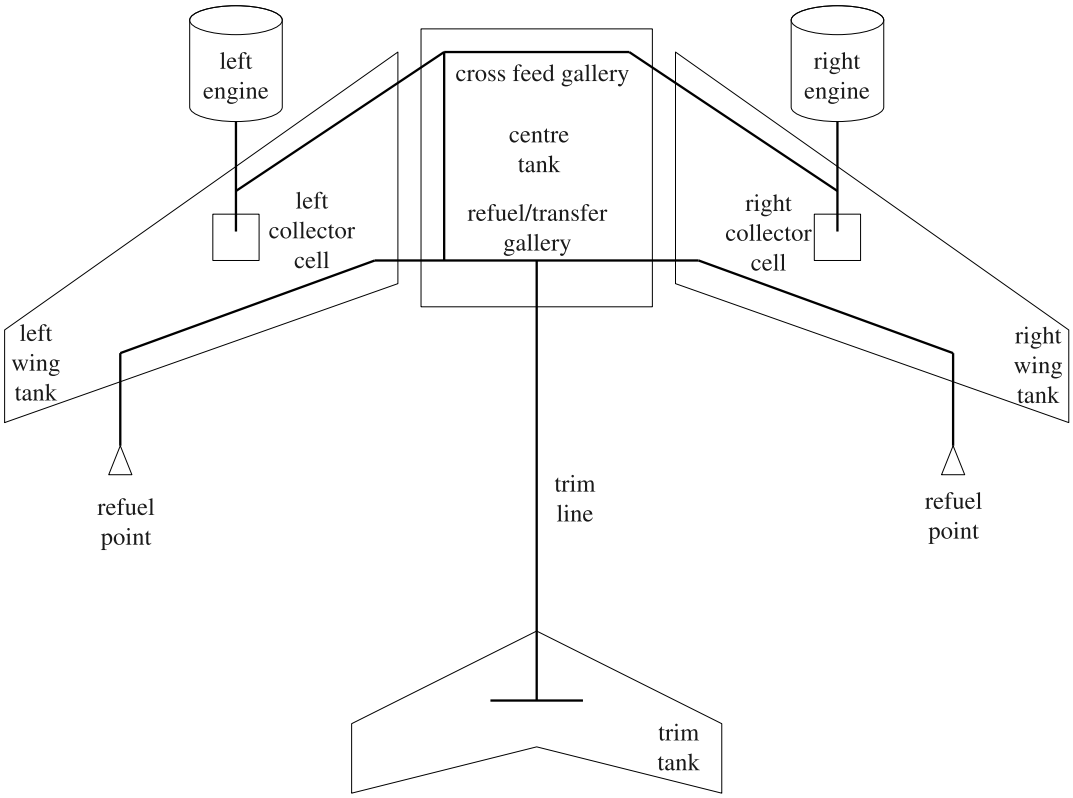

Figure 1.2: general fuel system tank and pipe layout

The centre tank is the main tank for engine feed, and is typically the largest tank in longer range aircraft. In some cases, if the wing tanks are sectioned, then the inner wing tanks can be used in place of a centre tank, although most longer range aircraft use a centre tank for extended range. For engine feed, fuel is transferred from the centre tank to the wing tanks, where it is used to maintain full collector cells. During flight, fuel can be transferred from the centre tank to the trim tank to move the aircraft centre of gravity to the rear, or vice versa to move the centre of gravity forwards. This method of centre of gravity control in subsonic civil transport aircraft is unique to Airbus aircraft and results in significant fuel burn improvements through trimming of the aircraft.

If no centre of gravity control is used to provide longitudinal trim, then it must be accomplished using the horizontal stabiliser surface, more correctly referred to as the Trimmable Horizontal Stabiliser (THS). This can be angularly deflected to provide the correct lift force balance. Such a system is distinct from a traditional trimmable elevator

control surface in the ability to change the deflection angle of the entire horizontal surface, rather than a secondary control tab on the rear of the elevators.

All aircraft must be capable of trimming in order to maintain level flight. Doing so using the control surfaces however introduces an extra drag component, and hence an increase in fuel burn. If the THS is not deflected, but the aircraft is balanced using the fuel distribution, then a minimum fuel burn condition will be reached. This balancing of the aircraft will also result in a slightly reduced tailplane lift loading in the downwards direction, which in turn reduces the loading on the wing. These reduced loads result in further drag reductions. Figure 1.3 shows this effect. It is estimated that the overall effect of centre of gravity control on cruise fuel burn for an Airbus A310 aircraft is a reduction of 1.5% [1]. Current systems operate the trim transfer pumps and valves using a simple on-off control logic to maintain the centre of gravity within 0.5% mean aerodynamic chord (MAC) of the rear limit.

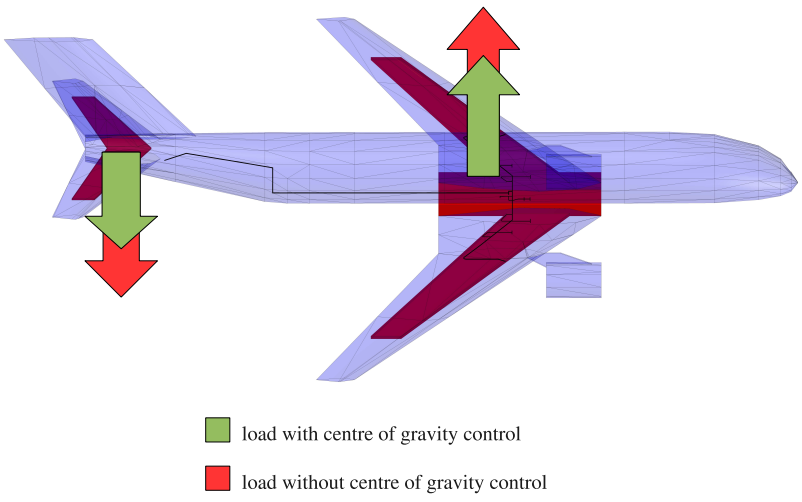

Figure 1.3: effect of centre of gravity control on lift forces

Trim of aircraft using centre of gravity is commonplace in military aircraft, where the ability to improve manoeuvrability to maintain tactical advantage is highly desirable. In civil aircraft, the technique was pioneered in Concorde, where the movement of

fuel was also useful for cooling the aircraft, and later in Airbus long range aircraft. It is also common in high speed power boats, where water ballast is used instead of fuel, although commonly for reducing pitch angle to improve view, rather than for performance advantage. Such a system tends to be operated in both directions - i.e. maintains the ability to shift the centre of gravity both forwards and rearwards. In aircraft, where the changes in centre of gravity are as a result of fuel burn, under normal operating conditions only forwards transfer is required.

The pumps for fuel transfer between trim and centre tanks, and between the centre and wing tanks are, in general for mid-sized civil airliners, centrifugal pumps. Typically, they operate at pressures in region of 2bar. Traditionally these were driven by AC induction motors, but current trends in aircraft electrical generation systems have seen a move to brushless DC motors. Decisions regarding pump motor supply are not simple, and are often influenced by the requirements of other aircraft systems to meet overall aircraft weight and certification targets. Future systems are likely to focus on simplicity and improved reliability, and as such may tend towards AC motors which operate at variable frequencies. The pump and motor assemblies are typically attached to structural elements within the fuel tanks, such as wing spars, and are fully submerged in the fuel. This means that isolation of the electrical supply from the fuel is extremely important, as is heating of the fuel by the electric motor.

The pumps currently have a pressure switch immediately downstream of their outlet port, which provides an indication if the pump is working or not. The pumps are typically running throughout the entire flight if there is fuel in the tanks. This is done in order to scavenge water in the tank and keep it well dispersed in the fuel. Since the fuel tanks are vented to atmosphere, water will always be present in the tanks to some degree, but extensive measures are taken to keep its concentration to a minimum. Some centrifugal pumps, typically in the centre or wing tanks, are also used to drive jet pumps for this purpose. The engine collector cells are maintained full throughout flight by either centrifugal or jet pumps, which again play a role in scavenging water. Engine feed from the collector cells tends to be accomplished by centrifugal pumps, although this can be boosted by gear pumps within the engine itself.

All tank isolation valves are commonly motor driven ball valves. They are driven by DC motors, and currently operate solely as on-off flow controls. Typical aircraft valves are designed to nominally operate at 18, 24 or 36 VDC, but in reality the supply voltage to the valve can lie anywhere in this range due to the variability of the electrical supply, which means the valves will typically close in 2 to 4 seconds. Work continues in this

area to produce constant speed actuators which result in a valve closure time which is independent of the supply voltage. Like the pumps, simple pressure switches can be used to indicate whether there is flow through the valve or not, although this is not typical of current aircraft. More typically, reed switches are used on the valve to determine if the valve is open, shut or somewhere in between. Such signals form the basis of current fuel system health monitoring.

Electrical power for driving fuel pumps and valves, as well as other secondary systems such as cabin lighting, is generated mechanically direct from the engines. This power is then regulated and distributed around the aircraft over a complex network. Historically aircraft electrical generation and distribution systems in civil airliners are based on a fixed frequency AC supply (115V at 400Hz). This is a well proven means of generating and delivering power, but has significant drawbacks in terms of weight and mechanical conversion reliability. The most recent Airbus aircraft has seen a switch to a variable frequency AC supply (115V in the range $350 - 800$Hz). In this case, the electrical generator can be driven directly from the engine, removing the need for mechanical conversion, reducing the system weight. The drawbacks include the variability of the supply frequency to the motors, resulting in variable pump speeds dependent on the engine speed, or the variation in valve closures mentioned previously.

Many military aircraft currently use DC electrical generation and distribution. This type of system lends itself well to situations where variable speed drives are used, but there exist significant health and safety problems with the demonstration of safe insulation of power busses carrying fault currents. Such systems remain the subject of investigation for civil applications.

The fuel level in each tank is monitored constantly throughout flight in order to determine the total quantity of fuel on board, its distribution throughout the aircraft, low or high level detection and the aircraft lateral and longitudinal centre of gravity. Level sensors are commonly capacitance probes, backed up by a secondary level detection system using dissimilar hardware. These are used, along with the aircraft's attitude and fuel density, to calculate the fuel quantity in each tank. These individual fuel tank quantities are summed and combined with the known aircraft and load weights to find the current aircraft gross weight and its estimated centre of gravity. The lateral centre of gravity is used to determine any imbalance in the aircraft as a result of improper fuel distribution, whereas the longitudinal centre of gravity is actively controlled to provide trim. The longitudinal centre of gravity must be maintained within certain limits for stability and control.

1.2 Current Aircraft Fuel System Operation

Consider the case where each tank is full at take-off (such a case might represent a maximum range flight with part load). During take-off and climb, fuel is burned from the centre tank only via the wing tanks, causing the centre of gravity to move aft. When it reaches a predetermined aft limit, fuel is transferred from the trim tank to the centre tank in order to maintain the centre of gravity position within the aft limit control band, but only above a predetermined altitude. The transfer pumps remain on whenever any fuel is present in the tank, in order to mix any water present fully with the fuel, by either using jet pumps or by spilling pumped fuel back to the source tank when pumping against a shut valve. The transfer valves are opened and shut as necessary to control flow of the fuel. Once the trim tank is fully depleted, the valves and pumps are shut off, and fuel is burned from the centre tank. Once the centre tank is depleted, the wing tanks will be used.

Consider the more detailed diagram of the fuel system shown in figure 1.4. Throughout the flight, the engine feed pumps P1, P2, P3 and P4 are always on to provide both fuel supply to the engines, and also to drive jet pumps for water mixing. The use of two pumps in each collector cell allows the system to operate in the event of a pump failure, or under certain reduced electrical supply conditions. The engine isolations valves, 1 and 2, are always open to allow fuel flow to the engine. During take-off, all other pumps are off, and all other valves are shut, resulting in fuel burn from the wing tanks only.

During the subsequent climb, the trim tank transfer pumps, T1 and T2 are switched on if there is fuel in the trim tank, although valves L, M and N remain shut while the aircraft is below the predetermined altitude. The transfer pumps are used purely to mix any water that may be present in the tanks with the fuel. To allow transfer of fuel from the centre tank to the wing tanks, and hence the engines, transfer pumps T5 and T6 are switched on and valves C, D, E and F are opened. This results in the wing tanks remaining full, whilst the centre tank level will reduce, causing the centre of gravity of the aircraft to move rearwards.

Above the predetermined altitude, valves M and N are opened if the centre of gravity moves rearwards of the aft limit, allowing fuel to flow from the trim tank into the centre tank, causing the centre of gravity to move forward again. The transfer pumps T5 and T6 remain on, and valves C, D, E and F remain open to allow transfer of fuel from the centre tank to the wing tanks. Once the centre of gravity has moved forward of a

predetermined control band, the valves M and N are shut again. This on-off control will continue throughout the flight. Transfer pumps T1 and T2 continue to operate to mix any water in the tanks with the fuel, provided there is still fuel in the trim tank. Once the trim tank is empty, transfer pumps T1 and T2 are shut off.

At the end of the cruise, the aircraft begins its descent. Above the predetermined altitude the fuel system continues to operate as it did in the cruise. Below the predetermined altitude the trim line isolation valves M and N are shut. Transfer pumps T5 and T6 continue to operate, and valves C, D, E and F remain open provided there is fuel in the centre tank. Once the centre tank is empty, pumps T5 and T6 are shut off, and valves C, D, E and F are shut. Fuel is then only burned from the wing tanks.

During landing, the fuel system operates in the same manner as in take-off. The engine feed pumps P1, P2, P3 and P4 remain on, and valves 1 and 2 are open. All other valves are shut, and all other pumps are off. The other pumps and valves not mentioned in

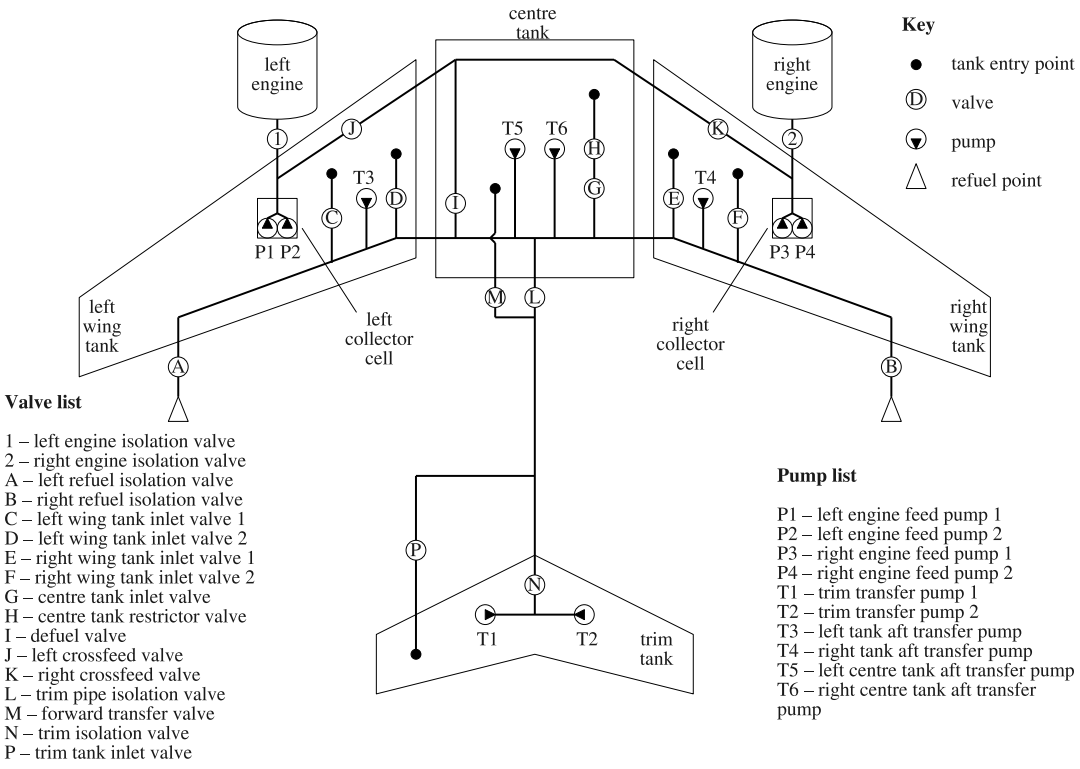

Figure 1.4: detailed diagram of aircraft fuel system showing tanks, pipes, valves and pumps

the above description are not required for normal operations. Pumps T3 and T4 are used to transfer fuel out of the wing tanks, either to the centre or trim tank. Such an operation might be required in order to move the centre of gravity rearwards, or to defuel the aircraft. Valves A, B, G and H are used during refuel of the aircraft on the ground. Valves I, J and K are used in emergencies such as pump failure to supply either engine from tanks on either side of the aircraft.

Figure 1.5 shows a typical time history of the fuel distribution in each tank for a long range flight, with the time normalised by total flight time, t_0, and the maximum individual tank masses, m_0.

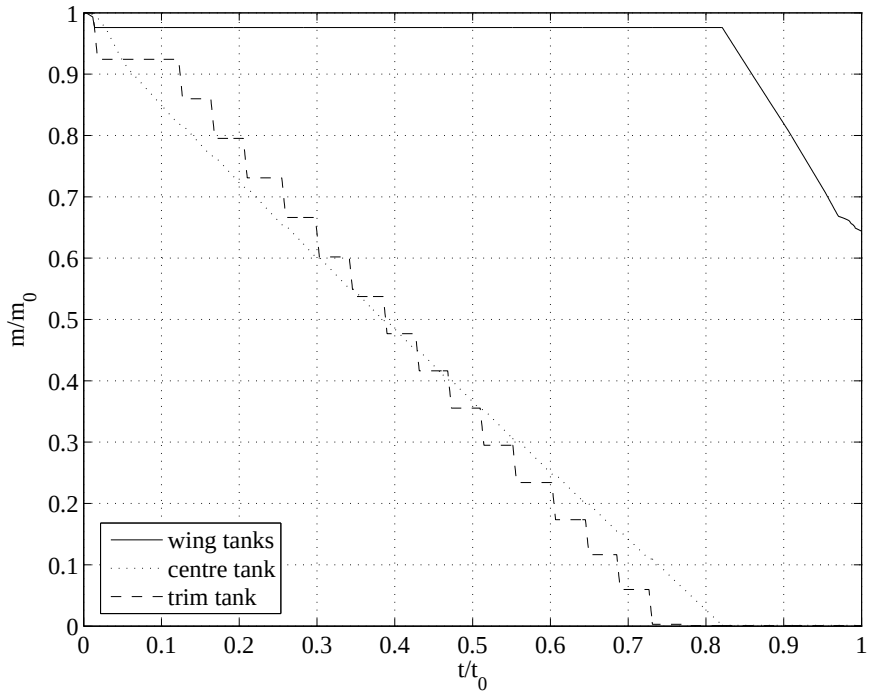

Figure 1.5: typical time history of fuel tank masses

1.3 The Active Valve and Pump Technology Project

A number of problems with the current fuel system design have been identified during discussions with Airbus UK, specifically related to fuel transfer targeting accuracy and the generation of fluid transients during sudden valve closures. Each of these has a

significant impact on the fuel distribution and hence operating cost of the aircraft during both ground refuel and in-flight transfer operations.

During ground refuel operations, fuel is supplied to the tanks via the refuel gallery, with an inlet to the system on each wing. The level of fuel in each tank is monitored, and once a pre-determined amount has been uploaded, the tank isolation valves are shut. Due to the length of the refuel gallery, which can stretch to around half the aircraft's wingspan, such valve closures can generate significant pressure surge and even transients. These must either be limited to avoid damage to the pipework and fittings, or the pipework needs to be overdesigned for these exceptional cases. Such overdesign inevitably leads to an undesirable gain in aircraft weight. Valve closures during in-flight transfers can lead to similar problems, especially in the trim to centre transfer gallery, as this is commonly around half the length of the aircraft, although the flow rates in this case are significantly less than the refuel case.

Flow through the valves at the almost-shut position is not well understood. This, combined with variable valve closure times as a result of variable electrical power generation, can lead to a greater quantity of fuel being uploaded to each tank than desired. It has been suggested such fuel quantity overshoots can be of the order of several hundred kilograms, leading to an undesirable increase in aircraft weight. Such quantity overshoots are also a problem during in-flight transfers, as it impacts the accuracy of the fuel management system.

Currently, the trim to centre transfer operations for centre of gravity control use a simple on-off control system to keep the centre of gravity within a specified control band. Whilst simple to implement and reliable, this system results in a centre of gravity position which is not optimal, and can mean a significant number of valve on-off cycles over the course of longer flights. This is known to have a significant negative impact on the valve life and associated higher maintenance costs. It has been proposed that a variable flow rate control system in this transfer route could solve both of these problems. The centre of gravity could be held at its optimal position during cruise by transferring the correct amount of fuel from trim to centre tank, without the need to open and shut valves repeatedly. Suggestions for how such flow control could be implemented include either throttling the flow with the existing ball valves, or introducing a speed control to the pump motors.

A research project was undertaken at the University of Bath to investigate the performance of valves during closure, pump operation and system modelling techniques

with a view to developing better component control and hence better flow control. This project was entitled "Active Valve and Pump Technology", which was planned to last 3 years, consisting of 3 PhD studentships and one post doctoral research officer position. The project was tasked with investigating the following:

- the effect of valve closure on pressure surge and pressure transients during both ground refuel and in-flight transfer operations;
- valve performance at the almost shut position to better understand fuel quantity overshoot;
- centrifugal pump performance during transient operations;
- system modelling tools, including valve, pump and pipe simulations;
- new valve and pump control techniques to improve system performance during both refuel and in-flight transfer.

1.4 Project Rôles

The research was split into 4 broad areas of responsibility between the 3 postgraduate researchers and the post-doctoral researcher. In general, the postgraduate researchers were tasked with analysing component performance, with a view to bringing these together for system analysis. The post-doctoral research officer was tasked with designing and building the test rig.

The component analysis areas of the project were broadly split as follows:

- Motor driven ball valve - analysis of valve performance in the almost shut position and generation of pressure transients;
- Electrical supply - investigation of modelling methods for AC motors and investigation of other drive technologies for future systems;
- Pump technology - development of pump simulation and modelling tools, to be applied to system simulations of the benefits of new control strategies.

It is the latter of these which is reported on hereafter. In subsequent discussions, these three project areas will be referred to as the Active Valve, Electrical and Pump projects respectively.

1.5 Aims and Objectives of the Pump project

The Pump project, itself a part of the Active Valve and Pump Technology Project, aimed to:

- develop generic centrifugal pump models which consider behaviour under steady-state and dynamic operating conditions, and during variable speed operation;
- investigate the benefits of variable fuel transfer rate in the trim to centre transfer route during flight, in terms of both the aircraft level (fuel burn), and the system level (number of valve cycles);
- demonstrate how the control of the pumps in the trim to centre transfer route could be changed to achieve variable fuel transfer rates;
- discuss how system simulations could be used to develop system health monitoring and fault detection tools.

1.6 Research Methodology

In order to achieve the aims set out in section 1.5, It was proposed that the Pump project would follow the methodology described below:

1. Perform a literature review to assess methods of centrifugal pump modelling
2. Use a test rig to develop a generic pump modelling method, an AC induction motor modelling method and generate an understanding of the behaviour of other fluid-mechanical components in typical aircraft fuel systems
3. From these modelling methods, develop generalised component models which could be extended to other systems similar to the test rig, such as aircraft fuel systems

4. Develop an aircraft level fuel system simulation to analyse the impact of introducing variable speed drives on the trim transfer pumps

5. Use the pump, motor and system models to simulate in detail the trim transfer simulation from the aircraft level simulation, and investigate the effect of changing the control on the system behaviour

6. Draw on the experience of producing such a system simulation to discuss its usefulness in health monitoring and fault detection systems

A test rig, described fully in chapter 2, was built at the University of Bath to investigate pressure transients during valve closure. This rig was used to measure the behaviour of a commercial centrifugal water pump driven by a variable speed AC induction motor, and to investigate the pressure-flow characteristics of aircraft fuel pipes and fittings. From these measurements, it was possible to develop a generic pump model, based on non-dimensional versions of the pressure, flow and torque characteristics, and AC induction motor models. The pump modelling method was developed such that a model could be developed for different applications, such as aircraft fuel system simulation, using a minimal specification of the pump's behaviour, thus resulting in a pump model which was validated against experimental data.

For the aircraft level simulations, an existing fuel system simulation from Airbus UK has been extended to look at the impact of centre of gravity on the forces acting on the aircraft, and hence the fuel burn. This method is based on a simple three degree of freedom simulation of the aircraft during its whole flight, which includes a number of simplifying assumptions. These simulations allow an estimate of the trends of effects of changes in centre of gravity control, rather than definite numerical benefits.

The system level simulations have been conducted using an in-house fluid power simulation package called Bath*fp*. This uses well established fluid system analysis methods to simulate fluid flow in pipe lines, and has been used extensively for industrial analysis [2]. It uses both existing and user defined libraries of Fortran 77 code, representing each of the component models, and an advanced adaptive LSODA numerical integrator to perform time based simulations. It can be compared loosely with Matlab/Simulink[1], although its major benefit and aesthetic difference is the method by which components are linked. Whereas Simulink uses signal links, with perhaps two connections to represent individual pressures and flows, Bath*fp* uses the representation of a physical pipe, which incorporates the pressures and flow rates being passed back and forth between

[1] "Matlab" and "Simulink" are registered trademarks of The Mathworks Inc.

two models. Bath*fp* is not limited to purely hydraulic applications, and some simulations for this project include both electrical and control models.

Bath*fp* simulations of the trim to centre transfer gallery have been used to develop the control system necessary to implement the proposed variable flow centre of gravity control system. These simulations demonstrate the level of control which is required to achieve this flow control, as well as the benefits to the system in terms of pressure surge reduction and reduction of valve on-off cycles.

All of the simulations were based on a hypothetical aircraft definition, which has been chosen to reflect a typical near-future long range, mid-sized, twin-engined civil airliner. It is not intended to reflect an actual aircraft, nor are any of the results intended to give definitive answers to specific aircraft problems. The aim of the work is to identify key benefits from some changes to current control systems as a result of representative simulations, both of aircraft level performance, and system level. A full description of the aircraft definition and its derivation can be found in chapter 7.

1.7 Scope of Thesis

This thesis describes the research conducted to achieve the aims and objectives set out in section 1.5, following the methodology described in section 1.6. It consists of 8 chapters, whose content is summarised below.

Following this introductory chapter, the test rig design and function is described in chapter 2. Chapter 3 describes the development of an existing fuel system simulation package to determine the benefits of variable speed fuel pumps in the trim to centre transfer route of a fictional aircraft. This examines the trends in the fuel burn and valve cycle reductions of different pump and valve control strategies. There then follow two chapters which describe the development of component models of the pump, motor and some fluid network components based on the test rig measurements. The first of these, chapter 4, describes the components' behaviour under steady-state operating conditions, and the second, chapter 5, their behaviour under dynamic operation. Chapter 6 then describes the validation procedure of all of these models, in terms of their combined predicted system performance. The component models are then used in chapter 7 to develop a simulation of the trim to centre transfer route described in chapter 3. This has been used to investigate how the control strategies suggested in

chapter 3 might be achieved in practice, and there follows a discussion of how such a simulation could be used to form part of a system health monitoring and fault detection tool. Finally, chapter 8 draws the thesis to some conclusions and outlines proposals for areas of further research.

Chapter 2

Test Rig

A test rig was built at the University of Bath to allow validation of modelling methods for each of the components under study in the Active Valve and Pump Technology project, and to validate the resulting system simulations. The design is modular, such that the behaviour can be changed depending on the focus of the tests. The main test rig for the AVPT project consists of a large, heated pressure vessel containing around 2000L of water connected to a commercial twin stage vertical centrifugal water pump, supplying flow through around 17m of 1.25″ nominal bore aircraft fuel pipes, via an aircraft fuel system motor driven ball valve, supplied by Parker Aerospace. A PC is used to record the signals from various pressure and temperature sensors, the flow rate, pump speed and valve angle, which are all collected using a 16 channel data acquisition card and signal conditioning suite.

Water has been chosen as the working fluid rather than aircraft fuel for safety reasons. Synthetic aircraft fuel alternatives were considered, but these presented health and safety concerns. The use of water greatly simplifies modification and repair of the test rig, although it also introduces greater uncertainty into the analysis of the results, as differences between water and aircraft fuel properties must be taken into consideration.

Figures 2.1 and 2.2 are photographs of the test rig, looking from the tank to the bend and a view of the pump and tank.

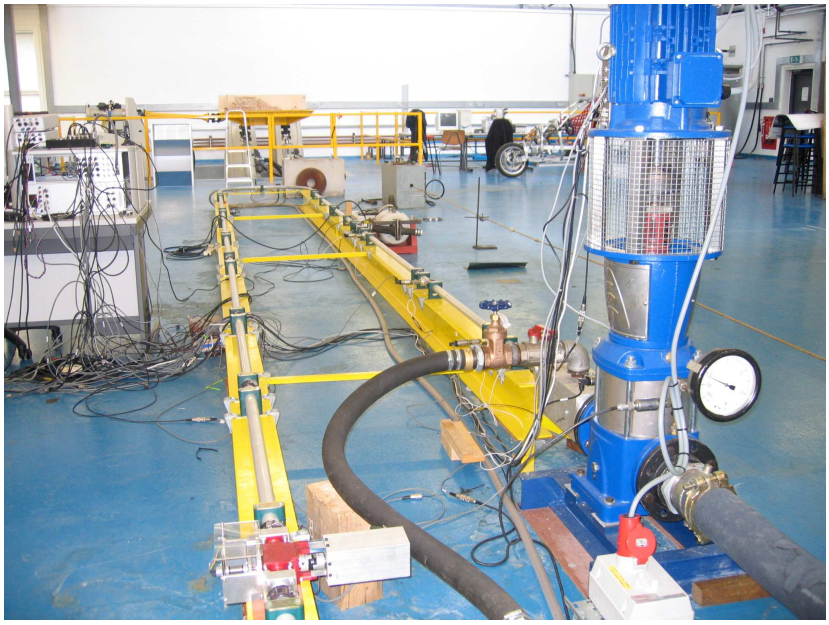

Figure 2.1: view of the test rig, looking from the tank towards the bend

Figure 2.2: view of the test rig, looking from the side at the pump and tank

2.1 The Hydraulic System

The water temperature in the tank can be held at a constant temperature in the range from ambient air temperature to 70°C using a 24kW immersion heater. The water heater can be controlled using a simple commercial control system in order to maintain a fixed tank temperature. This allows the performance of the system to be analysed over a range of fluid properties. The tank can be used as a sealed pressure vessel, and can be partially evacuated to −0.5bar (gauge) in order to investigate the effect of reducing the vapour pressure on cavitation in the system, mimicking real aircraft fuel systems at altitude. The system can be isolated from the tank using two ball valves.

The tank is connected to the inlet port of the pump via two 90° bends and a 1m length of 100mm diameter flexible hose. This serves to isolate the tank from any pump vibration and reduce the need for exact alignment of the tank outlet and pump inlet ports.

A Lowara SV66 commercial water pump was selected for the rig in order to supply the system with around 500L/min of flow and a pressure level of around 1.5bar at the valve inlet. This provides similar flow and pressure conditions to those typically found in the refuel line of an aircraft fuel system. A fuel pump from Parker Aerospace was considered, but was impractical given the use of water as the working fluid. The differences between the water pump and typical fuel pumps must be considered whenever looking at extending the modelling tools developed with the test rig to fuel system simulations. The pump is driven by a three phase, two pole AC induction motor, supplied from a frequency inverter in order to allow variable speed operation. This means the conditions within the rig can be altered to allow a large range of pressures and flows which are representative of current Airbus aircraft fuel systems during both refuel and fuel transfer operations. The pump is a centrifugal pump, with two impellers and diffusers arranged vertically in series. A cut-away CAD drawing of the impeller and diffuser arrangement is shown in figure 2.3. The shaft speed is measured by a magnetic pickup and toothed wheel assembly attached to the top of the pump-motor shaft coupling. An in-line torque transducer has been inserted into the shaft arrangement, thus separating the pump and motor. Four steel pillars were manufactured in order to provide the correct spacing and alignment of pump and motor. The pump-motor assembly is shown in figure 2.4.

In order to attach the 100mm outlet port of the pump to the 1.25″ (34mm approx.) aircraft pipes, a reducing section was manufactured from aluminium. This provides the

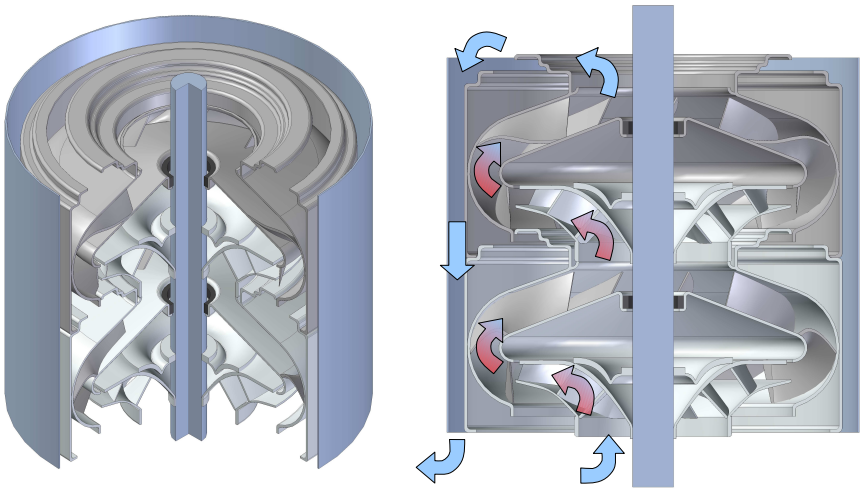

Figure 2.3: internal flow passage of Lowara SV66 centrifugal pump

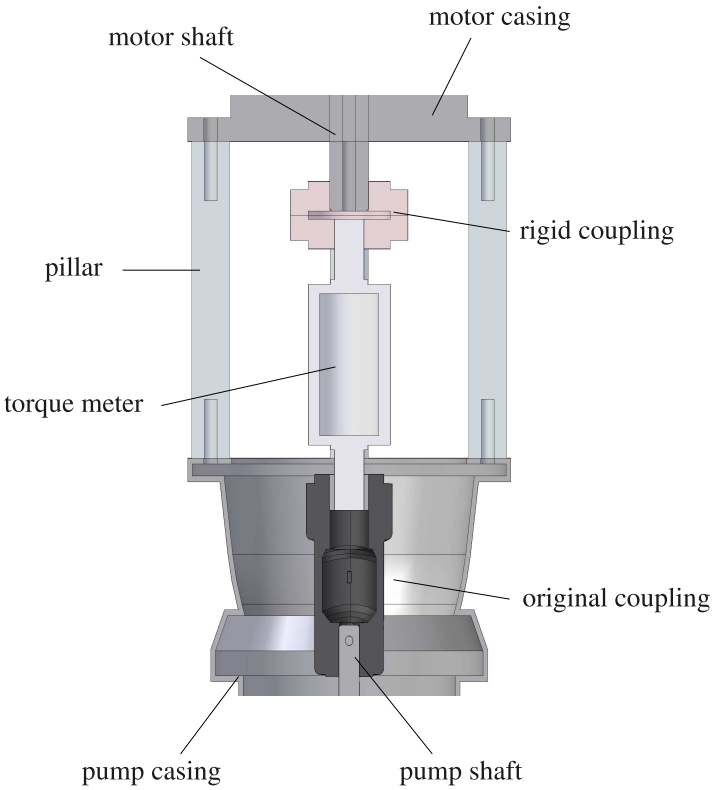

Figure 2.4: pump, motor and torque meter assembly

necessary reduction in pipe diameter over a 300mm long section. There is also a 1.5″ bore branch to the by-pass line, and a 8mm transducer port. The by-pass line allows operation of the main line at low flow rates, whilst maintaining a minimum flow rate of 500L/min through the pump, which is required over prolonged periods of running to cool the pump bearings. The bypass line consists of a 90° bend, gate valve to throttle the flow, ball valve to isolate the line and a 2″ bore flexible hose. The by-pass line can return to the system at one of two points relative to the flow measurement device (described later), depending on whether the total flow or the main line flow is of interest during tests.

The main pipework consists of a series of 1.25″ bore aluminium aircraft pipes of either 250mm, 1000mm or 1500mm lengths. The pipe wall thickness is greater than typically found in aircraft fuel systems for safety to allow for generation of higher pressures during sudden valve closure tests. These are connected together using standard aircraft pipe couplings from Stanley Aerospace. These allow flexible joints between pipes, and are used in aircraft to allow flexing of pipe joints in the aircraft wing and fuselage during flight. In aircraft, the couplings are typically fixed in the structure, with the pipes then floating in between joints. In the test rig, the pipes have been secured to I-section steel beams using plastic pipe clamps, effectively fixing the whole pipe to the structure. This secures the pipework in case of movement due to pressure transients in the system. The couplings do however still allow for longitudinal movement of the pipes to allow a slight stretching of the system and an investigation of the effect of coupling alignment on steady state pressure losses. Figure 2.6 shows a cut-away drawing of the pipe couplings, showing their constituent parts; (a) pipe ends, (b) o-ring seals, (c) inner metal sleeve and (d) outer clamp.

The 250mm long sections of pipe include bosses for pressure transducers and thermocouples. These were designed to be moved around the system, allowing the transducers to be moved to various positions. Two of the sections contain a single boss for Piezo-Resistive Pressure Transducers (PRPT), and four sections contain one PRPT boss and one thermocouple or Strain Gauge Pressure Transducer (SGPT) boss. Figure 2.6 shows one such section of 250mm pipe with a single PRPT boss. A 750mm long section with one PRPT and one SGPT/thermocouple boss was manufactured specifically for downstream of the motor driven ball valve, as this gives pressure measurements at the correct point for the valve analysis. Due to an error in manufacturing, the PRPT tips do not fit flush with the inner surface of the pipe, but instead sit in a small cavity in the pipe wall. Figure 2.7 shows a cut-away drawing of the pipe and boss, demonstrating the cavity in the wall.

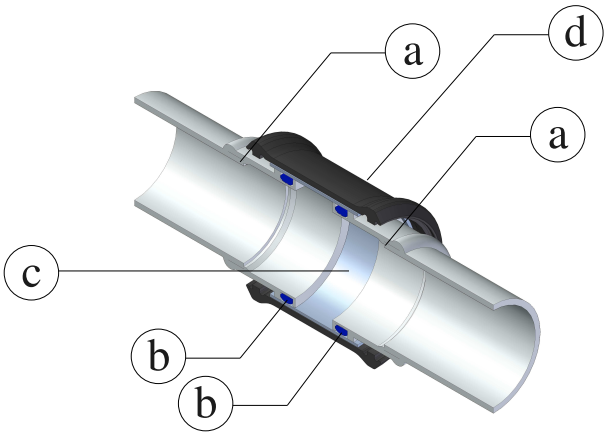

Figure 2.5: pipe coupling assembly

For the majority of the tests, the aircraft pipes were connected to the outlet of the reducing section via a gate valve and an aircraft coupling. However, during the pump transient analysis, the gate valve and the first few metres of the pipe work was replaced by a single section of Tungum hydraulic tubing of a similar bore. This contained pressure transducer bosses at suitable places for the secondary source technique, which is described in detail in section 5.1.7.

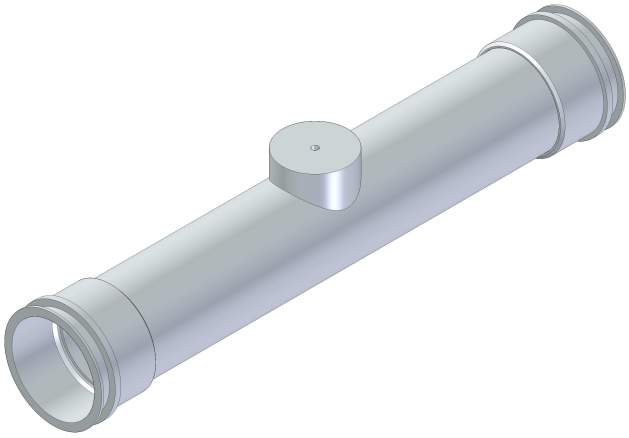

Figure 2.6: 250mm pipe section with PRPT boss

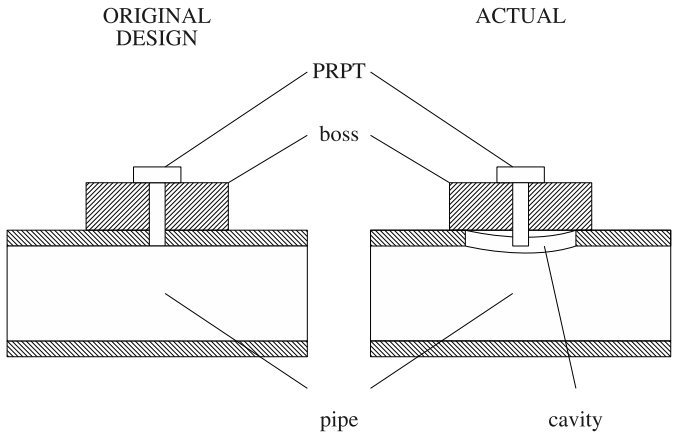

Figure 2.7: cut-away drawing of pipe and boss, showing manufacuring error and resultant wall cavity

The pipework contains a single 180° bend around 7m downstream of the pump. This is also 1.25″ bore, with a bend radius of around 0.5m, and is connected to the other pipes with the same pipe couplings. This does not try to replicate any particular aspect of an aircraft fuel system, but allows the return of flow to the tank without generating any significant reflection of pressure transients.

Two coupling sections have been machined from aluminium to connect the aircraft pipes to the motor driven ball valve. These replicate the sort of coupling typically used in aircraft fuel systems. The original drive motor for the valve has been replaced with a faster position controlled DC servo motor, capable of delivering more torque. This, when controlled externally, is capable of closing in a manner which follows a generic user input signal. The motor-valve assembly has been designed in order to shut in any period between 1s and 10s, thus replicating typical aircraft component behaviour. The valve angle is recorded by an angular potentiometer and an encoder on the motor drive shaft.

Downstream of the 750mm pipe section after the valve, the return line consists of various copper pipes and “T” sections. These include a filter branch and two extra branches to the system, one of which can be used for the by-pass return, all of which

can be closed off using ball valves. Downstream of these branches is a turbine flow meter, which is capable of measuring flows from 110L/min to 1100L/min. Details of the flow meter accuracy are given in appendix A. The return line then re-enters the tank near the top after a 90° bend and a 2m long section of 3″ bore flexible hose. Figure 2.8 shows a schematic of the test rig.

2.2 The Data Acquisition Suite

The signals from the pressure transducers, thermocouples, pump speed sensor, flow meter and valve angle potentiometer are connected to a Data Translation high speed acquisition board via amplifier and conditioning cards produced in-house by the department's instrumentation section. Full details of the data acquisition card can be found in appendix A. The signals from this acquisition board are recorded on a PC running Labview under Windows XP[1]. There are two manual controls for the pump speed and the valve angle for use in steady-state analysis. These controls also have a computer output mode, allowing the pump and valve to be controlled from within the data acquisition software.

The system is capable of measuring up to 16 signals at a maximum total sampling rate of 600kHz. A bespoke signal capturing program and GUI has been developed by the department's instrumentation section, which allows for the adjustment of the sampling rate, the real-time signals to be monitored and recorded, and a measurement of the time average of the signals to be recorded for steady-state analysis. The computer control of the pump is limited to setting a final steady-state demand speed. Control over the acceleration time is set from within the controller and frequency inverter supplied with the pump, and must be adjusted independently. The software has been designed to allow for a generic, user-defined position demand signal to be sent to the valve, allowing full control over the valve closure profile.

2.3 Fluid additive

To avoid corrosion and bacterial or fungal growth in the tank and pipework, two chemicals were added to the water. The first is a central heating additive, FERNOX CH-3.

[1] "Windows XP" is a registered trademark of The Microsoft Corporation

This renders water non-corrosive to steel, cast iron, copper, brass and aluminium, all of which are found in the test rig. It also protects against limescale damage, and contains a low-level biocide. The second chemical, FERNOX AF-10 is an extra biocide to prevent bacterial and fungal growth.

The impact of these chemicals on the fluid properties has been investigated. The variation of density and viscosity with temperature is well established for pure water, and full details can be found in the international standard [3]. However, it was felt that the presence of the additive may cause some change in both.

The density and viscosity can be easily obtained using standard densometers and viscometers, with samples of the fluid in a constant temperature bath. Using a sample of water from the test rig, the relationships between temperature, density and viscosity were measured. Figure 2.9 and 2.10 show the measured relationships, and their comparison against the data from the international standard. It became clear that the additive had no effect on the density to within the measurement accuracy of the equipment, although the viscosity of the test rig fluid can be said to be significantly higher than that for pure, distilled water. Tests conducted on distilled water showed very good agreement with data from the international standard, but the tests on the rig water are between 2% and 4% greater.

2.4 Data post-processing

The data acquisition software is capable of collecting either steady-state or transient data. The data is saved to a simple ASCII text file. A Matlab GUI has been programmed to allow these files to be read in to Matlab and analysed. This GUI, named AiRbus Test-rig Instrument Signal Toolkit, or ARTIST, allows the user to choose a file, load the data, apply filtering, measure pump speed and flow rate using the sensor pulse signals and plot graphs of any channel against time or against another channel. Figure 2.11 shows the ARTIST window, with a plot of the measured characteristic of the Lowarra SV66 pump. ARTIST also allows the user to perform a fast Fourier transform of a time based signal to analyse its frequency content.

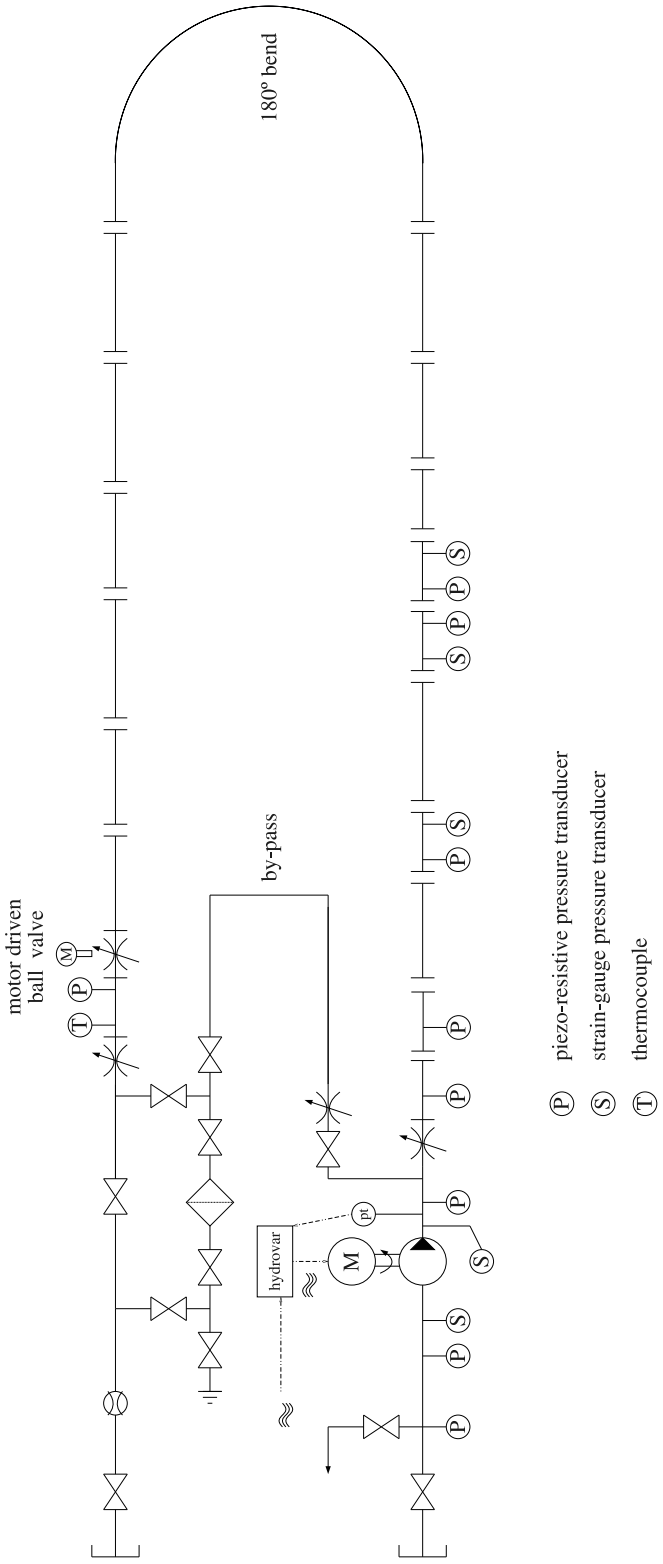

Figure 2.8: schematic of test rig

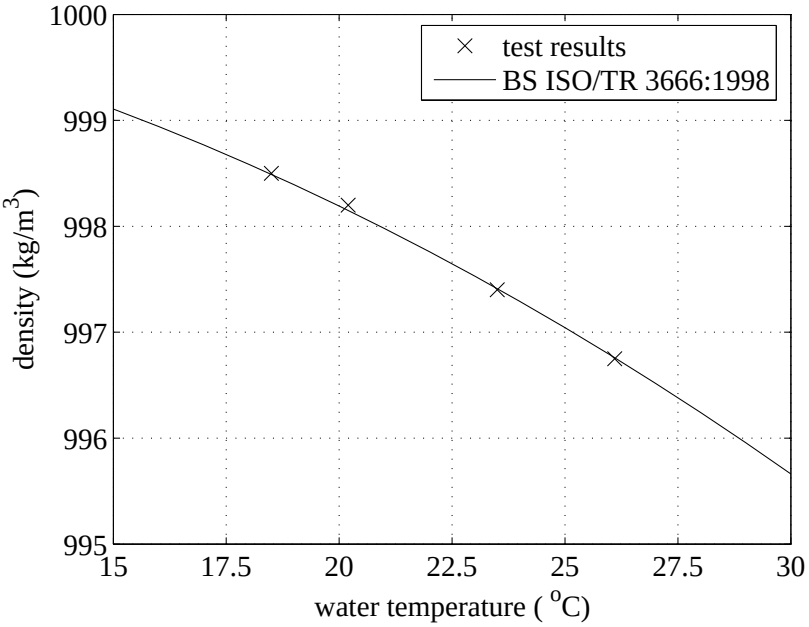

Figure 2.9: measured fluid density

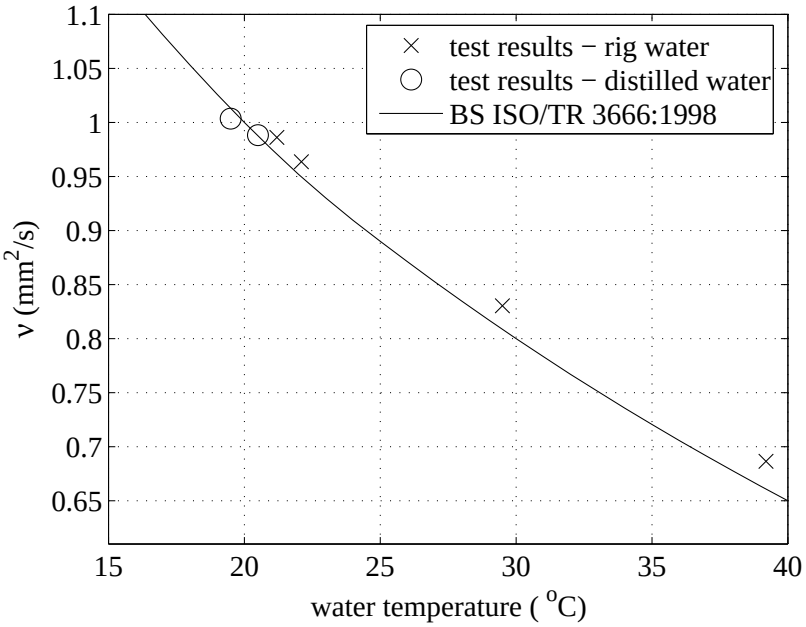

Figure 2.10: measured fluid kinematic viscosity

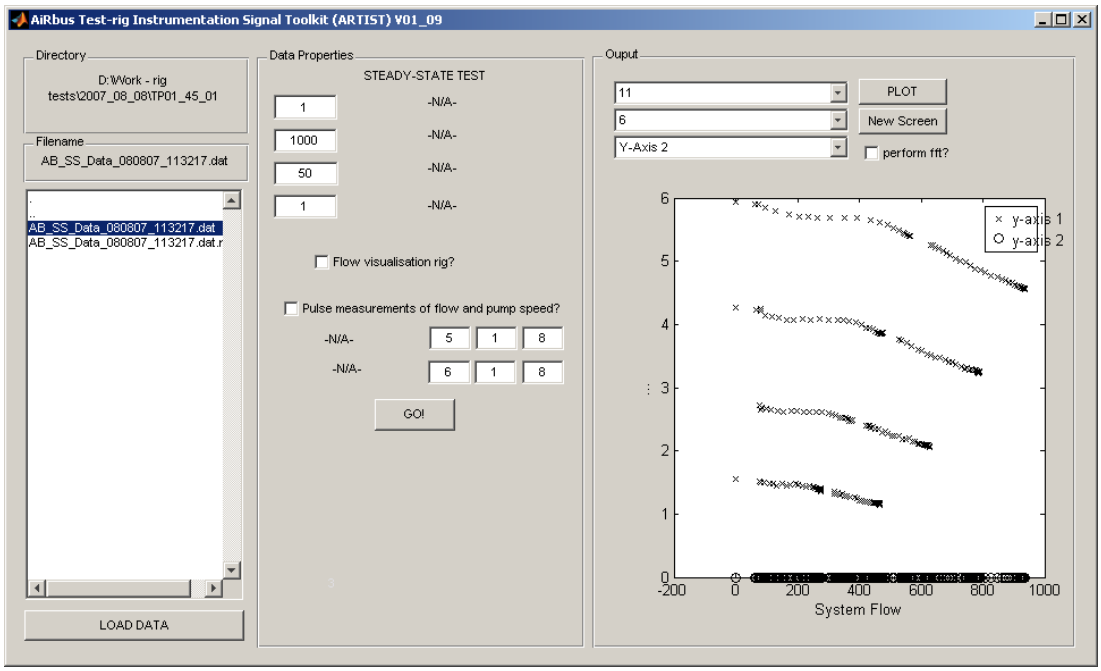

Figure 2.11: ARTIST Matlab GUI for post-processing test rig data

Chapter 3

Benefits of Variable Speed Pumps in Aircraft Fuel Systems

Optimisation of the fuel transfer from the trim to centre tank was identified in chapter 1 as a possible source of significant operating cost reduction. It has been suggested that a more exact match of supplied fuel flow rate to that required to fully balance the aircraft using centre of gravity control could reduce direct operating costs by reducing cruise drag, and reduce indirect operating costs by reducing valve on-off cycles, and hence valve wear. In order to investigate the benefits to be gained, an existing fuel system simulation package which determines the effect of fuel distribution during flight on the centre of gravity has been extended to examine the effect of centre of gravity location on cruise fuel burn. The simulation has been used to compare the current on-off control method and a proposed new variable fuel flow rate case.

This chapter describes the fuel system simulation package, and the simulations which have been conducted for a fictitious aircraft definition. The definition has been chosen to reflect a typical near-future, long-range, mid-sized, twin-engined civil airliner, and has been developed using standard initial aircraft design principles. It is not intended to reflect performance of an actual proposed aircraft, but to provide a best estimate for the purpose of this study. The definition technique is outlined in this section.

A number of results of these simulations are also presented in this chapter. They clearly indicate a small but significant reduction in fuel burn as a result of introducing variable fuel flows for the trim to centre tank transfer. The results highlight the benefit of the

reduction in valve cycle numbers as a consequence of the proposed control change. The study also demonstrates the negative impact on fuel burn if valve cycle reduction were to be implemented through changes to the current on-off system.

3.1 Modelling Tools

3.1.1 CGFlight

CGFlight is a Matlab/Simulink simulation of an aircraft fuel system, developed by Airbus UK. It is primarily used for fuel system control logic design and testing. Since it is proprietary software, this section will only briefly outline its purpose and fuctionality, rather than discuss it in detail.

The software performs a time based simulation of the centre of gravity of the aircraft during refuel operations on the ground and fuel transfer in flight over a user defined flight profile. The centre of gravity is calculated using fuel flow rates defined for the aircraft by the user, and a transfer logic, also input by the user. Through the front end Graphical User Interface (GUI), the user can then view the centre of gravity of the aircraft and the fuel tank quantities over the mission profile, and adjust transfer logic or aircraft parameters accordingly. It is an important tool for designing the transfer logic for a particular aircraft, and has been extensively validated using test flight data.

CGFlight contains three main parts; user files (to define aircraft, mission and transfer logic), the internal block diagram and the GUI. The aircraft is defined in terms of overall weights, fuel tank volumes and possible transfer routes of fuel. The centre of gravity and hence the moment of each tank about the aircraft's centre of gravity at a range of aircraft attitudes are stored in a library of files generated by an external program. The transfer routes determine the nominal fuel flow rate between each tank and to the engines. No flow dynamics are modelled, and the pumps and valves are assumed to act instantaneously. The mission profile is input in a number of data files, which supply the altitude, attitude, speed and fuel burn rate. The logic is a Matlab "S" function which acts like the aircraft's fuel management system to decide how fuel should be distributed around the aircraft by opening or shutting valves according to the flight profile and centre of gravity. The GUI allows the user to interact with the software by loading the initialisation file, which contains details of the initial fuel load and any faults which are to be injected into the simulation, and to view the outputs as

graphs of fuel volume against time, or as centre of gravity against aircraft weight.

Figure 3.1 shows a block diagram of the calculation at the heart of CGFlight. In order to implement the variable fuel flow rate concept, the block diagram was modified to include the elements in the dashed box. The centre of gravity target position is determined based on the aircraft definition and the current aircraft attitude from the flight profile. This is fed into the logic along with the current calculated centre of gravity in order to determine the required state of the valves and pumps. This could, for example, require that the trim to centre transfer is switched on to move the centre of gravity forwards. The valve and pump state is translated into flow rates between the tanks. This then is integrated over time to calculate the tank masses. From these and the library of tank moments, the center of gravity of the aircraft can be calculated. The moment files take into account the effect of the attitude of the aircraft on the centre of gravity. The simulation is set up to use a fixed time-step solver.

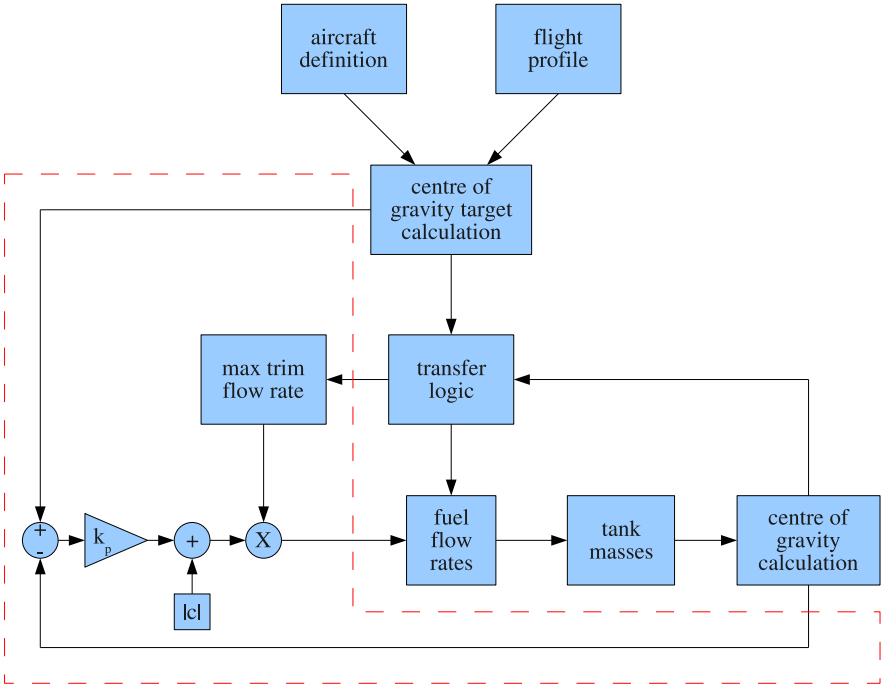

Figure 3.1: original CGFlight functionality, and additional proportional control feedback loop in CGFlight to implement variable fuel flow rate (shown in the dashed box)

The modification of CGFlight introduced the proportional feedback control system shown in figure 3.1. This finds the error in the centre of gravity position, which is then fed through a suitable gain. The result is used as a factor, which is multiplied by the

maximum flow rate for the trim to centre transfer route. This value is set to that which was used in the original simple on-off control case. The calculation of fuel flow rates, tank masses and centre of gravity then continues as before.

The centre of gravity target function is different for each aircraft. It is defined in relation to the aft limit for longitudinal stability and control. In the example simulation provided by Airbus UK, the target centre of gravity has been set to a constant pitching moment about the quarter chord of the mean aerodynamic chord of the wing (see section 3.1.2 for a definition). As this is hard-wired into the simulation, it has not been possible to update this for the aircraft definition used here. In the light of this, it must be stressed that the results in terms of fuel burn cannot be interpreted as absolute values which one might expect in a "real world" situation, but must be interpreted in terms of their relative magnitudes.

This simulation does not try to demonstrate how a variable fuel flow rate could be generated, but merely indicates the effect that it has on the centre of gravity of the aircraft. Further simulations, whose description follows in section 3.1.2, analyse the impact of the variable fuel flow rate on the mission fuel burn and the control structure which would be required to control pump speed to generate the variable flow rates.

3.1.2 AMPEC

The major limitation of CGFlight for this study is the independence of the fuel system preformance calculation and the flight profile. In its original state, CGFlight uses a fixed input of the aircraft's attitude and hence fuel burn to calculate the centre of gravity. This however, will not allow an investigation of the effect of fuel burn on the centre of gravity and vice versa. It was proposed that the flight profile could be calculated using a three degree of freedom simulation of the aircraft, which would require information about the centre of gravity and the weight of the aircraft from CGFlight. It would then return the fuel burn.

Using basic aircraft flight modelling principles to calculate the aerodynamic forces acting on an aircraft, a quasi-steady three degree of freedom simulation has been developed. It has been called "Aircraft Mission Performance Estimation Code", or AMPEC. In order for it to fit easily into the CGFlight simulation it has been developed in Matlab/Simulink. AMPEC also uses a fixed time-step solver in order to link with CGFlight. The impact of this on its accuracy has been assessed by running the same flight profile

with both a fixed and a variable time-step, and it has been shown to have a negligible effect on the calculated parameters.

Since AMPEC is designed to calculate the aircraft's performance from take-off until landing, the mission profile has been split into different sections, each of which require different calcuation routines and control conditions. The code is therefore designed to be modular, with a selection of the relevant mission section based on the aircraft's current situation, such as altitude and speed. The following sections describe how AMPEC is structured, how the aircraft is defined, the three-degree-of-freedom model, how each mission section is defined and how the calculation is performed.

AMPEC Structure

AMPEC has been designed to utilise both the robust Simulink equation solver and the ease of flow control within the Matlab "m" script language. The choice of current mission section, the calculation of orthogonal aircraft accelerations, the choice of relevant lift data and the interpolation of engine data is all accomplished using the Matlab scripts. The integration of the acceleration values to give velocities and displacements, and the feedback control loops are then handled in the Simulink environment.

Figure 3.2 shows a block diagram of the flow of data within AMPEC. The current centre of gravity and aircraft mass are supplied by CGFlight. These, along with the atmospheric data, altitude, speed and aircraft attitude data are used to decide which section of the flight is currently being executed. This mission section choice is passed to the wing lift curve slope block, which sets the wing lift to represent the wing and high lift devices in either take-off, cruise or landing configuration. The lift curve, mission segment and the aircraft's current condition are subsequently passed to the mission calculation block, which calculates the orthogonal accelerations of the aircraft. These are then integrated to give the velocities, and again for displacements. Two control loops are used. The first plays a dual rôle; it controls the attitude of the aircraft during climbs and descents in order to maintain a fixed speed at a fixed throttle setting, and it controls the attitude of the aircraft during cruise in order to maintain a steady altitude. The second loop is used during the cruise section in order to maintain a fixed Mach number and during the descent to maintain a constant equivalent airspeed (EAS).

The values of altitude, aircraft attitude, Mach number and fuel burn are returned to CGFlight. The values of individual tank masses, angles of attack of both the wing and

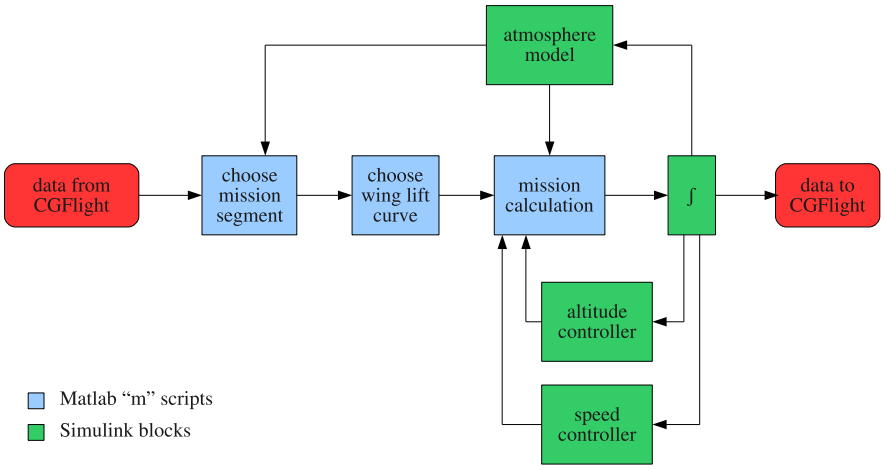

Figure 3.2: flow diagram of AMPEC calculation

the THS and the centre of gravity are also output to file for post analysis.

Aircraft Definition

AMPEC uses a simplified quasi-steady three-degree of freedom model to describe the aircraft during its flight. Roll and yaw are ignored; only pitch is considered. Moment of inertia effects are ignored - it is assumed that any rotation is quasi-steady. The weight of the aircraft acts through its centre of gravity, the lift from the wings through the wing centre of pressure and the lift from the THS through the THS centre of pressure. Thrust and drag forces act along axes which pass through the centre of gravity. The drag always acts in opposition to the direction of travel and the thrust along the aircraft's axis. The wing and body moment coefficient is said to act about the centre of gravity. Figure 3.3 shows the freebody diagram of the aircraft, and figure 3.4 shows the definition of the positions of the moment arms of each of the forces acting on the aircraft from the standard datum at the aircraft's nose.

The centre of gravity of the aircraft can be defined in one of two ways; absolute with reference to the nose datum, or more commonly with reference to the mean aerodynamic chord (MAC) of the wing. Figure 3.5 shows the planform of the wing and the definition of the chord, c, and span, s. The MAC, $\bar{c}$, can then be defined as:

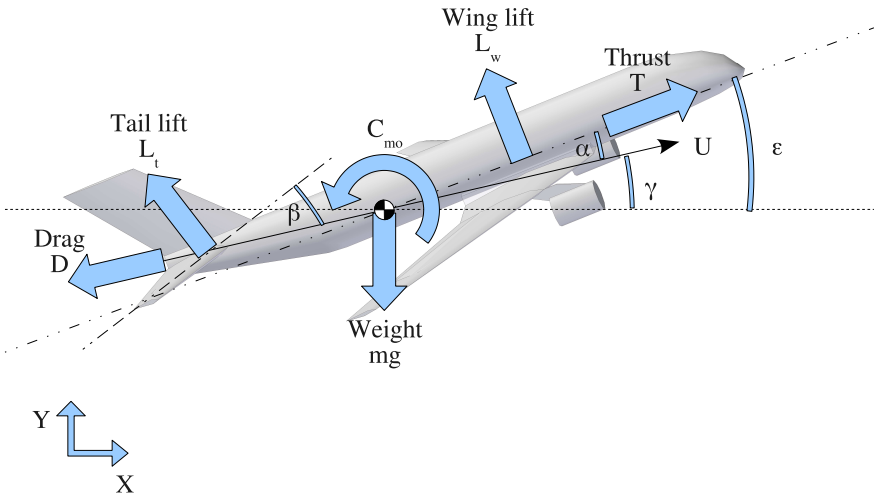

Figure 3.3: freebody diagram of aircraft for AMPEC analysis

$$\bar{c} = \frac{\int_{-s}^{+s} c^2 \, dy}{\int_{-s}^{+s} c \, dy} \tag{3.1}$$

The MAC is the chord-weighted average chord length of the wing, or is the chord of a rectangular wing, which has the same area, full aerodynamic force and position of the centre of pressure at a given angle of attack as the given wing has. The position of the MAC leading edge with respect to the datum, x_{mac} is then defined as the distance of the leading edge of the wing at the point spanwise where the chord length equals the MAC. The centre of gravity position, x_{cg} can then be defined as:

$$x_{cg} = x_{mac} + \chi \bar{c} \tag{3.2}$$

where χ is the centre of gravity position as a fraction of the MAC.

The global axes are defined as X and Y, and the aircraft has a velocity U, which

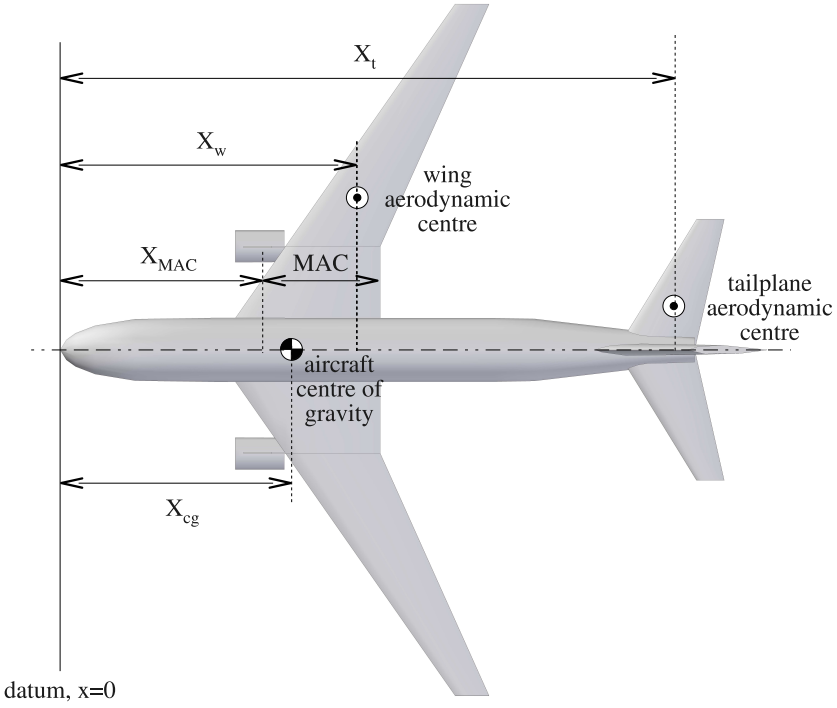

Figure 3.4: definition of characteristic aircraft lengths

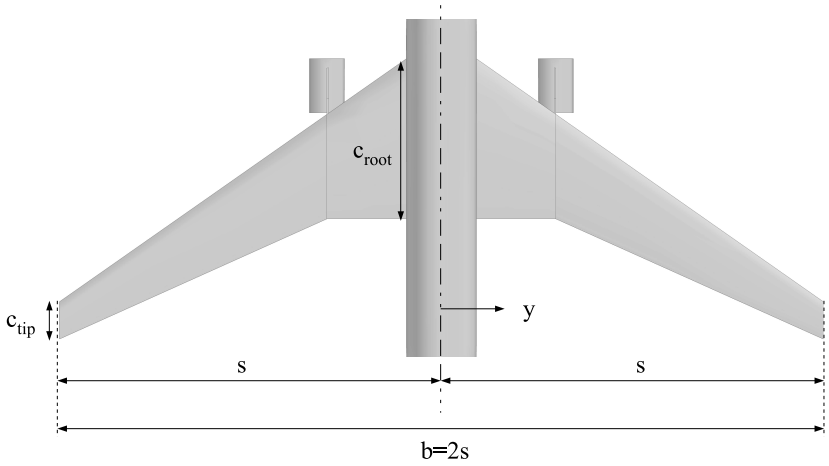

Figure 3.5: definition of wing planform

acts at an angle γ to X. The attitude angle of the aircraft, ϵ is defined as the angle between the aircraft's axis and X. The difference between the direction of travel and the direction in which the aircraft points is defined as the angle of attack of the wing, α. These angles are related by:

$$\epsilon = \gamma + \alpha \tag{3.3}$$

The angle of attack of the THS is defined as the difference between the THS deflection angle and the U vector, and is called β.

Any prediction of fuel burn will be dependent on the accuracy of the method used to model the performance of the engines. AMPEC uses a look-up table method to define the thrust and fuel consumption for a range of operating conditions. The user must supply two files containing the thrust and Specific Fuel Consumption (SFC) for a number of altitudes, Mach numbers and throttle settings in the correct format. These represent the engine performance during both take-off and for the rest of the flight. AMPEC then reads in these files and uses a multi-dimensional interpolation routine to find the engine performance in the simulation.

Mission Profile Definition

The mission profile describes the path which the aircraft follows from take-off to landing. It is intended to reflect a typical real-life commercial aircraft flight, and is split into five sections:

1. Take-off
2. Climb
3. Cruise
4. Descent
5. Landing

Each section is itself split into sub-sections, based on specific performance requirements set out in the Joint Airworthiness Requirements [4]. These are numbered 1 to 13 and

are described in detail in the following sections.

- The take-off section defines the aircraft's performance from the point where the aircraft begins to move until it has reached the end of its first segement climb to 457m (1500ft). This includes the taxi from gate to runway, ground roll to rotate speed, rotation to take-off attitude, initial climb to screen height[1] of 11m (36ft) and first segment climb.

  In AMPEC, this is modelled by:

  1. Calculation of fuel burn for the aircraft for a user-determined length of time at ground level, Mach 0.1 and the lowest throttle setting. During this period the actual aircraft speed remains at zero; the taxi is modelled simply as a fuel burn.
  2. For the ground roll, the take-off engine model is used. The horizontal and vertical accelerations are calculated from a force balance on the aircraft, including a Coulomb friction force with a coefficient of 0.02 [4]. This continues until the aircraft reaches a user-defined velocity, called the rotation velocity, V_r, which is a design parameter of the aircraft.
  3. When the aircraft reaches V_r, the aircraft attitude angle is increased linearly to the user-defined take-off attitude, which is again a design parameter. This rate of rotation is set at 2 degrees per second. The accelerations are again calculated from a force balance, with the friction force if the main wheels are still in contact with the ground. Once the speed has increased suitably, the lift force will be great enough for the aircraft to leave the ground, which may happen before the aircraft has reached its final take-off attitude.
  4. For the initial climb to the screen height, the attitude angle is held constant at the take-off attitude angle. The calculation continues as before until the aircraft reaches the screen height of 11m (36ft).
  5. The climb to the end of the take-off section at 457m (1500ft) continues as the climb to screen before.

  During the take-off, only the take-off engine model is used and the high lift devices are set to the take-off configuration, which corresponds to the slats and one stage of the flaps being deployed.

[1] This is an important stage of the take-off run when calculating the balanced field length of the aircraft as defined in JAR section 25 [4], although here is only used as a transitional stage between the aircraft leaving the ground and reaching the end of the take-off section.

Figure 3.6 shows the altitude, Mach number and attitude angle of an aircraft during the take-off flight section. The taxi portion (1) isn't shown. The climb to screen height occurs during the rotation to take-off attitude, so section (4) is not required, but instead the simulation moves directly on to section (5).

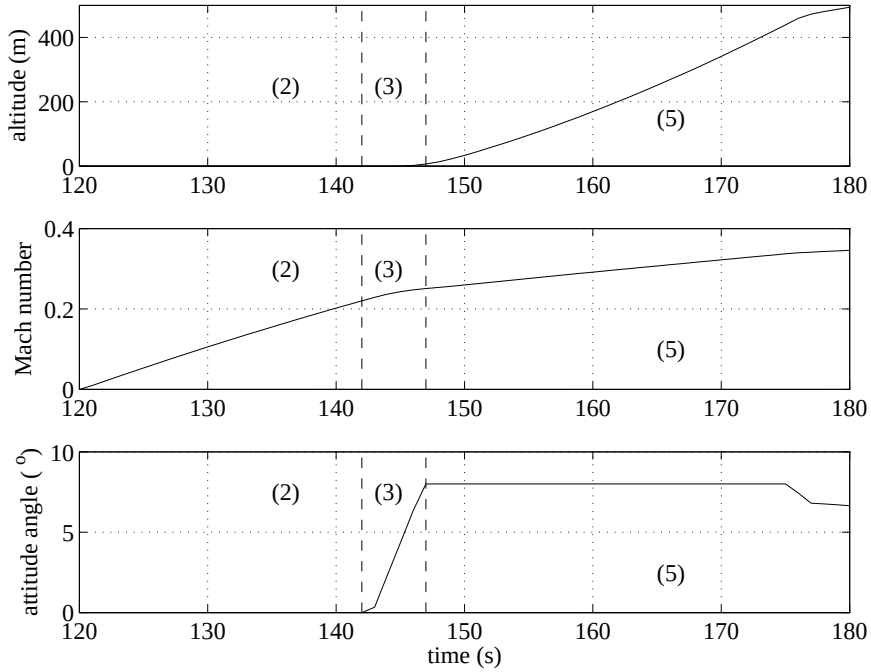

Figure 3.6: output of AMPEC for take-off section

- The climb section of the flight models the aircraft behaviour from the end of the take-off until the aircraft reaches its initial cruise altitude (ICA). The climb is split into three sections; climb to 3048m (10000ft) at 250kts (EAS), acceleration at 3048m (10000ft) to climb speed, climb to ICA at climb speed. They are modelled in AMPEC by:

  6. The high lift devices are set to the normal cruise setting, representing all flaps and slats retracted. The climb and cruise engine model replaces the take-off model, and the throttle is set to the maximum climb setting. The accelerations are found as before by the force balance. Now however, the rate of change of the attitude angle of the aircraft is varied using the "altitude controller" (figure 3.2) in order to maintain a constant speed of 250kts EAS.
  7. When the aircraft reaches 3048m (10000ft), the speed limit is increased to the climb speed. For this analysis, the climb speed was set to 250kts EAS to

avoid overspeed when the aircraft reaches ICA. In effect, this section is never used in this analysis but could be of use for different aircraft configurations.

8. The final climb segment is then the same as the first (6), with the rate of change of attitude angle being used to control the speed of the aircraft in order to maintain 250kts EAS until the aircraft reaches ICA.

Figure 3.7 shows the variation of altitude, Mach number and attitude angle against time for the climb section.

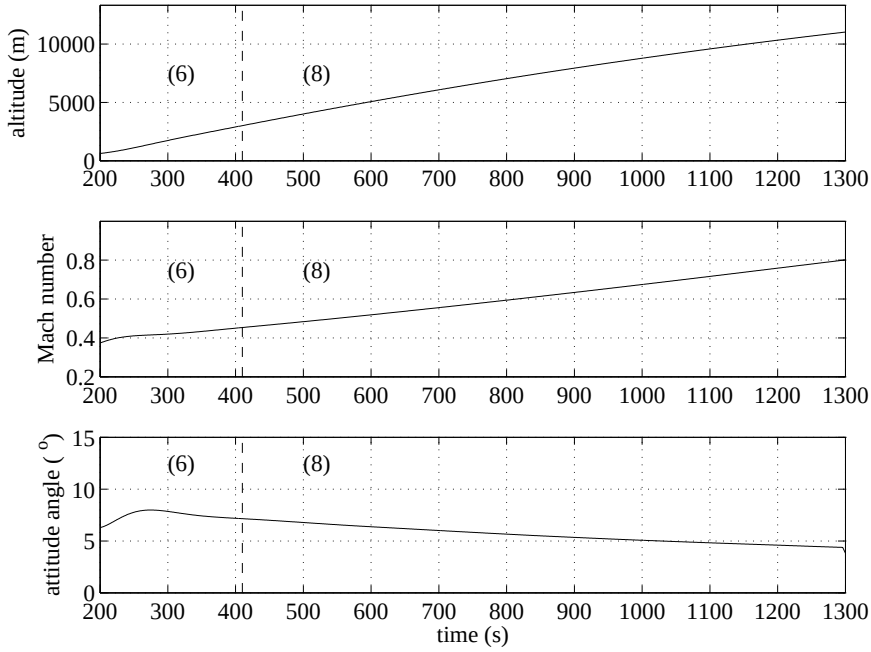

Figure 3.7: output of AMPEC for climb section

- In AMPEC, the cruise section is modelled as a simple constant altitude, constant Mach number cruise. Although a typical real-life cruise may include step changes in altitude over significant distances for fuel efficiency reasons, it was felt that a single altitude cruise would be best for comparing different fuel distribution logics on the cruise fuel burn.

9. The cruise has been modelled by performing a force balance as before. The rate of change of attitude angle and the throttle setting in the engine model are varied to control the altitude and Mach number respectively in order to accomplish a constant altitude and Mach number cruise. This continues until the aircraft has travelled a user-defined distance.

One consequence of this double control method is that the aircraft experiences a certain amount of oscillation in terms of altitude, attitude angle and Mach number during the transition from climb to cruise. This is obviously highly dependent on the control loops and their respective gains, which in turn are specific to a particular aircraft definition. Figure 3.8 shows the oscilation in altitude, attitude angle and Mach number for the example aircraft.

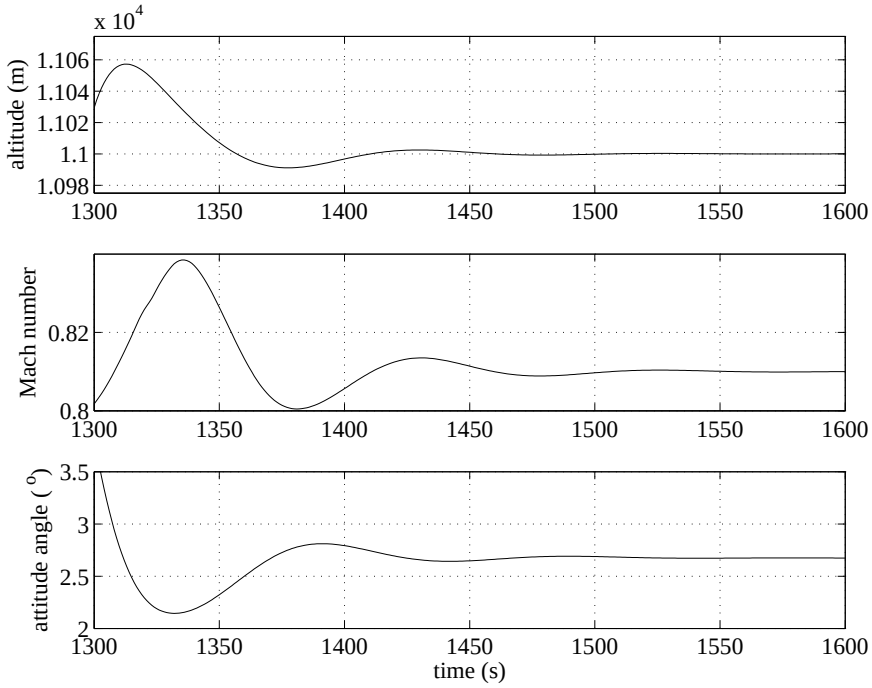

Figure 3.8: output of AMPEC at the beginning of the cruise section

Here, the controllers have been optimised manually to reduce the oscillations to acceptable levels. It can be seen that the altitude is kept in the range 10980m$<$ Y $<$ 11060m, and the Mach number does not exceed the maximum design speed of M0.91 for this aircraft. The oscilations die away after 4 minutes.

- The descent section analyses the performance of the aircraft from the end of cruise until the beginning of the landing section at 152m (500ft). It consists of three distinct segments; descent from the end of cruise to 3048m (10000ft) at the descent speed and a glide angle of $-4°$, a level deceleration to 250kts EAS at 3048m (10000ft), and a descent from 3048m (10000ft) to 152m (500ft) at 250kts EAS and a glide angle of $-3°$.

  This is modelled in AMPEC by:

10. The accelerations are found by the force balance. The rate of change of the attitude angle is varied in order to control the glide slope angle using the "altitude controller" (see figure 3.2), and the throttle setting is varied using the speed controller to maintain a constant speed equal to the descent speed.
11. When the aircraft reaches 3048m (10000ft), the speed limit is decreased to 250kts EAS. Like in the climb section, for this analysis, the descent speed was set to 250kts EAS to avoid overspeed when the aircraft finishes the cruise section. In effect, this section is never used in this analysis but could be of use for different aircraft configurations.
12. The final descent segment from 3048m (10000ft) to the beginning of the landing section at 152m (500ft) is modelled as the first descent section, but with a fixed glide slope angle of $-3°$ and a fixed target speed of 149kts EAS.

Figure 3.9 shows the variation of altitude, attitude angle and Mach number for the descent section.

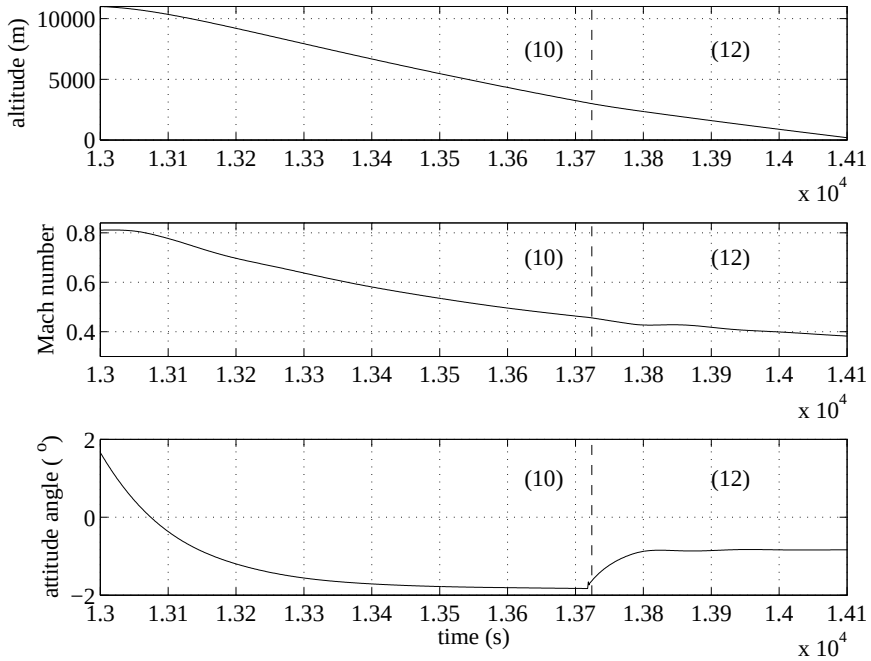

Figure 3.9: output of AMPEC for descent section

- The landing section is defined as the period between the aircraft passing through 152m (500ft) and the wheels touching the ground. In AMPEC, it is modelled as segment number (13), and is simply a continuation of the previous descent portion

(12) until the altitude is zero. The implementation of a full landing analysis was not thought to be necessary on the grounds that it would have no effect on the fuel burn calculations and would not increase the usefulness of the analysis tool.

Atmospheric Data

AMPEC uses the International Standard Atmosphere [5] to calculate the air temperature and pressure at any given altitude. The ISA assumes that the "near-earth" atmosphere[2] can be split into two distinct sections to model the troposphere and the tropopause. In the former, the temperature is said to decrease with altitude at a set rate, termed the lapse rate, L, and in the latter the temperature is constant. In the troposphere the temperature and pressure can be said to vary as follows:

$$T = T_0 - LY + \delta_{ISA} \tag{3.4}$$

$$p = p_0 \left(\frac{T}{T_0} \right)^{\left(\frac{g}{LR}\right)} \tag{3.5}$$

where $Y < 11000$m.

The tropopause temperature and pressure are given by:

$$T = T_0 - LY_{tropopause} + \delta_{ISA} \tag{3.6}$$

$$p = p_0 \left(\frac{T}{T_0} \right)^{\left(\frac{g}{LR}\right)} e^{\left(\frac{g(Y_{tropopause} - Y)}{RT} \right)} \left(\right. \tag{3.7}$$

The air density, ρ, and speed of sound, a, can then be calculated as:

$$\rho = \frac{p}{RT} \tag{3.8}$$

[2]that is, the atmosphere from sea level up to an altitude of 20km

$$a = \sqrt{\gamma RT} \tag{3.9}$$

Table 3.1 defines the nomenclature for equations 3.4 through 3.9.

symbol	parameter	units	value
g	acceleration due to gravity	m/s^2	9.81
L	lapse rate	°C/km	−6.5
R	specific gas constant	J/kgK	287.05
P_0	base pressure	kPa	101.325
T_0	base temperature	°C	15
δ_{ISA}	temperature delta	°C	0
γ	adiabatic index		1.4

Table 3.1: definition of terms in atmosphere equations

Performance Calculations

AMPEC uses a simple force balance method to calculate the accelerations in the X and Y directions. As it is a quasi-steady model, no account is taken of the moment of inertia of the aircraft about its pitch axis. Referring to figure 3.3, the accelerations in the X and Y directions can be calculated by:

$$\ddot{X} = \frac{1}{m}\left(T cos\left(\gamma + \alpha\right) - D cos\left(\gamma\right) - L_w sin\left(\gamma + \alpha\right) - L_t sin\left(\gamma + \beta\right)\right) \tag{3.10}$$

$$\ddot{Y} = \frac{1}{m}\left(T sin\left(\gamma + \alpha\right) - D sin\left(\gamma\right) + L_w cos\left(\gamma + \alpha\right) + L_t cos\left(\gamma + \beta\right) - mg\right) \tag{3.11}$$

The angle of attack of the wing, α, is found by:

$$\alpha = \epsilon - \gamma \tag{3.12}$$

where the angle of the velocity vector to the horizontal, γ, is given by:

$$\gamma = tan^{-1}\left(\frac{\dot{Y}}{\dot{X}}\right) \tag{3.13}$$

Lift and drag forces are calculated from user input lift curve data and drag polars for the aircraft and the THS respectively. The drag of the THS is defined seperately from the rest of the aircraft to allow AMPEC to estimate the additional fuel burn as a result of THS deflection. The lift curve slopes and drag polars are defined in terms of lift and drag coefficients by:

$$C_{L,w} = A\alpha + B \tag{3.14}$$

$$C_{L,t} = C\beta + D \tag{3.15}$$

$$C_{D,a} = d_{a,1}C_{L,w}^2 + d_{a,2}C_{L,w} + d_{a,3} \tag{3.16}$$

$$C_{D,t} = d_{t,1}C_{L,t}^2 + d_{t,2}C_{L,t} + d_{t,3} \tag{3.17}$$

These coefficients can be converted into forces by:

$$C_{L,w} = \frac{L_w}{\frac{1}{2}\rho U^2 S_{ref}} \tag{3.18}$$

$$C_{L,t} = \frac{L_t}{\frac{1}{2}\rho U^2 S_{ref} h} \tag{3.19}$$

$$C_{D,a} = \frac{D_a}{\frac{1}{2}\rho U^2 S_{ref}} \tag{3.20}$$

$$C_{D,t} = \frac{D_t}{\frac{1}{2}\rho U^2 S_{ref} h} \tag{3.21}$$

$$D = D_a + D_t \tag{3.22}$$

where h is the ratio between the wing and tailplance reference areas. Finally, the angle of attack of the THS can be found from performing a moment balance about the centre of gravity. Again, referring to figure 3.3:

$$\beta = \frac{-1}{C}\left(\frac{C_{mo} + (A\alpha + B)(x_{cg} - x_w)}{(x_{cg} - x_t)}\right) \tag{3.23}$$

3.1.3 PASS

The Program for Aircraft Synthesis Studies is a part of the Aircraft Design, Synthesis and Analysis digital text book provided by Stanford University [6]. It consists of a number of Java[3] applets embedded in the website to perform an initial design study of a commercial passenger aircraft using industry standard techniques, and a Java program to allow sensitivity studies of the aircraft design. In this case, the digital textbook has been used to produce an estimate of the design parameters for use in the AMPEC/CGFlight analysis, based on an input of a generic long-range mid-sized conventional passenger aircraft. The methods employed in the analysis will only be outlined here.

Inputs to the design analysis

In order to define a general specification for such an aircraft, basic data on the Airbus A350-900 was obtained from Airbus UK [7] and Flight International [8]. It should be noted that what follows is not directly related to the actual design of this aircraft, but

[3]Java is a trademark of Sun Microsystems Inc.

is an estimation of such an aircraft's specification. This study does not relate to the actual design of the A350 in any way.

The general aircraft definition is given in table 3.2.

parameter	units	value
MTOW	tn	245
pax		312
range	km	15300
length	m	60
fuselage width	m	5.89
wingspan	m	64
wingsweep	°	35
M_{cr}		0.85
engine thrust (sea-level static)	kN	387

Table 3.2: aircraft design specifications

Outputs from the design analysis

AMPEC requires inputs of:

- Take-off attitude and rotate speed definition
- Distances of the wing and THS centres of pressure from the datum
- Distance of the MAC leading edge from the datum
- MAC length
- Aircraft moment coefficient
- Wing reference area
- Ratio of wing and THS reference areas
- Wing, aircraft and THS drag polars

- Wing and THS lift curves

The take-off attitude has simply been estimated from the geometries of the fuselage, and is used only to limit the angle to which the aircraft is rotated during take-off. As take-off performance is not of interest, it will have no effect on the results of the simulations if it remains constant throughout. The rotate speed has been set to the wing stall speed at zero incidence and the high lift devices at the take-off condition. Again, it will not impact the overall mission fuel burn, provided it remains constant.

The characteristic lengths, such as MAC and distance of the aerodynamic centres aft of the datum are all defined directly by the design analysis. The nose of the aircraft is used for the datum.

In this analysis, the pitching moment of the wing and aircraft are assumed to be combined, and this is not variable with wing incidence. This has been identified as a possible source of error, as the moment coefficient is expected to vary linearly with angle of attack.

The wing reference area and the ratio of THS to wing reference area are direct outputs from the design analysis.

The drag polar for the aircraft can be plotted in the analysis program. This can then be read off for a discrete number of points, and a quadratic curve fitted to the data. The THS drag data is not readily available from the analysis program. However, the THS drag can be approximated as 2% of the overall drag of the aircraft [6]. In order to achieve this, the drag polar must be scaled appropriately:

$$D_t = 0.02 D_{ac} \tag{3.24}$$

$$C_{D,t} = \frac{0.02 C_{D,ac} \left(\frac{1}{2}\rho U^2 S_{ref}\right)}{\left(\frac{1}{2}\rho U^2 S_{ref} h\right)} \tag{3.25}$$

$$C_{D,t} = \frac{0.02}{h} C_{D,ac} \tag{3.26}$$

The design analysis provides the wing lift curve. For the THS, the wing analysis tool was set using the THS geometry, resulting in a lift curve definition.

Other design data have been used from the design analysis in order to develop a CAD model of the aircraft, and to develop the fuel system geometry definition. This CAD model has been used throughout this section to produce various figures.

Appendix B contains the design data derived as described above for the subject aircraft.

3.2 Simulations

In order to investigate the effect of the trim to centre transfer control method on the mission fuel burn, a number of simulations have been run using CGFlight with AMPEC providing the flight profile and fuel burn data. Four cases have been studied; a baseline case in which it is assumed the aircraft has no trim tank, two cases using the existing Airbus on-off control method but with different centre of gravity control bands, and a case using variable fuel flow rate to maintain a constant centre of gravity demand condition. These cases are referred to as the baseline case, and cases A, B and C. Table 3.3 summarises each of these simulations. In each case, the flight profile and aircraft definitions remained constant, using the definition set out in section 3.1.3.

name	description
baseline	no trim tank
case A	existing Airbus on-off control using 0.5% MAC control band
case B	existing Airbus on-off control using 5% MAC control band
case C	variable flow rate control to the aft limit

Table 3.3: summary of AMPEC & CGFlight simulations

The no trim baseline case was achieved by setting the fuel volume in the trim tank to zero, and increasing the size of the centre tank to accommodate the difference. Case A was the existing Airbus control logic, which aimed to maintain the centre of gravity

within 0.5% MAC of the target using on-off control of the trim line valve. Case B examined the benefits of increasing this control margin to 5% MAC in terms of the valve cycle reductions, and also any negative impact of the increase in error between the actual and demanded centre of gravity. Finally, case C examined what benefit was provided by changing the control method from on-off to variable fuel flow in order to maintain the correct centre of gravity position throughout the cruise.

Each of the four cases have been run for six different definitions of THS drag, in order to discern a general pattern in the comparison of the cases, and avoid the results being dependent only on the aircraft definition given in section 3.1.3. For each of the six definitions, the cruise fuel burn results have been calculated for each of the four cases. The fuel burn reduction as a result of using case A over the baseline case has been calculated, to give a measure of the benefit of using centre of gravity control over a no trim configuration. The benefit of using cases B and C is then calculated with respect to this. This allows the results of each case to be viewed independently of the aircraft configuration, and in terms of the change in cruise fuel burn from the current Airbus control method. The results are therefore presented in terms of percentage differences between each case and the corresponding benefit of using the trim tank, and not as absolute fuel burns.

The cruise fuel burn has been calculated by integration of the fuel burn rate provided by AMPEC over time. This has been accomplished using a Matlab GUI developed specifically for this application called ACRe (AMPEC/CGflight Results analysis tool). Figure 3.10 shows the ACRe interface during the analysis of an AMPEC/CGFlight simulation results. The flight fuel burn is summarised in the table in the bottom left of the screen, and the right hand pane contains time histories of the aircraft altitude, fuel burn, Mach number, attitude angle, aircraft angle of attack, THS angle of attack, mass and centre of gravity. ACRe also outputs a separate graph of the centre of gravity against aircraft mass, similar to the CGFlight fan plot.

The use of a fixed time-step solver has resulted in very long run times for the joint AMPEC/CGFlight simulations. A 15hr flight can take as long as three days to solve fully. Much could be done to reduce the solution times in terms of improving the programming efficiency and by removing parts of CGFlight which are not used in the analysis, such as failure modes and disc burst analysis. The engine model interpolation routines are also widely known to be slow and inefficient. A quicker bespoke interpolation routine could be written.

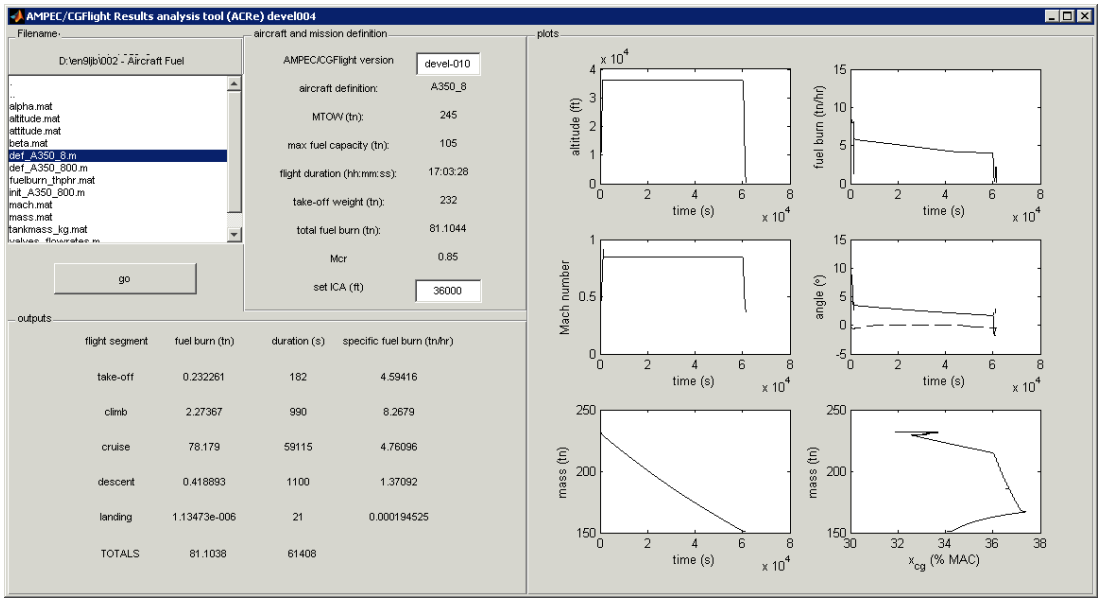

Figure 3.10: ACRe Matlab GUI for the post analysis of AMPEC/CGFlight simulations

3.3 Results

All the results of the AMPEC/CGFlight simulations have been normalised by their maximum value to allow more direct comparison of each case and THS configuration, as well as to present the results independently from the aircraft definition. Examples of the altitude and Mach number variations with time have already been presented in section 3.1.2, and do not vary significantly from one case to another, and so have been omitted here. Of greater interest when examining the difference in total fuel burn from one case to the next are the attitude angle, wing and THS angles of attack, fuel burn rate and centre of gravity position. Figures 3.11 through 3.16 show the time histories of wing angle of attack, α, THS angle of attack, β, aircraft attitude angle, ϵ, fuel burn rate, r, centre of gravity position with respect to MAC, χ, and the mass-centre of gravity, m and χ respectively, for one set of results for the baseline case, case A, case B and case C. The time period shown is the cruise portion of the flight.

It can be seen that the angle of attack, attitude angle and fuel burn rate tend to decrease during the flight. This is to be expected, as the aircraft mass will reduce, requiring less lift, and hence a reduction in angle of attack, allowing a reduction of attitude angle (see equation 3.3), and resulting in reduced drag (equations 3.16 and

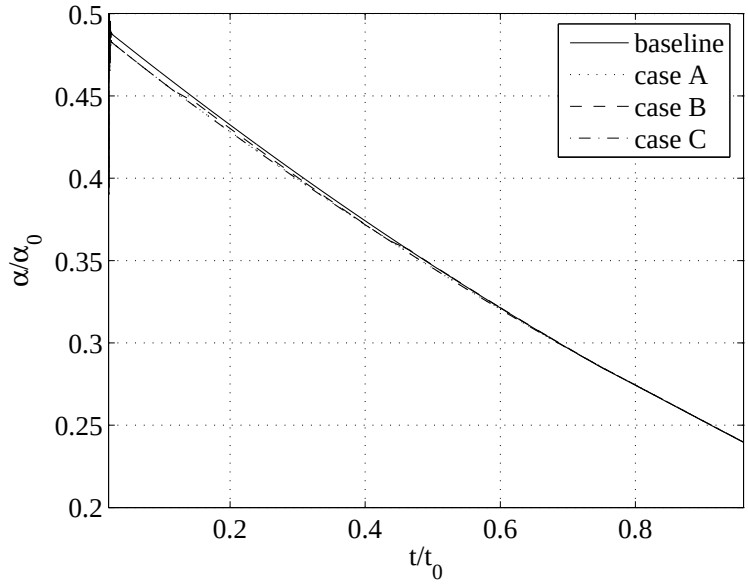

Figure 3.11: AMPEC/CGFlight simulation results: wing angle of attack, α, over time

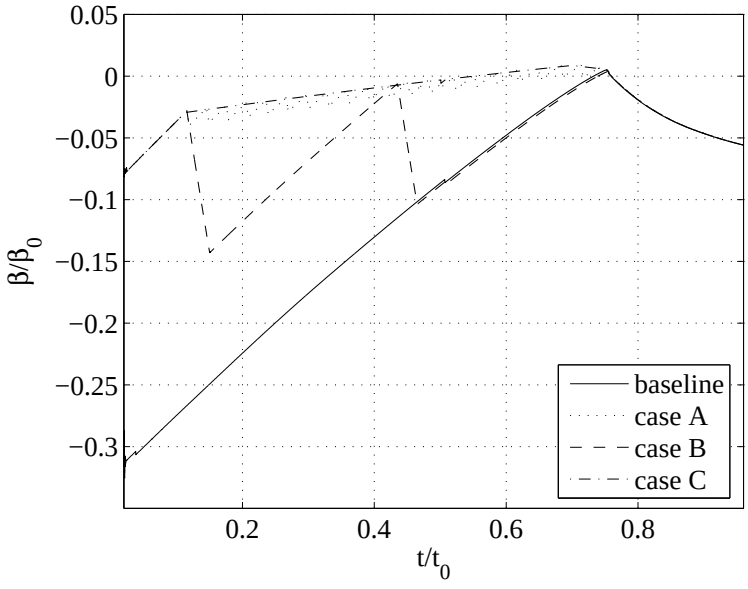

Figure 3.12: AMPEC/CGFlight simulation results: THS angle of attack, β, over time

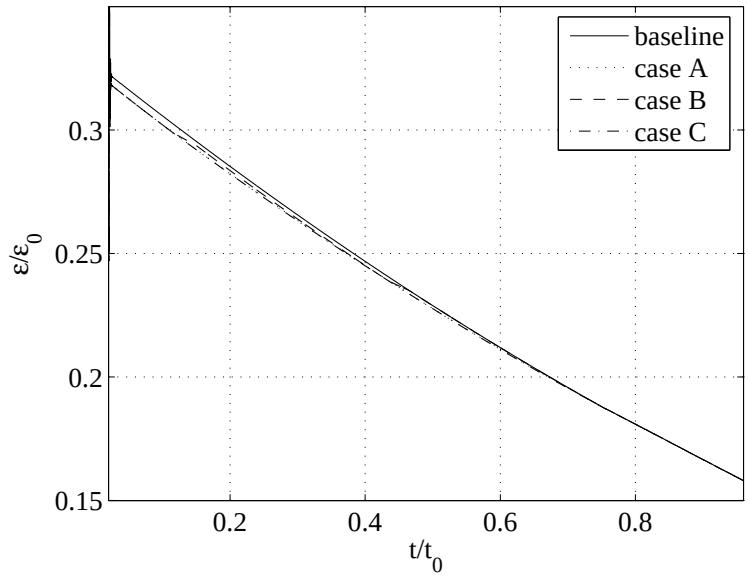

Figure 3.13: AMPEC/CGFlight simulation results: aircraft attitude angle, ϵ, over time

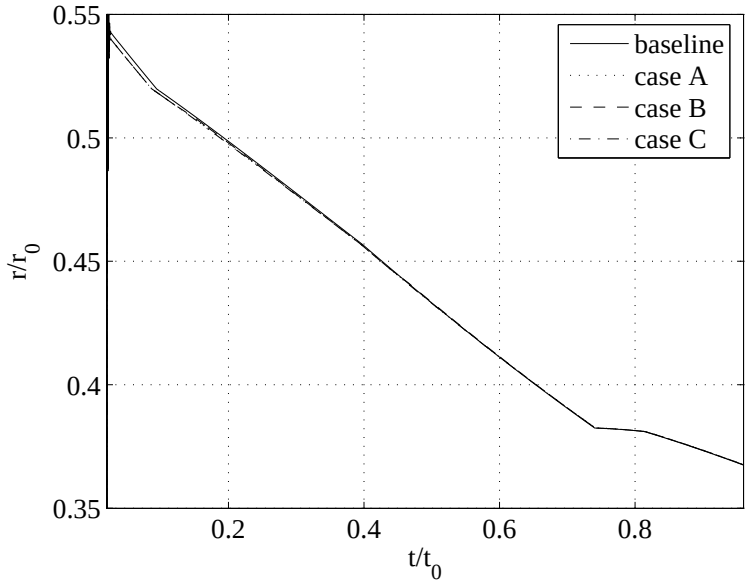

Figure 3.14: AMPEC/CGFlight simulation results: fuel burn rate, r, over time

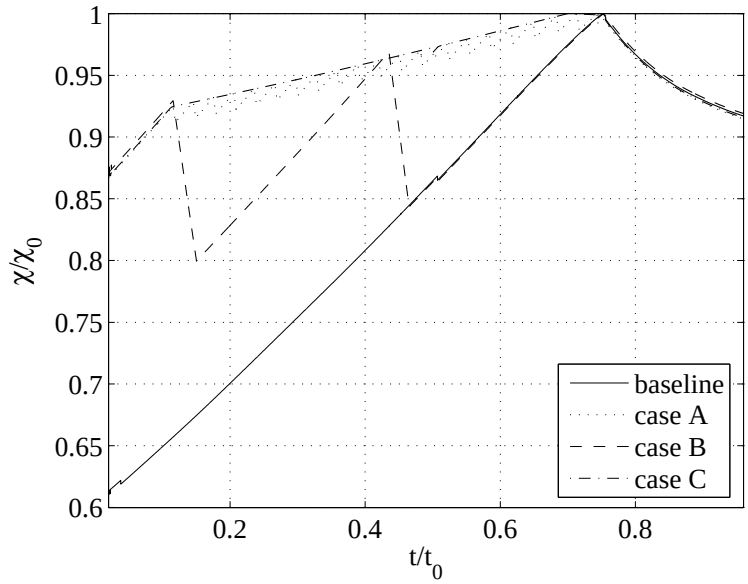

Figure 3.15: AMPEC/CGFlight simulation results: centre of gravity position with respect to MAC, χ, over time

3.17), and hence fuel burn rate. At $t/t_0 = 0.725$ the fuel burn rate plot, figure 3.14, suddenly changes gradient. This occurs at the point where the centre tank fuel is used up and the engine feed from the wing tanks starts, and coincides with the point where the centre of gravity position is fully aft with respect to MAC, as shown in figure 3.15. Figure 3.12 shows that the THS angle of attack tends to increase towards zero (a negative angle denoting a downwards lift force, as expected from figure 1.3).

It is clear from figures 3.11, 3.13 and 3.14 that there is not much difference between cases in terms of angle of attack, aircraft attitude and fuel burn rate. In each case, it is possible to see a slight change from the baseline, with α, ϵ and r reducing due to the introduction of a trim tank. The differences between each case with a trim tank are not clear. Figures 3.12, 3.15 and 3.16 however, show a much clearer difference between cases.

The most striking difference is in the number of on-off cycles of the valves, seen as the saw-toothed shape of the case A and case B lines (dotted and dashed lines respectively). In this example, the baseline case will require no valve operations, as no flow control is required, and case C requires only a single operation - the valve is opened at the start of cruise, and shut at the end according to the fuel system logic. For cases A and B the

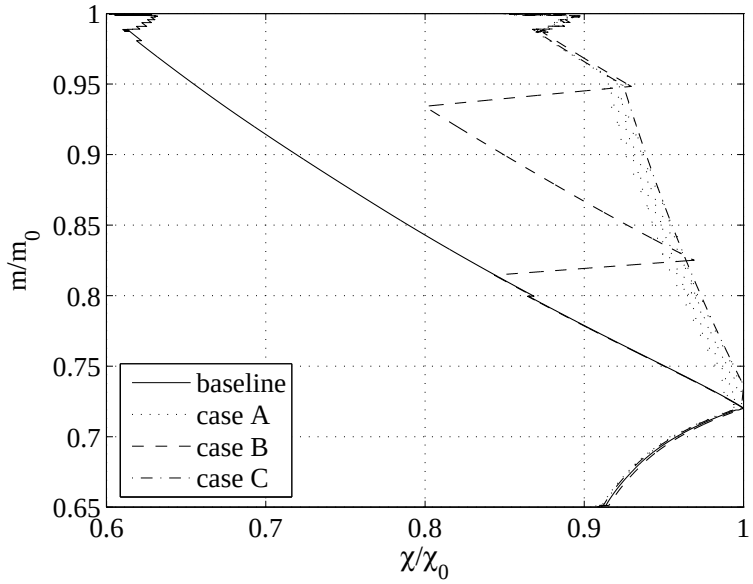

Figure 3.16: AMPEC/CGFlight simulation results: mass (m) - centre of gravity (χ) fan plot

valves are shut on and off to control the centre of gravity position. Using the control in case B with a 5% MAC control range for χ reduces the number of valve operations from 20 to 3.

From figure 1.3, a reduction in THS load is known to result in a reduction in aircraft drag and hence fuel burn. Therefore, it is clear from figure 3.12 that case C should see a significantly reduced fuel burn when compared to the baseline case and case B, and a smaller reduction when compared to case A.

In order to assess the impact of the trim to centre transfer control on the cruise fuel burn, the fuel burn rate has been integrated over time. The resulting cruise fuel burn for case A has been compared to that for the baseline case for each THS configuration. The differences in cruise fuel burn for cases B and C has then been compared to the difference between the baseline case and case A. Table 3.4 details these calculated differences. A positive value indicates an increase in cruise fuel burn, whereas a negative value indicates a decrease.

The results show a consistent trend of a significant increase in fuel burn for case B over case A, but a smaller decrease in fuel burn for case C. The actual fuel burn change

configuration	case B %	case C %
1	44	−4
2	39	−5
3	35	−3
4	46	−4
5	35	−3
6	37	−3

Table 3.4: summary of AMPEC & CGFlight simulation results: changes in cruise fuel burn as a percentage of the difference between the baseline case and case A

is dependent on the overall benefit as a result of the introduction of centre of gravity control. This is itself highly dependent on the inputs to the simulation.

3.4 Minimum trim condition control

Currently, the trim tank is used in Airbus aircraft to move the centre of gravity to a desired postion, in order to best balance the aircraft and reduce fuel burn. The control system is based on an estimate of the aircraft centre of gravity from the fuel distribution within the various fuel tanks, and is as such, a rough estimate at best. It is proposed that, if minimum fuel burn is the required aim, and such a condition can be said to be met when there is zero trim from the THS, then the control of the centre of gravity could be accomplished using the THS deflection angle as the input. This results in a control system which is designed to optimise the correct target variable, fuel burn, directly rather than using an estimate of centre of gravity to within a specified window. Figure 3.12 shows β for both the baseline case and case B for the set of results described in section 3.3. It is clear from this plot that none of the presented control strategies result in a zero trim condition for this particular aircraft.

The AMPEC/CGFlight simulation has been modified to investigate this control. Instead of comparing the current centre of gravity position with the demand, the THS deflection angle, β, is used as the error signal in the feedback loop. For this control

however, the controller was altered to include both proportional and integral control. Figure 3.17 shows the modified program structure.

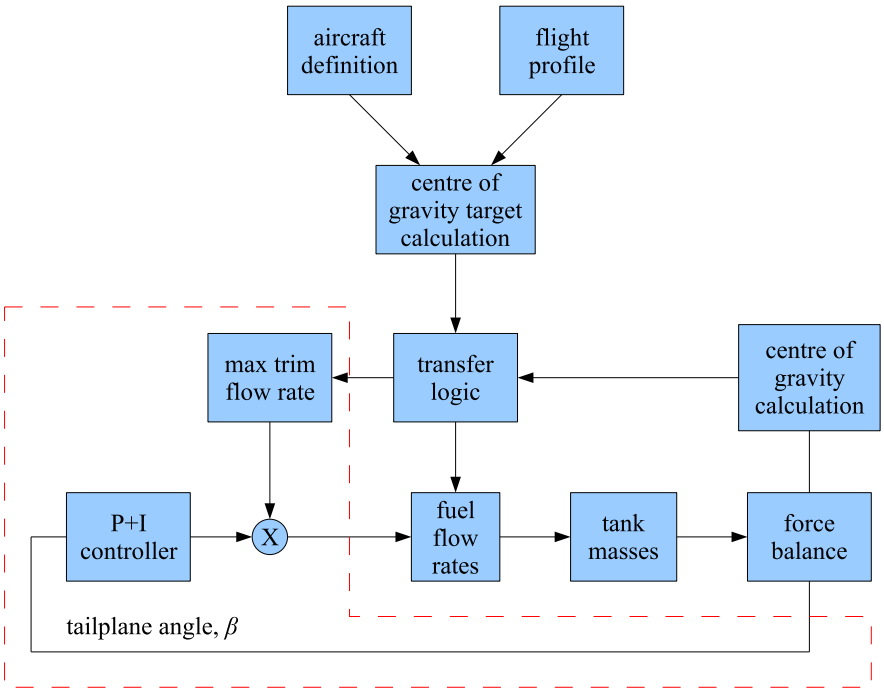

Figure 3.17: modification of CGFlight control loop to acheive zero trim during cruise

Using this modified AMPEC/CGFlight simulation, two of the THS configuration sets of simulations have been re-run, and are referred to as case D. The total fuel burns for these cases were then found as before and compared to the previous results. Figure 3.18 shows the comparison between the THS trim angle for the original case C using variable fuel flow control and the new simulation using variable fuel flow control and the zero-trim target, case D. Figure 3.19 shows the comparison of the fan plot for these two cases. Table 3.5 summarises the fuel burn benefit of using this new control target for the two cases, with the data presented in the same way as table 3.4. The large difference in fuel burn in these cases is an indication of the lack of optimisation of the centre of gravity target position in the CGFlight software for the particular aircraft definition used here, and not necessarily as an absolute fuel burn reduction which might be achievable in a real world situation. Further discussion of this can be found in section 3.5.

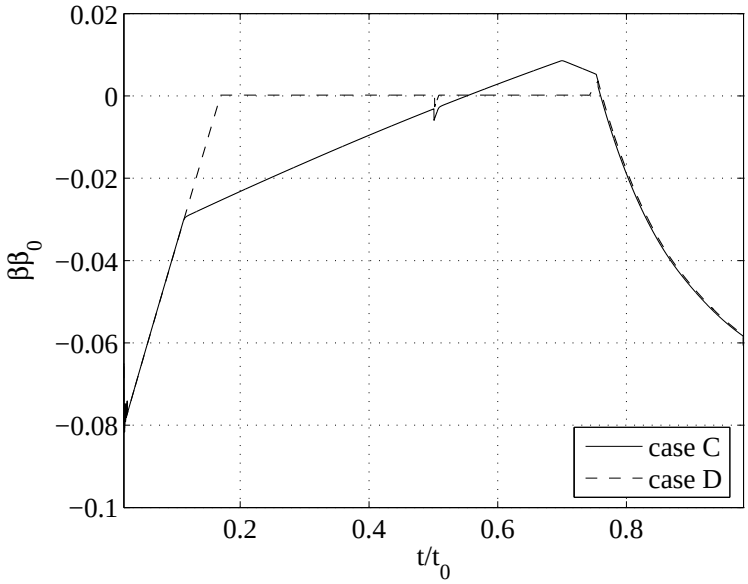

Figure 3.18: AMPEC/CGFlight simulation results: THS angle of attack, β, over time using proposed β control

configuration	case D %
5	−270
6	−283

Table 3.5: summary of AMPEC & CGFlight simulation results: changes in cruise fuel burn as a percentage of the difference between the baseline case and case A for zero-trim control

3.5 Discussion

It is clear that the results in sections 3.3 and 3.4 show a consistent trend. By changing the centre of gravity control method to maintain the centre of gravity at the rear of its range, cruise fuel burns are reduced. In general, centre of gravity control to trim the aircraft has been shown to lead to a reduction of around 1% of the cruise fuel burn, with

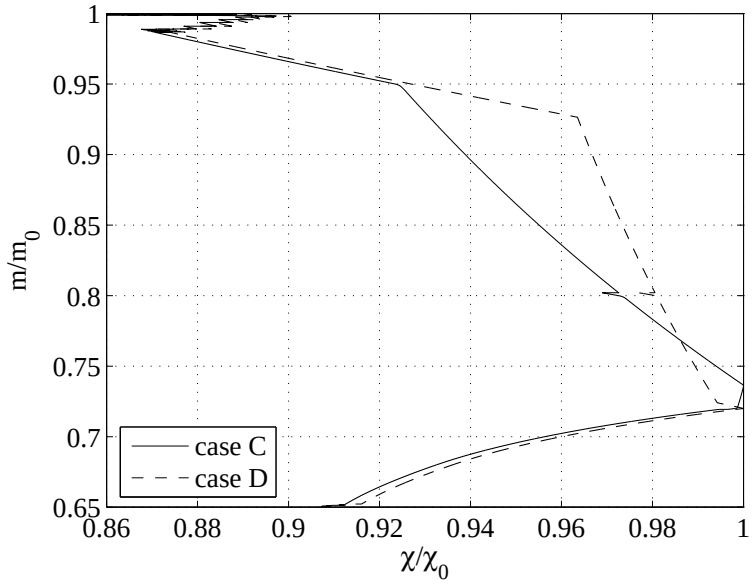

Figure 3.19: AMPEC/CGFlight simulation results: mass (m) - centre of gravity (χ) fan plot using proposed β control

any variation in the control method providing little further change in real terms. The value of using such a centre of gravity control must therefore be examined in the light of such fuel burn reductions and any negative impact on aircraft weight and system complexity as a result of including the infrastructure necessary to implement it.

Whilst the introduction of trim control has been shown to deliver a significant improvement in cruise fuel burn, the change from the current on-off method to a variable fuel flow rate is much less significant. The simulations conducted here show a fuel burn reduction of between 3% and 5% of the benefit of using trim control. Such a decrease in fuel burn could not in itself be considered a reason for changing the control method. Instead it must be viewed in the light of the reduction in valve cycles. Using the variable fuel flow control method eliminates the need for valve cycling during cruise. This will have a significant impact on the indirect costs concerned with valve wear and maintenance operations.

Likewise, changing the current control to use a larger centre of gravity control band will reduce the number of valve cycles. In the simulations conducted here, changing the control band from 0.5% MAC to 5% MAC reduced the number of valve cycles by a factor of nearly 7. This however means a significant increase in fuel burn of between

35% and 46% from the current method with respect to the benefit this has relative to the no trim tank case. Clearly, a balance could be found between acceptable fuel burn increase for a reduction in valve operations. In order to fully understand the cost benefits of such a change, a full lifecycle cost analysis on a particular aircraft would need to be undertaken, but this is outside the scope of this current study.

Without details of a particular valve design and a particular aircraft maintenance costs, it is impossible to estimate the effect of reducing valve operations on direct maintenance costs. Information from industry suggests that such valves may need replacement after a few years of service on long-haul aircraft if in constant use. Much of their wear is attributed to the number of cycles. Any reduction in this over prolonged periods would be of great benefit in increasing component service life.

It must not be forgotten that introducing variable speed drives in order to accomplish the proposed variable fuel flow rate transfer method will incur an increase in both weight and system complexity. With the recent move from fixed frequency electrical supply to variable frequency supply, commercial airliners have seen a shift from traditional AC induction motors to brushless DC motors to drive centrifugal pumps. Brushless DC drives lend themselves much more readily to variable speed operation, with relatively light power electronics required, rather than frequency inverters required for induction machines. Again, without details of a particular system or components, it is impossible to determine the exact weight increase that would be required, although it is expected to be small [9]. Perhaps more important is the increase in system complexity. Any change from current operation brings with it the costs associated with technology proving, certification, and the perceived reliability of the system by the operators. Such cost increases must be considered over a system's lifecycle, and in the light of the expected cost reduction through reduced valve wear and cruise fuel burn.

Currently, the centrifugal pumps in the trim tank perform two tasks: transfer fuel, and mix any water present in the tank with the fuel. The pumps are run against the closed valve when transfer is not required, and it is in these periods that most of the mixing occurs. If the variable fuel flow rate case were to be employed, such mixing would not be taking place, and may have a significant negative impact on the mixing of water in the fuel. Information from industry however, suggests that this mixing process is not as effective as once thought, and that new techniques may need to be employed. Since in this case, the fuel which is transferred from the trim tank to the centre tank is not then burned directly in the engine, mixing is not of primary importance, as mixing of water and fuel could be accomplished in the wing tanks or the engine collector cell. If

mixing is found to be essential in the trim tank, then the trim transfer pumps could be used to drive jet pumps in a similar way to the engine feed pumps in the collector cells.

The simulations described in section 3.2 suggested that the largest decrease in cruise fuel burn occurred when the β control, or control for zero-trim was employed. In the two cases investigated, this method suggested improvements of between 270% and 283% of the benefit from using trim control, although this is most likely as a result of the disparity between the aircraft definition and the target centre of gravity function. The latter is set within the CGFlight software, and while the former is based on the same aircraft definition as the CGFlight simulation, it is necessarily slightly different. On the face of these values, it would appear that such a control method is most desirable. Indeed, this conclusion fits with the hypothesis presented in section 1.1, that reducing THS trim will result in reduced fuel burn. The relative benefit of such a control method over the centre of gravity control method used in cases A, B and C however is perhaps more questionable. It can be reasonably thought that for a fully defined aircraft, the centre of gravity target should coincide with the zero-trim condition, and hence it would be expected that there should be little difference between cases C and D. For the purposes of this study however, the centre of gravity target was defined for a different aircraft definition to that of the three degree of freedom simulation.

The important point to note in these simulations however, is that the centre of gravity control method currently employed requires prior knowledge of how the centre of gravity position affects the required THS angle. Instead, if the control system were to use an input of the THS angle, then the zero trim condition could always be met. The trim control would then be implemented directly using a direct measurement relative to the minimum drag condition, instead of relying on an estimate of centre of gravity position from the fuel distribution and a predefined target function. It is of course conceivable that this zero-trim control could also be employed alongside the existing on-off control system, using a angle range, rather than the current centre of gravity range. The practicalities of such a control method do of course depend on the way in which the THS angle is measured during flight, and the nature of this measured signal. Introducing such a control system would of course increase the system complexity further, as it requires a `P+I` controller. If this were to be combined with the variable fuel flow rate method, it is reasonable to expect further development costs associated with proving the technology and certification.

On balance, it is proposed that the best control method for the centre of gravity aircraft

trim system is the use of variable fuel flow rates based on THS trim angle. This however can only be true provided that any increases in cost, weight and complexity do not override the expected benefits, and that such a system does not have a significant negative impact on the perceived reliability of the system from the point of view of the aircraft operators. If using variable speed pumps for fuel transfer is deemed too risky in terms of extra development costs and questions of system reliability, then implementing the current on-off control using THS trim angle instead of centre of gravity position would be possible. If valve wear is seen as a greater issue than cruise fuel burn, then the control band of the tailplane angle can be adjusted to reduce valve cycles.

3.6 Closure

The trim to centre transfer route has been identified as one where different control methods could have a significant impact on the performance of the whole aircraft. It has been proposed that by changing the way in which the flow between the trim and centre tanks is controlled in order to trim the aircraft during cruise, the cruise fuel burn and the number of valve on-off cycles can be reduced from their current levels.

An existing aircraft fuel system Matlab/Simulink simulation from Airbus UK, CGFlight, has been modified to allow investigation of the impact of variable fuel flow rates in the trim to centre transfer route. A new simulation has been developed to allow calculation of the effect of aircraft centre of gravity on fuel burn, based on a simplified three degree of freedom aircraft model. This new simulation, AMPEC, has been integrated into CGFlight. Using a new aircraft definition, based on a generic near-future, long-range civil transport aircraft, a number of simulations have been conducted. These aim to investigate the effect of changing the trim to centre transfer control on cruise fuel burn. Four cases have been evaluated: one with no trim tank and no control, one with the current Airbus on-off control, one using the current Airbus on-off control method with a larger control band, and a variable fuel flow rate case using a simple proportional controller.

These simulations have concluded that the use of the trim tank does in fact reduce the cruise fuel burn. The effect of changing the control method from the current on-off control to the variable control is small, but the effect on reducing the number of valve on-off cycles is significant. Changing the on-off control band has been shown to reduce the valve operations also, but the fuel burn penalty of doing so is much greater.

A different control method has been proposed, where the control is not based on the centre of gravity position, but instead on the THS trim angle. It has been proposed that a zero trim condition should result in a minimum fuel burn. The simulations have shown that this is true in this case, and so a trim control based on the THS angle is proposed as the ideal solution, provided that such changes can be shown to not result in significant cost or weight increases, or any reduction in the system's perceived reliability.

There exist a number of caveats to this study. The simulations of aircraft performance can not be properly validated in the course of academic research, and the aircraft definitions in each of CGFlight and AMPEC do not fully match. For these reasons, the results have been presented in terms of their relative benefit, rather than in absolute fuel burn changes. The results can not be seen as definitive for a particular aircraft, but highlight the expected trends relating the centre of gravity position control method and cruise fuel burn, as well as highlighting the effect of reducing the number of valve operations.

Chapter 4

Component Modelling: Steady-state

In order to analyse the behaviour of aircraft fuel systems as discussed in chapter 3, detailed models of the components need to be developed. The steady-state behaviour of centrifugal pumps will vary enormously from one pump to another [10], and so it is desirable to create as generic a model as possible to describe the pump's performance. Since variable speed drives are of interest in order to accomplish variable fuel flow rate transfer, the pump model should be capable of predicting off-design speed performance. The steady-state performance of pipes, including bends, changes in section and pipe joins is, in the main, well understood and documented [11]. Current aircraft fuel pumps are driven by AC induction motors, although future trends are likely to include a shift towards either variable frequency AC or DC electrical supplies, precipitating a change to brushless DC motors [12].

Modelling techniques for each of these components have been researched and investigated. With a view to developing system simulations, and including some dynamic analysis, these modelling methods have been used to develop component models in the Bath*fp* fluid power simulation environment, and their behaviour has been validated against experimental data from the test rig, described in chapter 2. It is intended that these models then be extended to predict the behaviour of aircraft fuel systems, and to investigate the control systems described in chapter 3. For this reason, the models must be as generic as possible, and they must be shown to be applicable to a wide range of components.

This chapter describes the methods used to investigate and subsequently model the steady-state behaviour of the components. The dynamic modelling is dealt with in chapter 5, and the validation of the models is dealt with in chapter 6. The extension of the modelling techniques to investigate aircraft fuel systems can be found in chapter 7.

4.1 Centrifugal pumps

A number of centrifugal pump modelling methods have been identified in the literature. Each of these has been evaluated in terms of their applicability to the modelling of variable speed aircraft fuel system pumps. A number of pump models have been developed by the author in both Matlab/Simulink and the fluid power simulation software Bath*fp*.

The pump modelling methods identified in the literature can be broken down into two categories:

1. The classical turbomachinery modelling method applies a one-dimensional equation to find the ideal pressure rise due to the angular acceleration of the fluid through an impeller, from which losses can be subtracted. These losses often take the form of empirical, or at very least semi-empirical formulae with numerous parameters which can be hard to quantify precisely. Since the method analyses only the mean flow in one dimension, it is often poor at representing pump performance off-design or during fast transient operations where three-dimensional flow phenomena such as wake mixing, cavitation and flow recirculation are present.
2. Steady-state and low-speed transient performance can be predicted by using the steady-state characteristic of the pump - often supplied by the manufacturer. Off-design speed behaviour can be approximated using pressure, flow rate and power scaling, commonly referred to as the affinity laws.

The following sections consider these modelling methods in more detail.

4.1.1 One-dimensional Euler turbomachinery analysis

This analysis states that the ideal flow through and the pressure rise across a centrifugal impeller can be related by the change in angular momentum of the fluid. The analysis is one-dimensional, and considers the flow behaviour along the mean streamline path only. It is widely documented in fluid mechanics and turbomachinery text books. For example, it is described in detail by Karassik et al. [10] and is well summarised in Dixon, Chapter 7 [13]. The method is the same as that used for centrifugal compressor analysis, usually in terms of initial conceptual design work, as detailed in Whitfield and Baines [14]. In order to predict the actual expected performance of a real pump however, the calculated pressure rise and flow must be adjusted for losses, which is done mostly by applying semi-empirical or wholly empirical loss functions, some of which are reviewed in [15], [16] and [17]. Also of concern, and related to losses, is the prediction of slip factor.

Thanapandi and Prasad [18] have presented a paper which uses the Euler method and a number of empirical loss models to show, by comparison with experimental data, that such methods can be used for quasi-steady analysis. It is suggested in the paper that the transient behaviour seen mostly in starting and stopping of centrifugal pumps tends to be quasi-steady. An experimental programme is set out in the paper, and the results on pump starting and stopping are compared to those computed for steady-state operation and the system head curve. These show that the starting and stopping of the pumps in this particular case can in fact be taken as quasi-steady. Given this, Thanapandi and Prasad go on to describe the development of a performance prediction method, based on the steady-state Euler equation. This model takes an input of the variation of the actual flow rate and the pump rotational speed with time as found from experimentation in order to compute the velocity triangles of the flow on the mean flow line at inlet to and outlet from the impeller. From these, the Euler equation can be applied to find a theoretical pressure rise. Empirical loss models are then applied in order to calculate the actual pressure rise. Comparison of the results with those gained from experimentation shows that the model is able to accurately predict the performance of the pump, given that the rate of acceleration of the rotational speed is small. The important conclusion from this paper however, is that a steady-state model has been shown to be applicable to performance prediction during dynamic operation, as it has been shown that such operations can be considered quasi-steady-state. However, such quasi-steady-state behaviour will not represent the effect of pipeline transients, which occur at much higher frequencies and must be considered by dynamic analysis.

Veres [19] has presented a comprehensive computer model for predicting the performance of a range of pumps, including centrifugal pumps, for cryogenic rocket engines. The method is presented as a preliminary design tool, based on the same 1D Euler method described above, and empirical correlations for rotor efficiency. The model requires an input of the diffusion losses at the design point, which are then varied by an empirical relationship for off-design conditions. The stall criteria are also derived empirically. The code allows the user to predict the full performance map of the pump.

Jansen and Sunderland [20] presented a method for the off-design performance prediction of centrifugal pumps. The model is based on the Euler equation and existing steady-state loss models for design point performance. These models account for the losses due to friction, blade loading, leakage and diffusion; however the paper does not qualify the exact models used. At off-design performance, the paper then presents a number of further losses due to flow phenomena not found during operation at the design point. These include incidence losses, flow separation and flow recirculation. Incidence losses will occur at low flow conditions, and result in an increase in the relative velocity at inlet. This in turn has been shown to result in losses due to flow separation, which move from the trailing edge to the leading edge as the flow rate reduces, and will have a significant effect on the slip factor (discussed later) and the pressure rise. When the separation point reaches the inlet, it will result in further losses due to recirculating flow in the blade passages. Jansen and Sutherland present a new recirculation loss model and apply existing separation criteria to form a performance prediction model. The results of this are compared to experimental work, and it is concluded that the model provides an accurate, simple means of calculating pump performance at a wide range of operating conditions.

Khalafallah, Abolfadl and Sadek [21] have developed a similar model for predicting the performance of centrifugal pumps at off-design conditions. Their comparison of predicted results with those from experimentation led them to conclude that the existing disc friction models needed modification, and that this was significant as they found disc friction to be the major source of losses. They suggested that such a model could be applied with a good degree of accuracy within the conventional operating range of centrifugal pumps, nominally from 30% to 120% of the design flow rate. No qualification was made of the applicability of such models to dynamic performance prediction.

A number of the methods outlined here require semi-empirical loss models in order to accurately predict the performance of a given pump. In fact, the accuracy of the

models will depend greatly on the accuracy of these loss models and the accuracy of the inputs to them. Some of these loss models are given in text books such as Whitfield and Baines [14], and some are defined in papers which use them in performance prediction models such as Thanapandi et al. [18]. A number of papers have been published however which analyse various different methods for each associated loss, and summarise the ones which best fit the experimental analysis to which they are compared. These papers provide a useful means of comparison of the different methods available for loss modelling.

Thanapandi and Prasad [18] suggest that the losses associated with a centrifugal pump may be modelled as losses at the impeller due to friction and secondary flow, blade loading, wake mixing at impeller outlet, shock losses at outlet and impeller inlet losses. Their paper on submersible low speed pumps [22] extends this to include losses in the return passage, found only in submersible pumps, and also a disc friction loss. Such losses were found to be the major source of pressure loss in the work presented by Khalafallah et al. [21], whose model agrees with that of Thanapandi and Whitfield.

A paper by Aungier [23], using the one-dimensional mean streamline analysis discussed previously, suggests a number of loss models for centrifugal compressors, which have been shown to be in close agreement with experimental data.

Oh Yoon and Chung [15] have presented a comprehensive study of loss models for one-dimensional mean flow analysis of centrifugal pumps. Here the losses are grouped into internal losses and parasitic losses. Internal losses consist of incidence loss, blade loading loss, skin friction loss, clearance loss, mixing loss and diffuser loss, whereas the parasitic losses are due to disc friction, recirculation and leakages. A number of loss models are proposed for each from various sources, including among them Aungier's paper [23], and a number of combinations of these loss models are compared against one another and experimental loss measurements. As a result, the authors have drawn together a list of the loss models which best fit their experimental data.

The loss models used in [15] are also proposed in a paper by Oh and Kim [16]. Here however, the analysis is for mixed-flow impellers, and a different loss model for recirculation is proposed.

While not exactly a loss from the system, the slip factor, or the slipping of fluid from the blades at the impeller exit such that the exit angle is increased, will have a significant effect on the pressure rise and flow rate. It is essential therefore that this is calculated

with a good degree of certainty to distinguish its effect from that of other losses. A number of methods have been investigated and compared, and it has been shown that some of the more historically common methods may not in fact be particularly accurate in all cases.

Many text books on centrifugal pumps or compressors [13] often quote the methods of Stodola [24], Stanitz [25] and Wiesner [26]. These can indeed be accurate for performance prediction of impellers for steady-state models, but are based solely on the blade exit angle and the number of blades. A comprehensive review of slip factors by Visser et al. [27] developed a complex formula for the calculation of slip factor, using the method of conformal mapping of functions of a complex variable, to analyse irrotational and solenoidal flow. The resulting expressions are however extremely complex and the suggested simplified forms are not suitable for any practical applications. Therefore, Paeng and Chung [28] developed simplified expressions based on experimental data from the work of Visser et al. This new slip factor, based on investigations of relative eddies contained between two adjacent vanes and the exit circle of a centrifugal impeller, takes into account the ratio of the radii of the blades at inlet to and outlet from the impeller. The correlations shown in the literature with results from [27] suggests this new slip factor is more accurate than previous approaches over a larger range of blade exit angles and blade number.

One further method has been found, which determines the difference in flow exit and blade exit angles, and not the classical "slip factor". The paper by Sherstyuk and Erofeev [29], like that of Paeng and Chung, allows for a variation of radius ratio, but also of blade width ratio.

4.1.2 Steady-state characteristic and the affinity laws

It is well known that the performance of a centrifugal pump can be expressed in terms of a simplified characteristic curve. Chapter 2 of Karassik et al. [10] provides a lengthy description of general pump characteristics. This describes the general shape of pressure-flow curves with respect to overall impeller design and pump specific speed, and details means of scaling pump performance based on overall dimensions for the purpose of sizing a pump for a given application. The generalised form of the efficiency-flow and power-flow curves are discussed. The discussion is extended to look at the effect of adding pumps in parallel and series on their overall characteristic.

Some discussion of the behaviour of the pump "off-design" is included, following previous studies by Donsky [30] and Kittredge [31]. Here, the behaviour of the pump is analysed for both forward and reverse flow, for the purposes of understanding pump behaviour during sudden, transient operation. This consists of normalised plots of pump head and torque against flow rate. The rotational velocity of the impeller is used to reduce the pump's performance curves for different operating speeds to a single curve following the affinity laws. These state that:

$$q_2 = q_1 \frac{\omega_2}{\omega_1} \tag{4.1}$$

$$p_2 = p_1 \left(\frac{\omega_2}{\omega_1} \right)^2 \tag{4.2}$$

$$P_2 = P_1 \left(\frac{\omega_2}{\omega_1} \right)^3 \tag{4.3}$$

where q, p and P are the flow rate, pressure rise and power respectively, and ω is the pump shaft speed. Further discussion of pump characteristics and their interaction with system characteristics is given in chapter 8 of Karassik et al., which also includes the torque characteristics of typical pump drives. It is suggested that such characteristics can help to determine the behaviour of the pump during transient operations as well as the steady-state.

A model proposed by Rizwan-Uddin [32], based on the steady-state characteristic equation, assumes that the rate of change in the pressure rise will be proportional to the rate of change of the square of the shaft speed, and that the rate of change of flow rate is proportional to the pressure rise, the square of the flow rate, and the square of the shaft speed. The system characteristic is assumed in order to provide an operating point. The head rise of the pump is calculated from the known shaft speed variation over time, from which the flow rate is found from the steady-state characteristic. The equations include an inertia term, based on an equivalent length of pipe, which is discussed later in section 5. The results are compared to those from experimentation, and show good comparison over starting and stopping operations, provided that any change in speed of the pump shaft is small, and can be considered to be quasi-steady, as in Thanapandi and Prasad [18].

Tsukamoto and Ohashi [33] present a similar, non-dimensionalised equation for the steady-state performance of the pump, to which they connect some pipe flow models in order to analyse the pressure rise across the pump. They include a dynamic term from the inertia of the fluid inside the pump, which is assumed to behave as a straight pipe of constant cross-sectional area. Here, the pump characteristic is reduced to a single curve using the affinity laws, but the pressure and flow rate are presented in a fully non-dimensional form, rather than the normalised form given in Karassik. The pressure and flow coefficients, ϕ and ψ respectively, are defined as:

$$\psi = \frac{p}{\frac{1}{2}\rho U^2} \tag{4.4}$$

$$\phi = \frac{q}{\pi d_2 b_2 U^2} \tag{4.5}$$

where U is the impeller blade speed at the impeller exit, and hence is directly proportional to the shaft speed, and d and b are the outer diameter and blade passage width of the impeller. No analysis is made of the torque or power requirements of the pump. The model is used to predict the behaviour of the pump during a sudden start up (a companion paper, by Tsukamoto, Matsunaga, Yoneda and Hata [34] looks at the same analysis for a sudden deceleration). The speed of a pump taken from experimentation is input into the model, and the pressure rise and flow rate are calculated. These data are compared to the experimental data. By plotting the non-dimensional characteristic and the non-dimensional test results together, it is possible to view how the transient behaviour compares to the known steady-state. The paper concludes that such sudden accelerations do in fact show signs of dynamic effects and that including the simple inertia term can capture this to some extent. The paper also makes clear the usefulness of the non-dimensional characteristic for determining the pump's steady-state performance at any given shaft speed.

4.1.3 Comparison of methods

The one-dimensional Euler method described in section 4.1.1 is, primarily, a design tool. It has been developed to allow engineers to determine the required impeller and diffuser blade shape to produce a given pump design point. It is clear from the published literature that such analysis will not be adequate for fully describing the

performance of a pump over its full range of operating speeds and system conditions. In terms of pump performance prediction, it can only be of use in the case where the pump in question is well defined in terms of blade shape. Even then, the modelling technique requires the user to define a large number of empirical parameters to account for various losses in the impeller passageways, such as skin friction and wake mixing. Such parameters are effectively used to tune a given pump performance model to give the required output.

For use in system modelling, it is clear that a centrifugal pump model based on a steady-state characteristic is of more use. For a given, existing pump, the internal geometries of the impeller and diffuser passageways are set, and as such are not of interest to the system designer. Of more importance is the overall pump performance. If this can be measured and then used to derive an empirical model, then the system performance can be analysed with some confidence in its behaviour. Clearly it is important to design a model which can also predict the behaviour of a pump for a wide range of conditions, including changes in shaft speed. This will be important for analysis of pump start up and shut down, as well as in the case of variable speed drives, such as those proposed for the trim to centre route of the aircraft fuel system.

One further benefit of the steady-state characteristic model is the ability to easily incorporate dynamic effects such as fluid inertia, as discussed in [33]. Including such effects in the one-dimensional Euler method may present problems in terms of validating that the assumptions stated in the modelling method still hold true during sudden transient operation, although the paper by Thanapandi [18] suggested such modelling technique can be used for situations where such transients remain quasi-steady-state.

On these grounds, it was decided that a centrifugal pump model should be devised based on a measured steady-state characteristic from the test rig, but including the non-dimensionalised form of the pressure-flow relationship discussed in [33]. The pump torque would also be measured, and, based on the affinity laws, the non-dimensional model would be extended to include this. It was felt that such an approach would readily allow the method to be extended to generic pump definitions for use in the fuel system analysis, although this would clearly require a different characteristic from that determined from the test rig. Therefore, a method has been devised in this chapter to generate a non-dimensional characteristic from a minimal specification of pump performance, and this has been applied to an aircraft fuel system simulation in chapter 7.

4.1.4 Experimental programme to determine the pump characteristic

The test rig described in chapter 2 was used to measure the pressure, flow and torque characteristics of the pump. A Strain-Gauge Pressure Transducer (SGPT) was placed in a tapping on the top of the flange at the inlet of the pump. As this is the low pressure side of the pump, a $0-5$bar transducer was chosen, and calibrated to give a maximum range of $0-2$bar. A second $0-20$bar SGPT was placed downstream of the pump, again in a tapping on the top of the flange. This allowed measurement of the pressure rise across the pump. The system flow rate could be measured by the turbine flow meter in the main return line, and the torque by the in-line torque meter. The data acquisition system was set up to allow recalibration of the zero point of each transducer, and this facility was used at the beginning of each test to set the zero pump speed, no-flow, tank head condition as the datum. This means all pressures were measured relative to the tank head.

In order to measure the steady-state performance of the pump, the steady-state recording function of the data acquisition system was used at a large number of discrete pump operating points. This steady-state measurement takes a time-averaged sample of data from each sensor over a user-defined period. For all tests conducted on both the pump and the rest of the system, this period was set to 10s. The sampling rate used for each test was 1kHz per channel.

The pump was run at a constant demand speed by applying a constant current to the motor controller. Then, the motor driven ball valve was closed from the open position in discrete steps of around 2.5°, with a steady-state measurement taken at each step. This was then repeated with the pump demand set to a lower speed, covering the range from maximum demand to around half speed. Over the course of the research project this method was repeated in order to investigate any degredation of the pump's performance with time. Figures 4.1 and 4.2 show the raw measured pressure-flow and torque-hydraulic power data for one such set of tests.

The original pump characteristic was measured in week 75 of the project. Subsequently, tests were also conducted in weeks 113, 121 and 138. The behaviour of the pump in each of these cases was compared in order to track how the pump performance changed over time. This trend is investigated in section 4.1.6.

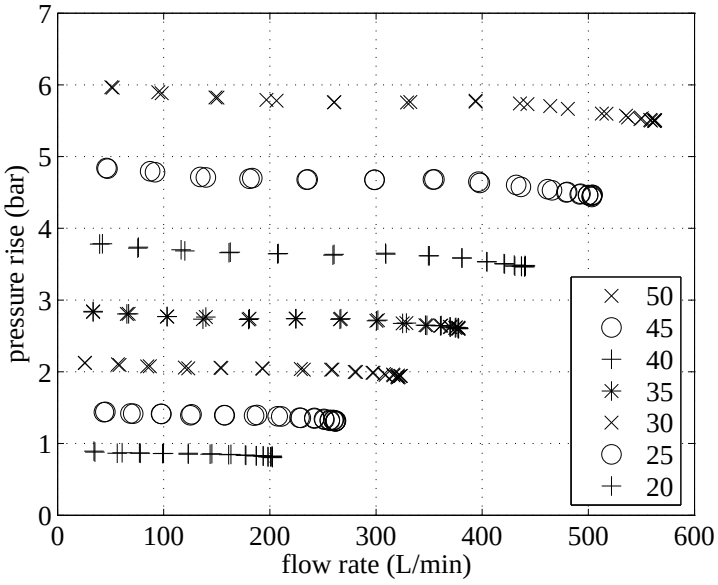

Figure 4.1: measured dimensional pressure-flow characteristic of test rig centrifugal pump (legend shows motor speed in Hz)

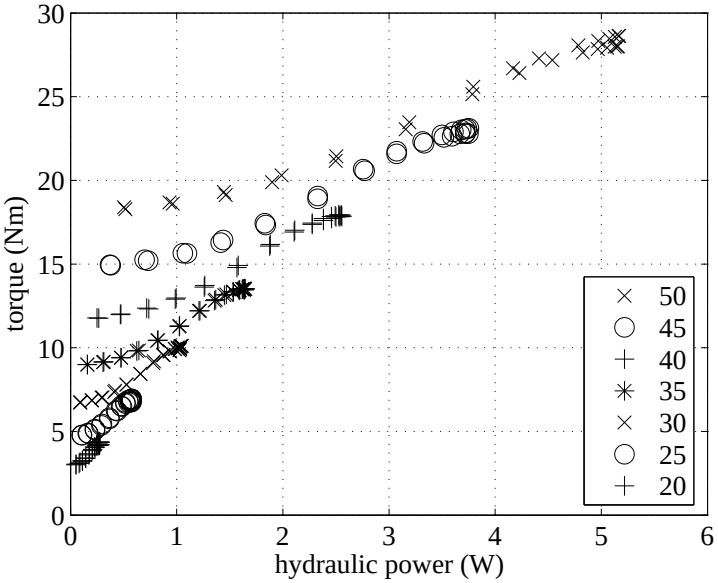

Figure 4.2: measured dimensional torque-hydraulic power characteristic of test rig centrifugal pump (legend shows motor speed in Hz)

4.1.5 Development of non-dimensional characterstic

It is clear from figures 4.1 and 4.2 that the results for each pump speed form a family of similar curves, as one would expect from the affinity laws (equations 4.1 to 4.3). In order to fully describe the pump's behaviour, the pressure-rise, flow rate and torque were reduced to non-dimensional parameters, based on the affinity laws and the pressure and flow coefficients given in Tsukamoto [33] (equations 4.4 and 4.5).

The pressure coefficient from Tsukamoto was used directly, resulting in:

$$\psi = \frac{\delta p}{\frac{1}{2}\rho U^2} = \frac{\delta p}{\frac{1}{2}\rho \left(\omega r\right)^2} \tag{4.6}$$

However, the flow coefficient given in Tsukamoto included some internal geometries of the pump impeller. It was felt that, whilst these parameters provided the correct units for non-dimensionalising the flow rate, they were not representative of a particular pump, and the relative performance of two pumps could not be immediately compared. Therefore, a new parameter based on the maximum flow rate and pump speed was developed, which gave a measure of the pump's maximum performance, akin to a axial piston or gear pump's displacement. Equation 4.5 then becomes:

$$\phi = \frac{q}{\omega v} \tag{4.7}$$

where the equivalent displacement, v is given by:

$$v = \frac{q_{max}}{\omega_{max}} \tag{4.8}$$

Torque can similarly be non-dimensionalised, although Tsukamoto [33] did not comment on this. Here, torque is non-dimensionalised using the same dynamic pressure and equivalent displacement terms:

$$\tau = \frac{T}{\frac{1}{2}\rho \left(\omega r\right)^2 v} \tag{4.9}$$

Using the definitions of ϕ, ψ and τ, an expression for the hydraulic efficiency of the pump can be derived. If efficiency is defined as the ratio of the power supplied to the fluid and the input power from the motor, then:

$$\eta = \frac{pq}{T\omega} \tag{4.10}$$

$$\eta = \frac{\left[\phi \frac{1}{2}\rho\left(\omega r\right)^2\right]\left[\psi\omega\frac{q'}{\omega'}\right]}{\tau\frac{1}{2}\rho\left(\omega r\right)^2\frac{q'}{\omega'}\omega} \tag{4.11}$$

$$\eta = \frac{\phi\psi}{\tau} \tag{4.12}$$

In order to apply these non-dimensional coefficients to the test data from the test rig (section 4.1.4), some further information about the pump was required. Both the pressure and torque coefficients (ψ and τ) require a length scale of the impeller, chosen here as the radius of the impeller at flow outlet. Such data was not readily available for the test rig pump, so an identical impeller was obtained and measured. Figure 4.3 shows a three-dimensional view of a CAD drawing of the impeller constructed using measurements of the impeller. From this the outlet impeller radius was found to be 73.5mm. The equivalent displacement was found by fitting a curve to the measured pressure-flow characteristic (figure 4.1) and extrapolating this to the zero-pressure rise condition to give a nominal maximum flow. This was then divided by the nominal maximum rotational speed of the motor, 3000rev/min, to give $v = 6.1 \times 10^{-4}\text{m}^3$.

The measured pressure-rise, flow rate and torque have been non-dimensionalised using the above method. Figure 4.4 shows the resulting relationship between ϕ and ψ. It is clear from this plot that the data for each of the discrete speeds can adequately be described by a single curve. In this case, a fifth order polynomial fit has been used for the low flow rates, and a second order fit for higher flow rates, in order to capture the dip in the characteristic between $\phi = 0$ and 0.04. These fits were determined using a similar gradient condition at their intersection, and a least-squares fit for both curves. The pressure-flow rate relationship for the pump can therefore be described as:

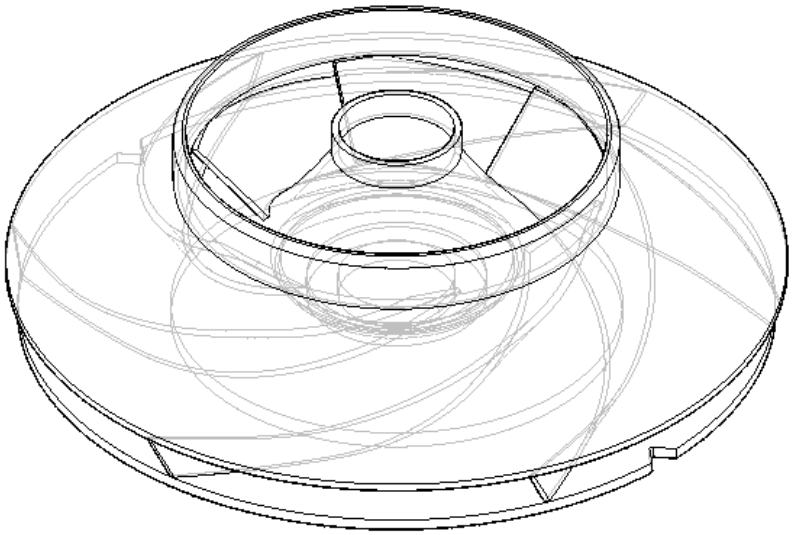

Figure 4.3: three-dimensional view of test rig pump impeller CAD model

$$\begin{aligned}\psi &= \alpha_1 (\phi - \phi_0)^5 + \alpha_2 (\phi - \phi_0)^4 + \alpha_3 (\phi - \phi_0)^3 \\ &\quad + \alpha_4 (\phi - \phi_0)^2 + \alpha_5 (\phi - \phi_0) + \alpha_6 \qquad \text{for } \phi \geq \phi_0 \end{aligned} \tag{4.13}$$

$$\psi = \alpha_4 (\phi - \phi_0)^2 + \alpha_5 (\phi - \phi_0) + \alpha_6 \qquad \text{for } 0 < \phi < \phi_0 \tag{4.14}$$

where ϕ_0 is the point at which the two curves meet, and this and the coefficients α_i are given in table 4.1.

Similarly, the resulting relationship between the torque coefficient, τ and the non-dimensional hydraulic power, defined as $\phi\psi$ can be seen in figure 4.5. Again, it is clear that a single line can define this relationship for all the measured pump speeds, although in this case a simple linear fit has been applied with a view to reliably extrapolating the fit outside of the measured data range. The torque-hydraulic power relationship can therefore be described by:

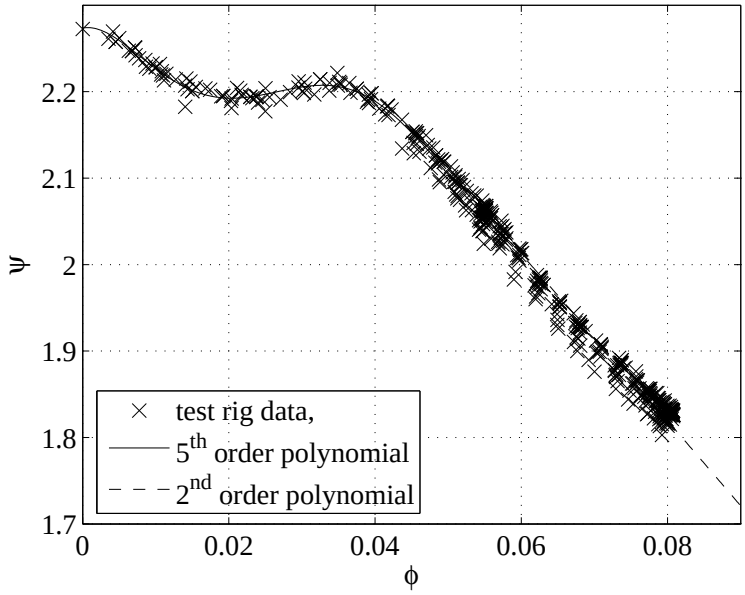

Figure 4.4: measured non-dimensional pressure-flow characteristic of the test rig centrifugal pump

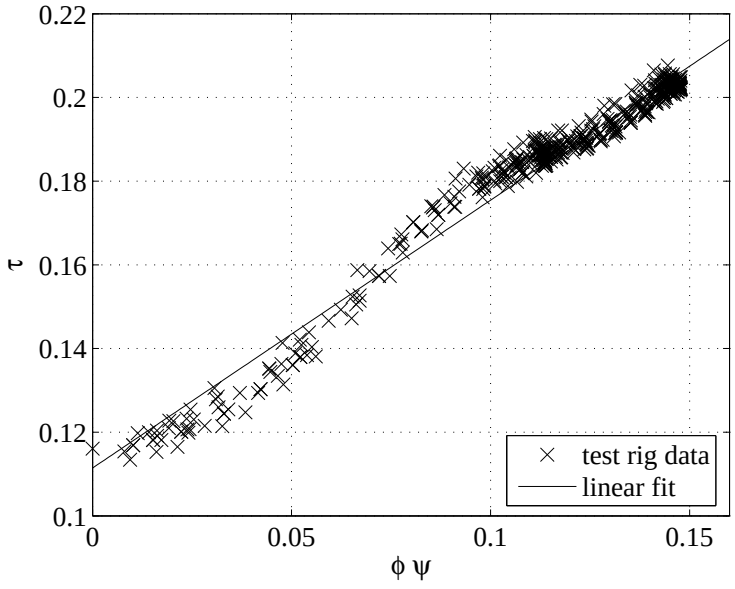

Figure 4.5: measured non-dimensional torque-hydraulic power characteristic of the test rig centrifugal pump

$$\tau = \gamma_1 \phi \psi + \gamma_2 \tag{4.15}$$

where the coefficients are given in table 4.2.

α_1	1.0835×10^7
α_2	1.1643×10^6
α_3	3.436×10^4
α_4	17.8113
α_5	-10.4845
α_6	2.1193
ϕ_0	0.0493

Table 4.1: coefficients of the non-dimensional pressure-flow characteristic of the test rig pump

γ_1	0.6355
γ_2	0.1117

Table 4.2: coefficients of the non-dimensional torque-hydraulic power characteristic of the test rig pump

This can be extended to examine the efficiency-flow relationship, following equations 4.10 through 4.12. Figure 4.6 shows this relationship. It has been extended outside of the flow region in which the tests were conducted, in order to compare the calculated maximum efficiency and corresponding operating point data from the pump manufacturer: 80% efficiency at 1250L/min and 2980rev/min. This has been non-dimensionalised in the same way as the measured data. The manufacturer's data does not identify the efficiency, and it is thought it may include the motor and inverter efficiency, resulting in a total "wire-to-water" efficiency, rather than hydraulic efficiency as in equation 4.10.

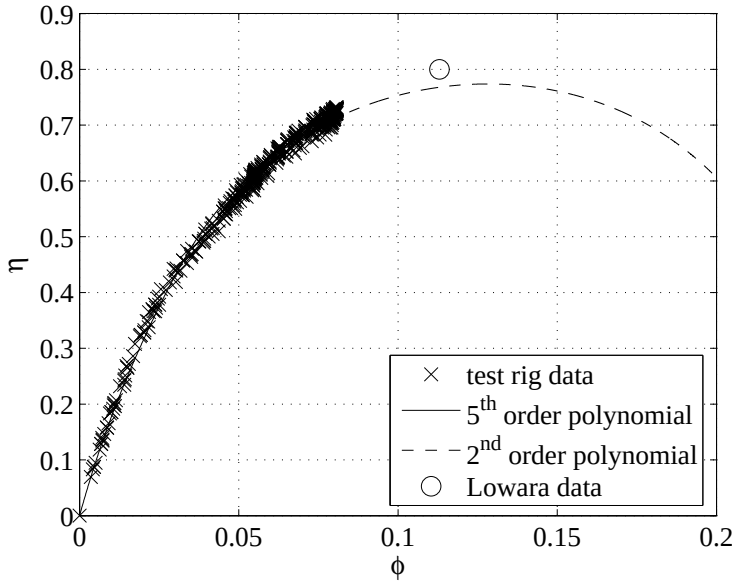

Figure 4.6: measured hydraulic efficiency of the test rig centrifugal pump

4.1.6 Change of characteristic over time

The pressure rise-flow rate and torque-hydraulic power characteristics of the pump have been measured at four and three points in time respectively and the effect of time in terms of changes to the pump characteristic can then be assessed. The first set of tests, conducted in week 75 of the project, measured only the pressure rise-flow rate characteristic, as the torque meter was not installed at this time. Subsequent sets of tests in weeks 113, 121 and 138 measured both characteristics. Figures 4.7 and 4.8 show the polynomial fits to these data sets for both the characteristics. In figure 4.7, the numbers in brackets in the legend denote the 2nd and 5th order polynomials. Table 4.3 defines these tests using the same convention as in the legends of figures 4.7 and 4.8, and details each test date and subject.

During week 101 of the project, the in-line torque transducer was inserted into the test rig. In doing so, the pump and motor shafts were aligned slightly differently. The shaft is floating axially in the bearings and mechanical seal, and under normal conditions is held in the correct vertical alignment by the motor coupling. This will probably have accounted for a certain amount of change to the characteristic. It is still clear however that a certain degradation of performance has occurred, and this is most noticeable

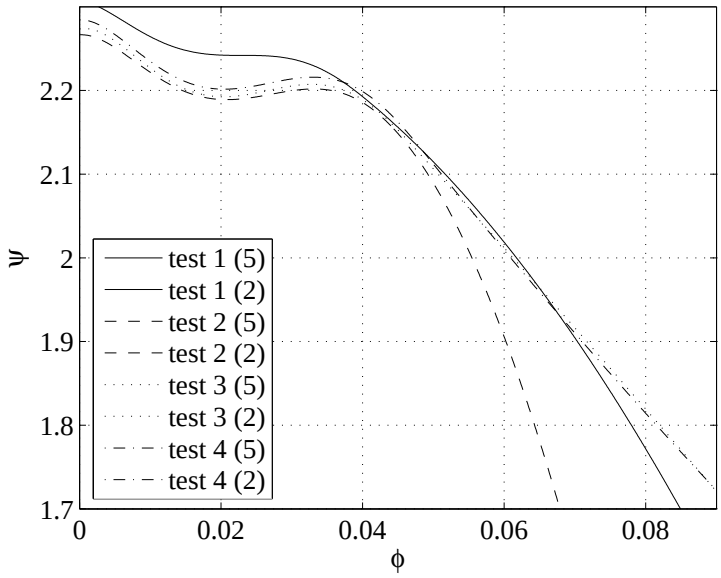

Figure 4.7: change of non-dimensional pressure-flow characteristic of the test rig centrifugal pump with time

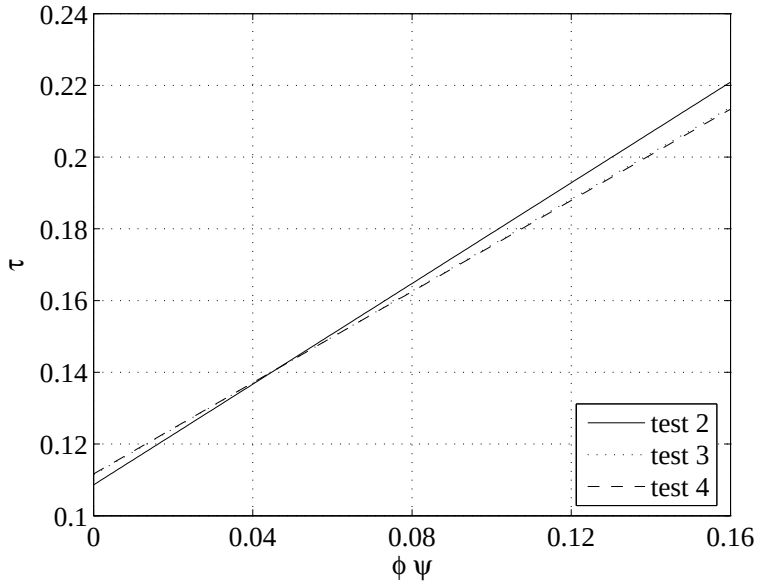

Figure 4.8: change of non-dimensional torque-hydraulic power characteristic of the test rig centrifugal pump with time

test number	date	subject
1	week 75	pressure and flow
2	week 113	pressure, flow and torque
3	week 121	pressure, flow and torque
4	week 138	pressure, flow and torque

Table 4.3: summary of the characteristic tests conducted on the test rig pump

in the low flow region of the characteristic. From test 1 to the subsequent tests, the low flow region exhibits a very marked dip, whereas the higher flows show relatively good agreement, save for test 2. This test was conducted with a different return line pipe arrangement, which significantly reduced the maximum flow rate from the pump. The cross-over point between the second and fifth order curves lies very close to the maximum measured flow rate, and so the second order curve uses only a few data points. Higher flow rate predictions from this fit are understood to be innaccurate. Perhaps of more interest is the low flow region, where, after the initial dip from test 1 to test 2, the pressure-flow characteristic sees a small increase in pressure with subsequent tests 3 and 4, although in this case the differences between tests is within measurement accuracy (consider the range of spread of measured data points on figure 4.4).

The torque-hydraulic power plot shows a marked increase in torque, and hence a reduction in hydraulic efficiency, from test 2 to tests 3 and 4. Again there is a small change from test 3 to test 4, but this lies within measurement accuracy.

4.1.7 Effect of fluid temperature on non-dimensional characteristic

The non-dimensional characteristics have been analysed for a range of different water temperatures. It was expected that such analysis should result in a single characteristic, as the change of temperature could be accounted for in the fluid density term. In order to achieve this, the variation of fluid density and viscosity with temperature from section 2.3 was required.

Figures 4.9 and 4.10 show the measured non-dimensional pressure-flow and torque-hydraulic power characteristics of the pump for a range of temperatures. They are

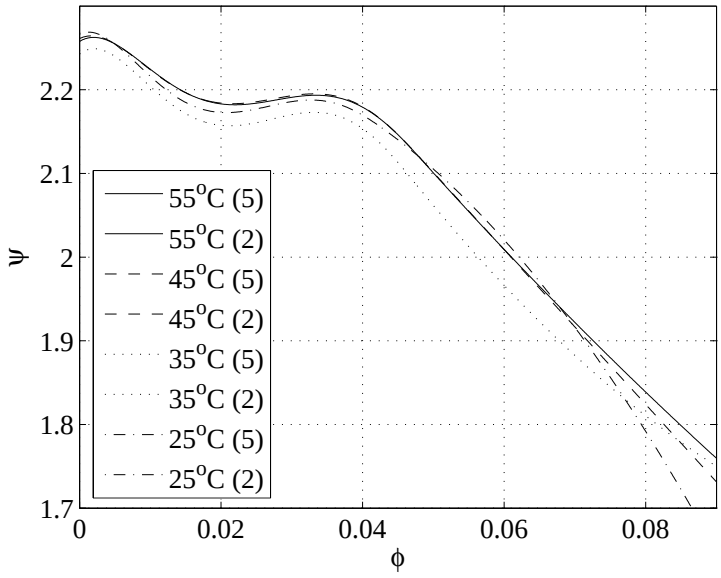

Figure 4.9: effect of fluid temperature on measured non-dimensional pressure-flow characteristic

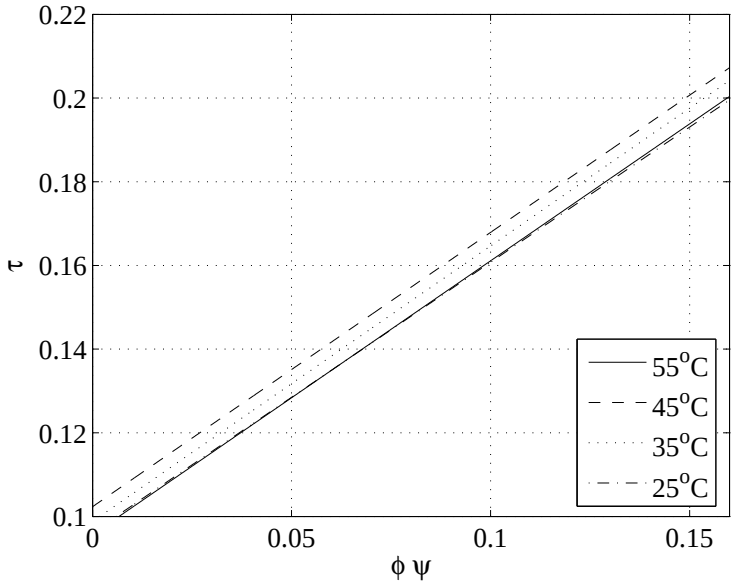

Figure 4.10: effect of fluid temperature on measured non-dimensional torque-hydraulic power characteristic

presented as the polynomial and linear fits to the data. The entries marked `(5)` and `(2)` in the legend of figure 4.9 denote the 5^{th} and 2^{nd} order polynomial fits to the pressure-flow data respectively.

It is clear that the pressure-flow results do not show any significant changes with fluid temperature outside of the range expected from experimental accuracy (see figure 4.4 for a comparison of test result scatter to polynomial fit), save for the result at 35°C. During the course of the tests it became evident that the settling time of the tank at the elevated temperature had a significant impact on the results. In figure 4.9, the 35°C test was conducted after a significantly shorter settling time than the other results.

Figure 4.10 shows a good comparison between torque-hydraulic power characteristics at each temperature, within the experimental accuracy (compare with figure 4.5).

4.1.8 Application of non-dimensional characteristic

A method was developed in order to produce a simple non-dimensional characteristic of a generic centrifugal pump, based on a minimal set of inputs. This was intended to be used to develop a description of fuel transfer pumps for Bath*fp* simulations, where little information was available about the pump's performance. Figure 4.11 shows a general pressure-flow and efficiency-flow curve, defining the no-flow pressure, p_0, operating pressure, flow and shaft speed, p_1, q_1 and n_1, and peak efficiency, η_{max}. Also shown is the system pressure-flow characteristic, where this can be assumed to be a square law using the factor k. Consider a simplified non-dimensional pump characteristic curve set, where the pressure and flow are related by a square law and the torque and hydraulic power by a linear relationship, such that:

$$\psi = \alpha_1 \phi^2 + \alpha_2 \tag{4.16}$$

$$\tau = \gamma_1 \phi \psi + \gamma_2 \tag{4.17}$$

The values of the coefficients, α_i and γ_i can be determined if a number of dimensional operating points are defined using the following method. If the pressure-flow characteristic of the pump can be assumed to follow a square law, then:

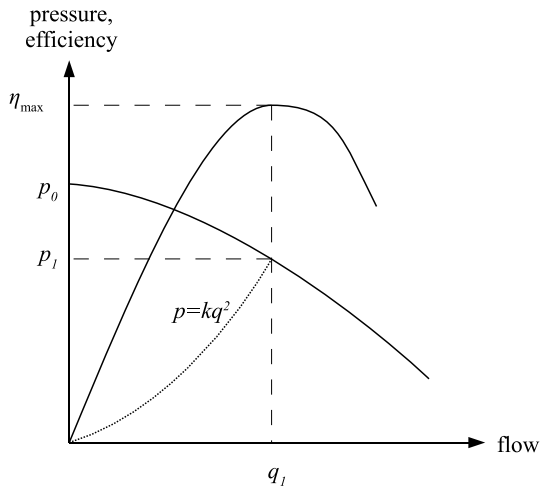

Figure 4.11: generalised pressure, flow and efficiency characteristic of a centrifugal pump

$$p = A_1 q^2 + A_2 \tag{4.18}$$

$$\psi = \alpha_1 \phi^2 + \alpha_2 \tag{4.19}$$

The coefficients of the non-dimensional form in equation 4.19 can be found if the no-flow pressure, the operating pressure, flow and shaft speed are all known, and a value of the radius can be assumed. The operating pressure and flow can optionally be related depending on the system for which the pump definition is to determined using the simplified form of the system characteristic given in figure 4.11.

$$\alpha_2 = \frac{p_0}{\frac{1}{2}\rho\left(\omega r\right)^2} \tag{4.20}$$

$$\alpha_1 = \frac{\psi_1 - \alpha_2}{\phi^2} \tag{4.21}$$

where the pressure coefficient, ψ_1, and flow coefficient, ϕ_1, for the operating point are

defined as:

$$\psi_1 = \frac{p_1}{\frac{1}{2}\rho\left(\omega r\right)^2} \tag{4.22}$$

$$\phi_1 = \frac{q_1}{\omega_1 v} \tag{4.23}$$

In the above, the operating shaft speed, ω_1 has the units of rad/s, related to the shaft speed n_1 of units rev/min by:

$$\omega_1 = \frac{2\pi n_1}{60} \tag{4.24}$$

If the non-dimensional torque can be said to vary linearly with the hydraulic power, then, if the no-flow torque is known, using equation 4.15:

$$\gamma_2 = \frac{T_0}{\frac{1}{2}\rho\left(\omega r\right)^2 v} \tag{4.25}$$

$$\gamma_1 = \frac{1}{\eta_{max}} - \frac{\gamma_2}{\phi_1 \psi_1} \tag{4.26}$$

The equivalent displacement of the pump, v, can be found from:

$$q_{max} = \sqrt{\frac{-A_2}{A_1}} \tag{4.27}$$

$$v = \frac{q_{max}}{\omega_1} \tag{4.28}$$

This method has been applied to the pump in the test rig using the inputs given in table 4.4. Figure 4.12 shows the resultant non-dimensionalised pressure-flow data as compared to that from test data (figure 4.4 in section 4.1.5), and figure 4.13 shows the

resultant non-dimensionalised torque-hydraulic power data as compared to that from test data (figure 4.5 in section 4.1.5) for three motor speeds (the values of which in Hz are shown in the legends). Figure 4.14 shows the comparison between the measured dimensional pressure-flow characteristic of the pump from test 3 (4.1.6), the redimensionalised data from the model and the manufacturer's data from table 4.4. Figure 4.15 shows the same but for the torque-hydraulic power characteristic. It was not possible to run the pump at its designed operating condition. Therefore, the operating point data for this comparison have been taken from the manufacturer's data. From this, the maximum efficiency point has been extracted, and this has been compared to the maximum efficiency predicted from the measured non-dimensional characteristic in section 4.1.5 in figure 4.16.

parameter	units	value
impeller radius	mm	73.5
p_0	bar	6
p_1	bar	4
q_1	L/min	1250
T_0	Nm	17.5
η_{max}	%	80
n_1	rev/min	2980
ρ	kg/m^3	998

Table 4.4: test rig pump model inputs

4.1.9 Implementation of method in Bath*fp* simulation environment

A steady-state centrifugal pump model has been developed in Bath*fp*. The model is based on a non-dimensional characteristic representing the pressure rise and flow rate relationship, and a hydraulic orifice between the pressure rise and the outlet port of the pump. This arrangement, shown in figure 4.17, allows the model to operate as a flow source, requiring an input of the pressure on either side of the pump, and a shaft speed, greatly simplifying the solution of the pressure-flow characteristic. The flow rate is then returned at each port, along with seven internal variables. These are summarised in table 4.5.

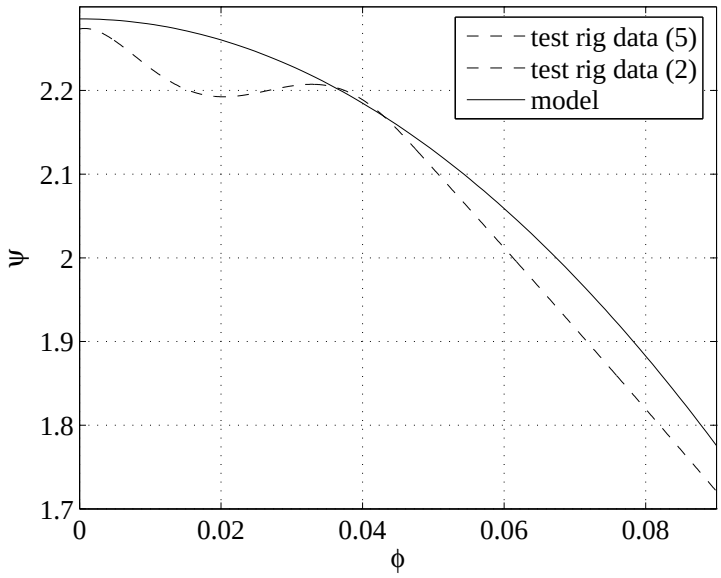

Figure 4.12: comparison of non-dimensional pressure-flow characteristic from the generalised pump model and the test rig pump

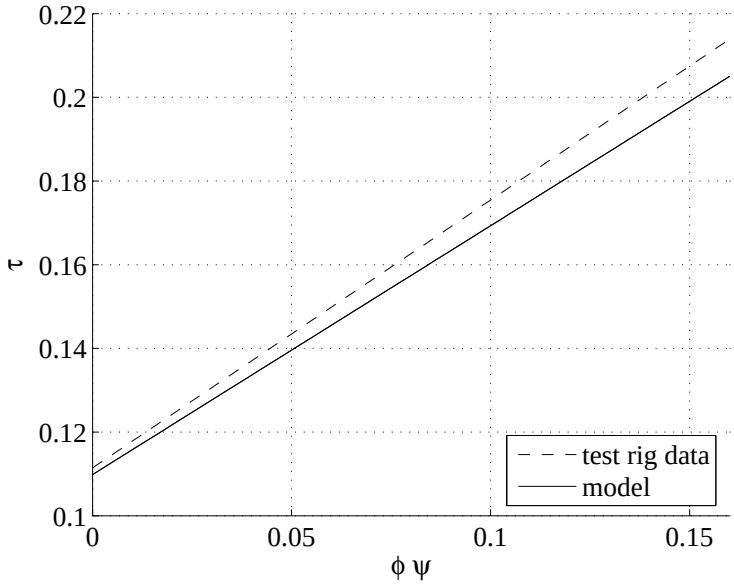

Figure 4.13: comparison of non-dimensional torque-hydraulic power characteristic from the generalised pump model and the test rig pump

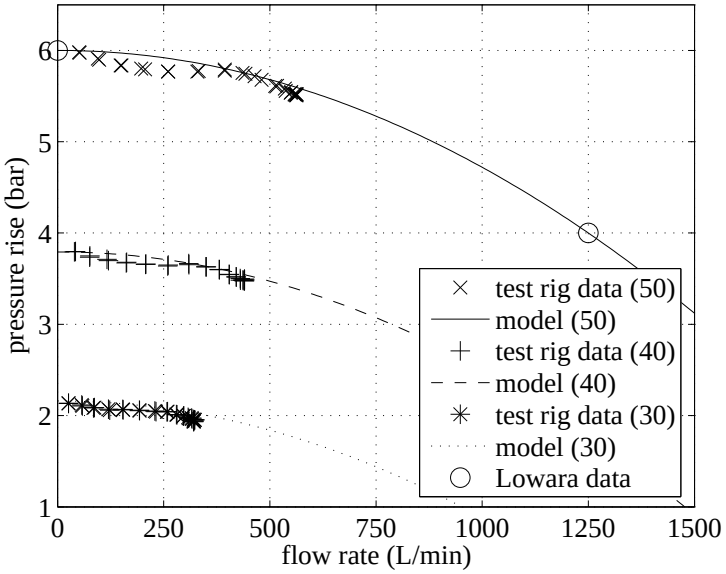

Figure 4.14: comparison of dimensional pressure-flow characteristic from the generalised pump model and the test rig pump

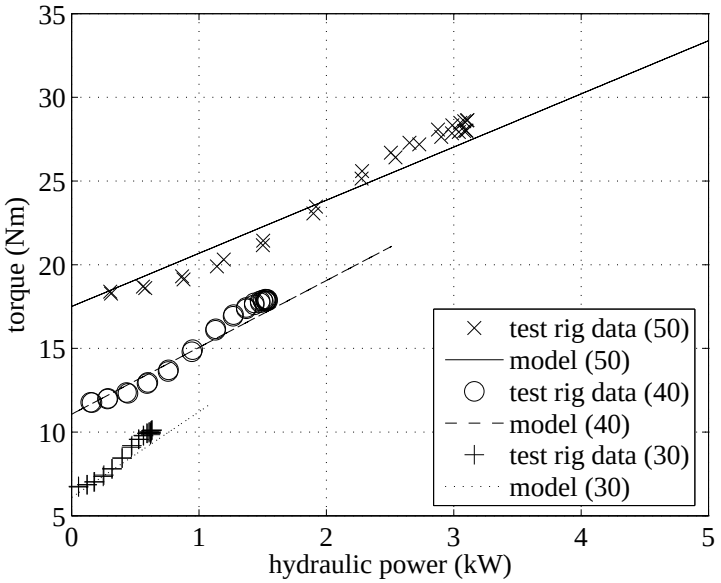

Figure 4.15: comparison of dimensional torque-hydraulic power characteristic from the generalised pump model and the test rig pump

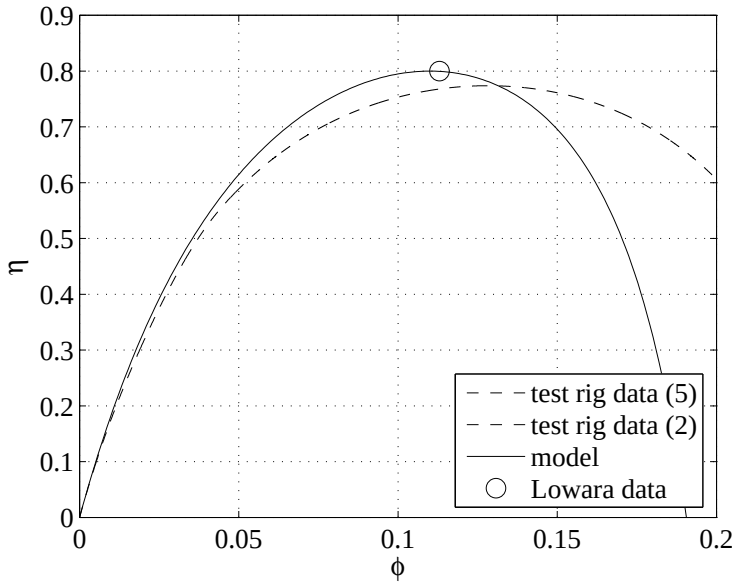

Figure 4.16: comparison of hydraulic efficiency from the generalised pump model and the test rig pump

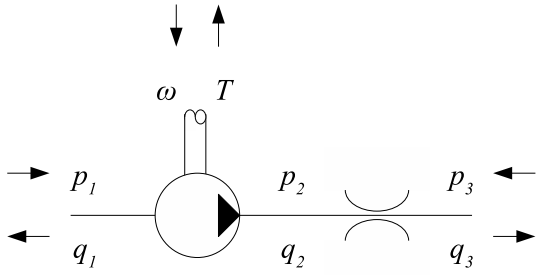

Figure 4.17: schematic of Bath*fp* centrifugal pump model

parameter	units	description
ϕ		non-dimensional flow rate
ψ		non-dimensional pressure rise
τ		non-dimensional torque
η		hydraulic efficiency
p_2	bar	intermediate pressure
q_2	bar	intermediate flow rate
$\dot{q_2}$	(L/min)/s	derivative of intermediate flow rate

Table 4.5: internal variables of steady-state Bath*fp* centrifugal pump model

Provided that the shaft speed is greater than zero the flow coefficient, ϕ, is calculated using equation 4.7. The pressure coefficient is then calculated from a user defined characteristic. For this, the user must supply the coefficients for a fifth order fit to the non-dimensional characteristic, and a value of ϕ above which the characteristic becomes second order. This reflects the particular measured characteristic of the pump in the test rig, as well as a more general second order characteristic if certain coefficients are set to zero. The torque coefficient, τ, is calculated from a user defined linear relationship with the non-dimensional power, as per equation 4.15, and the hydraulic efficiency, η, calculated from equation 4.12.

The intermediate pressure, p_2 is calculated by re-dimensionalising the pressure coefficient, ψ, and the intermediate flow rate, q_2, is set to the inlet flow rate, q_1. Finally, the flow rate at the outlet port q_3, is calculated from the pressure drop across the hydraulic orifice, using the standard hydraulic orifice sub-model. This hydraulic orifice must be defined by the user in terms of a pressure-flow rate relationship. This, along with the pressure-flow and torque-hydraulic power relationships are input by the user as what Bath*fp* calls real essential parameters. Table 4.6 summarises these inputs.

The model has been validated by comparison against test rig data. As this is in essence a system modelling task, more details of the process can be found in section 7.

parameter	units	description
α_1		
α_2		
α_3		coefficients of pressure-flow fit
α_4		
α_5		
α_6		
γ_1		coefficients of torque-hydraulic power fit
γ_2		
r	mm	impeller radius at outlet
v	m^3	equivalent pump displacement
ϕ_0		transition point from 5^{th} to 2^{nd} order fit
c	$(L/min)/bar^{0.5}$	pressure-flow relationship of outlet orifice

Table 4.6: real essential parameters of steady-state Bath*fp* centrifugal pump model

4.2 Electric drives

A simple, steady-state electric drive model has been developed from equivalent circuit analysis. Initially, development of this model began as a part of the pump technology project, but moved to the electric drive project as work progressed in this area. The model was developed from methods and motor definitions described in published literature, although a fuller definition of the motor in the test rig became available as the electric drives project progressed. The initial development of the motor using the definitions from literature was undertaken as a part of the pump project, whereas further details of the model and manufacturer's motor parameters can be found in the electric drive project thesis [12]. The following section summarises the model description and application in Bath*fp*.

4.2.1 Equivalent or Thévenin circuit analysis

An induction motor can be modelled as pairs of resistances and reactances, representing the stator and rotor, and a slip dependent resistance [35]. Figure 4.18 shows the circuit diagram for such a model.

The torque supplied by the motor is the quotient of its mechanical power and rotational speed:

$$T = \frac{P_m}{\omega} \tag{4.29}$$

where the mechanical power of an induction motor is given by:

$$P_m = 3I_r^2 R_r \frac{1-s}{s} \tag{4.30}$$

This leads to:

$$T = \frac{3I_r^2 R_r}{\omega_s s} \tag{4.31}$$

In the above, the variable s is the slip factor, defined as the ratio of the shaft speed to the synchronous speed:

$$s = \frac{\omega}{\omega_s} \tag{4.32}$$

Therefore, in order to calculate the torque developed by the motor, the rotor current, I_r, must first be found. By applying Thévenin's theorem, it can be shown that this is a function of both the Thévenin voltage and impedance, V_{TH} and Z_{TH}. the resultant expression for torque is then [35]:

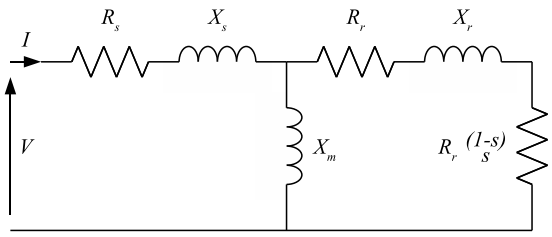

Figure 4.18: circuit diagram for steady-state motor model

$$T = \frac{3{V_{TH}}^2 R_r}{s\omega_s \left[\left(\frac{R_s+R_r}{s}\right)^2 + (X_s + X_r)^2\right]} \tag{4.33}$$

The Thévenin voltage, V_{TH}, can be expressed in complex notation as [35]:

$$V_{TH} = \frac{V X_m j}{R_s + (X_m + X_s)\, j} \tag{4.34}$$

4.2.2 Implementation of method in Bath*fp* simulation environment

The steady-state electric motor modelling technique described in section 4.2.1 has been implemented in Bath*fp*, in order to represent the behaviour of the induction motor in the test rig, and to allow modelling of a full aircraft trim-to-centre transfer route of typical current generation aircraft. The model expects an input of the supply voltage and frequency, and the load torque on the shaft. It returns the shaft speed to the load and five internal variables. These are summarised in table 4.7. The user must supply the model with ten inputs, or real essential parameters. These are summarised in table 4.8. Figure 4.19 shows the input and output variables of the motor model.

parameter	units	description
ω_{out}	rev/min	feedback signal of shaft speed
s		slip
P	kW	power
T	Nm	electric torque
V_{TH}	V	Thévenin voltage

Table 4.7: internal variables of steady-state Bath*fp* induction motor model

The model begins by converting both the shaft speed and input frequency into rad/s, and calculating the slip factor, s. A check is made to ensure the slip is not zero, to avoid division by zero error at a later stage in the calculation. The Thévenin voltage is

parameter	units	description
ω_s	rev/min	synchronous speed
X_m	Ω	magnetising reactance
X_s	Ω	stator reactance
R_s	Ω	stator resistance
R_r	Ω	rotor resistance
X_r	Ω	rotor reactance
c_f	Nm	friction coefficient
c_s	Nm	stiction coefficient
c_c	Nm	coulomb coefficient
J	kgm^3	motor and load inertia

Table 4.8: real essential parameters of steady-state Bath*fp* induction motor model

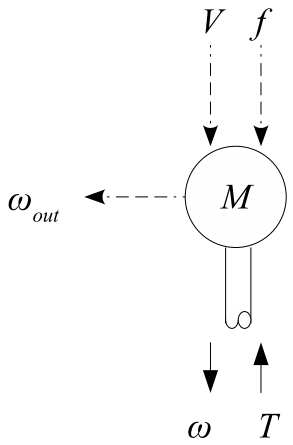

Figure 4.19: schematic of steady-state motor model

calculated according to equation 4.34, using the Fortran 77 complex number variable type, `cmplx`. The calculation of the electric torque and power then follow, using equations 4.33 and 4.29. Finally, the shaft speed is calculated, using the standard stiction sub-model, by:

$$\dot{\omega} = \frac{T_e}{\pi J} \tag{4.35}$$

where T_e is the effective torque, defined as the sum of the load torque, the electric torque and the coulomb and stiction torques if these are defined by the user.

The model is designed to be fed by a voltage and frequency signal, to reflect the V/f control implemented in the test rig using the frequency inverter. A simple V/f control model has been developed which supplies a constant V/f input to the motor up to a maximum frequency. For voltages above this range, the frequency is fixed. Figure 4.20 shows this relationship for the range of voltages and frequencies which apply to the motor. More detailed analysis of the electrical supply for such motors, in both the test rig and aircraft fuel systems, has been undertaken as a part of the electrical drives project, and details can be found in the thesis [12].

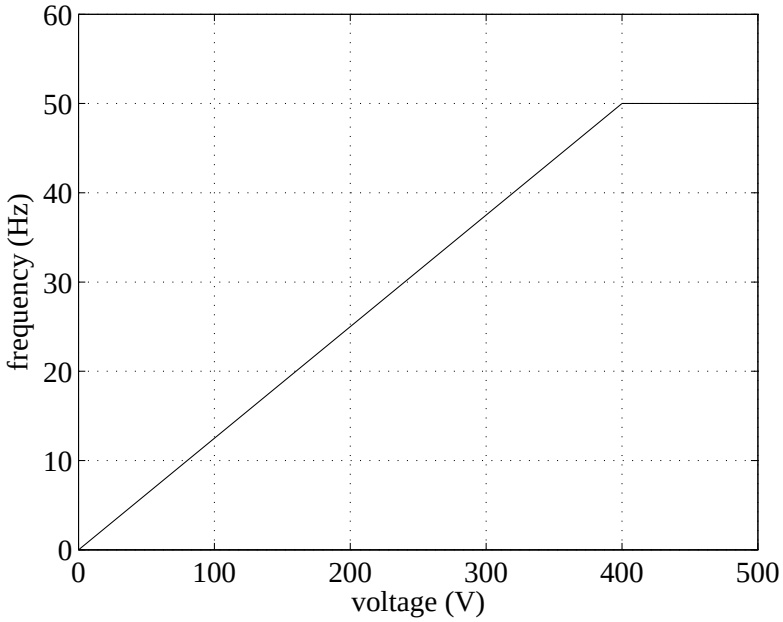

Figure 4.20: V/f control strategy

4.2.3 Available data for the test rig motor

The motor model described in section 4.2.2 requires inputs of the stator and rotor reactances and resistances, which are difficult to quantify. During the course of the electrical drives project, estimates of these parameters were provided by the manufacturer. Experimental studies on a similar motor were undertaken, and resulted in a second set of estimated data. These experiments followed the techniques discussed in Krause [35], and are fully described in the electrical project thesis [12]. Table 4.9 details the values of the parameters from both the manufacturer and experimentation.

parameter	units	manufacturer - no load	manufacturer - at load	test 1	test 2
X_m	Ω	105.73	75.60	93.26	94.56
X_s	Ω	1.808	1.808	1.775	1.784
R_s	Ω	0.783	0.783	0.779	0.773
R_r	Ω	0.984	0.984	0.921	0.898
X_r	Ω	2.544	2.040	2.663	2.663

Table 4.9: stator and rotor resistance and reactance values from both the manufacturer and experimentation

Figure 4.21 shows a comparison of the resulting no-load acceleration curve for these two sets of data using the Bath*fp* steady-state motor described in section 4.2.2. It can be seen that the two sets of experimental data are in close agreement, both in terms of the values of the parameters in table 4.9 and their respective torque-speed curves. The data provided by the manufacturer however predicts a much higher peak torque at a lower speed for the load case. The no load data matches the experimental data more closely, although the peak torque occurs at a lower speed. It should be noted however that for the linear torque-speed region, in which the motor will operate, all the models agree well, showing less than 3.5% difference at 2700rev/min and zero difference at 3000rev/min.

Figure 4.22 shows a comparison between the predicted steady-state torque-speed curve from the Bath*fp* model using the the manufacturer "at load" data and that measured using the main test rig for the linear operating region. This test data is taken from the same set of steady-state data as figure 4.1, using the data for the maximum demand

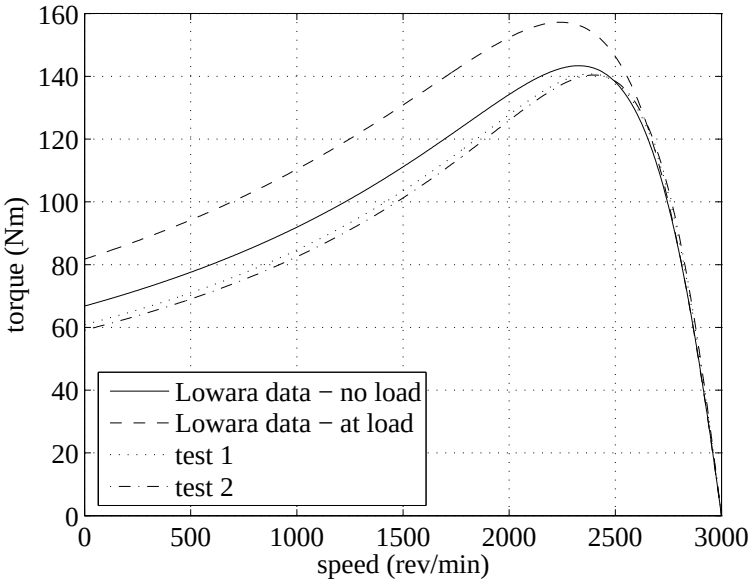

Figure 4.21: comparison of motor model using both parameters from manufacturer and from rig tests [12]

speed of 50Hz only. In this case, it is clear that there is a significant difference between the actual and predicted motor performance. In order to match the model performance to that measured in the test rig, the input voltage and frequency were altered to reflect the fact that the actual values of these as delivered by the Hydrovar inverter are unknown. The effect of this on the comparison between predicted and measured performance of the motor is shown in figure 4.22.

4.3 Pipework

In order to fully model the behaviour of the test rig, validate the system model, and apply the modelling tools to aircraft fuel system simulations, each of the individual components which make up the pipework needed to be analysed in terms of their steady-state performance. Tests were conducted to analyse the pressure-flow characteristics of the pipe sections, couplings, the reducing section downstream of the pump, the pump inlet line, the return line and the pipe bend. Each of these aspects were then combined with the centrifugal pump and motor driven ball valve models to analyse the system performance. This section details the experimental procedure to measure the

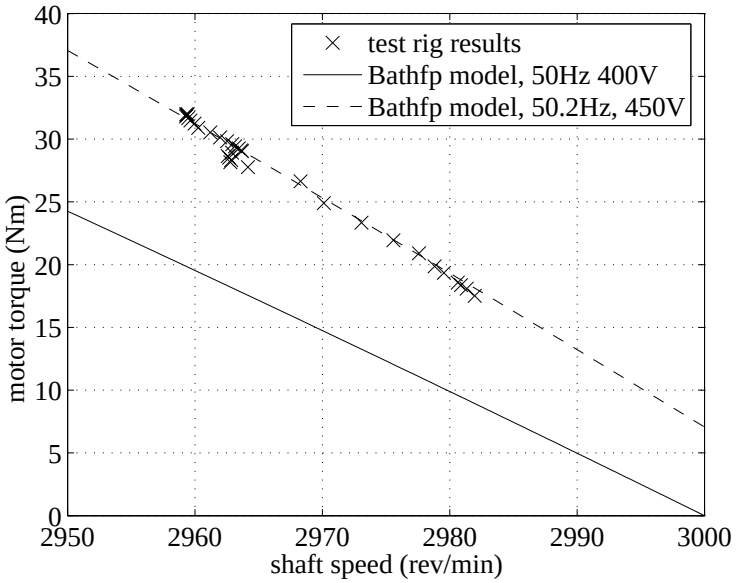

Figure 4.22: comparison of motor model using the manufacturer's data and test rig results for the linear torque-speed region.

pressure-flow characteristics of each of these components and their resulting models.

4.3.1 Pipe friction and coupling losses

The measurement of the pipe friction factor and the pressure losses due to the couplings are inextricably linked, and so have been treated as one analysis. In order to estimate the effect of each component, two methods were employed:

1. the pressure drop per unit length of pipe is calculated from measured data, and the coupling losses are subsequently inferred, and the pipe roughness calculated;
2. the pressure drop in the pipes is assumed from an empirical formula, the pressure loss from the couplings is then calculated from this and the measured data, and the pipe friction factor is adjusted for pipe roughness.

For each method, the rig was set up with two sections of different length pipes in between three transducer sections. Figure 4.23 shows a schematic of the test rig in

this configuration. Strain gauge transducer points are marked "S", and piezo-resistive transducer points "P". The pressure drops across these two pipes downstream of the bend and their couplings was then measured over the full range of possible flow rates using the strain gauge pressure transducers, as the steady-state performance of the piezo-resistive transducers was shown to be inaccurate due to sensor tip cooling when using water as the working fluid. Each set of tests were conducted twice, with the couplings in their fully stretched and fully compressed state, in order to ascertain the effect of their position on their pressure drop.

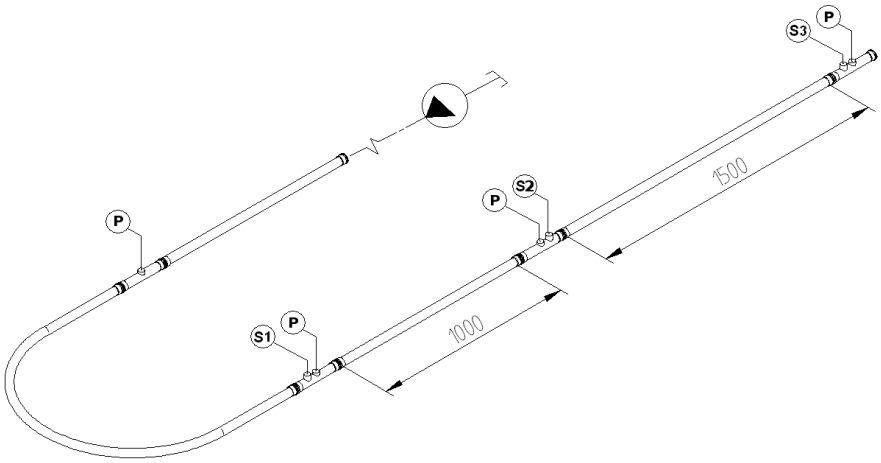

Figure 4.23: pipe and transducer arrangement for assessing pipe and coupling pressure losses

Method 1

It was proposed then that the difference in these pressure drops would be due solely to the difference in length of the two pipes. This could then be used to estimate the pipe friction loss, and hence the coupling loss. Referring to figure 4.23, if the pressures at transducers $S1$, $S2$ and $S3$ are p_1, p_2 and p_3 respectively, and the pipe lengths marked as 1000mm and 1500mm are l_1 and l_2 respectively, then the pressure drop per unit length of pipe, $\delta p_p/l$, can be described as:

$$\frac{\delta p_p}{l} = \frac{2p_2 - p_1 - p_3}{l_2 - l_1} \tag{4.36}$$

Using this value, the pressure drops across each of the sections of pipe in between transducers and couplings can be assessed. Consider figure 4.24. Here, the pressure drops, δ_p, across each of the lengths of pipe, l labeled a, b, c, d, e and f can be calculated from the pressure drop per unit length. Then, these are subtracted from the overall pressure drop to give the pressure loss due to the couplings, δp_γ, labeled γ:

$$4\delta p_\gamma = (p_1 - p_3) - \delta p_a - \delta p_b - \delta p_c - \delta p_d - \delta p_e - \delta p_f \tag{4.37}$$

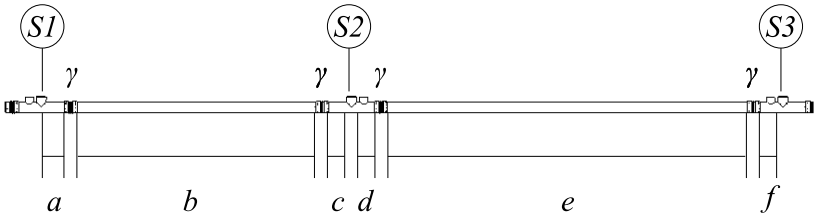

Figure 4.24: definition of pipe lengths for pressure loss analysis

Finally, the coupling pressure losses were converted into a K loss factor, and the pressure drop per unit length of pipe converted into a friction factor, using the definitions given in Miller [11] and White [36] respectively:

$$K = \frac{\delta p}{\frac{1}{2}\rho U^2} = \frac{\delta p}{\frac{1}{2}\rho \left(\frac{q}{A}\right)^2} \tag{4.38}$$

$$f = \frac{d}{\frac{1}{2}\rho \left(\frac{q}{A}\right)^2} \frac{\delta p_p}{l} \tag{4.39}$$

From equation 4.38, it is clear that the K factor will be dependent on the fluid density, and hence temperature. For all values of K quoted in the following, the fluid temperature has been assumed to be 20°C, and hence the fluid density is 998kg/m^3. The K factor can then be scaled according to the density ratio for analysis where the fluid temperature differs from that used to calculate the original factor. Figure 4.25 shows the measured relationship between pressure and flow rate for the pipe couplings. It is presented here as pressure drop against flow rate squared, with a linear fit through the data. If this is constrained to pass through the origin, then the gradient of this curve can be used to calculate K using equation 4.38. The measured K factors for the

couplings from both pipes are in close agreement, with $K_1 = K_2 = 0.11$ (2 sig. fig.) for the fully compressed state. Figure 4.26 shows the calculated friction factors for pipe sections b and e, plotted against the Reynolds number, which is defined for pipe flow as [36]:

$$R_e = \frac{Ud}{\nu} \tag{4.40}$$

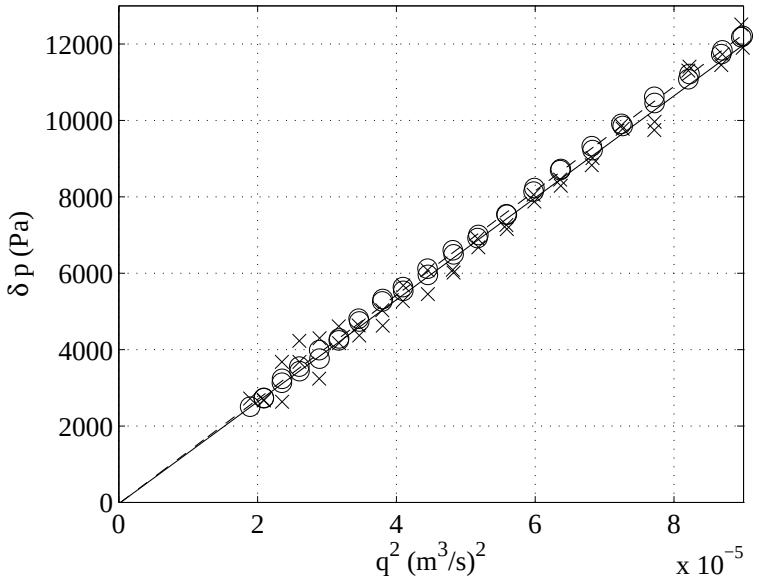

Figure 4.25: measured pressure-flow rate squared relationship for pipe couplings

Haaland's equation, an explicit alternate form of the Colebrook formula for pipe friction whose accuracy is within 2% for the range $10^3 < R_e < 10^8$, has been used to calculate the friction factor for a smooth-walled pipe. Flow in the test rig resulted in a Rynolds number of around $R_e = 3.5 \times 10^5$. Haaland's equation is [36]:

$$\frac{1}{f^{\frac{1}{2}}} = -1.8log\left[\frac{6.9}{R_e} + \left(\frac{\epsilon/d}{3.7}\right)^{1.11}\right] \tag{4.41}$$

By re-arranging equation 4.41, it is possible to estimate the relative roughness of the pipes, ϵ/d:

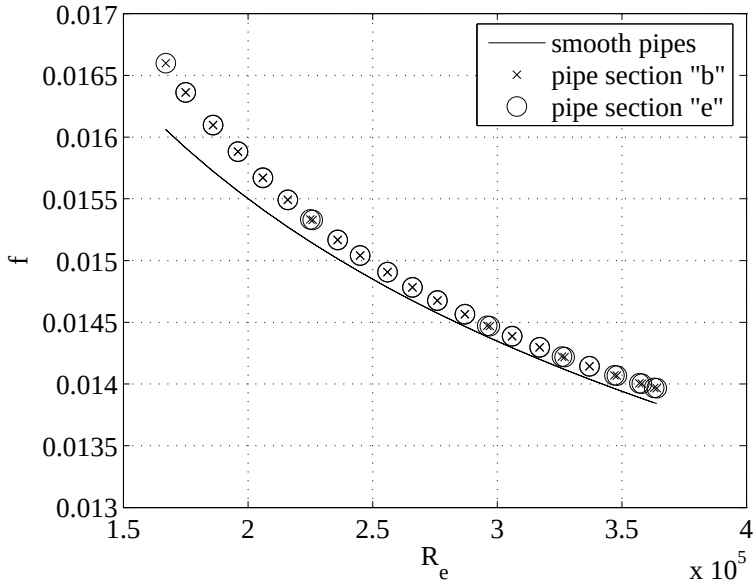

Figure 4.26: measured pipe friction factor

$$\epsilon/d = 3.7 \left[10^{\frac{1}{-1.8 f^{\frac{1}{2}}}} \right) \left(- \frac{6.9}{R_e} \right]^{\frac{1}{1.11}} \tag{4.42}$$

Figure 4.27 shows the resulting relationship between relative roughness and Reynolds number for the two sections of pipe. It is clear that the results predict a relative roughness of the order of $1 \times 10^{-5} < \epsilon/d < 9 \times 10^{-5}$, which fits well with as estimated value of $\epsilon/d = 5.8 \times 10^{-5}$ for drawn aluminium pipes [36].

As mentioned in chapter 2, the transducer pipe bosses suffered from a manufacturing error, whereby the inner surface of the boss was not flush with the inner surface of the pipe, creating a small cavity. The above analysis was conducted assuming that the sections of pipe between the pressure measurements and couplings were straight, constant section pipes. In order to investigate this assumption and any effect of the cavities, an amendment to the test procedure was introduced. Figure 4.24 shows the strain gauge pressure transducers 1 and 2 next to the pipe couplings between the transducer pipes and pipe section b, pressure transducers 2 and 3 have piezo-resistive bosses in between them and the pipe couplings connected to pipe section e. A second

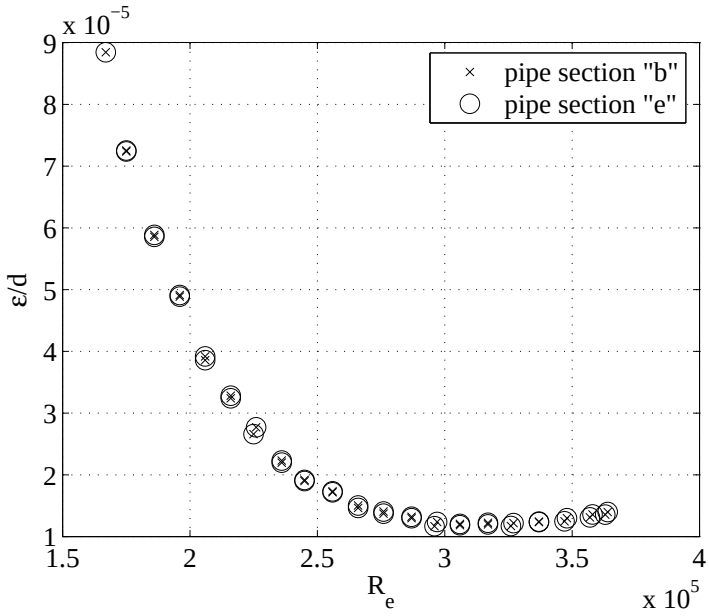

Figure 4.27: measured pipe relative roughness

set of tests were conducted with the pressure transducer pipes containing transducers 2 and 3 rotated through 180°, as shown in figure 4.28.

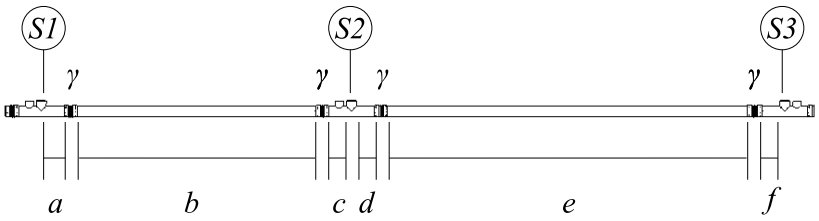

Figure 4.28: definition of pipe lengths for pressure loss analysis, with inverted pressure transducer boss positions

The same test procedure can be applied to find the pressure losses in each of the pipes and couplings, in terms of friction factors and K factors. However, instead of comparing the pressure drop between the three transducers for one test only, the pressure drop $p_1 - p_2$ from the first test is used with the pressure drop $p_2 - p_3$ from the second test in equation 4.36 to calculate the pressure drop per unit length of pipe. The resulting pipe coupling K factors and pipe friction factors however were unrealistic and were not repeatable. For example, two consecutive tests produced very different results, with one

giving a negative pipe roughness and a large coupling K factor, of the order of $K = 0.3$, and the other a very high pipe roughness and a coupling K factor which did not fit to the expected square law relationship of equation 4.38. Subsequent re-testing of the first case revealed that these results, using the single pipe configuration method, were not repeatable either, resulting in non-square law pressure-flow relationships. One such example is given in figure 4.29, which demonstrates that the linear fit through the pressure-flow rate squared data is clearly inappropriate. Whilst it is known that the relationship between pressure and flow rate at low flows, where conditions are changing from laminar to turbulent, is not necessarily described by a square law, the range of Reynolds numbers encountered during the tests was broad enough to model the components in such a way. In the light of these inconsistencies, most likely as a result of measurement accuracy, the second test method was developed.

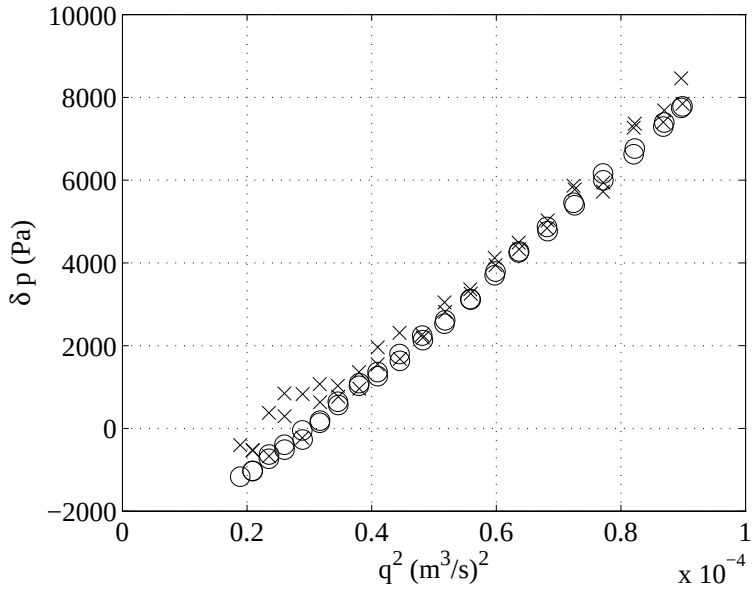

Figure 4.29: example of non-repeatable results, leading to poor estimate of coupling K factor

Method 2

It was proposed that, if the pipe pressure loss due to friction could be assumed using an existing empirical formula, then the coupling pressure loss could be obtained by subtracting the pipe loss from the measured pressure drop. It would then be possible

to estimate the actual pipe roughness and iterate to find the actual coupling pressure loss. Haaland's equation (equation 4.41) was used, with ϵ/d set to zero to represent a fully smooth pipe, to find the expected pressure losses in the pipe sections labeled a, b, c, d, e and f in figure 4.24. These were then used to calculate the pressure losses associated with each of the couplings, $\delta p_{\gamma,1}$ and $\delta p_{\gamma,2}$:

$$2\delta p_{\gamma,1} = (p_1 - p_2) - (\delta p_a + \delta p_b + \delta p_c) \tag{4.43}$$

$$2\delta p_{\gamma,2} = (p_1 - p_2) - (\delta p_d + \delta p_e + \delta p_f) \tag{4.44}$$

The pressure losses were again expressed as a K factor based on equation 4.38, calculated using the pressure-flow rate square fit as before. The pressure losses due to the couplings were then subtracted from the measured data, and the resulting pipe friction factors for pipe sections b and e were calculated from equation 4.39. By plotting these calculated friction factors against Reynolds number, it was possible to then plot a friction factor line for a positive relative roughness to achieve a close match. This relative roughness was then used to calculate the pipe friction as at the start, and iterate to find the coupling losses and a relative roughness value. Once again, the test method was repeated with the two transducer sections rotated through 180° in order to assess the impact of the boss cavities on the pressure drops.

Figure 4.30 shows the final estimated friction factors for pipe sections b and e, and the best fit of the Haaland equation. Table 4.10 details the calculated coupling K factors for both the single and double test methods, and in each case for the couplings in their stretched and compressed states.

4.3.2 The pump outlet reducing section

In order to connect the 100mm pump outlet port to the 35mm ($1.25''$) pipework, an aluminium reducing section was created. Figure 4.31 shows the components which constitute the reducing section. The outlet of the pump is connected to the reducing section via a flange and threaded pipe nipple. It consists of a linear change in section from 100mm to 35mm with a $2''$ branch line for the by-pass and a PRPT transducer port. It is connected to the aluminium aircraft piping by a threaded pipe nipple, gate

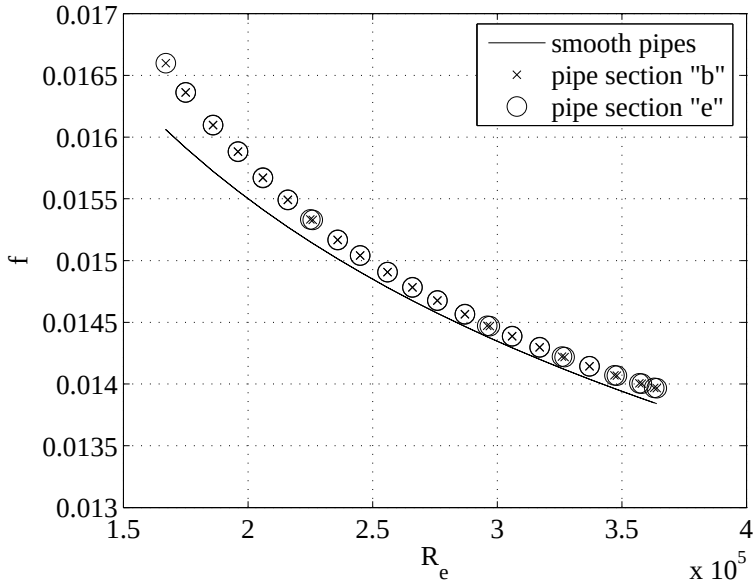

Figure 4.30: estimated pipe friction factors compared to Haaland equation for smooth pipes

coupling state	single method	double method
compressed	0.10	0.08
stretched	0.12	0.11

Table 4.10: measured K factors for the pipe couplings in both their compressed and stretched state, using both the single and double test methods

valve and dummy pipe coupling block.

The pressure drop between the pump outlet port and the transducer downstream of the reducing section was recorded using transducers S2 and S3 for a range of flow rates. The pressure loss due to the short section of pipe between the transducer and the exit of the reducing section is calculated using the relative roughness value from section 4.3 and equation 4.41. The reducing section K factor was found during the same tests as the bend. Table 4.11 gives the values from each of these.

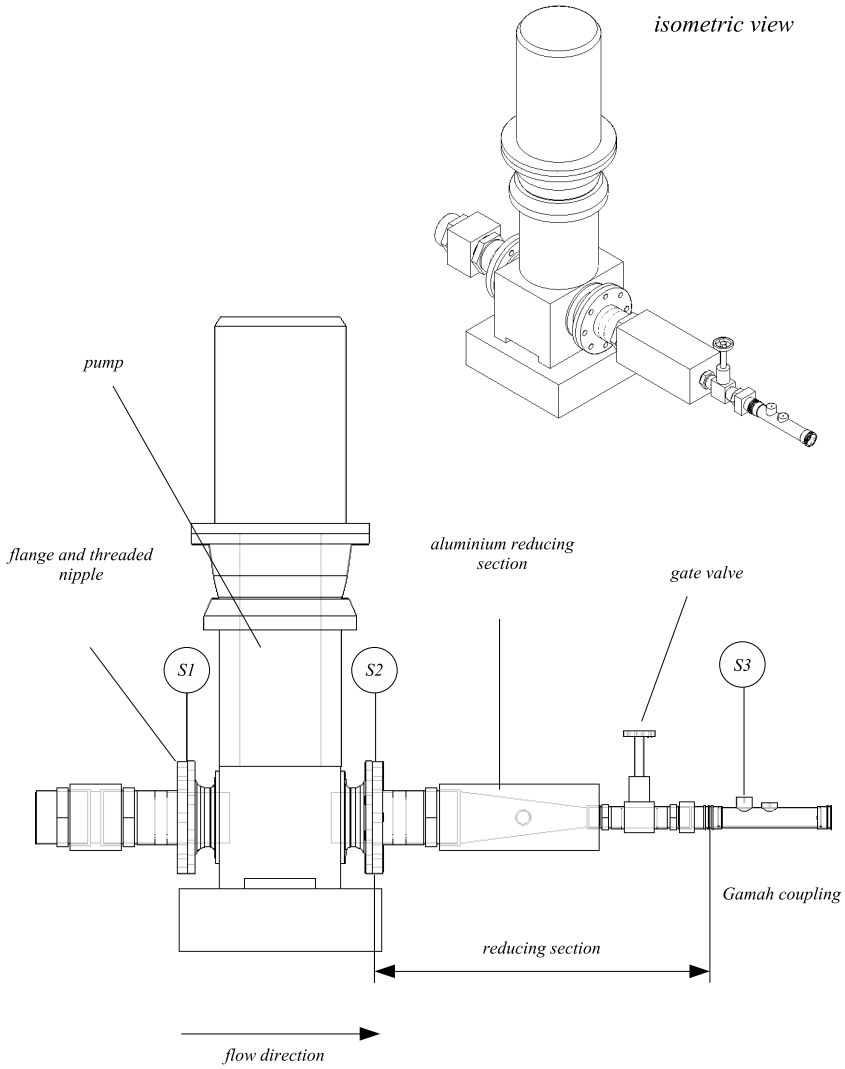

Figure 4.31: definition of the reducing section downstream of the pump

test number	reducing section K factor based on outlet area
1	1.10
2	1.08
3	1.09

Table 4.11: reducing section K factor

For subsequent modelling work, the mean of these values ($K = 1.09$) has been used.

4.3.3 The pump inlet line

The pressure measurement at the inlet of the pump, located in a pressure tapping on the top surface of the flange at the pump inlet, was subject to a lot of scatter from test to test. The results from the full range of tests repeatedly showed a similar trend between pressure drop and flow rate, although the no-flow pressure measurement was often quite different from one test to the next. This has been attributed to the unsteady nature of the flow in a centrifugal pump inlet line [10], where complex flow patterns such as swirl and cavitation can lead to spurious pressure measurements. Instead of taking the directly measured pressures, the results have been normalised to give a zero pressure drop at no flow. The measured pressure drop is then used to define a K factor as in equation 4.38. Figure 4.32 shows some typical raw test data, where the offset nature of the no-flow condition is clear, and figure 4.33 shows the normalised inlet pressure data, plotted against q^2 to facilitate the calculation of the inlet line K factor.

From these data, the pump inlet loss factor has been calculated as $K_{inlet} = 3.55 \times 10^{-3}$ using an outlet diameter of 100mm. The pressure never decreases below atmospheric during pump operation, as the tank head is approximately 0.176bar, and the maximum possible flow rate in the system, 1100L/min produces a pressure of 0.086bar at pump inlet.

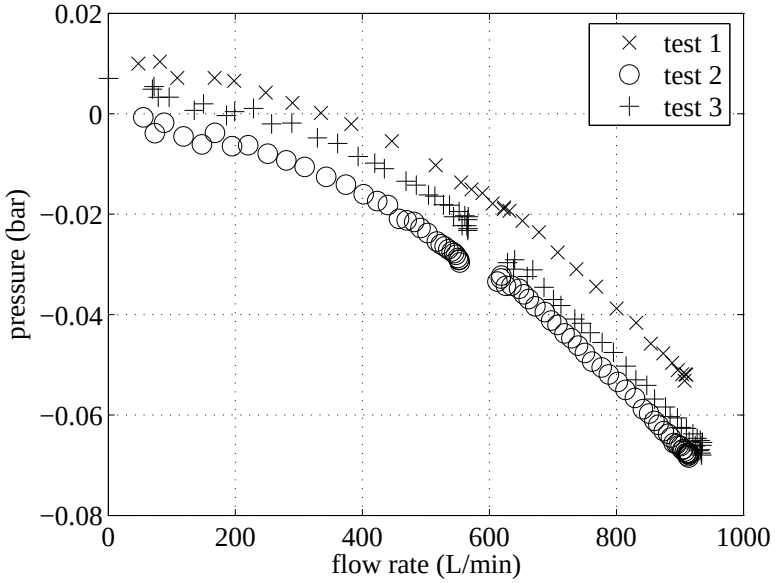

Figure 4.32: measured pump inlet pressures relative to tank head

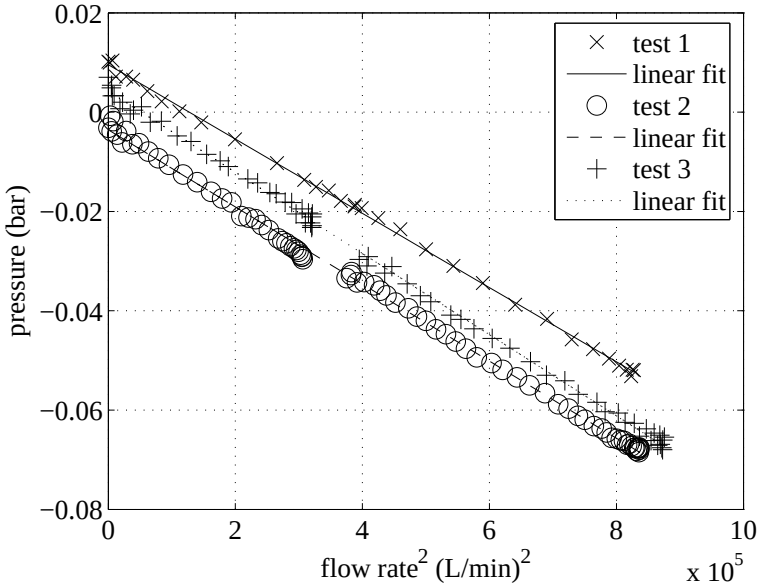

Figure 4.33: measured pump inlet pressures relative to tank head, plotted against q^2 to estimate K

4.3.4 The bend

The pressure loss associated with the 180° bend (see figure 4.23) was found by calculating the pressure loss due to the pipes, including the bend as though it was a straight pipe, and the couplings using the K factors from section 4.3. The additional loss was attributed to the bend. It was converted into a K factor as before (see equation 4.38). The resultant bend K factors from the tests with compressed and stretched couplings are given in table 4.12.

coupling state	bend K factor
stretched	0.22
compressed	0.22

Table 4.12: bend K factors using both compressed and stretched pipe couplings

This K factor is around half of what might be expected for such a bend [11]. Figure 4.34 shows the expected K factors for bends of circular cross section and different geometries. The 180° bend in the test rig has a (r/d) ratio of 14.6, leading to a K factor of about 0.4. It is clear however that this involves extrapolating the data well outside of the range of the graph in Miller [11], and so may not be accurate.

4.3.5 The return line

Since the behaviour of the rig downstream of the pressure sensor after the motor driven ball valve is not of interest, the pressure losses of this section have been combined into a single K factor. These are found from the pressure measurements downstream of the motor driven ball valve assuming the tank pressure is zero. The value to be used in the modelling work is $K = 0.73$.

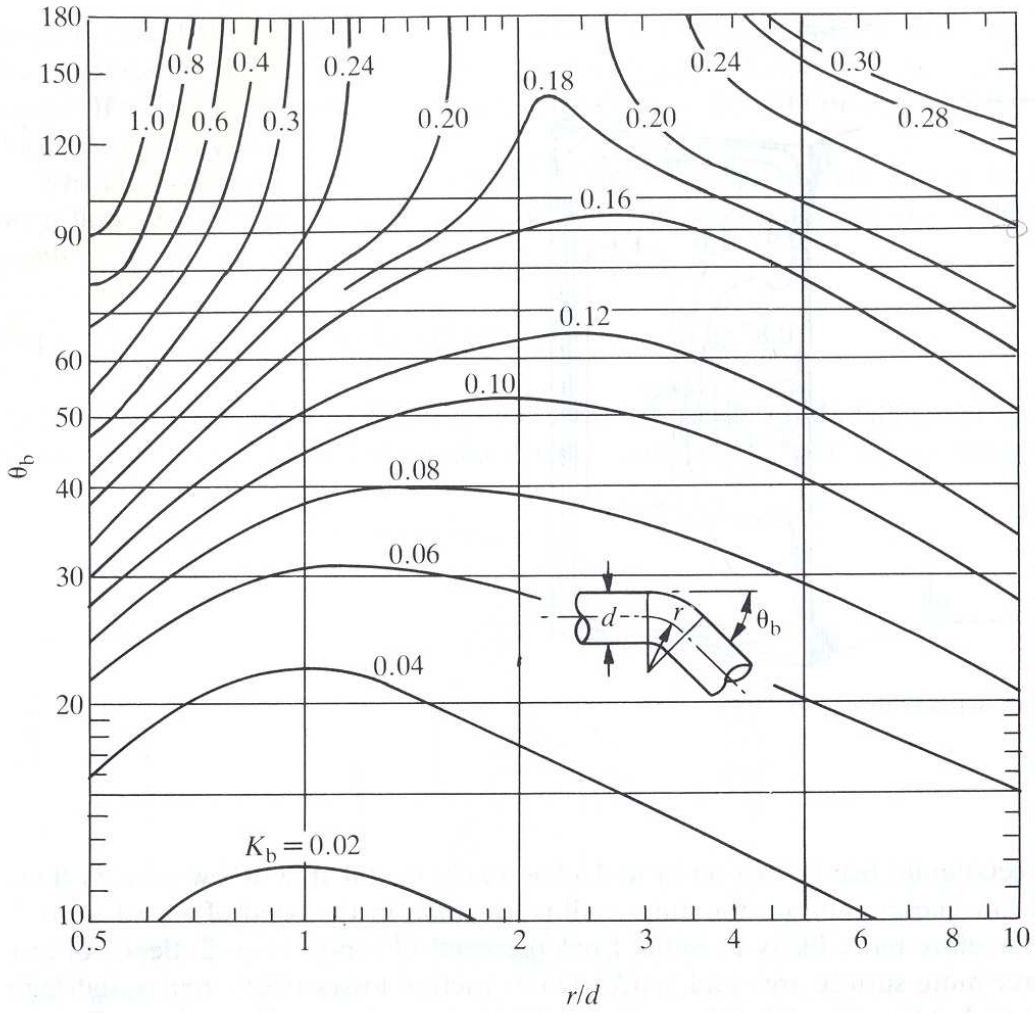

Figure 4.34: bend K factors, reproduced from Miller [11]

4.3.6 Implementation of loss models in Bath*fp* simulation environment

Bath*fp* pipe models include an input of additional loss factors, defined using the same K factor definition as in equation 4.38. This facility can be used to simulate the pressure losses due to the reducing section, the couplings and the bend. The pressure loss due to friction is also incorporated in the Bath*fp* pipe model as an input of relative roughness, ϵ/d. The pump inlet line and system return line could be modelled using the existing Bath*fp* hydraulic orifice model, although this does not require the input in the standard K factor form, but in a simple pressure-flow rate factor using Bath*fp*'s standard unit inputs of bar and L/min. Therefore, a simple pressure loss model was developed. This requires an input of pressure at each port, a K factor defined as in equation 4.38, the base fluid density for which the K factor was derived and the diameter of the flow path upstream of the source of the pressure loss. Figure 4.35 shows the Bath*fp* circuit for steady-state rig analysis, with two pressure loss models for the pump inlet line and system return line.

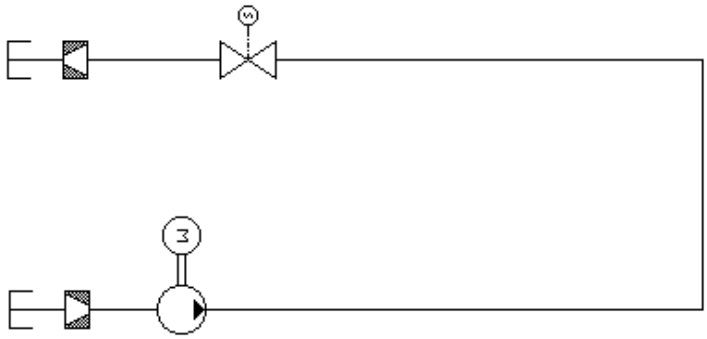

Figure 4.35: Bath*fp* circuit of test rig, showing pressure loss blocks in pump inlet and system return lines

4.4 Closure

In order to simulate an aircraft fuel system, or subsystem thereof, such as the trim to centre transfer route, detailed knowledge of the steady state behaviour of the individual components is required. The fuel system can be said to be comprised of two tanks,

connected via a long section of pipe containing various bends and couplings, with flow provided by induction motor driven centrifugal pumps and controlled by motor driven ball valves. Steady-state models of each of these components is required.

A literature review of centrifugal pump modelling suggests that detailed one-dimensional analysis of the flow path, whilst ideal for pump design, is not adequate at predicting pump performance off-design. In such situations, such as when operating the pump with a variable speed drive, a more "black-box" style of model using a measured pressure, flow and torque characteristic is beneficial. Such a model has been developed, based on the measured characteristics and the affinity laws, resulting in two simple non-dimensional relationships between pressure and flow, and hydraulic power and torque respectively. Such a modelling technique has been applied to the pump in the test rig, and has been shown to agree closely with the measured data.

A steady-state AC induction motor model has been developed using equivalent circuit analysis. Using parameters supplied by the manufacturer and from experimentation on a related project, this model has been applied to the motor in the test rig. It has been shown that the model and test rig data are in close agreement, given that the electrical supply to the test rig can be assumed to vary from the expected norm for the UK. It has been noted however, that such a modelling technique is perhaps not suitable for modelling systems where details of the motor such as resistances and reactances are not known. It is difficult to extend such a modelling technique to produce a generic motor model for system analysis.

The steady-state pressure losses associated with various components of the pipe work have been measured. The pump inlet line, pump outlet reducing section, pipe couplings, 180° bend and return line have been characterised as simple K factors based on the definition in Miller [11]. The pipe friction factors have also been measured, and from these an estimate of the pipe roughness has been obtained, which was close to the expected value for drawn aluminium pipes.

Chapter 5

Component modelling: Dynamic

Just as the steady-state performance of each of the components in the test rig and in typical aircraft fuel systems is of importance when modelling their behaviour for typical fuel transfer operations, their dynamic behaviour is equally crucial to quantify whether the system operation ever deviates from the expected steady-state. To this end, the dynamic behaviour of each of the components in a typical trim to centre fuel transfer system have been investigated.

As with the steady-state behaviour of centrifugal pumps, it is desirable to develop a "one size fits all" generic model of pump dynamic behaviour, although due to the nature of the variation of pump internal geometry from one design to another, such models are practically impossible. Instead, the dynamic behaviour of the pump in the test rig has been investigated using the existing standard secondary source technique, and an attempt has been made to develop a new acoustic test method. The acoustic test method is extended to investigate the dynamic response of ball valves, typically used aircraft fuel systems. Both of these methods have been used to develop dynamic models of the fuel system components in Bath*fp*.

For simulating fuel system performance, the dynamic behaviour of the electric drive of the pump is of great importance. A model is developed based on an extension of the Thévenin circuit analysis of AC induction motors to include an axis transformation into the rotating frame. This allows accurate simulation of the torque produced as a

consequence of the rotating magnetic field, but suffers when detailed information about the motor is unavailable. It is suitable for analysing the behaviour of the test rig, or for current aircraft generations which use AC motors.

As with the steady-state component models, the dynamic models have been validated, where possible, against data from the test rig.

5.1 Centrifugal pumps

Four centrifugal pump modelling techniques which encompass dynamic behaviour have been identified in the literature. Each of these have been evaluated in terms of their applicability to the modelling of variable speed aircraft fuel system pumps. A number of pump models have been developed in both Matlab/Simulink and the fluid power simulation software Bath*fp*.

The pump modelling methods identified in the literature can be broken down into four categories:

1. Analytical solution of an unsteady one-dimensional Euler equation. The basic Euler equation from chapter 4 is extended to consider the rate of kinetic energy change as a consequence of its angular acceleration, as well as the static pressure rise considered in the steady-state analysis. Like the steady-state analysis, certain pressure losses are accounted for using simplified relationships.

2. The unsteady flow on a representative flow surface can be modelled as a rotational flow field. The flow on the impeller blade surface can be modelled as a linear cascade, approximating a rotating cascade. Such analyses contain a number of fundamental approximations which are thought to limit its applicability, and often lead to the steady-state performance of the model differing significantly from experimental data.

3. The steady-state characteristic of a pump can be extended to include a dynamic term, which represents the effect of fluid inertia within the pump passageways. Like the steady-state characteristic itself, the source and nature of the fluid inertia is of no consequence, but its effect is considered, producing a “black box” style model. Such a model is therefore applicable to the case where little detailed information about the pump geometry is known

4. The pump can be modelled as a source impedance, which can be characterised as a matrix relating input pressure and flows to outlet pressures and flows. The matrix can be represented by a lumped parameter model, often drawing on electrical circuit analogies. The inertia effect case above can be considered a special case of a transmission matrix model.

The following sections consider these modelling methods in detail.

5.1.1 Unsteady one-dimensional Euler analysis

Several authors have applied an unsteady form of the Euler equation to perform one-dimensional analysis of the behaviour of centrifugal pumps during start up and shut down operations. Saito [37] presents an experimental programme which aimed to determine the effect of three factors on the transient characteristics of a pump during start up. These factors were the mass of fluid in the discharge pipe, valve opening duration and pump start up time. The results are presented graphically as loci of the operating point of the pump in both a dimensional pressure-flow domain ($H - Q$) and in a non-dimensional pressure-flow domain ($\psi - \phi$), using a similar definition of pressure and flow coefficients to those given in chapter 4. The results clearly indicate that an increase in the discharge pipe fluid mass led to a flow rate lag, associated with the requirement to accelerate the fluid in the pipe, and that longer starting times lead to the pump following the steady-state system characteristic, indicating the pump acceleration is quasi-steady. The Euler equation for steady-state head rise as a result of the angular acceleration of the fluid has been developed to include a dynamic element by considering the rate of change of kinetic energy of the fluid. The theoretical pressure rise due to the impeller is calculated using a number of coefficients, which are based on the blade angles and blade passage areas at impeller inlet and outlet. The same is done for the diffuser. Pressure losses as a result of steady-state friction and shock are included, although the derivation of these is unclear. The pipeline has been characterised as a simple steady-state pressure loss due to friction and a fluid inertia term, and assumes that compressibility is negligible, and that the flow instantly becomes turbulent at pump start up. The valve is characterised as a simple hydraulic orifice model. The pressure rise across the pump is calculated as a result of the input of the experimental shaft speed. The model is shown to behave in a similar way to the experimental results for different pipe lengths, valve openings and start up times.

Thanapandi, Tsukamoto and Prasad [38] have presented a similar centrifugal pump model to that of Thanapandi and Prasad [18], which presented an experimental programme to determine the start up characteristics of a pump. The first paper [18] suggested that the behaviour of the pump could be considered quasi-steady state. The unsteady Euler equation for the pump is solved numerically for pressure rise, using finite difference approximations for the derivative terms. The pipeline is not modelled, but instead the model requires an input of both shaft speed and flow rate from the experimental data. The resultant pressure rise across the pump is compared to the experimental data, and against the predicted pressure rise as a result of a previous steady-state model from [18]. The paper claims a good agreement between the computed and measured results.

5.1.2 Rotational flow field analysis

Two-dimensional flow analysis of impeller passageways have been conducted in the past by Busemann and Acosta (both referenced in [39]), among others, although the work was restricted to impellers with logarithmic spiral blades. Kumar and Rao [39] have extended this work to examine impellers of varying width, which is of importance when considering three-dimensional flow in impellers with twisted blades, such as Francis impellers. Assuming that the flow can be considered irrotational and quasi-two-dimensional, the flow can be analysed along the axisymmetric flow surface. The stream surface is then mapped from a radial cascade to a rectilinear cascade. The method is complex, and results in a head coefficient for a given range of flow coefficient. The results are compared to experimental data, and are shown to be in good agreement for points close to the best efficiency operating point.

Tsukamoto and Ohashi's paper on transient characteristics of centrifugal pumps during start up [33], and the companion paper on shut down by Tsukamoto, Matsunga, Yoneda and Hata [34] use a two-dimensional circular cascade, similar to that discussed in Kumar and Rao [39] to model the pressure and flow distribution along the mean streamline of the impeller. In order to analyse the performance of the pump and compare results with experimental data, the pipeline is modelled using a simplified lumped parameter model, where the steady-state pressure loss due to friction is separated from the inertia effects. The compressibility of the fluid is ignored. On comparison with the experimental data, the model shows a similar dynamic trend for both start up and shut down, highlighting that the flow tends to lag the pressure rise, indicating a significant inertia effect. However, in both cases, the model is incapable of capturing the

steady-state characteristic, with the non-dimensional pressure-flow curve differing from the measured curve by as much as a factor of two. The authors determine a criterion for quasi-steady performance, based on pump operating speed, deceleration time and operating flow rate.

5.1.3 Extension of steady-state characteristic-based model

Tsukamoto et al. [33] and [34], suggested that any deviation from the steady-state performance of the pump was purely as a result of fluid inertia within the pump casing. This conclusion was as a result of analysis of the non-dimensional pressure-flow loci pattern during start up and shut down periods. The model makes no attempt to describe why such an inertia effect should be present, or if other dynamic factors should be considered such as fluid compressibility. The fluid inertia in the pump is modelled as a simple lumped parameter, with a numerical value equivalent to a length of constant section pipe. Neither paper considers how the discharge pipe geometry affects the pump dynamics, and the assumptions regarding the pipe behaviour are not investigated.

5.1.4 Characterisation of pump as an impedance source

Much work has been conducted on the characterisation of pumps as sources of pressure or flow ripple, as such ripple is the source of fluid borne noise, which, when transmitted via structure, can lead to airborne noise. Such modelling is particularly useful in the case of positive displacement pumps, where the pressure and flow output will be oscillatory as a consequence of the cyclic nature of the pump [40]. Centrifugal pumps have also been shown to produce pressure and flow ripple as a consequence of the impeller and diffuser or volute interaction [41]. The same techniques which were developed for positive displacement pumps have been applied to centrifugal pumps.

In his introduction to fluid borne noise in the marine environment, Whitson [42] gives a brief summary of how fluid borne noise from pumps can be modelled. Positive displacement pumps can be considered as a flow source and source impedance, resulting in a one-port, two-pole source. This source impedance and flow ripple can be measured using, among other techniques, the secondary source method. Examples of such a test method on positive displacement pumps can be found in [40] and [43]. For rotodynamic pumps, such as centrifugal pumps, the model is more complicated, as a result of the

direct flow path connection between inlet and outlet ports. The model is extended to a two-port, four-pole model, where the pressures and flows at inlet and outlet are connected via a transmission matrix. This passive element, equivalent to the source impedance of the one-port model, is supplemented by a pressure or flow source.

Whitson and Benson [44] have analysed the applicability of the one-port, two-pole method to centrifugal pumps, where the connection between inlet and outlet port might normally lead to the assumption of the applicability of a transmission matrix model. The work concentrates on pump operation well below the normal operating, or best-efficiency point. The secondary source method is used to analyse the source flow and impedance of the pump at a number of different pump speeds, including a stationary case. The results agree well between each case, although it is noted that the measured impedance-frequency relationship becomes less smooth at higher pump speeds, indicating the importance of using a secondary source which can dominate the levels of noise produced at the pump. A number of secondary sources are investigated. The tests were conducted using a secondary flow from a positive displacement pump through a partially shut ball valve, which produced cavitation and subsequently a broad band noise source across a relatively wide frequency range. The pump flow source was analysed at a number of different loads and pump speeds. Whilst the load was shown to have no effect on the flow source, an increase in the pump speed was shown to increase the levels of broad band noise. The one-pole method was shown to be of use in mid-frequency ranges, although it was found to be less useful at very low frequencies. It is suggested that multi-stage pumps may see less of a connection between inlet and outlet ports, and as such may be more suitable for the one-port model. In general, the one-port model is shown to be of use when analysing the impedance of centrifugal pumps.

The use of a two-port, four-pole model for centrifugal pumps is well documented. De Jong, Kriesels, Bruggeman and Van Bockhorst [45] present an investigation of the transmission matrix of a centrifugal pump using both a two-microphone method, and a two-load method. France and Bilyk [46] applied the secondary source method to determine the transmission matrix of a centrifugal pump although they found that the transmission matrix at lower frequencies was unobtainable due to high attenuation of the pressure signals across the pump.

Stirnemann, Eberl, Bolleter and Pace [47] used the secondary source method to predict the transmission matrix of a centrifugal pump. The resultant matrix was compared to a simplified electrical circuit model, similar to those proposed by Edge [48] and Johnston

and Drew [40] for positive displacement pumps. The model was adjusted for different cavitation numbers according to experimental results. Kawata, Takata, Yasuda and Takeuchi [49] present a similar experimental programme to determine the transmission matrix of a prototype centrifugal pump. The likelihood of the pump to result in previously identified system instabilities was assessed. The new pump was shown to be suitable for the system under investigation. Bardeleben and Weaver [50] investigated the use of a scattering matrix rather than a transmission matrix, following on from work by Davies [51]. The scattering matrix relates the acoustic plane waves travelling towards and away from the pump at both inlet and outlet. The traditional transmission matrix requires some estimate of where the noise production occurs in relation to the pump ports, whereas using the scattering matrix assumes a more "black-box" style of model, where only the overall effect of the noise production is considered. Bardeleben and Weaver demonstrate how the scattering matrix can be found from the measured transmission matrix.

5.1.5 Comparison of methods

Like the steady-state Euler equation method, both the unsteady Euler and rotational flow methods require a large amount of detailed information about the internal geometries of the pumps under investigation. The methods lend themselves more readily to initial design studies of pumps, where estimates of the predicted dynamic behaviour of the pump are of importance. Even if the internal geometries of the pump are well known, the method relies heavily on estimated parameters to model the losses associated with steady-state friction and shock.

Neither the unsteady Euler nor rotational flow methods make a clear distinction between the effect of the pump and the connected pipe work on the measured pressure and flow response. The analysis can only be considered accurate for the particular experimental set up described in the papers. Where any account has been taken of the pipe work on the dynamic response of the system, a lumped parameter model has been applied, which seeks to describe the fluid inertia, compressibility and pressure loss as single parameters. Such a modelling technique is known to be acceptable for low frequencies, but at higher frequencies distributed parameter models are more accurate. Depending on the length and diameter of the pipe work, such lumped parameter models may not be appropriate.

Whilst the unsteady Euler method does satisfy the steady-state performance of the

pump, provided that the model is well defined and the analysis is restricted to the design operating point, the rotational flow method has been shown to be inaccurate for steady-state analysis. In order to match the steady-state performance of the pump model to the experimental data, extra loss factors would need to be included, possibly based on some of the loss models derived for the steady-state models described in chapter 4. Such a model would then become less accurate for off-design performance analysis.

It was decided that the dynamic behaviour of the pump in the test rig would be assessed using the secondary source technique to measure its impedance, following a similar test method to that set out for positive displacement pumps by Johnston and Drew [40] and for centrifugal pumps by Whitson and Benson [44]. This impedance would then be modelled as an electrical circuit as in Johnston and Drew [40], Stirnemann [47] and Edge [48]. It was decided, based on some early tests of the measured level of pressure ripple on the inlet line and from the work by Whitson and Benson [44], that a one-port model was more appropriate. The pressure ripple was applied downstream of the pump and measured on the inlet line. It was clear from the results that the coupling between the inlet and outlet ports was weak, possibly because the pump was two-stage, and the inlet line had a very low impedance. This is discussed further in section 5.1.8.

The measured impedance could be combined with the measured non-dimensional steady-state pressure-flow characteristic to produce a pump model capable of capturing the pump's behaviour in both steady-state and dynamic operation at any operating point. Such a pump model would not however be directly applicable to aircraft fuel pumps, as their design is significantly different to that of the pump in the test rig. However, much of the work identified in the literature suggests that the dynamic behaviour of centrifugal pumps, in general, is dominated by fluid inertia. It was proposed that a simplified pump model could be developed based on a non-dimensional steady-state characteristic and an equivalent inertia. Such a model could then be used for analysis of a system where the pump definition is unknown, but the effect of fluid inertia needs to be considered.

5.1.6 The secondary source technique

An analogy between hydraulic circuits and electrical circuits can be drawn, as when considering long distance electrical distribution systems or long hydraulic pipelines. In such cases, the usual lumped parameter assumptions break down and wave propagation

must be considered. The flow of fluid in an hydraulic system can be said to be analogous to electric current, and the pressure to voltage. Thus, hydraulic impedance can be said to be the quotient of pressure and flow rate [52]. It can be shown that the pressure and flow at any point in a pipe can be described by the wave equation, and that they can be defined as [52]:

$$P_x = Fe^{-\gamma x} + Ge^{\gamma x} \tag{5.1}$$

$$Q_x = \frac{Fe^{-\gamma x} - Ge^{\gamma x}}{Z_0} \tag{5.2}$$

This analysis is subject to several assumptions, namely:

1. The fluid is homogeneous and Newtonian
2. Heat transfer is negligible and conditions are isentropic
3. Flow is axisymmetric and laminar
4. Pressure distribution and fluid velocity are uniform across the pipe diameter
5. Changes in fluid properties due to perturbations are small
6. Propagation of waves in pipe walls is negligible
7. The speed of sound in the fluid is much greater than the mean fluid velocity

If a simple fluid network containing a pump, pipe and valve, such as that shown in figure 5.1, is considered, then it can be shown that the coefficients in equations 5.1 and 5.2 can be expressed as [52]:

$$F = \frac{Q_s Z_s Z_0}{Z_s + Z_0} \frac{1}{1 - \rho_s \rho_T e^{-2\gamma l}} \tag{5.3}$$

$$G = \frac{Q_s Z_s Z_0}{Z_s + Z_0} \frac{\rho_T e^{-2\gamma l}}{1 - \rho_s \rho_T e^{-2\gamma l}} \tag{5.4}$$

where Q_s is the source flow ripple from the pump, Z_s is the source impedance of the pump, Z_0 is the characteristic impedance of the pipe, ρ_s and ρ_T are the source reflection and termination reflection coefficients respectively, and γ is the wave propagation coefficient. They are related to the source and termination impedances by:

$$\rho_s = \frac{Z_s - Z_0}{Z_s + Z_0} \tag{5.5}$$

$$\rho_T = \frac{Z_T - Z_0}{Z_T + Z_0} \tag{5.6}$$

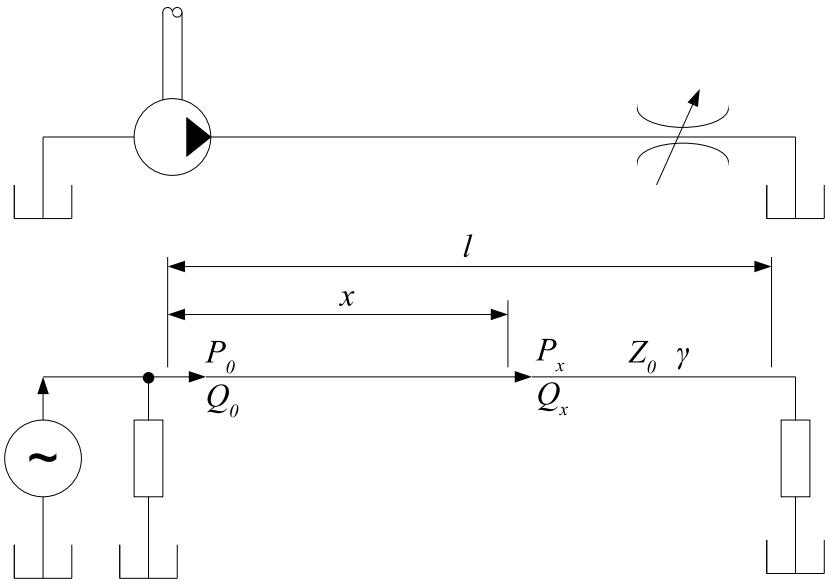

Figure 5.1: a simple hydraulic circuit

If pressure measurements are taken at two points in a system, then the coefficients F and G can be found using equation 5.1. The termination reflection coefficient, ρ_T, and hence the termination impedance, Z_T can then be calculated. However, it is not possible to directly determine the source reflection coefficient or source impedance as reflections of waves at the source will be travelling in the same direction as the original waves from the source, rendering them indistinguishable. More information is required about the circuit in order to calculate ρ_s and Z_s. This can be supplied by physically changing the length of the circuit in question. One such method for achieving this is the so-called called the hydraulic trombone method, details of which can be found

in [53] where it was used for the measurement of positive displacement pump impedance and flow ripple. However, doing so is time intensive and prone to error. Therefore, a new method, called the secondary source method, was developed at the University of Bath. The theory behind the secondary source technique can be found in detail in [43] and [52]. It is summarised in the following section.

It was proposed that, if a secondary source of fluid borne noise was introduced into the circuit, then the original pressure ripple source becomes the termination to the secondary source. Provided that the pressure waves from both the original and secondary source can be examined in isolation, then the source reflection coefficient and impedance can be calculated. If necessary, it is also then possible to calculate the flow ripple. This theory is the basis of the secondary source method. It has been used extensively to examine the impedance characteristics and flow ripples of various pumps [40, 44, 54], and the passive impedance of restrictor and flow control valves [55] and relief valves and accumulators [56]. It forms the International Standard for pump fluid borne noise testing [57].

5.1.7 Test rig alterations

A number of secondary sources were considered, based on those reported in the literature. Most commonly suggested is the use of a secondary pump, either in-line or attached to a branch line. A variable speed piston pump allows analysis at a wide range of frequencies, and produces a signal which contains stable harmonics and measurable harmonics over a broad band of frequencies [42–44, 55, 56]. Other methods include rotary valves [42, 43, 56], shaker driven pistons [42–44] and broadband noise from cavitating valves [42]. The secondary pump and rotary valve methods presented problems in terms of using water as the working fluid. Typically, such devices require a certain amount of lubrication from the working fluid which could not be provided. The shaker driven piston is difficult to set up correctly, as the piston must be pre-tensioned to maintain the correct equilibrium point, which will change as the pressure in the system changes. Such a system is also difficult to seal adequately. The motor driven ball valve could have been used to produce noise from cavitation, although this would have restricted tests to a single operating point. A positive displacement pump was available, but no suitable variable speed drive could be found. Instead, a new secondary source was proposed, based on the shaker driven piston arrangement.

A 430mm length of $2''$ (50.8mm) bore flexible hose was attached to a branch line

in the circuit, immediately downstream of the pressure measurement section, itself immediately downstream of the pump. The hose was blanked off using a plug made from aluminium, held in place using Jubilee clips. Figure 5.2 shows the arrangement. The hose could then be laterally compressed using a mechanical shaker using a single frequency sine wave input, thus supplying an oscillatory pressure and flow signal.

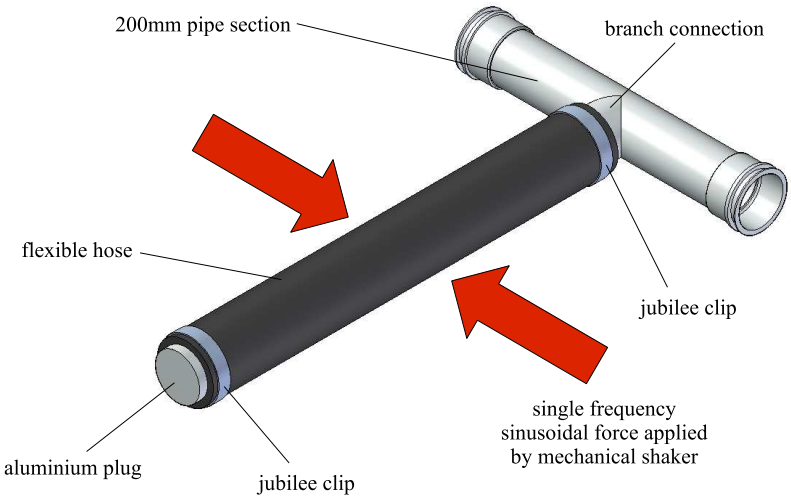

Figure 5.2: secondary fluid borne noise source

In order to apply the secondary source method to find the pump impedance, three pressure measurements were required downstream of the pump. Initially, it was thought that the existing aluminium pipes and piezo-resistive pressure transducers could be used by combining them as shown in figure 5.3. Subsequent tests revealed that this arrangement did not produce repeatable results, most likely due to the cavities in the pipe wall by the transducers as a result of the manufacturing error (see chapter 2) and the small changes in pipe section across each of the couplings. A single, straight section of Tungum tubing from previous secondary source tests at the University of Bath was used instead, as shown in figure 5.4. This section of pipe contains custom made bosses for a separate set of high bandwidth piezo-electric pressure transducers. This arrangement results in a straight, constant-bore section of pipe where the pressure transducers are flush-mounted with the inside surface of the pipe, and as such is much more suited to this analysis. In attaching this new pipe, the gate valve and associated connections were also removed, resulting in a cleaner connection between the pump and the system. The Tungum tubing set up results in a pressure transducer spacing ratio of $2:1$, whilst the aluminium pipe set up resulted in a spacing ratio of $5.3:1$.

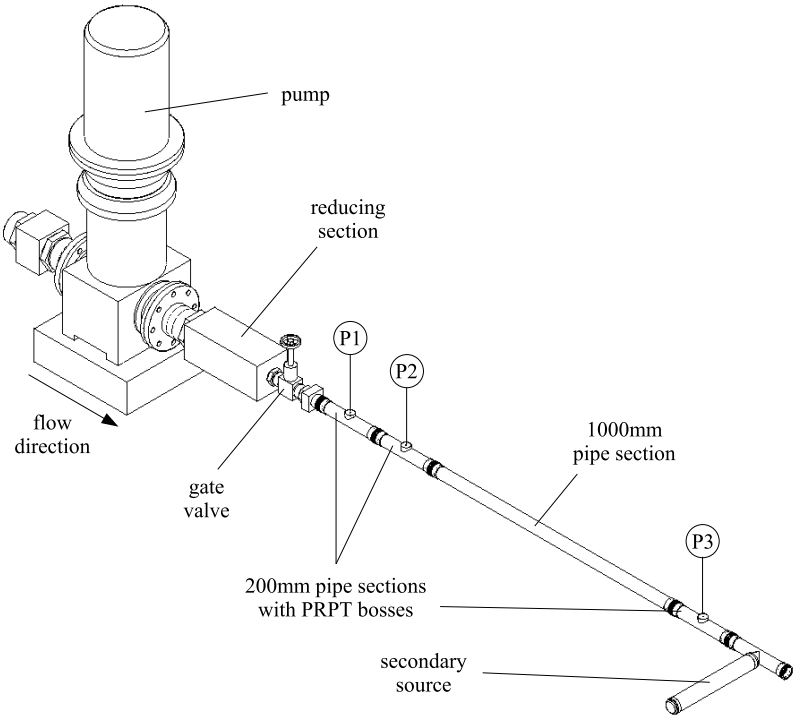

Figure 5.3: test rig set up for secondary source testing using aluminium pipe sections

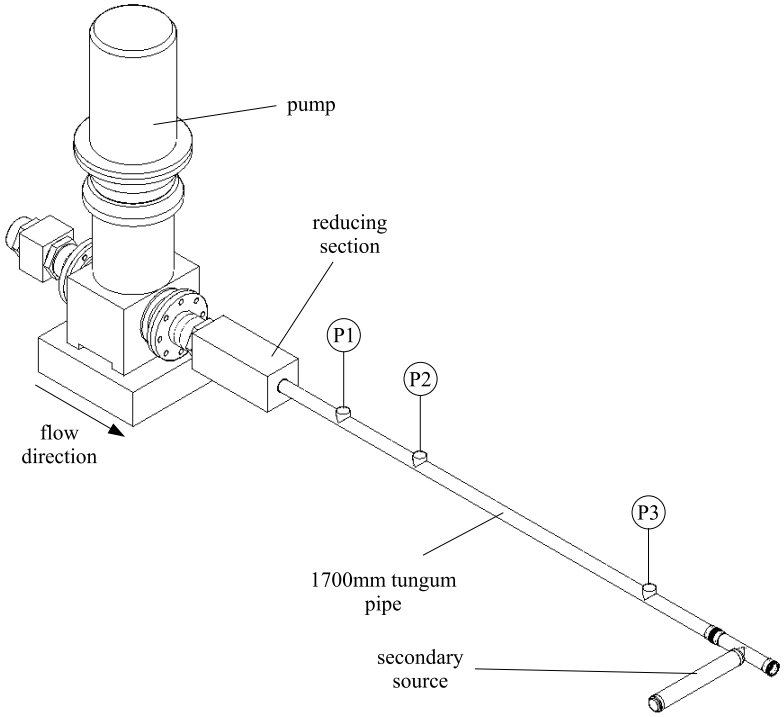

Figure 5.4: test rig set up for secondary source testing using Tungum tubing

5.1.8 Justification of the one-port model

In order to ascertain if the pump in question could be modelled accurately using a one-port model as suggested by Whitson and Benson [44], the pressures seen in the system as a result of the secondary source were measured. Figure 5.5 shows the measured pressures at four transducer points over the full test range of 50Hz to 700Hz for the stationary pump case. Three pressure transducers, marked P1, P2 and P3, were located downstream of the pump as shown in figure 5.4, and one immediately upstream of the pump, labelled P4, in the pump flange (see the test rig schematic in chapter 2). It is clear that the measured pressure level upstream of the pump is significantly lower than that downstream (around $2-5\%$ of the upstream level).

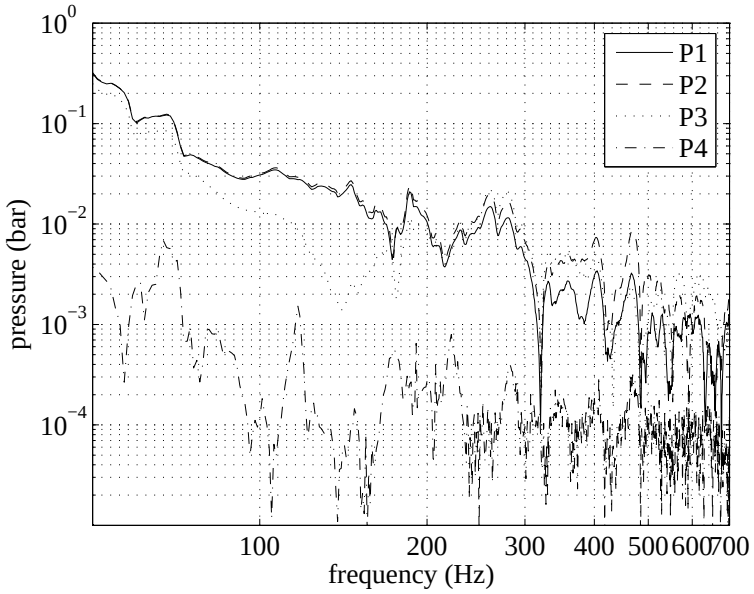

Figure 5.5: measured pressure levels for the capacitance test

5.1.9 Measuring pump impedance

The pump impedance was measured using the FBN software developed at the Centre for Power Transmission and Motion Control at the University of Bath. This software can be used to generate a single frequency sine wave as an input to the mechanical shaker, and measure the response from each of the three pressure transducers. The

data is saved in an ASCII text file in the form of amplitude and phase response for each transducer. In order to use the FBN Matlab toolbox to analyse the data and produce the required impedance, a Matlab GUI called AFBN was produced. This loads in the raw data from the test, writes an appropriate header to the output file from the user's input of fluid temperature, pressure in the flexible hose, rig and transducer set up, and writes the raw test data into columns. The order of these will depend on the user's input of transducer and rig set up. Figure 5.6 shows the AFBN interface. Once the test data is correctly formatted, then the FBN Matlab toolbox is used to calculate the pump impedance.

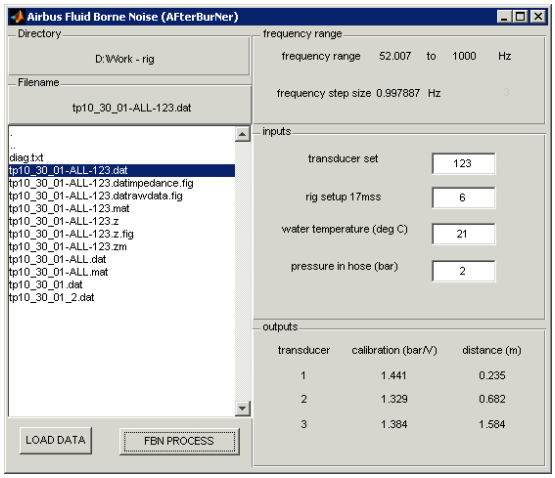

Figure 5.6: AFBN Matlab GUI

5.1.10 Validation of the secondary source

In order to check that the proposed secondary source was suitable for performing measurements of the pump impedance, the circuit was set up to measure a known impedance. The gate valve immediately downstream of the reducing section (using the initial aluminium pipe work set up) was fully closed to provide complete termination of the pipe. This should result in a capacitive impedance, which is theoretically well defined. Such a test is useful to check that the experimental set up is suitable for determining the pump impedance. Two tests were conducted. For the first test the pump was stationary and the pressure in the secondary source hose was atmospheric plus tank head. The second test was conducted with the pump running and the by-pass line open, raising the pressure in the hose to around 1bar above tank head, but with

no mean flow.

Figure 5.7 shows the measured pipe impedance for these two tests, presented as a Bode plot. The theoretical impedance for a capacitance is also shown, having been adjusted to fit the test data as best as possible. This has an amplitude of gradient -20dB/dec and a constant phase of $-90°$. The impedance of this capacitance has been calculated using the equation:

$$Z_c = \frac{B}{j\omega v_{eqiv}} \tag{5.7}$$

where B is the fluid bulk modulus and v_{eqiv} the equivalent volume of the system. The bulk modulus was calculated during the course of the FBN calculations as 18700bar. This is significantly lower than the expected value of around 20500bar for pure water at 20°C. Here, the volume, v_{equiv}, has been manually adjusted to produce the fit shown in figure 5.7. In theory, this should be considered to be the volume of fluid within the pipe work between the shut valve and a user defined datum. This datum can be chosen at any point between the valve and the secondary source. Figure 5.8 shows the datum chosen for this analysis.

The ratio between the actual and equivalent volumes is around 2.6. It is known that the compliance of the pipe walls will affect the bulk modulus, and may cause this increased equivalent volume. Edge [48] has shown that, for positive displacement pumps, such ratios can vary enormously, and that values between 1 and 4.35 are reasonable. It is also known that the presence of dissolved and entrained air within the fluid will affect the measured bulk modulus. The effect of pipe compliance and entrained air on the fluid bulk modulus, B_{fluid} can be evaluated using the effective pipe modulus, B_{pipe}, and the gas bulk modulus, B_{gas}:

$$\frac{1}{B_{eff}} = \frac{1}{B_{fluid}} + \frac{v_{gas}}{v_{fluid} + v_{gas}} \frac{1}{B_{gas}} + \frac{1}{B_{pipe}} \tag{5.8}$$

where the pipe modulus is evaluated as:

$$B_{pipe} = \frac{E}{2\left(\frac{(\epsilon^2+1)}{(\epsilon^2+1)} + \nu\right)} \tag{5.9}$$

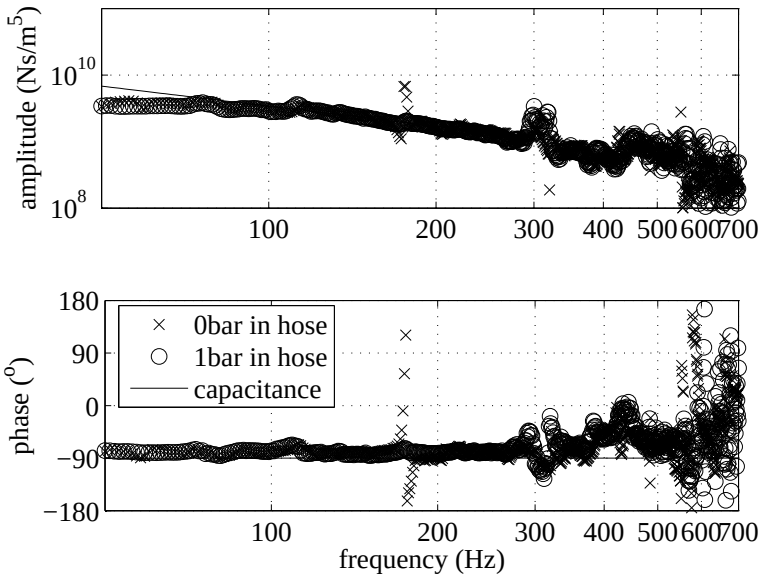

Figure 5.7: measured impedance of short pipe section and closed valve, showing fit of capacitive model

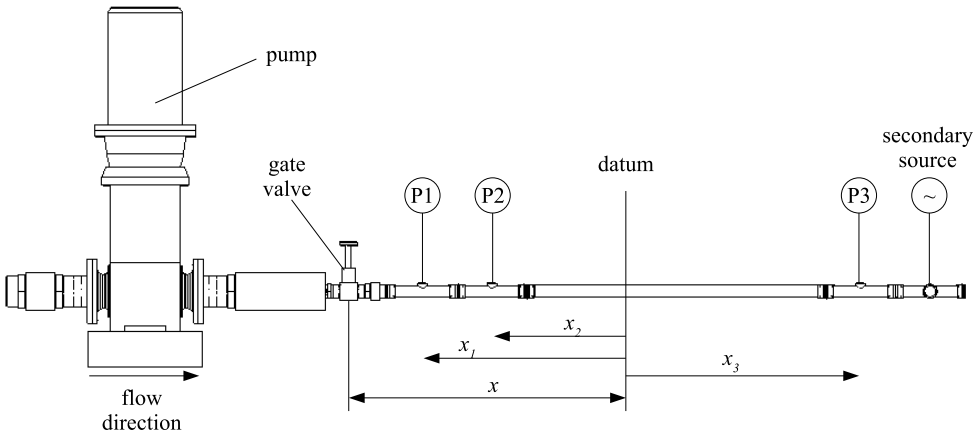

Figure 5.8: defined datum for capacitance measurement

In equation 5.9, ϵ is a function of pipe wall thickness, t, and pipe diameter, d, and is given by:

$$\epsilon = 1 + \frac{2t}{d} \tag{5.10}$$

and E and ν are the pipe material Young's modulus and Poisson's ratio respectively. It can be shown that as the thickness to diameter ratio increases, the pipe bulk modulus can be approximated by [58]:

$$B_{pipe} = \frac{tE}{d} \tag{5.11}$$

Using equation 5.8, it is possible to estimate the effect of pipe compliance only on the fluid bulk modulus by setting the volume fraction term to zero. Using standard values of water bulk modulus (22000bar [59] isentropic bulk modulus of water at 20°C) and Young's modulus for Tungum (117GPa[1]), and measurements of the Tungum pipe wall thickness and diameter, it can be shown that the effective bulk modulus reduces to 19300bar. By rearranging equation 5.8, it can be shown that, in order to reduce this to 18700bar as measured in the test rig, a gas to fluid volume ratio of less than 1% is required. Such a level of dissolved air in the fluid is quite probable, given the proximity of the measurements to the centrifugal pump. Estimating effective bulk modulus is extremely difficult [58, 60], and it is known that direct measurements are often more accurate. The method used in the secondary source measurement toolbox has been shown to be accurate in the past, and so there is a good level of confidence in this measured value.

It is clear from the figure that the technique does measure an impedance dominated by capacitance in the frequency range 100Hz to 400Hz. The measured phase shows good agreement in the lower frequency range, but the amplitude is clearly significantly less than that predicted from equation 5.7. Two cases of measurement instability are clear; at around 170Hz and 300Hz. Here, there is a sudden spike in both the amplitude and phase plots, possibly indicating a mechanical resonance. For frequencies greater than 400Hz the results are subject to considerable scatter, suggesting that the technique is unsuitable in this range. By examining the measured pressure levels downstream of the pump in figure 5.5, it can be seen that the pressure levels for frequencies greater

[1] from Bath*fp* documentation

than around 400Hz are smaller than those at low frequencies, and it is expected that the accuracy of the technique will suffer in this region. As the pressure in the hose increases with pump speed, these pressure levels fall further, due to the greater force required to compress the hose.

5.1.11 Test results

Secondary source tests were conducted on the pump at five different pump speeds. Table 5.1 details these tests in terms of pump speed, flow rate through the test section and pressure in the flexible hose.

test number	pump speed (rev/min)	flow rate (L/min)	pressure in hose (bar)
1	0	0	0
2	1810	330	1.6
3	1810	330	1.6
4	2007	370	2
5	2205	410	2.4
6	2969	562	4.3

Table 5.1: summary of secondary source tests for pump impedance

The measured pump impedance from each of the tests is shown in figure 5.9, in the same format as the data from section 5.1.10. It is clear from the results that tests 2 through 6 show very good agreement in the frequency range 100Hz to 400Hz, identified as the range of interest from the capacitive impedance tests. Once again, in the lower and higher frequency ranges, the results are subject to a significant amount of scatter. In general, the amplitude is seen to steadily rise with frequency, and the phase generally remains close to $+90^\circ$ across the full frequency range. Between 100Hz and 200Hz, the amplitude plot exhibits a peak at around 136Hz with an equivalent drop in phase. The amplitude then drops and rises again from 136Hz to 196Hz, coinciding with a sudden rise then drop in phase. The amplitude drops down from 196Hz to 180Hz, before rising again steadily over the remainder of the frequency range. The phase also returns to $+90^\circ$ thereafter. The stationary pump test (test 1) however shows some significant

differences. The amplitude plot does not peak at 136Hz as for the other tests, but instead continues to rise steadily. The amplitude does rise sharply at around 175Hz, coinciding with a sharp fall in the phase towards $-90°$. This is followed by a second, smaller amplitude peak at around 197Hz, before the amplitude returns to its steady rise as before, and the phase returns to $+90°$.

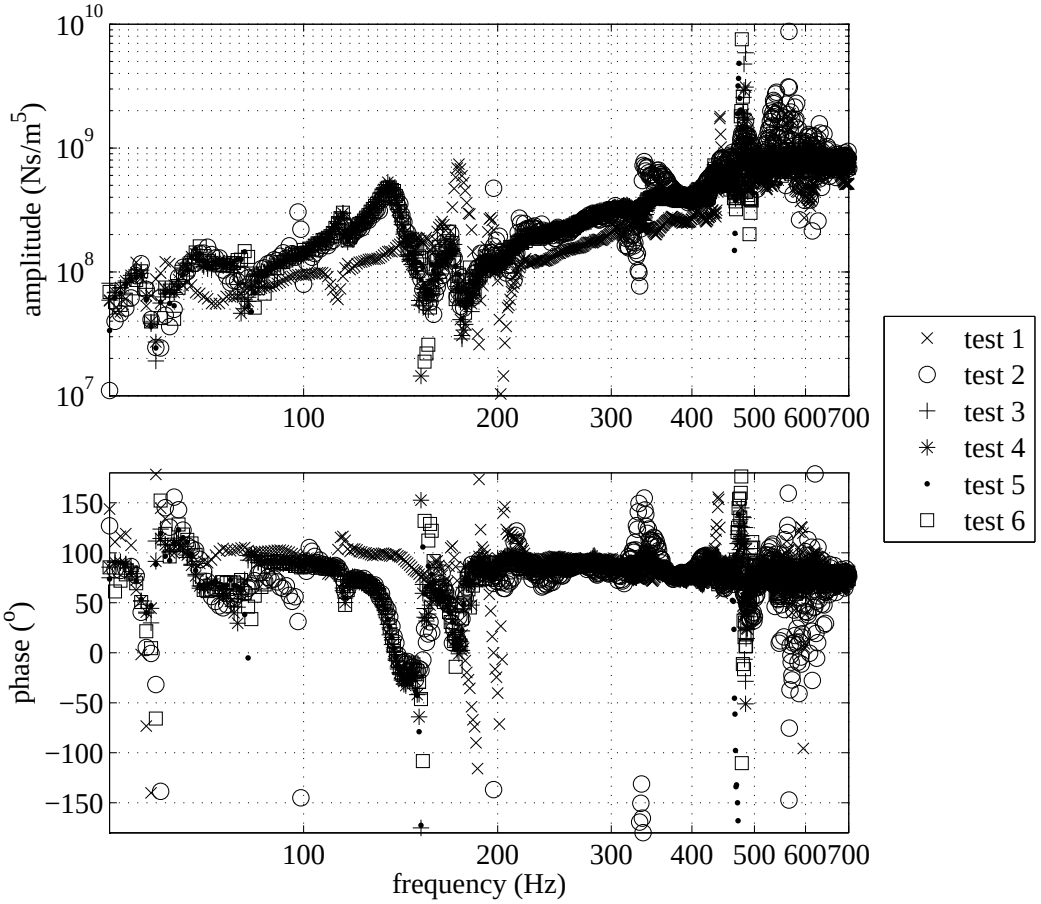

Figure 5.9: measured pump impedance

In general, the measured impedance follows the same trend as might be expected for an inertance, for which the amplitude will steadily rise at 20dB/dec and the phase will remain constant at $+90°$. The impedance of an inertance can be calculated from:

$$Z_l = j\omega L \tag{5.12}$$

where L is the inertance of units kgm^{-4}. It is often expressed in terms of an equivalent pipe of length l and cross-sectional area A:

$$L = \rho \frac{l}{A} \tag{5.13}$$

Figure 5.10 shows a best fit approximation to the test data from test 1 for a simple inertance. Figure 5.11 shows a similar fit for test 2. In each case the inertance, L has a value of 1.09×10^5 kg/m^4 and 1.35×10^5 kg/m^4, and the measured fluid bulk modulus was 19700bar and 18400bar respectively. The reason for differences between the stationary and pump-running cases are unclear, although Edge and Johnston [54] reported a similar phenomenon for positive displacement pumps. It was suggested that such differences could be due to a lower bulk modulus when the pump is running, due to a higher entrained air content as a result of cavitation and air release within the pump passageways. This was seen to raise the frequency of an observed anti-resonance, in a similar fashion to the observed increase in frequency of the first amplitude peak of the amplitude in case 1. Any change in bulk modulus would not affect the response of a purely inertive system. However, from figures 5.10 and 5.11, it is clear that this system does not behave as an inertance only, so it could reasonably be expected that the system response would change with bulk modulus as a result of entrained air.

The measured impedance includes not just the pump, but also the aluminium reducing section immediately downstream of the pump (see figure 4.31). Due to its simple internal geometry, the effect of fluid inertia in this component can be estimated using relatively simple techniques. The effective pipe length model of inertance can be generalised to consider a straight section of ducting, whose cross-sectional area is a known function in the flow direction. Consider a section of circular duct of length l, whose cross-sectional area, A, is a function of distance in the flow direction, x. The inertance can be determined as:

$$L = \rho \int_0^l \frac{1}{A} dx \tag{5.14}$$

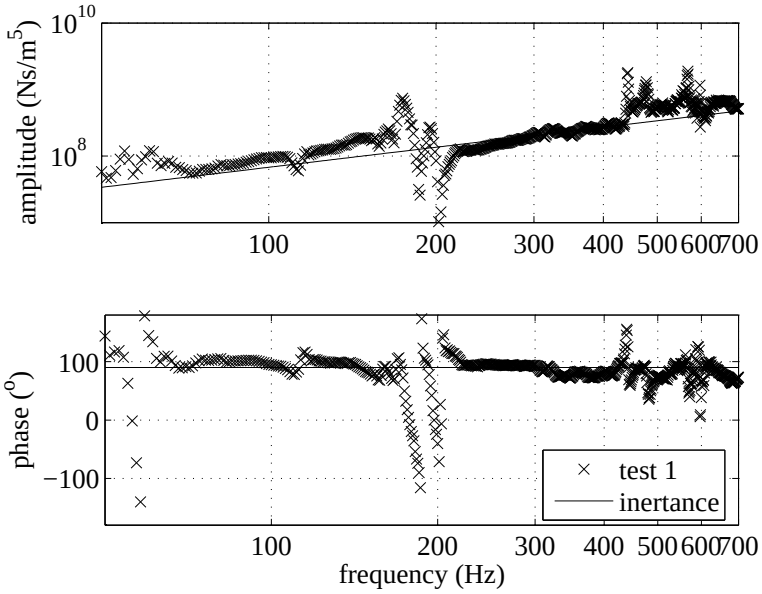

Figure 5.10: measured pump impedance and best fit inertive impedance from test 1

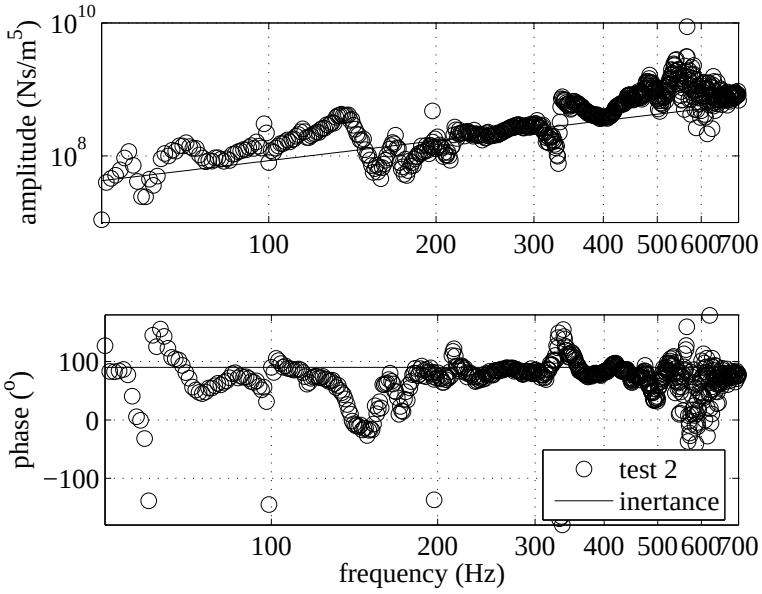

Figure 5.11: measured pump impedance and best fit inertive impedance from test 2

Using the measurements of the reducing section, the inertance was calculated as 1.09×10^5 kg/m^4 using a fluid density of 998 kg/m^3, corresponding to water at 20° C.

The fluid inertance of the reducing section has also been assessed using a Computational Fluid Dynamics (CFD) method, first proposed by Johnston [61], and used by Boyd et al. [62]. More details of this method can be found in section 5.3. The reducing section inertance was predicted by this method to be 1.11×10^5 kg/m^4. It is clear that, since the reducing section inertance is between 81% and 100% of the measured pump inertance, the behaviour of the pump is therefore dominated by the reducing section.

It has been suggested that the behaviour of the impedance in the region 100Hz to 150Hz could also be as a result of mechanical vibration within the system, or perhaps indicative of the natural frequency of the main line or hose. It should be noted that the same behaviour was noted in the test for capacitive impedance earlier (section 5.1.10), suggesting that it is independent of the pump, as the valve immediately downstream of the pump was shut in this case. The natural frequency of the hose can be estimated, and it can be shown that it is of the same order as the amplitude peak seen in figure 5.9. The natural frequency of the main pipeline is much lower, but it can also be shown that it or some of its higher harmonics is of a similar order to the amplitude peaks and phase shifts observed below 100Hz in figure 5.9. However, the capacitive test revealed that this region was perhaps outside of the useful region of the secondary source. In any case, the secondary source method has been shown in the past to be robust to not detecting any behaviour outside of the region of interest, which in this case was the pump and the short section of pipe immediately downstream, before the source branch and hose.

Analyses of centrifugal pumps in the literature have previously reported general dynamic behaviour which is dominated by fluid inertia effects [33, 34, 44]. The analysis conducted as a part of this study also suggests that the behaviour of the pump in the test rig will be dominated by inertia effects in the frequency range from 100Hz to 400Hz, although the results also revealed that a more complex model may be required to describe the impedance in the range 100Hz to 150Hz. The behaviour in this region could be described by a complex transfer function, but doing so would shed no light on how such a behaviour was generated, and it would be extremely difficult to determine a representative model which would describe the behaviour in terms of phenomena such as inertance and compressibility.

It has been shown that the secondary source technique can be effectively applied to

find the impedance characteristics of centrifugal pumps. In the case of the pump in the test rig, this impedance was shown to be dominated by fluid inertance, which concurs with general conclusions from previous studies on centrifugal pumps.

5.1.12 Comparison of pump and circuit impedance

The effect of fluid inertia within a typical system, such as the test rig, can be estimated using the simple equivalent pipe method given in equation 5.13. The test rig pipe work consists of around 17m of 34.3mm bore pipe. Using equation 5.13, this yields an inertance value of $L = 1.84 \times 10^7$ kg/m^4, which is 136 times greater than the largest predicted value of the pump, using the test data for the pump running at four different speeds. It is clear that the dynamic response of any such system will be dominated by the dynamics of the pipe work, and that using a steady-state pump model should be sufficient.

5.1.13 Implementation of method in Bath*fp* simulation environment

The steady-state centrifugal pump model described in chapter 4 has been extended to include an inertance term. The steady-state characteristic can be considered analogous to a resistance using the electrical circuit analogy proposed in section 5.1.6. Using this same analogy, the inertance is equivalent to an inductance, and both of these can be said to act in series, such that the pressure rise across the pump can be expressed as:

$$\Delta p = f(q) + L\frac{dq}{dt} \tag{5.15}$$

where $f(q)$ is the steady-state characteristic as a function of flow rate from chapter 4, and L is the inertance of the pump. The pump model requires an input of pressure at both inlet and outlet ports, returning the flow rate to connected models. The load torque of the pump is calculated as before, and the speed is required. Figure 5.12 shows a schematic of the pump model, detailing each of the input and output parameters at each of the three ports. The model also outputs four internal variables, detailed in table 5.2, and requires inputs of the real essential parameters detailed in table 5.3.

The calculation procedure is very similar to the steady-state pump model, described in

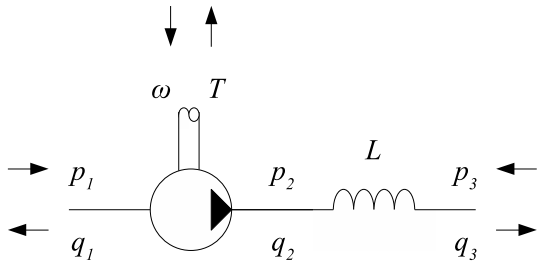

Figure 5.12: schematic of the dynamic Bath*fp* centrifugal pump model

parameter	description
ϕ	non-dimensional flow rate
ψ	non-dimensional pressure rise
τ	non-dimensional torque
η	hydraulic efficiency

Table 5.2: internal variables of dynamic Bath*fp* centrifugal pump model

chapter 4, save for the calculation of outlet flow rate. The hydraulic orifice is replaced by the calculation of rate of change of flow rate at the outlet port, based on the pressure difference across the inertance, and the value of L:

$$\frac{dq_3}{dt} = \frac{(p_3 - p_2)}{L} \tag{5.16}$$

Finally, the inlet flow rate and intermediate flow rate, q_1 and q_2 respectively, are set equal to the outlet flow rate, q_3.

parameter	units	description
α_1		
α_2		
α_3		coefficients of pressure-flow fit
α_4		
α_5		
α_6		
γ_1		coefficients of torque-hydraulic power fit
γ_2		
r	mm	impeller radius at outlet
v	m^3	equivalent pump displacement
ϕ_0		transition point from 5^{th} to 2^{nd} order fit
L/ρ	1/m	fluid independent pump inertance

Table 5.3: real essential parameters of steady-state Bath*fp* centrifugal pump model

5.2 Electric drives

There exist in publications a wide range of methods for analysing the dynamic performance of AC induction drives during start up and shutdown periods, as well as during changes in load or demand speed for variable speed drives. The most common of these are based on generalised machine theory, and a transformation of axes from the rotational to a stationary reference frame using either generalised transformations, or more specific transformations such as those developed by Park, Stanley, Kron and Brereton, referenced in Krause [35]. Such methods have successfully been employed to model existing drives, and have been validated against experimental data. Krause [35] and Yu, Baines and Chalmers [63] are two such examples, the latter of which has been shown to work for a PWM inverter-fed permanent magnet motor.

Other modelling methods have been proposed, based on transfer function analysis and reduced order approximations to the standard generalised machine theory. Salama and Holmes [64] have presented a paper which discusses the use of a transfer function model, which is based on a linearised mathematical model. This is derived by determining the changes in all input and output variables as a consequence of small changes about a steady-state operating point, and subsequent elimination of steady-state terms.

The resultant linear equation relates the rates of change of currents and speed to the small changes in current, speed, voltage and torque. The resultant responses to step inputs are described, although they are not compared to experimental data. The paper concludes that the method is suitable for understanding the system response to step changes in input voltage, torque and speed.

Richards [65] presents an alternative method to the common generalised machine theory, which relies on separating forced and transient components of flux linkage, torque and current responses. The equations for flux linkage are derived in the usual arbitrary rotating reference frame using the transformation of axes, resulting in fifth order simultaneous equations for flux linkage and speed. By separating the forced and transient components, these are reduced to a single order model, which are then shown to accurately describe the performance of the motor during start up and shutdown periods.

A detailed dynamic electric drive model has been developed, using the voltages and currents in the rotor and stator of an AC induction motor based on generalised machine theory, in a similar way to [35]. Like the Thévenin circuit model described in chapter 4, this requires detailed knowledge of internal motor parameters such as resistances and reactances. Such a model is suitable for analysis of the AC induction motor in the test rig.

5.2.1 Generalised machine theory and the dq0 transformation

Krause [35] gives a detailed description of, among other things, generalised machine theory, upon which the work in Monaghan [66] is based. The model describes an AC induction motor as a set of coupled differential equations for the voltages and currents in the rotor and the stator. This requires a transformation of variables from the physical axes of the phases to a rotating reference frame, removing the time dependence of the inductances.

Figure 5.13 shows the rotor and stator axes for a three phase machine, labelled A_s, B_s, C_s, A_r, B_r and C_r, with reference to a fixed orthogonal frame, denoted α and β. The stator axes are, by definition, fixed in space, with A_s, B_s and C_s separated by 120°. The rotor axes, A_r, B_r and C_r, are rotating with respect to the stator, and the angle between each stator and rotor phase axis is θ_r. An arbitrary rotating frame of reference can be defined, shown here as the d and q axes, angularly displaced from the α axis by

θ, rotating with speed ω.

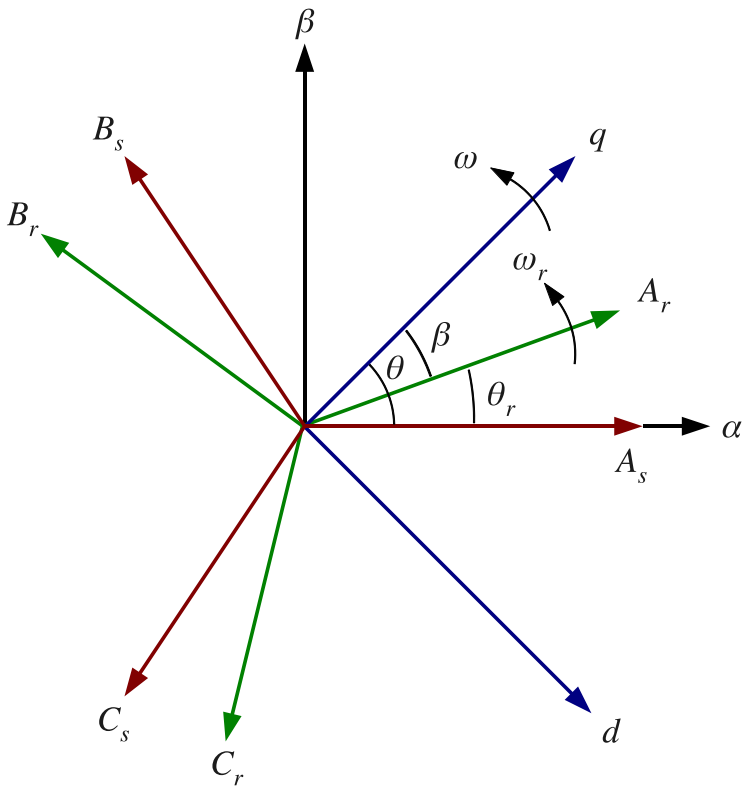

Figure 5.13: definition of ABC and $dq0$ reference frames

The derivation of the equations in the arbitrary reference frame is not covered in detail here. This model has been developed as a part of the Electric Drives project, and full details of its derivation can be found in the thesis [12]. The model has been applied in Bath*fp* using the following method.

It can be shown that the voltages in the rotor and stator in each of the three phases, a, b and c, can be expressed in vector form as:

$$\mathbf{v_{abc,s}} = \mathbf{R_s i_{abc,s}} + \dot{\gamma}_{\mathbf{abc,s}} \tag{5.17}$$

$$\mathbf{v_{abc,r}} = \mathbf{R_r i_{abc,r}} + \dot{\gamma}_{\mathbf{abc,r}} \tag{5.18}$$

Following the transformation into the $dq0$ axes, these can be expressed as four simultaneous equations:

$$v_{d,s} = R_s i_{d,s} + \dot{\gamma}_{d,s} - \omega\gamma_{q,s} \tag{5.19}$$

$$v_{q,s} = R_s i_{q,s} + \dot{\gamma}_{q,s} + \omega\gamma_{d,s} \tag{5.20}$$

$$v_{d,r} = R_r i_{d,r} + \dot{\gamma}_{d,r} - (\omega - \omega_m)\,\gamma_{q,r} \tag{5.21}$$

$$v_{q,r} = R_r i_{q,r} + \dot{\gamma}_{q,r} + (\omega - \omega_m)\,\gamma_{d,r} \tag{5.22}$$

These are re-arranged to solve for the rate of change of flux, $\dot{\gamma}$. In order to solve, the currents are required. These can be found from the current-flux relationship, using the intermediate variables, G, expressed in vector form as:

$$\mathbf{i_s} = \mathbf{G_s}\gamma_\mathbf{s} - \mathbf{G_m}\gamma_\mathbf{r} \tag{5.23}$$

$$\mathbf{i_r} = \mathbf{G_r}\gamma_\mathbf{r} - \mathbf{G_m}\gamma_\mathbf{s} \tag{5.24}$$

where:

$$G_s = \omega\frac{X_r + X_m}{X_s X_r + X_s X_m + X_r X_m} \tag{5.25}$$

$$G_m = \omega\frac{X_m}{X_s X_r + X_s X_m + X_r X_m} \tag{5.26}$$

$$G_r = \omega \frac{X_s + X_m}{X_s X_r + X_s X_m + X_r X_m} \tag{5.27}$$

For a motor with n phases and p poles, the motor torque is then calculated from the currents in each of the stator and rotor d and q axes:

$$T = \frac{np}{4} \frac{X_m}{\omega} \left(i_{d,r} + i_{d,s} + i_{q,r} + i_{q,s} \right) \tag{5.28}$$

5.2.2 Implementation of modelling methods in Bath*fp*

The dynamic induction motor model is very similar to the steady-state model described in section 4.2.2. It requires an input of the supply voltage, frequency and load torque. The shaft speed is returned to the shaft output and to a separate signal output port for feedback control, along with six internal variables. These are summarised in table 5.4. The user must supply the model with six user input constant parameters. These are summarised in table 5.5. The model input and output ports are the same as for the steady-state Thévenin circuit model, described in figure 4.19.

parameter	units	description
$\gamma_{d,s}$	Wb	stator flux in d axis
$\gamma_{d,r}$	Wb	rotor flux in d axis
$\gamma_{q,s}$	Wb	stator flux in q axis
$\gamma_{q,r}$	Wb	rotor flux in q axis
P	kW	power
T	Nm	electric torque

Table 5.4: internal variables of dynamic Bath*fp* induction motor model

The model begins by setting the synchronous speed from the frequency input signal. The stator and rotor voltages in the d and q axes are set from the input voltage, v,

parameter	units	description
X_m	Ω	magnetising reactance
X_s	Ω	stator reactance
R_s	Ω	stator resistance
R_r	Ω	rotor resistance
X_r	Ω	rotor reactance
J	kgm^3	motor and load inertia

Table 5.5: user input constant parameters of dynamic Bath*fp* induction motor model

accordingly:

$$v_{d,s} = \sqrt{2}v \tag{5.29}$$

$$v_{q,s} = 0 \tag{5.30}$$

$$v_{d,r} = 0 \tag{5.31}$$

$$v_{q,r} = 0 \tag{5.32}$$

The intermediate variables, G_s, G_m and G_r are calculated according to equations 5.25 through 5.27, and the stator and rotor currents in the d and q axes according to equations 5.23 and 5.24. Then the rates of change of fluxes in the stator and rotor d and q axes are calculated by rearranging equations 5.19 through 5.22. Finally, the torque is calculated from equation 5.28, which is passed, with the input load torque, to the same stiction subroutine as the steady-state model (see chapter 4). This returns the shaft speed.

Like the Thévenin circuit model in chapter 4, the $dq0$ model is designed to be used in

conjunction with a frequency inverter model, which provides a frequency and voltage signal to the motor. This frequency inverter model applies V/f control, as described in chapter 4.

5.2.3 Application to test rig AC induction motor

The $dq0$ induction motor model requires the same inputs as the steady-state Thévenin circuit model (see section 4.2.2). Using the parameters obtained from the manufacturer (see table 4.9), the motor model has been run for a no-load acceleration case. In order to compare the model's steady-state performance, the load torque has then been increased in steps over time. The $dq0$ model has been compared to the Thévenin circuit model. Figure 5.14 shows the torque-speed curve for both models for the no load acceleration to the synchronous speed (3000rev/min). Figure 5.15 shows a comparison of the linear torque-speed region for step increases in load torque with time.

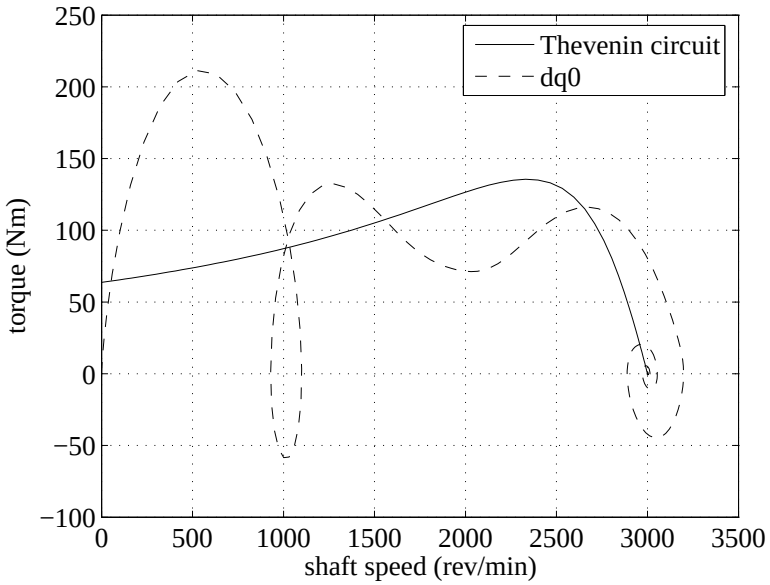

Figure 5.14: comparison of motor models' no-load acceleration

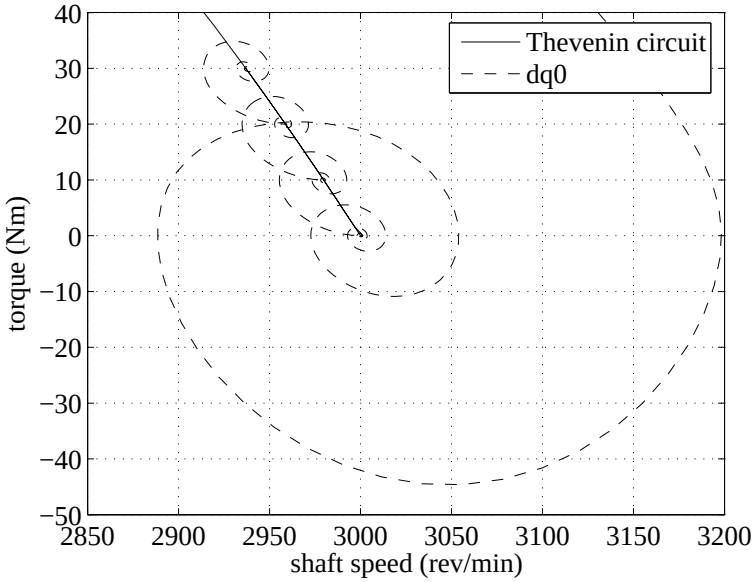

Figure 5.15: comparison of motor models' linear torque-speed region under step changes to load torque

5.3 Fluid inertance

The inertia of fluid within the passageways of hydraulic components and systems is known to have a significant effect on their dynamic response and fluid-borne noise producing characteristics. Fluid inertance will dictate the changes in pressure as a result of changes in the rate of change of flow rate, and as such can be considered analogous to inductance in electrical circuits, where the pressure is equivalent to voltage and flow rate to AC current.

To date, much work has been concerned with estimating a component's inertance as a part of its impedance when looking at fluid-borne noise or system pressure ripple. Many components, such as valves, accumulators and pumps tend to exhibit impedances which are highly dependent on inertance.

Edge and Johnston used the secondary source technique to analyse the impedance characteristics of relief valves and accumulators [56], as well as restrictor and flow control valves [55]. These studies showed that the component's impedance played

an important role in determining the level of pressure and flow ripple within hydraulic circuits. Their investigations suggested that for relief and restrictor valves the dynamic response is dominated by resistive effects at low frequencies, and inertance effects at higher frequencies. Tests on the accumulator showed the capacitance to be dominant at low frequencies, but with inertance effects being important at higher frequencies. A two-stage relief valve and the flow control valve both displayed more complex behaviour. The effects of wave propagation within the internal passageways were shown to have a significant effect on the response of the flow control valve.

Edge [48] showed that, while it is possible to model a positive displacement pump as a simple series of lumped parameters, its actual impedance cannot be accurately determined from known geometries, but must be determined using dynamic measurements. Johnston and Drew [40] presented a new method for smoothing experimental data from the secondary source method and a mathematical model of the pump discharge passageway. For simpler responses, it was shown that a simple Helmholtz damper model was accurate, but in some cases it was best to use the impedance smoothing technique.

It is often hard to quantify the effect of fluid inertance experimentally or theoretically, save for simple geometries such as straight pipes. Johnston [61] proposed a numerical method for predicting the inertance of fluid within complex passageways using commercial Computational Fluid Dynamics (CFD) packages. The approach was to find the steady-state pressure drop through the component filled with a highly resistive porous medium. The results were scaled and used to find the inertance of the passageway if it were clear of the porous medium.

By using the electrical circuit analogy, it is possible to model a simple system as a series of inertances and capacitances, representing areas of high inertia and high compressibility respectively. If a component is considered to act purely as an inertance, then it can be connected to a component of significantly greater volume with negligible inertance, such that the system inertance will be dominated by the component in question. The larger volume will act purely as a capacitance. From this electrical model, it is then possible to determine the system natural frequency. It is proposed that this natural frequency can be measured using acoustic measurements, and, if the capacitance is known, then the test component's inertance can be inferred.

This section presents this theory, and shows the results of tests using a number of ball valves. The results are compared against those from CFD using the method given in [61].

5.3.1 The acoustic method

Using the analogy between fluid flow and electrical circuits, any fluid system can be modelled as a series of lumped parameter elements. For example, a component consisting of an inlet and outlet port of high inertance and a central large volume could be modelled as a simple T network of a capacitance in series with two inertances, as shown in figure 5.16. Here, resistance, or steady-state pressure loss, is neglected.

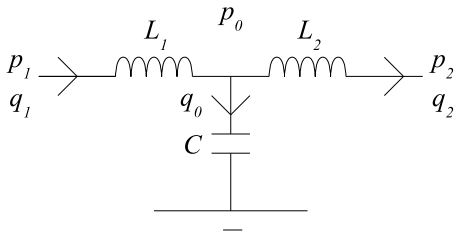

Figure 5.16: T network

In such a situation, the relationships between inlet and outlet flows can be expressed in the form of an impedance matrix [67]:

$$\begin{bmatrix} p_2 \\ q_2 \end{bmatrix} = \begin{bmatrix} 1-\omega^2 L_2 C & -j\omega L_1 - j\omega L_2\left(1-\omega^2 L_1 C\right) \\ -j\omega C & 1-\omega^2 L_1 C \end{bmatrix} \begin{bmatrix} p_1 \\ q_1 \end{bmatrix} \tag{5.33}$$

If port 2 is open to the atmosphere, then $p_2 = 0$. Assuming a stiff flow source (one of high impedance), q_1, then the chamber pressure p_0 is given by:

$$p_0 = \frac{q_1}{j\omega C + \frac{1}{j\omega L_2}} \tag{5.34}$$

This will exhibit a natural frequency when $p_0/q_1 = \infty$, or:

$$\omega_n = \sqrt{\frac{1}{L_2 C}} \tag{5.35}$$

However, if a low impedance pressure source, p_1, is used, then the chamber pressure is given by:

$$p_0 = \frac{p_1 L_2}{L_1 + L_2 - C L_1 L_2} \tag{5.36}$$

Provided that the source impedance $Z_s \ll j\omega L_1$, then the natural frequency will occur when $p_0/p_1 = \infty$, such that:

$$\omega_n = \sqrt{\frac{1}{L_p C}} \qquad \text{where} \qquad L_p = \frac{L_1 L_2}{L_1 + L_2} \tag{5.37}$$

The natural frequency is therefore governed by the inertances L_1 and L_2 acting in parallel.

Based on this, a test method is proposed to determine the inertance of a component, L_2. One port of the component is connected to a chamber of capacitance C, and the other port is left open to atmosphere. The chamber and component are left empty, such that the working fluid is air. A loudspeaker is used to excite the system via a small diameter pipe attached to the side of the chamber. The loudspeaker can be considered a low impedance source, such that $Z_s \ll j\omega L_1$. A microphone is located inside the chamber to measure the acoustic response of the system to the loudspeaker's input. If the natural frequency of the system can be determined, then the inertance of the component, L_2, can be inferred, given that inertance of the pipe, L_1, and chamber capacitance, C, are known. The inertance of a straight pipe of length l and constant cross-sectional area A can be found by:

$$L = \rho \frac{l}{A} \tag{5.38}$$

and the capacitance of a tank of volume V_t can be found from:

$$C = \frac{V_t}{B} \tag{5.39}$$

The idealised model can be extended to match the real experiment more closely. End

effects for the pipes must be considered. Blackstock [67] has shown that the length of the pipe must be extended due to wave expansion at any point where the pipe expands into a volume. This means the effective inertance for a pipe is found by applying an end correction for each end, e_1 and e_2:

$$L = \rho \left(\frac{(l + (e_1 + e_2)\, d)}{A} \right) \tag{5.40}$$

where the correction factor $e = 0.31$ for expansion from a free tube (i.e. into the atmosphere), or $e = 0.43$ for expansion from a flanged end (i.e. expansion into the tank) [67]. These values have been investigated using the CFD method reported by Johnston [61] and Boyd et al. [62], and have been found to agree reasonably well. For flanged ends, CFD suggests a difference of 11.7% from above, and 2.2% for unflanged ends.

The volume of the pipe and component also needs to be included. This may be done by adding a third of the capacity of the pipes to the capacity of the tank in equation 5.39, as is common when considering a lumped parameter mass-spring system [68].

Experimental setup

Two components have been tested using the acoustic method: a hand-operated 1.25″ BSP (31.75mm nominal outer pipe diameter) ball valve and a motor driven 1.41″ (35.8mm) nominal bore diameter aerospace ball valve. The components were connected to a cylindrical copper tank of volume 1.443L. This was connected to a 75W cabinet speaker via a 200mm long section of 14.5mm inner diameter steel pipe. The speaker front was covered over with a panel of wood to direct the speaker output into the system, and the pipe connected directly into the panel immediately opposite the centre of the speaker cone. Figure 5.17 shows the experimental setup. The acoustic measurement was taken using a flat frequency response condenser microphone, connected to a port on the side of the tank to ensure measurement of the system response only.

Analysis of the system's response was conducted using two methods: a Solartron Schlumberger 1250 Frequency Response Analyser (FRA), and a HP 3582A Spectrum Analyser (SA).

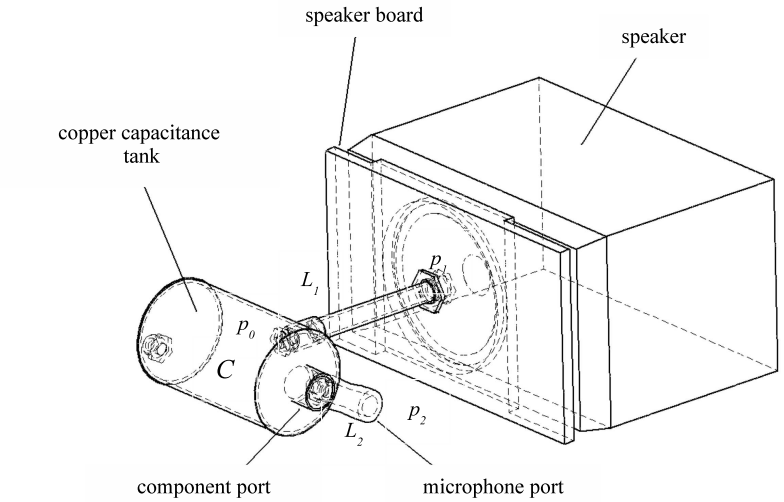

Figure 5.17: experimental setup [62]

The FRA was set up to measure the amplitude and phase of the input signal and the measured response over a range of discrete frequencies. The results were integrated over a 1s period for each frequency. Initial tests were conducted over a broad range of frequencies (typically $50 - 130$Hz) using large frequency steps of 2.5Hz, then, once a resonant peak was identified, this was improved by measuring over a narrower frequency band (typically 5Hz) using 0.25Hz steps.

The SA was set up to provide a broadband random noise source. The transfer function between this and the measured response was then plotted on the screen. Measurements were root-mean-square averaged over 32 cycles. Again, a broad band of frequencies was analysed first (typically 50Hz) to identify the resonant peak to within 0.4Hz. This could then be improved to an accuracy of 0.04Hz.

For both valves, the change in inertance during valve closure was of interest. Therefore, each component was analysed at a range of different closure positions. The hand-operated ball valve angle was measured from a protractor attached to its handle, whereas the aerospace valve closure was determined from a potentiometer connected to its driving motor.

5.3.2 The computational fluid dynamics method

It was proposed by Johnston [61] that if fluid compressibility is ignored, the pressure drop across a component is represented by the addition of a resistive term and an inertial term:

$$\Delta p = f(q) + L\frac{dq}{dt} \tag{5.41}$$

It has been shown that, for simple geometries, the inertance can be determined by solving Laplace's equation. A method was developed to indirectly solve Laplace's equation for a given geometry using a commercial CFD simulation package. This gives the advantage that complex geometries can be considered. In order to solve Laplace's equation, the fluid passageway of the component in question is modelled as a porous medium. Johnston [61] and Boyd et al. [62] detail the theory behind this method.

By examination of the Navier Stokes equations, it is possible to show that, when the source term is sufficiently large and the flow is assumed to pass through a porous medium, the velocity vector can be expressed as:

$$u_k = -\frac{1}{R}\frac{\partial p}{\partial x_k} \tag{5.42}$$

For an isotropic porous medium of sufficiently high resistivity such that inertia effects can be neglected, substituting equation 5.42 into the continuity equation for incompressible flow results in a form of Laplace's equation:

$$\sum_{k=1}^{3}\frac{\partial u_k}{\partial x_k} = 0 \rightarrow \sum_{k=1}^{3}\frac{\partial^2 p}{\partial x_k^2} = 0 \tag{5.43}$$

It can then be shown that the inertance of the component can be given by examining the pressure drop, such that:

$$L = \frac{p_{in} - p_{out}}{q}\frac{\rho}{R} \tag{5.44}$$

where R is the resistivity. Figure 5.18 shows the CFD model used for the ball valve analysis, described in section 5.3.4.

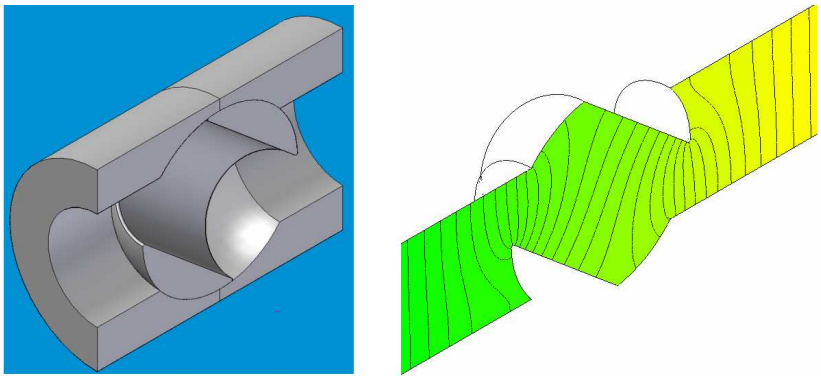

Figure 5.18: ball valve CFD model - solid domain (left) and fluid domain (right)

5.3.3 Validation of methods against theory

Both the acoustic and CFD methods have been compared against the known theoretical result for a straight section of pipe. A 200mm long section of 34mm inner diameter aluminium aircraft fuel pipe was connected to the acoustic test equipment. Using equation 5.38, this pipe should have an inertance of 269.8 kgm^{-4}. From CFD, this was found to be 260.6 kgm^{-4} – an error of 3.4%. This was thought to be a good comparison, and as such a good benchmark for comparing with the inertance from the acoustic test.

Using the theoretical value of inertance for the pipe, the predicted natural frequency of the system at an air temperature of 20°C was 90.7Hz. When the aluminium pipe was connected to the test equipment, the system resonant frequency was found to be 91.4Hz using the FRA – an error of only 0.8%. This suggests that the results of the CFD simulations and the acoustic tests can be compared against one and other, and, if they agree, there can be a good degree of confidence in their accuracy.

5.3.4 Comparison of acoustic and CFD results

The variation of inertances of the valves have been found using both the CFD and the acoustic testing methods outlined above. The CFD calculations, experimental work and

analysis were conducted by Collett, under supervision of Boyd and the other authors of [62]. Details of the CFD simulations and experimental work can be found in [69]. These comparisons are presented below.

Figure 5.19 shows the variation of valve inertance with valve angle from both the CFD simulations and the acoustic tests. Here it is clear that there is a small discrepancy between the two methods at the valve open case (14.7%). The theoretical inertance of the ball valve can be found using equation 5.38.

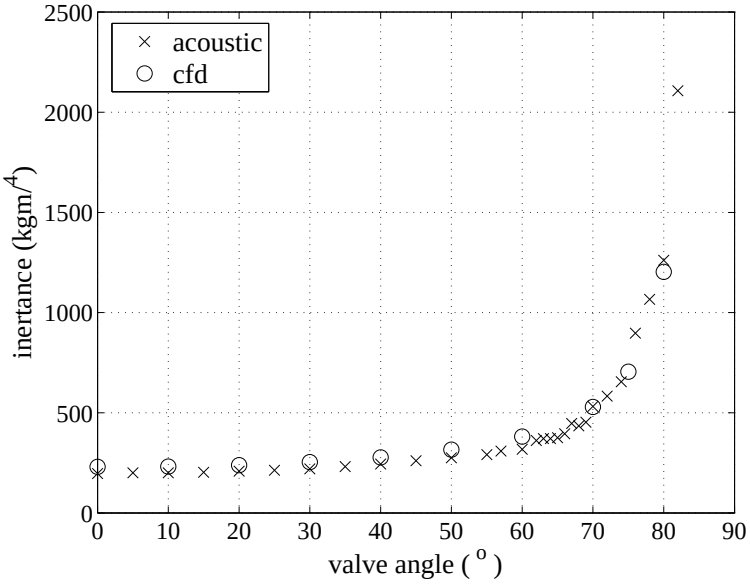

Figure 5.19: comparison of inertance from CFD and acoustic test for 1.25″ BSP ball valve

The valve inertance from equation 5.38 when open agrees well with the CFD result (0.3% error), suggesting that there must be some source of error in the acoustic test for this valve.

The pipe upstream of the 1.25″ BSP ball valve was less than two ball inner diameters in length. It was suggested from the CFD simulations that this may have an effect on the inertance values. The flow upstream of the ball orifice may not have been uniform, or may have been influenced by the orifice. In order to evaluate the inertance of the component, the inlet and outlet flows should be independent of the distance up or downstream from the centre-line of the ball. This may not have been the case here, as

the pipe was not long enough. It would be useful to analyse the effects of the inlet pipe length using the acoustic method, and compare these new results against the CFD.

At higher valve angles, the two results begin to agree better, although they diverge again at angles approaching closed (80°). This is most likely due again to a significant reduction in the through flow passage area leading to a poor cell density in the CFD analysis, and due to the speaker's own resonant frequency.

In general, both methods suggest the same trend in the results, although not in terms of their absolute numerical values.

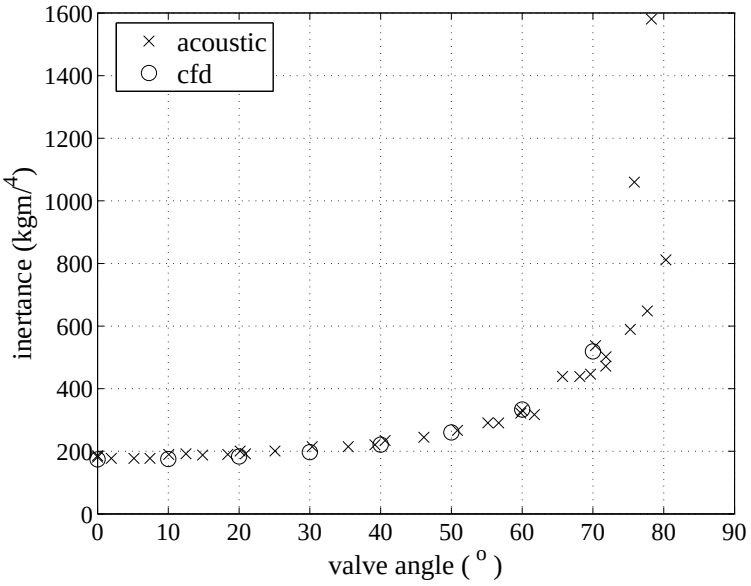

Figure 5.20: comparison of inertance from CFD and acoustic test for 1.41″ aerospace ball valve

Like the 1.25″ BSP ball valve, the aerospace valve can be thought of as a straight pipe when fully open, and as such the results from CFD and the acoustic test can be compared against the theory. It can be seen from figure 5.20 that the CFD and acoustic results are in close agreement with each other, and the acoustic inertance compares very well against that expected from theory. The error between the acoustic and the CFD inertances is 7.3%, and the error between the theoretical inertance and that from the acoustic test is 1.4%.

As before, the acoustic and CFD results diverge as the valve reaches fully shut at around 80°, although up to 70° they agree very favourably. At high valve angles the same problems are thought to be at fault for the error – small through flow passage size and the speaker response.

5.4 Closure

Methods of simulating the dynamic behaviour of centrifugal pumps have been investigated. From the four methods identified during the literature search, the secondary source measurement method has been used to determine the impedance of the pump in the test rig. This has then been used to augment the steady-state pump model using a simplified fit to the measured impedance data.

The test rig was altered in order to perform the secondary source tests. A new means of providing a secondary flow ripple was developed, using a short length of flexible hose on a branch line, which could be laterally squeezed by a mechanical vibrator. The aluminium pipes and piezo-resistive pressure transducers were used at first to predict the capacitance of a section of pipe, in order to validate the secondary source. These results suggested that the test rig was suitable for measuring the impedance in the frequency range of 100Hz to 400Hz. In this range, the method was shown to predict the correct impedance. For impedance tests on the pump, the aluminium pipes were replaced with a length of Tungum tubing to remove the small changes in section from the aluminium pipe couplings and cavities from the pressure transducer bosses.

Using this technique, the impedance of the pump was measured for a range of different pump speeds. The results showed very good agreement over the full range of measured frequencies, although the stationary pump case exhibited some small differences. In general, the response of the pump was similar to a simple inertance, although a more complex model would be needed to fully describe the dynamic behaviour. It has been shown that previous work on centrifugal pumps in published literature suggests that fluid inertia is prominent.

As a general pump model is of more interest than specific measurement of the pump in the test rig, a Bath*fp* centrifugal pump model has been developed using the assumption that such pumps dynamic behaviour can be represented by an inertance. This model builds on the non-dimensional steady-state characteristic reported in chapter 4. The

inertia term is included in series with the resistive steady-state pressure rise, and is used to calculate the rate of change of flow rate at pump outlet based on the pressure difference.

Two dynamic motor modelling methods have been investigated. A generalised machine theory model has been developed to analyse the dynamic behaviour of AC induction machines, like that in the test rig and used in current generation aircraft fuel systems. This model uses an equivalent circuit model, which is transposed into a rotating reference frame using a $dq0$ transformation. It requires the same inputs of motor parameters as the steady-state Thévenin circuit model. A dynamic DC electric motor model has been developed in order to look at the behaviour of future generation aircraft fuel systems. This is based on the steady-state electric motor model, but also includes a dynamic term to consider the relationship between rate of change of current and voltage.

A new method for measuring the inertance of a hydraulic component using acoustic measurements has been presented. By comparing the results of this method with CFD analyses using a porous medium analogy, the acoustic method has been shown to be appropriate for two ball valves.

It is clear that the results of the two methods compare well in general, especially when considering the trend of the inertances through the whole range of valve positions from open to shut. The acoustic method has been shown to agree well with the simple test case using a straight section of aluminium aircraft fuel pipe. In the case of the hand-operated ball valve, the agreement when the valve is open is not so close, although it has also been shown that for the motor-driven aerospace ball valve that the two methods agree very closely.

It has been shown that the boundary conditions set in the CFD modelling have a significant effect on the resultant inertances [62]. In the case of the ball valve, the entrance length of pipe upstream of the ball was probably not long enough in the acoustic test to remove the effect of the entrance to the pipe. In future work, this could be checked by increasing the pipe length in both the acoustic test and the CFD and then comparing the results.

The acoustic method provides a simple and quick method for determining the effect of fluid inertia on the dynamic response of a hydraulic component. It is much easier to set up than the secondary source technique, and allows for an explicit measure of

inertance only. It is also much quicker than the CFD simulation, although this is still very useful in checking the influence of aspects such as end effects and entry conditions on the inertances found using the acoustic method. The CFD simulations of the valves took up to twelve hours to complete on a modestly equipped office PC, whereas the response of the component over its full range of opening could be assessed in a matter of a few hours using the acoustic method.

Chapter 6

Model Validation

In order to use the pump, motor and other component models described in chapters 4 and 5 to analyse the behaviour of aircraft fuel systems, they must first be validated against data from the test rig. Each of the models have been developed independently using data from the test rig. Validation therefore, must be conducted with respect to the overall system behaviour, in order to validate that each of the models link correctly to model the system as a whole. This chapter details this system modelling validation approach, and presents the results in order to demonstrate that the system can be accurately described using the pump, motor and other component models.

In a similar approach to the model development, the system modelling validation has been divided into two distinct sections, to cover both the steady-state and the dynamic behaviour of the test rig. The steady-state behaviour of the system is analysed for a number of operating conditions. This is to present evidence that the system model is capable of predicting the rig performance over the full range of pump speed as well as load valve opening. If the steady-state behaviour can be predicted accurately, then the model behaviour during transient operations such as pump acceleration can be assessed with confidence in the boundary conditions.

6.1 The Bath*fp* circuit for rig validation

A Bath*fp* circuit has been created to represent the test rig. It consists of a centrifugal pump delivering flow through a single pipe loop and a ball valve from one tank to

another. The pump is driven by an AC induction motor, which is fed through a frequency inverter. Figure 6.1 (a) shows this arrangement. In order to separate the effects of the motor model and hydraulic circuit model on the system model accuracy, a second circuit was developed which uses a user-defined pump speed input instead of the motor model. In this case, the actual measured pump speed from the test rig data can be input into the system model to investigate the hydraulic behaviour independent of the motor model. This circuit is shown in figure 6.1 (b).

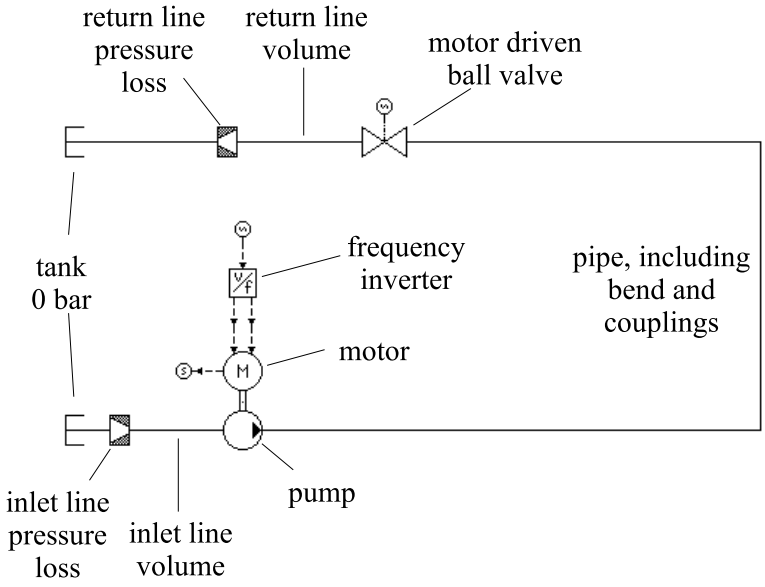

a) system model including motor model

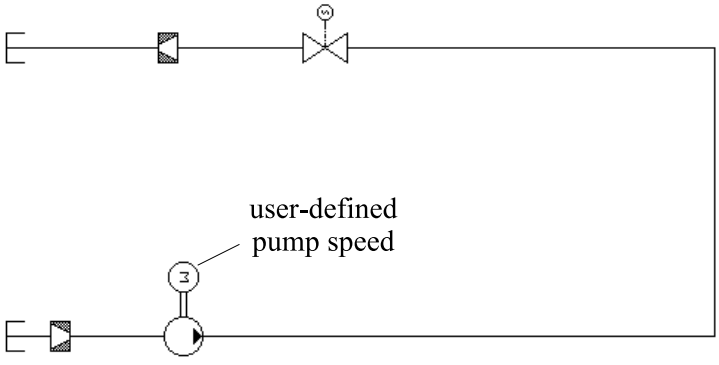

b) system model using user-defined motor shaft speed

Figure 6.1: Bath*fp* circuit for system model validation

The tank models are the basic Bath*fp* tank model, which simply supply a pressure to the connected model. No account is taken of the volume of fluid within the tank. For the steady-state simulations, the tank pressure has been set to zero, to reflect the zero point used during the rig testing.

The inlet line consists of two models, representing the pressure loss and the fluid volume. The pressure loss model takes a user input of K factor and outlet pipe diameter, and a pressure input from the two connected models in order to calculate the flow rate through the component. For these simulations, the K factor has been set as 3.47 with an outlet pipe diameter of 100mm (see chapter 4). The pipe volume is represented by the standard Bath*fp* pipe volume model. This represents the volume of fluid within a 1m long, 100mm inner diameter pipe, but accounts for no pressure loss or fluid inertia.

For the steady-state analysis, a centrifugal pump model has been created based on the non-dimensional modelling technique set out in chapter 4. This model requires an input of shaft speed from the motor model, and pressures from each of the components connected to its inlet and outlet ports. It then returns the flow rate. The pressure-flow and hydraulic power-torque characteristics are input in terms of α and γ coefficients as detailed in chapter 4. The values of these used in the following simulations depends on which test rig data are being used for comparison, as both the pressure-flow and hydraulic power-torque characteristics were shown to change over time (see chapter 4). The pump impeller radius and effective volume are also required. The reducing section K factor is used to calculate the hydraulic orifice constant. For the dynamic analysis, a second, dynamic pump model is used. This requires a further input of fluid inertance, but no input of reducing section K factor. Otherwise, the two pump models are identical. During dynamic analysis, the pressure loss due to the reducing section can be accounted for by an appropriate increase in K factor in the main pipeline model.

The pump shaft speed required by the pump model is supplied either from the AC induction motor model for the steady-state and dynamic simulations respectively, or from the general Bath*fp* motor model when using a direct input of the measured pump speed. The steady-state model is based on the Thévenin circuit analysis in chapter 4, and the dynamic model on the generalised machine theory method in chapter 5. Both require an input of voltage and supply frequency, which in this case are supplied by a simplified frequency inverter model. This supplies a constant V/f signal as described in chapter 4, given a demand input of shaft speed from the signal input. As discussed in chapter 4, the supply voltage and frequency have been adjusted to a maximum of 450V and 50.2Hz to reflect the measured motor performance. For the simulations using

an input of the measured shaft speed, a simple duty-cycle motor model is used. This simply defines the time history of shaft speed in ten discrete steps.

Bath*fp* contains a library of existing pipe models, which have been developed over time and have been extensively validated against experimental data. For steady-state analysis, a simple, steady-state pressure loss and volume pipe model has been used. This model represents the pipe as two equal volumes, separated by a hydraulic orifice. The volumes therefore represent the compressibility of fluid in the pipe, and the orifice represents pressure losses due to friction and fittings. The friction is calculated using Darcy's equation using a friction factor obtained from the Colebrook equation. It has been shown to be accurate for analysis of circuits where fluid inertia is not considered to be significant.

For the dynamic analysis, a distributed parameter pipe model is used. This uses a finite-element distributed-parameter model, which is reduced to a series of ordinary differential equations using the method of lines. The pipe is split into 4 elements along its length. Friction is again taken into account using Darcy's equation and the Colebrook formula for pipe friction factor. Compressibility, air release, cavitation, gravity and inertia are all taken into consideration. The model is able to determine if the flow is laminar or turbulent, and apply the correct friction factor. It has been shown to accurately model the behaviour of longer pipe lines, where fluid inertia is known to be significant.

Each element within the pipe model refers to a group of capacitive, inductive and resistive elements. The model is arranged such that it forms a series of four *RLC* elements, one of which is shown in figure 6.2. Each of the inductances represent a calculation of the rate of change of flow rate across the pipe element as a function of inertia and the pressure difference, and each capacitance represents the rate of change of pressure as a result of compressibility. The resistances represent pressure drop due to friction.

Of course, there exist in publications many methods for modelling flow in hydraulic pipelines. Here, transmission line theory has been applied using the standard Bath*fp* models. Soumelidis et al. present a summary of current modelling methods for pressure transients [70]. Here, the comparative benefits of the transmission line method, the method of characteristics, modal analysis and the finite element method in terms of their accuracy and computational efficiency are investigated. The transmission line method is shown to be the most efficient, whereas greater accuracy can be achieved

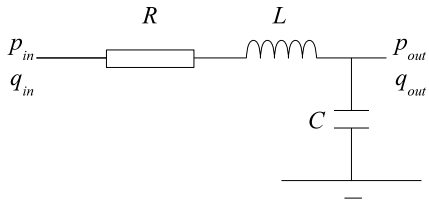

Figure 6.2: Bath*fp* dynamic pipe model

using the modal approximation method. All of the above methods have been used in all manner of applications and references can be found throughout the published literature.

Both of the pipe models require similar inputs. The pipe inner diameter has been set to 34.3mm, and the length to 16.16m. The relative roughness value of 5.5×10^{-5} obtained in chapter 4 is used. The pipe model allow for additional pressure losses, defined as a K factor. This has been set to either 1.55 or 1.86 for the steady-state simulations, to reflect the minimum and maximum values for 16 couplings and the bend from chapter 4. For the dynamic simulations, these are increased by 1.09 (see chapter 5) to include the reducing section pressure losses.

The motor driven ball valve is modelled using the Bath*fp* model developed as a part of the Active Valve project. It has been developed using test rig data in a similar manner to the centrifugal pump. Details of the modelling work and validation can be found in the Active Valve project thesis [71].

Like the pump inlet line, the return line has been modelled as a pressure loss and a fluid volume. The pressure loss model is used to model the losses, using the K factor of 0.729 and outlet diameter of 34.4mm from chapter 4. The fluid volume is modelled using the pipe volume model, using a diameter of 34.3mm and length 15m, giving an approximately equivalent volume to the physical system.

Tables 6.1 through 6.9 detail the inputs to each of the models in the circuit. Unless otherwise stated, these values remain constant throughout all of the validation work.

parameter	units	value
tank pressure	bar	0

Table 6.1: Bath*fp* circuit definition: tank model inputs

parameter	units	value
K factor		3.47
outlet diameter	mm	100

Table 6.2: Bath*fp* circuit definition: inlet line pressure loss model inputs

parameter	units	value
inner diameter	mm	100
length	m	1

Table 6.3: Bath*fp* circuit definition: inlet line volume model inputs

6.1.1 Fluid properties

Using the measured temperature-density and temperature-viscosity relationships for the test rig water, the density and kinematic viscosity at a number of temperatures are detailed in table 6.10. The bulk modulus has been measured during the course of the dynamic pump modelling work. The measured value of 18700bar is used in all of the following simulations. These properties have been adjusted in the Bath*fp* simulations accordingly.

parameter	units	value
α_1		9.1468×10^6
α_2		7.0809×10^5
α_3		6.9823×10^3
α_4		-434.3703
α_5		-9.1507
α_6		2.1541
ϕ_0		0.0444
γ_1		0.7019
γ_2		0.1086
r	mm	73.5
v	m^3	6.0686×10^{-4}
c	$L/min/(bar^{0.5})$	752.76
L/ρ	m^{-1}	135.27

Table 6.4: Bath*fp* circuit definition: centrifugal pump model inputs

parameter	units	value
ω_s	rev/min	3000
X_m	Ω	105.73
X_s	Ω	1.808
R_s	Ω	0.783
R_r	Ω	0.984
X_r	Ω	2.544
c_f	Nm	0
c_s	Nm	0
c_c	Nm	0
J	kgm^2	0.0115

Table 6.5: Bath*fp* circuit definition: AC induction motor model inputs

6.2 Steady-state

The steady-state behaviour of the test rig has been simulated at three different demand speeds, and three valve angles. In each case, the results of the simulations have been

parameter	units	value
V_{max}	V	450
f_{max}	Hz	50.2

Table 6.6: Bath*fp* circuit definition: frequency inverter model inputs

parameter	units	value
pipe diameter	mm	34.3
pipe length	m	16.16
relative roughness		5.5×10^{-5}
additional K factor	m	$1.55 - 1.86(+1.087)$

Table 6.7: Bath*fp* circuit definition: pipe model inputs

parameter	units	value
K factor		0.73
outlet diameter	mm	34.3

Table 6.8: Bath*fp* circuit definition: return line pressure loss model inputs

compared against measured test rig data. This data is the same as that used in chapter 4 to determine the pump characteristic, where it is labelled "test 2", and was obtained during week 113 of the project. This validation represents a number of "spot checks" of the simulation performance against the measured data.

Two initial simulations have been conducted to examine the steady-state behaviour of

parameter	units	value
inner diameter	mm	34.3
length	m	15

Table 6.9: Bath*fp* circuit definition: return line volume model inputs

temperature (°C)	density (kg/m^3)	kinematic viscosity (cSt)
15	999.1	1.152
20	998.2	1.023
25	997.1	0.909
30	996.6	0.820

Table 6.10: Bath*fp* circuit definition: fluid properties

the full rig simulation as shown in figure 6.1 (a) when the motor demand speed is set to the maximum. The first uses $K = 1.55$ in the pipe model, the second $K = 1.86$, and in both the valve angle is set to zero. These simulations, labelled hereafter as simulations 1 and 2, are intended to predict the behaviour of the whole rig and to validate the motor model as well as the hydraulic circuit model. They are compared against test rig data from what is labelled hereafter as test 1.

Subsequent tests use the circuit shown in figure 6.1 (b), where the pump speed is supplied by the duty-cycle model. This is set to the same as the measured steady-state pump speed, in order to validate the hydraulic circuit independently of the motor model. Table 6.11 lists the various tests and simulations from which the data has been collected, as well as the demand pump speed and measured valve angle. For simplicity, this naming convention will be used throughout the following section.

test number	simulation number	demand speed (rev/min)	valve angle (°)
1	1	3000	0
	2	3000	0
	3	3000	0
	4	3000	0
	5	3000	33
	6	3000	60
2	7	2400	0
	8	2400	35
	9	2400	60
3	10	1800	0
	11	1800	35
	12	1800	61

Table 6.11: definition of Bath*fp* simulations and test rig data for steady-state validation

6.2.1 Comparison of Bath*fp* and test rig data

Each of the simulations has been compared to the test rig data using eleven parameters. These are:

1. pump shaft speed, ω
2. pump load torque, T_l
3. system flow rate, Q
4. pump inlet pressure, $p_{pump,in}$
5. pump outlet pressure, $p_{pump,out}$
6. pump pressure rise, δp_{pump}
7. pump non-dimensional flow, ϕ
8. pump non-dimensional pressure rise, ψ
9. pump non-dimensional torque, τ

10. pump efficiency, η

11. valve outlet pressure, $p_{valve,out}$

Simulations including motor model

Tables 6.12 and 6.13 detail the comparison between the simulations and test rig data where the motor model has been used.

parameter	units	simulation 1	test 1	% diff.
ω	rev/min	2965	2971	0.19
T_l	Nm	28.6	28.6	0.07
Q	L/min	560.0	562.9	0.51
$p_{pump,in}$	bar	−0.02	−0.02	3.30
$p_{pump,out}$	bar	5.42	5.50	1.38
δp_{pump}	bar	5.45	5.52	1.36
ϕ		0.050	0.050	0.33
ψ		2.10	2.12	0.98
τ		0.18	0.18	0.31
η		0.57	0.58	1.61
$p_{valve,out}$	bar	0.37	0.41	9.45

Table 6.12: comparison of Bath*fp* simulation 1 and test rig data 1

The presented data show that the simulation is capable of predicting the overall rig performance to a good degree of accuracy. In both of the cases presented here, the model predicts the pump speed to less than 0.2% of the measured data. The resulting flow rate for the first case is then around 0.5% different from the measured, while increasing the pipe K factor to allow for the coupling alignment increases this error to 1.8%. The pump pressure rise in case 1 is less than 1.4% different, and this reduces to less than 1% difference using the increased K factor. The valve outlet pressures see the largest difference between simulated and measured results. For simulation 1 the difference is as much as 9.5%, but this reduces significantly to less than 0.5% when the K factor is increased.

parameter	units	simulation 2	test 1	% diff.
ω	rev/min	2965	2971	0.19
T_l	Nm	28.5	28.6	0.41
Q	L/min	553.0	562.9	1.76
$p_{pump,in}$	bar	−0.02	−0.02	0.72
$p_{pump,out}$	bar	5.44	5.50	0.96
δp_{pump}	bar	5.47	5.52	0.96
ϕ		0.049	0.050	1.58
ψ		2.10	2.12	0.58
τ		0.18	0.18	0.04
η		0.57	0.58	2.12
$p_{valve,out}$	bar	0.37	0.41	0.43

Table 6.13: comparison of Bath*fp* simulation 2 and test rig data 1

In both cases, the pump non-dimensional parameters agree well between the simulated and measured results. For case 1, all of the parameters show a less than 1% difference, although for case 2 the difference in the non-dimensional flow rate, ϕ increases to 1.6%.

It is clear that both cases 1 and 2 represent the overall performance of the rig well. If the system flow rate is taken as the best overall indicator of simulation accuracy, then case 1 can be seen to be more representative of the measured performance. Therefore, for the following simulations, where the pump speed is input, the pipe K factor has been set to $K = 1.55$ as in case 1.

Figure 6.3 shows the variation in percentage difference between simulated and measured data for four key parameters for three different pump demand speeds. It is clear that the best match between simulation and measured data is seen when the demand speed is at a maximum for all of the parameters shown, save for the pump pressure rise. At 50Hz demand speed, the flow rate error is less than 1%, but this increases to as much as 2.5% at 30Hz. The torque sees an increase from around 0.1% to 4.5%, and the valve outlet pressure from 9.5% to 11%.

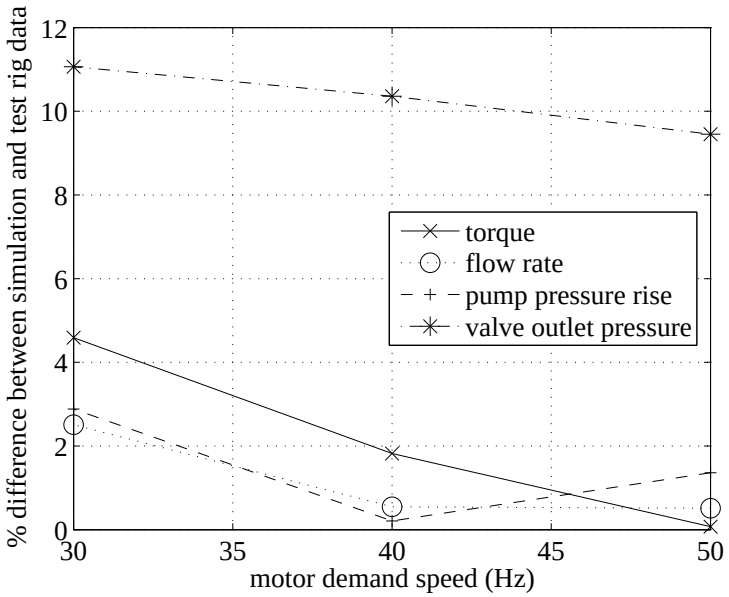

Figure 6.3: percentage difference between simulated and rig data against pump demand speed for a valve angle of zero

Simulations without motor model

Table 6.14 details the comparison between the simulations and test rig data where the motor model has not been used, but instead the pump speed is set according to that measured during the corresponding test for a pump demand speed of 50Hz and zero valve angle.

It can clearly be seen that using the exact pump speed from the measured test data has improved the correlation between the predicted and measured flow rate from a 0.5% difference to a 0.3% difference. The predicted pump pressure rise is within 1% of the measured, although the non-dimensional parameters are very similar to those predicted using the motor model. The pressure at the valve outlet is also slightly closer to the measured value than in the case with the motor model, a 9% difference compared to 9.5% previously.

The results for the subsequent simulations and their comparison to equivalent test rig data are not presented in full here. Instead, the comparisons between the simulation and test rig data for the cases where the pump speed and valve angle are varied are

parameter	units	simulation 3	test 1	% diff.
T_l	Nm	28.7	28.6	0.31
Q	L/min	561.1	562.9	0.31
$p_{pump,in}$	bar	−0.02	−0.02	3.72
$p_{pump,out}$	bar	5.44	5.50	1.00
δp_{pump}	bar	5.47	5.52	0.98
ϕ		0.050	0.050	0.32
ψ		2.10	2.12	0.98
τ		0.18	0.18	0.32
η		0.57	0.58	1.60
$p_{valve,out}$	bar	0.37	0.41	9.08

Table 6.14: comparison of Bath*fp* simulation 3 and test rig data 1

presented in terms of selected representative trends within the results.

Figures 6.4 through 6.6 show the changes in the percentage differences between simulated and measured data for four of the key system performance parameters as a result of closing the valve at three demand operating speeds. In each case, the simulation pump speed has been set to match the measured pump speed.

In general, it can be seen that, for each of the three pump demand speeds presented, the differences between simulated and measured torque, flow rate and valve outlet pressures increase significantly as the valve closes. The torque difference increases from around 1% in each case at zero valve angle to around 5 to 10% at 60°. The flow rate increases from around 1% to around 10%, whereas the valve outlet pressure exhibits the largest change, from around 10% at valve open to 18% at 50Hz, 27% at 40Hz and 35% at 30Hz. The maximum error for the 40Hz case occurs when the valve angle is 35°, where the error reaches just under 40%.

It can be shown that the non-dimensional parameters follow a very similar trend to their dimensional counterparts, as is expected given the fact that the pump speed is set to the exact, correct value. Figures 6.7 and 6.8 show graphs of the non-dimensional pressure-flow and hydraulic power-torque characteristics, overlaid with the simulation

and test rig data points for all of the cases mentioned above. It is clear that the simulated data points lie on the measured characteristic, as is expected due to the modelling method employed (see chapter 4). The measured test rig data points exhibit significantly greater scatter, in a similar fashion to the raw test results presented in chapter 4, from which the characteristics were derived. It serves as a clear example of one of the limitations of the accuracy of this method, as the characteristic used in the model can only estimate the exact performance at any given point.

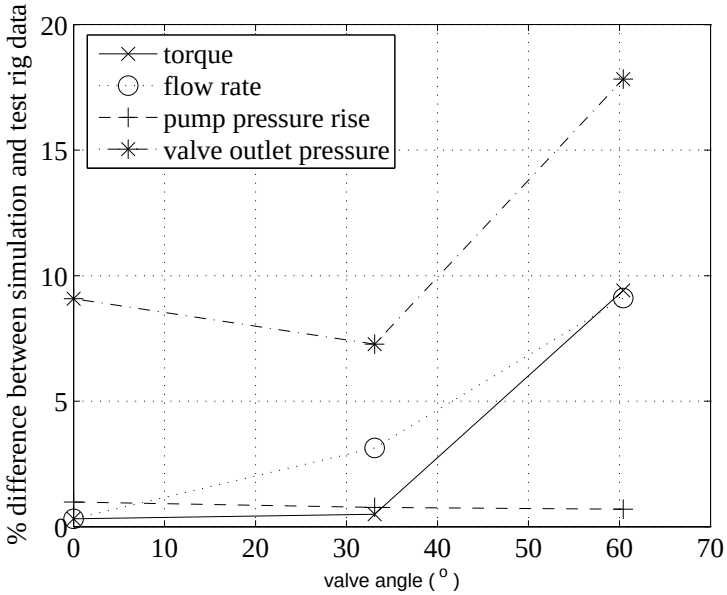

Figure 6.4: percentage difference between simulated and rig data against valve angle for demand speed of 50Hz

Figures 6.9 and 6.10 show the same comparison, but using the dimensionalised pressure-flow and hydraulic power-torque data. Again, the comparison between the simulated and measured data is good across the full range of points. The most noticeable deviation of the simulated results from the measured data occurs in figure 6.10 at lower flow rates, resulting in a poor local fit of the linear trend to the test data (see chapter 4).

6.2.2 Optimisation of the model

Three optimisation studies have been conducted on the Bath*fp* simulation of the test rig. Given the uncertainty in the values of the K factor for the couplings as a result

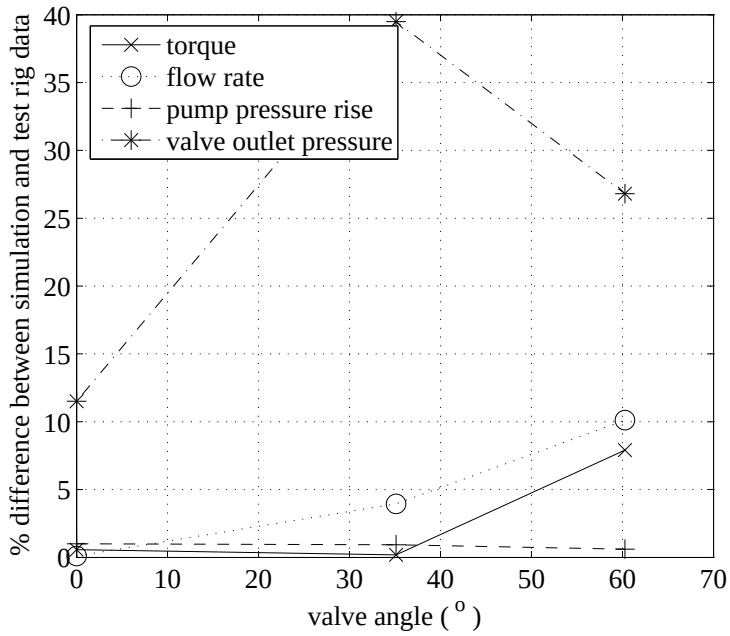

Figure 6.5: percentage difference between simulated and rig data against valve angle for demand speed of 40Hz

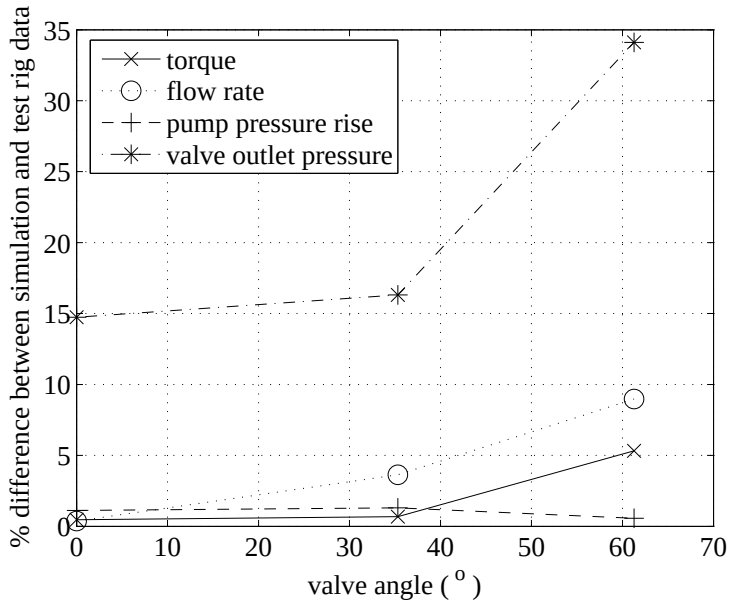

Figure 6.6: percentage difference between simulated and rig data against valve angle for demand speed of 30Hz

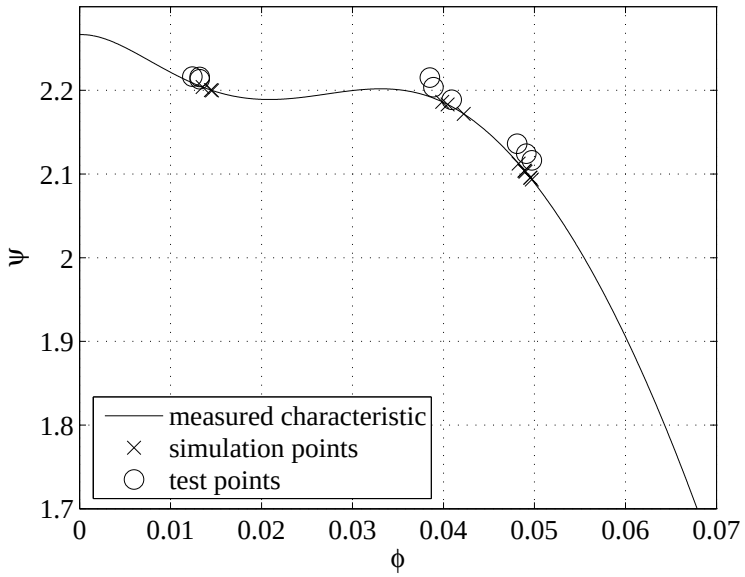

Figure 6.7: comparison of simulated results, measured test data, and measured non-dimensional pressure-flow characteristic

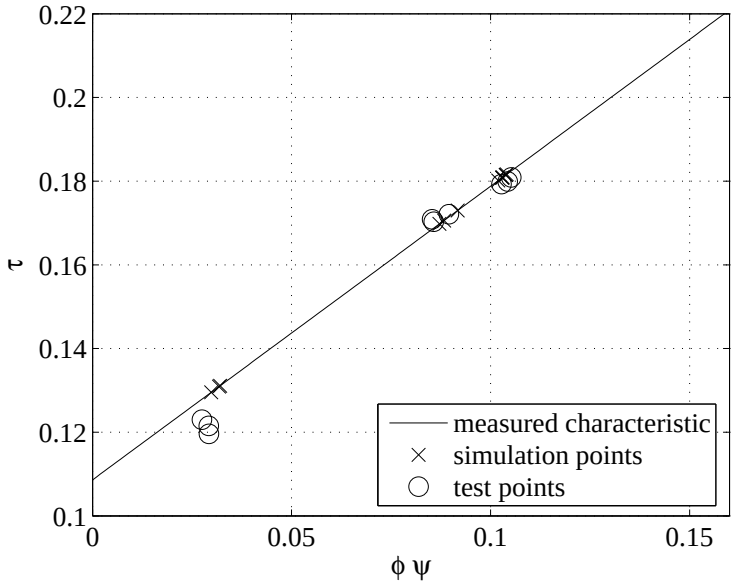

Figure 6.8: comparison of simulated results, measured test data, and measured non-dimensional hydraulic power-torque characteristic

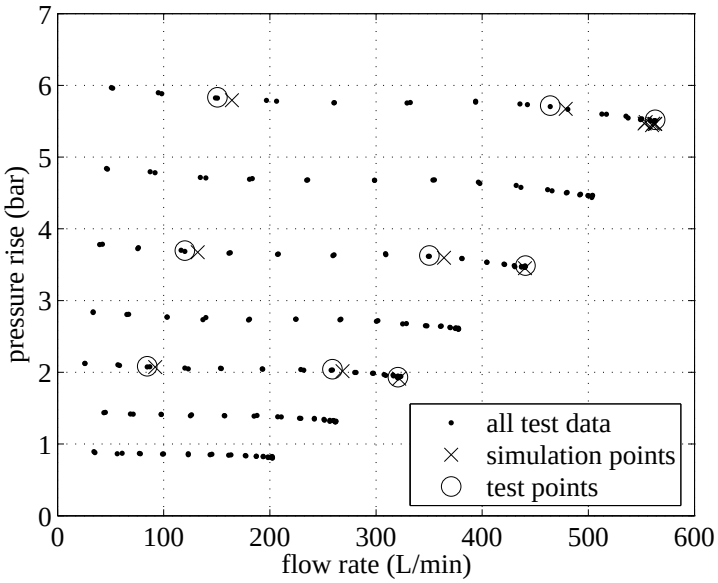

Figure 6.9: comparison of simulated results, measured test data, and measured dimensional pressure-flow characteristic

of their longitudinal alignment, the uncertainty in the exact length of each of the pipe sections, and the measurement accuracy of the valve angle transducer, these three quantities have been optimised for the three valve open cases described in section 6.2.1. The Tabu-based optimisation routine developed for use with Bath*fp* by Connor and Tilley [72] has been used to evaluate the best pipe K factor, pipe length and valve angle in order to match the simulation flow rate to the measured data. Table 6.15 details the optimum values of these parameters.

simulation number	parameter	units	original value	optimum value
13	additional pipe K factor		1.55	1.46
14	pipe length	m	16.160	15.985
15	valve angle	°	0	1.79

Table 6.15: results of optimisation of pipe K factor, pipe length and valve angle

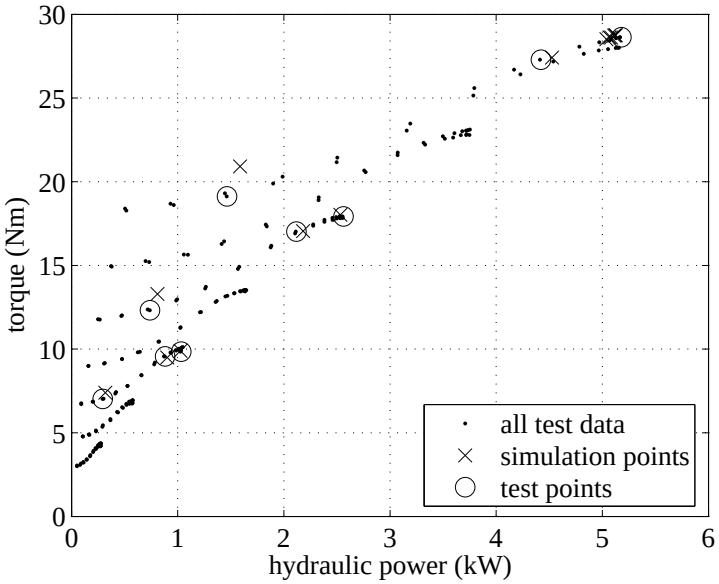

Figure 6.10: comparison of simulated results, measured test data, and measured dimensional hydraulic power-torque characteristic

The optimisation of each of these variables reduces the error in flow rate to an almost negligible degree, although has no significant effect on the other parameters. The valve outlet pressure error reduces from around 9% to 8.5%, although the pump pressure rise increases from 0.98% to 1.1%.

6.2.3 Discussion

From the results presented in section 6.2.1, it can be seen that the full system simulation is capable of predicting the behaviour of the rig to within an acceptable accuracy with the valve at its fully open position. The accuracy of the simulation reduces as the pump demand speed decreases from the design speed of the motor. This is most probably due to the accuracy of the motor modelling parameters supplied by the manufacturer and obtained from tests (details in chapter 4), which were supplied and measured on the assumption that the motor is operating at full speed and under full load. More research needs to be conducted to assess the suitability of the Thévenin circuit model for motors driven from variable frequency supplies.

When the hydraulic circuit is analysed independently of the motor model, using the measured pump speed as the input to the pump model, the system simulation has been shown to agree well with the measured test data, especially in the maximum demand speed and zero valve angle case. The additional pipe K factor, which has been included to model additional pressure losses from the couplings and bend, was known to lie in the range $1.55 < K < 1.86$, although the indeterminate relative longitudinal alignment of each of the couplings meant that this could not be known exactly. The simulations have shown that the lower boundary of this range produced the best match of system performance, when the flow rate was used as the primary comparison. Optimisation of the K factor value suggested a lower value of $K = 1.48$ resulted in an almost exact match of flow rate to the measured data, and a similar match could be obtained by changing the pipe length or valve angle. What is clear is that, even if such an optimisation is performed, the system simulation is still capable of modelling the measured performance of the rig to a good degree of accuracy.

The least satisfactory parameter in each of the comparisons of simulation and test rig data is undoubtedly the pressure at the valve outlet. At the maximum demand speed and valve angle of zero the pressure at the valve outlet was around 9% different to the measured data. As the valve was shut off, this difference was increased further to as much as 18% for the maximum speed case, although when the demand speed was set

to 40Hz this maximum error reached as high as 40%. This is clearly significantly worse than the other performance indicators.

It has been suggested that such a large difference is perhaps not surprising, given the way in which the return line is modelled, the uncertainty over the accuracy of the valve model, and the very low pressures which are recorded at the valve. The return line has been modelled as a simple K factor, assuming that the pressure-flow relationship can be reduced to a square law. Such an assumption is known to be true in the main, but can break down in the transition region and under highly cavitating conditions. Such conditions were noted to be prevalent at valve angles between 40° and 60° [71]. Test 3 and simulation 12 recorded flow rates of less than 100L/min, which is known to lie outside of the accurate range of the flow meter, reducing confidence in the accuracy of this measurement. The inlet line can also be shown to suffer from reducing accuracy with reducing flow rate or increasing valve angle. This element of the system model has been modelled in the same manner as the return line. Again, the measured pressure levels in this part of the system are very low, and the measurements were shown to suffer from a significant amount of scatter (see chapter 4).

From the non-dimensional and dimensional pump characteristic curves, the pump model has been shown to accurately represent the measured behaviour. The comparison of the dimensional hydraulic power-torque plot (figure 6.10) showed that in the low flow rate conditions, the simulated torque was significantly different to the measured. This could clearly be attributed to the accuracy of the linear fit applied to the data to form the model. The non-dimensional pressure-flow curve again highlights how the measured data at a given point can in fact lie off the average fitted characteristic curve, and hence result in an error between measured and simulated data at that point. This underlines the main limitation of the modelling method, that the accuracy of any simulation is subject to the degree of scatter which is present in the data from which the characteristics are derived.

The results presented here suggest that the system model is capable of accurately describing the steady-state performance of the test rig. It does however suggest that the K factor method for modelling both the inlet and return line may not be wholly suitable for analysing the steady-state behaviour at certain conditions, most notably low flow rates as a result of larger valve angles.

6.3 Dynamic

One aspect of the dynamic behaviour of the test rig has been examined in order to validate the models. The test rig has been used to record the system response to acceleration of the pump from rest to its maximum operating speed with the valve fully open. The pump controller was set up to carry out these operations at the maximum permissible rate, which resulted in an acceleration time of 2.34s from rest to 2968rev/min. The pump and pipes were fully primed at the beginning of the tests. Figure 6.11 shows the time history of the pump pressure rise, flow rate, pump speed and torque for the test. Note that the data has been normalised by their respective maximum values in order to reduce the data to a single plot.

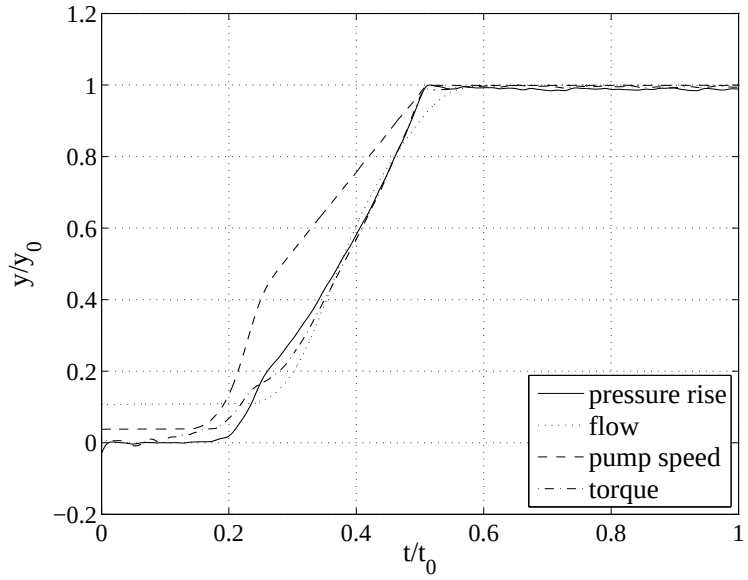

Figure 6.11: results of pump acceleration test

Two initial simulations of the test rig were conducted in order to tune the pipe K factor to match the steady-state flow rate at the end of the acceleration test to the measured data. This allowed all subsequent validation simulations to be conducted with the correct boundary conditions.

In a similar fashion to the steady-state validation, two initial simulations were conducted to analyse the full system simulation using the motor model developed in chapter 5, using the Bath*fp* circuit described in figure 6.1 (a). Three subsequent simulations

were conducted using the circuit described in figure 6.1 (b). These use the measured pump speed as an input, in order to validate the hydraulic system model independently of the motor model. The first of these cases uses both the dynamic pump model, which includes an inertia term to account for both the pump and the reducing section, as discussed in chapter 5, and the dynamic pipe model. This allows analysis of the impact of including pump inertia in the system simulation. The second simulation uses the dynamic pipe model with the steady-state pump model, in order to assess the impact of pipe inertia on the rig behaviour. Finally, the third simulation uses the steady-state pump and pipe models, which do not include inertia effects. This simulation shows the predicted steady-state behaviour of the system, and is useful in order to assess if the rig behaviour can be simplified to the steady-state.

Table 6.16 details the tests and simulation which have been conducted. The naming convention given is used hereafter to refer to the test and simulation data. The following section details the comparison between the measured test data and the simulation data.

test no.	simulation no.	motor model	pump model	pipe model	input
1	1	D	D	D	step
	2	D	D	D	ramp
	3	S	D	D	ramp
	4	S	S	D	ramp
	5	S	S	S	ramp

Table 6.16: definition of Bath*fp* simulations and test rig data for dynamic validation ("S" denotes a steady-state model, "D" a dynamic model)

6.3.1 Comparison of Bath*fp* and test rig data

Figure 6.12 shows the simulated pump speed for simulations 1 and 2 and the measured pump speed from test 1. Simulation 1 was conducted with a step input from rest to the maximum demand speed of 50.2Hz, occurring at the point in time when the measured pump speed is first seen to increase. Simulation 2 used a two stage ramp input of demand speed, based on the measured pump shaft speed. It is clear that simulation 1 represents an unrealistic case where the pump reaches its full speed in around 0.2s. The

resultant maximum torque in this case was more than 200Nm, requiring an input power in excess of 40kW. Such an acceleration would of course in practice be impossible, and the motor model does not include any non-linearities to model behaviour outside of the typical operating conditions.

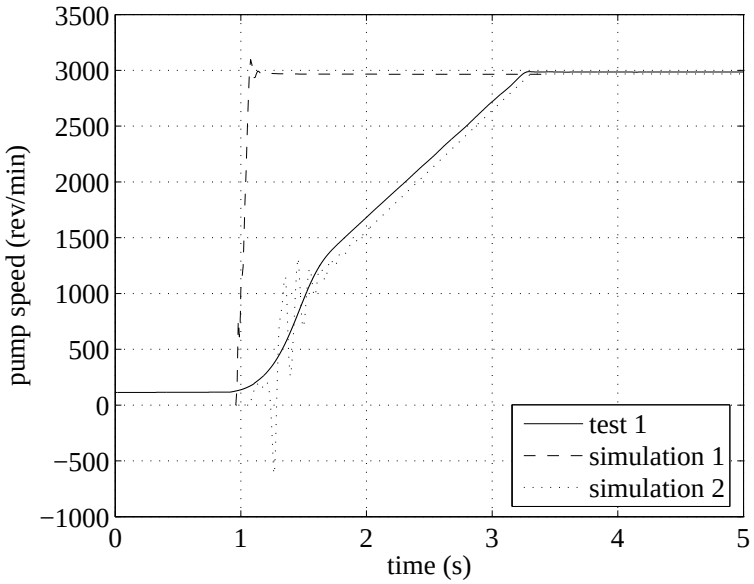

Figure 6.12: comparison of measured pump speed and simulated pump speed using dynamic motor model for acceleration tests

Whilst simulation 1 does not represent a realistic pump acceleration, it can be seen that simulation 2 does. The pump speed is oscillatory in the initial stage of the acceleration until around $t/t_0 = 0.3$. The resultant pressure, torque and flow plots also display oscillatory behaviour as a result. Thereafter, all of the parameters follow a similar trend to those measured in test 1. However, as the actual input signal to the motor from the inverter is unknown and not easily measured, these results are subject to a significant amount of uncertainty. They do show that the motor model can be used in conjunction with the hydraulic circuit simulation to predict the general behaviour of the system.

The measured pump speed has been used as the input to all subsequent simulations. Figure 6.13 shows a comparison between the measured data and that input in Bath*fp*. It can be seen that the two are in close agreement from around 500rev/min to 3000rev/min. At lower speeds the shaft speed sensor has been shown to be inaccurate. It can also be seen from the figure that the speed sensor has a minimum

measurement speed of around 115rev/min, which, after filtering, has resulted in the measured data curve not starting from zero.

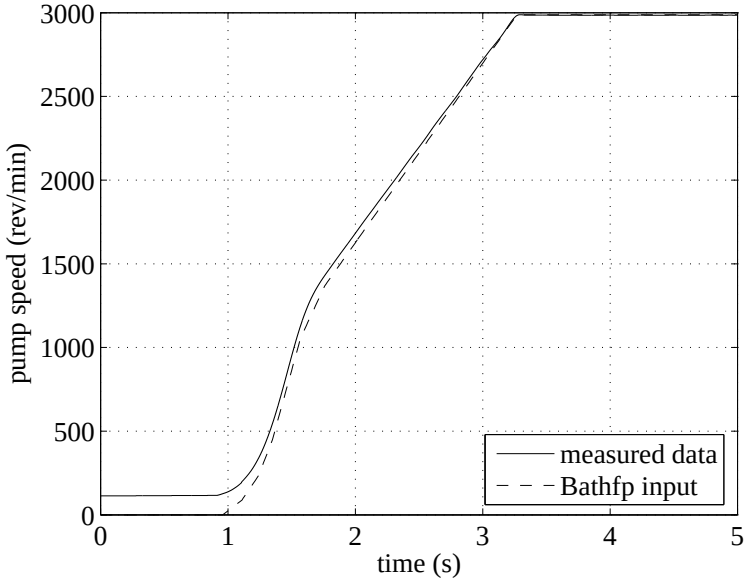

Figure 6.13: comparison of measured pump speed and input to Bath*fp* for acceleration tests

Figures 6.14 through 6.16 present the predicted pump pressure rise, flow rate and pump torque for simulations 3, 4 and 5 and the measured data from test 1. The results show clearly that the simulated pressure rise from each of the simulations follows the measured data closely, although closer inspection reveals that the full dynamic simulation and pipe only dynamic simulation provide a much closer match to the measured data than the steady-state simulation. In order to clarify this, the error between each simulation result and the measured test data is shown in figure 6.17.

The plot of flow rate shows a much clearer difference between simulations 3, 4 and 5. The two simulations which use the dynamic pipe model follow the test data much more closely, although it is very difficult to distinguish any difference between simulations 4 and 5. The measured flow rate shows a similar behaviour to the shaft speed. Flow rates below 100L/min are outside the accuracy of the flow meter, and it is incapable of measuring flows less than 30L/min due to friction in the turbine. The measured data is shown to start from a minimum of around 60L/min due to the way in which the data has been filtered. Above 100L/min, the simulated and measured data show good agreement.

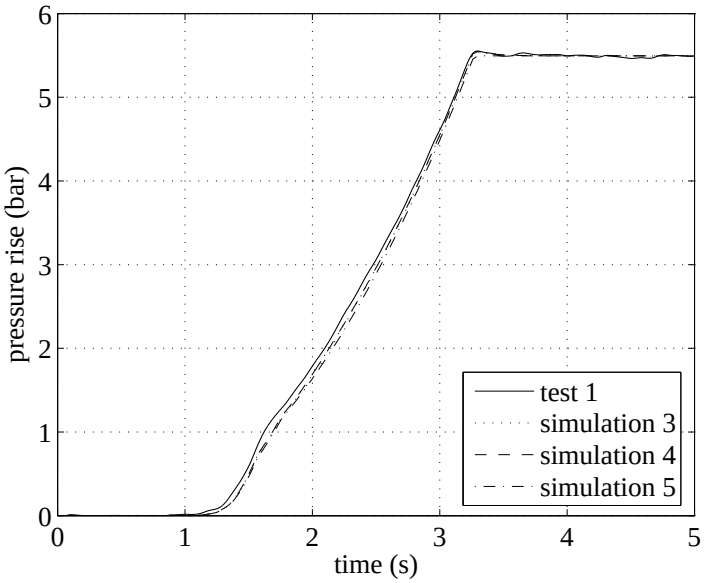

Figure 6.14: comparison of measured and simulated pump pressure rise for acceleration tests

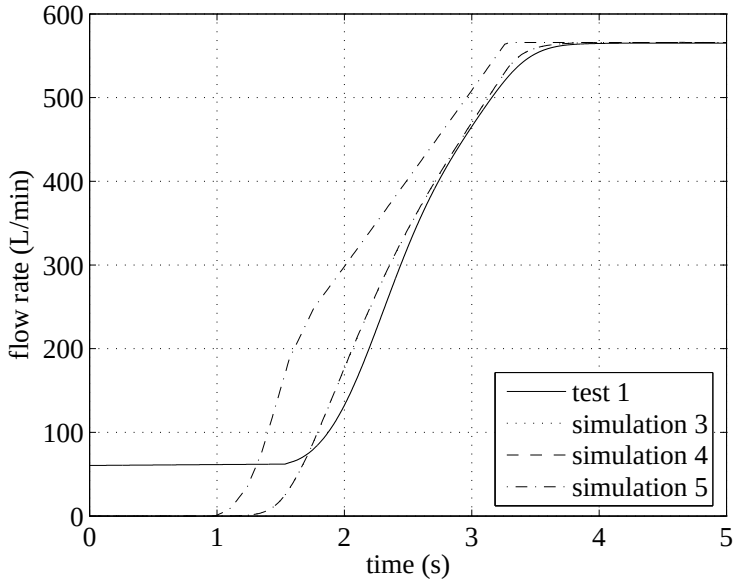

Figure 6.15: comparison of measured and simulated flow rate for acceleration tests

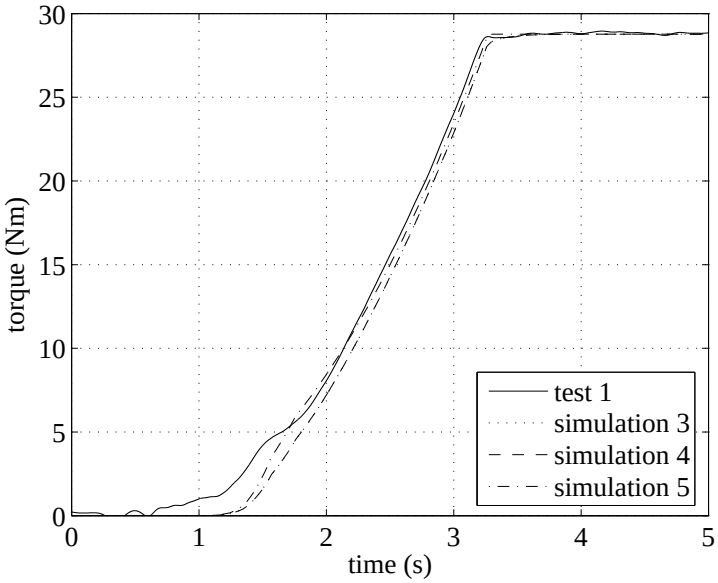

Figure 6.16: comparison of measured and simulated pump torque for acceleration tests

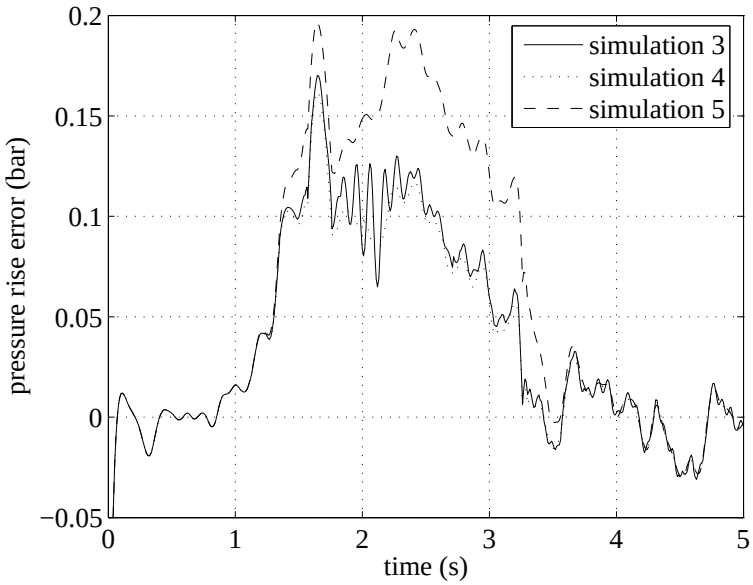

Figure 6.17: error between measured and simulated pump pressure rise for acceleration tests

Figure 6.16 shows a good agreement between all the simulated data and the measured data in terms of rate of increase of torque. The predicted torque from simulation 5 appears to model the measured data more closely in terms of absolute value, but the data from simulations 3 and 4, which are very similar, show a more consistent match in gradient over the full acceleration. Figure 6.18 shows the error between the test data and each of the simulated data sets, again to clarify the differences in each case. It is clear that steady-state simulation 5 shows the closest agreement to the test data, and that there is little difference between simulations 3 and 4. However, closer inspection of figure 6.16 shows that the data from simulations 3 and 4 follow the trend of the measured data more closely over the full range.

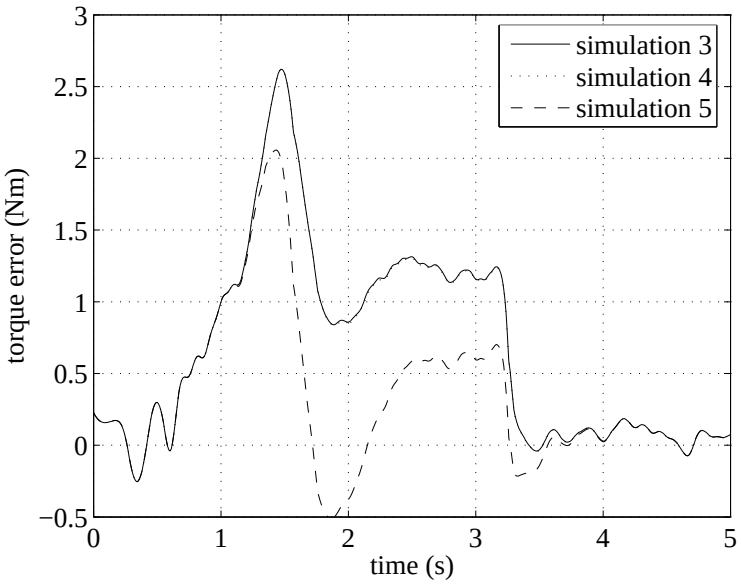

Figure 6.18: error between measured and simulated pump torque for acceleration tests

There is a clear lag between the measured torque and the simulated torque from simulations 3 and 4. This can be attributed to the fact that the torque meter measures the torque produced by the motor, not the load torque from the pump. The difference in the two accounts for the rate of acceleration, following equation 4.35. The estimated motor torque can be found by re-arranging equation 4.35, and calculating the measured rate of change of pump speed with time, $\dot{\omega}$. Figure 6.19 shows a comparison of the measured torque to the estimated motor torque from simulation 3 data using an inertia value of 0.0115kg/m^2, which is similar to that predicted for the motor and pump. It can be seen that this analysis results in a very good match between the measured

and simulated torque data. Oscillations in the derived motor torque are as a result of numerical differentiation of the motor speed data.

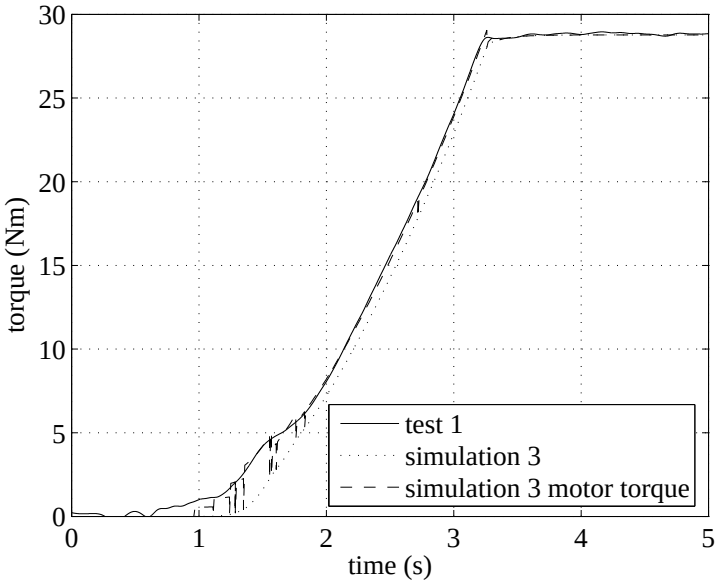

Figure 6.19: comparison of measured and simulated motor torque for acceleration tests

In order to ascertain if the rig behaviour during pump acceleration follows the steady-state characteristic, and can effectively be considered a quasi-steady operation as suggested by Thanapandi et al [18,38], the test results have been plotted as loci on a ψ/ϕ and a $\tau/\phi\psi$ plane. Figures 6.20 and 6.21 show these plots, superimposed on top of the steady-state characteristic curves, themselves generated from the simulation 5 data. In each case, letters have been used to indicate chronologically ordered points on the graphs to aid their interpretation. The torque coefficient, τ, has also been calculated for the simulation 5 data using the estimated motor torque.

Consider figure 6.20. The region A to D indicates a highly oscillatory period during the early stages of the acceleration up to around 1.5s, corresponding to the acceleration to around 1000rev/min. In this region, there is little information to be gained. The region D to E indicates the majority of the acceleration period, and the measured data can be seen to follow reasonably closely to the predicted steady-state trend, given that the steady-state characteristic is derived from experimental data which is itself subject to significant scatter. The measured line can be seen to settle onto the same steady-state operating point as predicted by the simulation at point E.

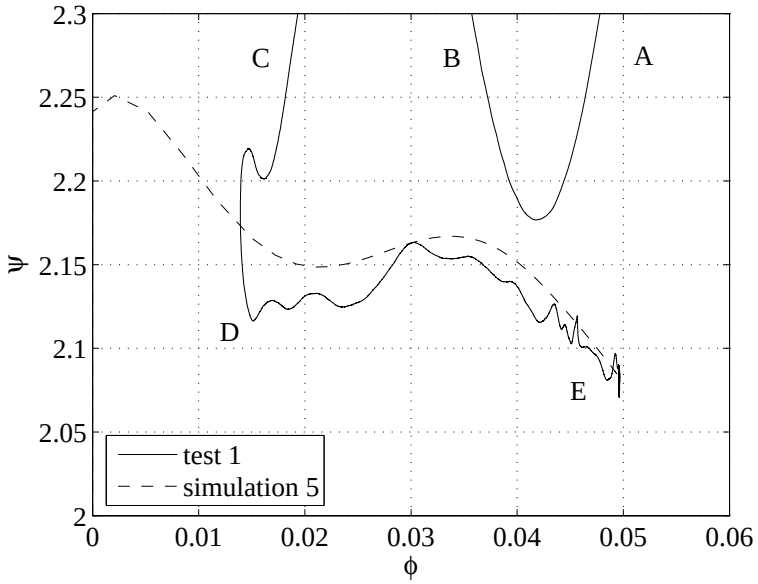

Figure 6.20: comparison of measured non-dimensional pressure-flow characteristic to simulated data for acceleration tests

The hydraulic power-torque plot, figure 6.21, can be analysed in the same way. Again, the region A to F indicates a highly oscillatory region in the initial stages of the acceleration. Point F corresponds to a time of around 1.7s, where the shaft speed is around 1500rev/min. It could be suggested that the region A to F lies outside of any accurate analysis due to its oscillatory nature. The region F to G describes the acceleration from 1500rev/min to 3000rev/min, where it can be seen that the measured torque is significantly greater than that predicted for the steady-state pump load torque. Once the pump reaches its maximum speed, then the measured non-dimensional hydraulic power-torque plot drops on to the predicted steady-state line, and settles on the correct steady-state operating point, indicated by the region G to I. The measured torque can be seen to follow the simulated motor torque curve more closely than the load torque curve, suggesting that the model and experimental data are in closer agreement than is shown by the load torque data.

Whilst the data presented in figure 6.20 suggests that the pump behaviour in terms of pressure and flow rate can be described as quasi-steady-state, it is difficult to discern if the same can be said for the torque. It is instructive to examine the time histories of each of the non-dimensional parameters also. Figures 6.22 through 6.24 show how ϕ, ψ and τ respectively change with time. The measured data is compared to the

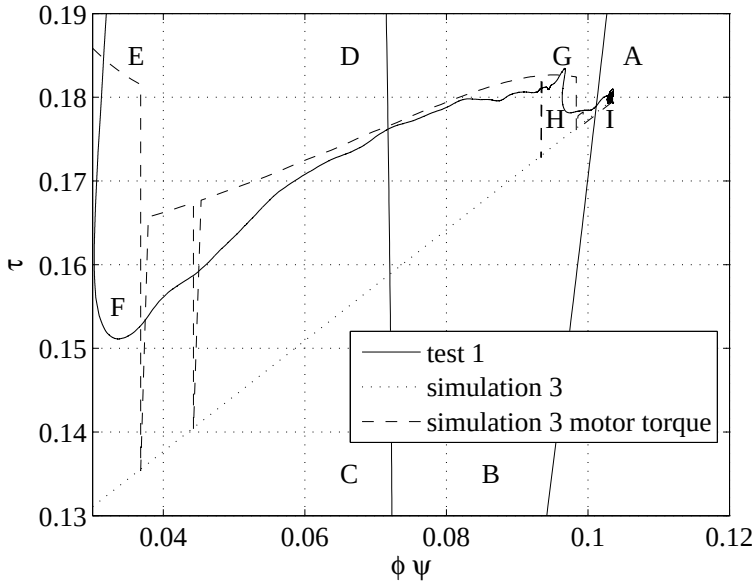

Figure 6.21: comparison of measured non-dimensional hydraulic power-torque characteristic to simulated data for acceleration tests

simulated data from simulations 3 and 5. Once again, the torque data from simulation 3 is presented for both the load and motor torques. Simulation 4 can be shown to follow nearly exactly the same trend as simulation 3.

In the case of figure 6.22 and 6.23, it is clear that the simulated data from simulation 3 fits well to the measured data, whilst the steady-state simulation 5 can be seen to follow quite a different trend. Figure 6.24 shows a much more clear difference between the measured data and that from simulation 3 in terms of absolute values, although they both clearly follow a similar trend. At time $3s$, at the point when the acceleration has finished, there is a clear shift in the measured data, whereafter it matches the simulated data well.

6.3.2 Discussion

The Bath*fp* simulations of the test rig during pump acceleration can be seen to represent the measured behaviour in terms of pump pressure rise, flow rate and torque. Using a ramp input of demand speed to the dynamic motor model, the simulation follows

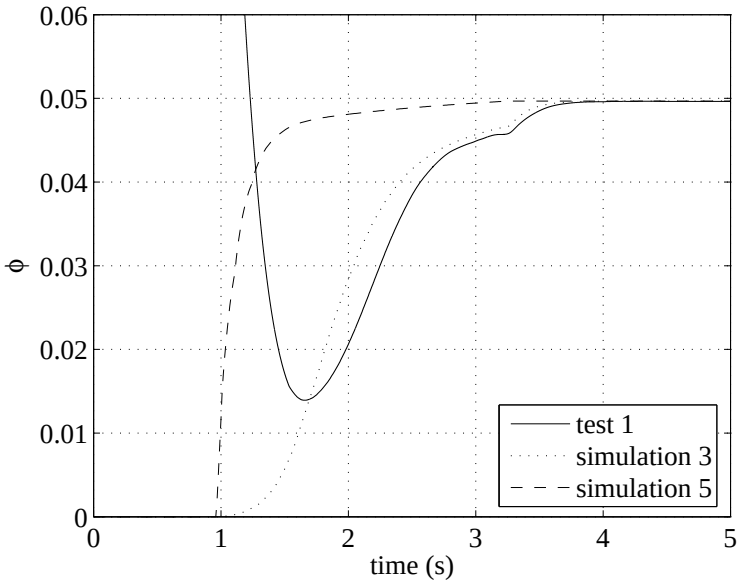

Figure 6.22: comparison of measured non-dimensional flow rate to simulated data for acceleration tests

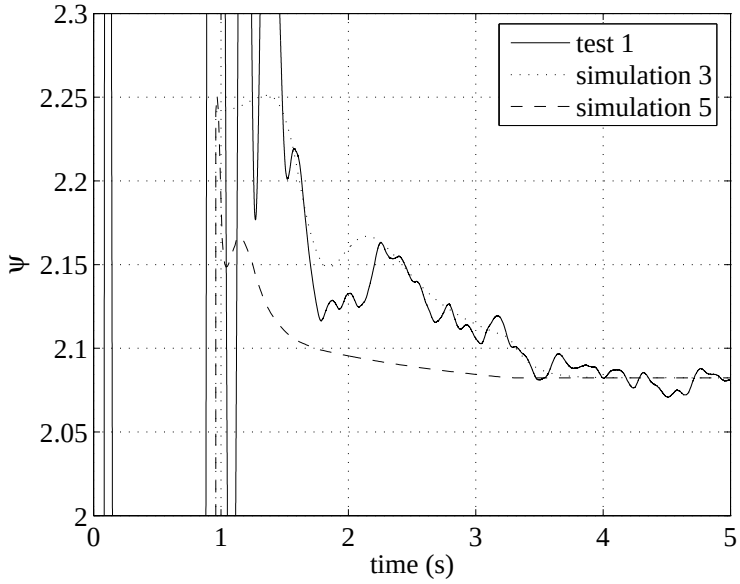

Figure 6.23: comparison of measured non-dimensional pressure rise to simulated data for acceleration tests

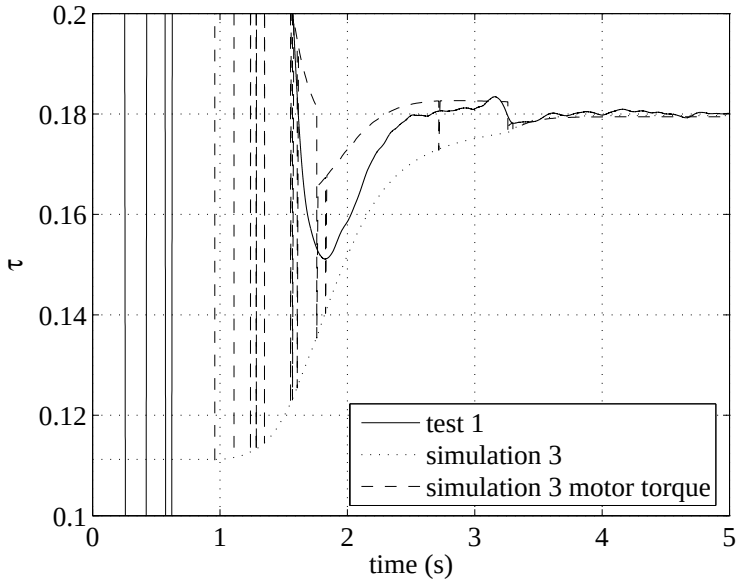

Figure 6.24: comparison of measured non-dimensional torque to simulated data for acceleration tests

similar trends in each of the parameters to the measured data once the pump speed has settled from its oscillations during the initial acceleration period. However, as the motor parameters used for the modelling and the actual change in motor speed demand are subject to uncertainty, it is difficult to determine the accuracy of the hydraulic system model.

In order to examine this, the motor model was replaced by a direct input of the measured pump speed. The pressure rise can be seen to be accurately predicted by each of the simulations, although the dynamic pipe model is the most appropriate as pressure rise data from simulations 3 and 4 match the measured data best. The fact that the steady-state model in simulation 5 predict the pressure rise well is most likely attributable to the fact that both the dynamic and steady-state pipe models account for fluid compressibility, and that the simulations have been conducted with a suitable fluid bulk modulus value. The plot of pressure coefficient, ψ, against time clearly indicates that the system model is capable of capturing the measured pressure rise of the pump during the acceleration.

It has been shown that the flow rate is most accurately represented by the dynamic model, although it is clear that the inclusion of the pump and reducing section inertance

has little effect on the results. This is not surprising, given that the system inertance has been shown to be several orders of magnitude greater. The measured flow rate can be seen to lag the simulated data in the initial and final stages of the acceleration. This might be expected due to the nature of turbine flow meters. They are well known to suffer from slow response during transient measurement, during which time their accuracy is questionable. It is possible that optimisation of the system model, especially in terms of the pipe length, could improve the fit between measured and simulated data. The plot of the flow coefficient, ϕ, against time clearly indicates that the system model is capable of capturing the trend of the measured data very well.

From the comparison of the measured and simulated pressure-flow non-dimensional characteristic, it is clear that the model captures the measured behaviour of the system. It would suggest that the measured pressure rise and the flow rate show that, during an acceleration of this nature, the pump behaves as a quasi-steady-state component, and that fluid inertance within the pipe is the only dynamic property which needs to be considered. The measured data has been shown to lie along the steady-state characteristic curve, within the scatter of the measured data from chapter 4.

The measured motor torque and predicted pump load torque have been shown to compare favourably in terms of trend during the acceleration period. By accounting for the torque required to facilitate the acceleration, the simulated motor torque data has been shown to match the measured data well, assuming a value of system inertia which is within the expected range. From the non-dimensional data, it can be seen that the predicted trend of the torque is similar to the measured data. The measured value of τ is shown to lie within those calculated using the simulated load and motor torques. Given the uncertainty over the accuracy of the torque meter under transient operations and the oscillatory nature of its measurement due to axial misalignment from its installation, the comparison of the measured and predicted trends is good. It is suggested therefore that the torque characteristic of such a pump during such an acceleration can be considered to be quasi-steady-state.

6.4 Closure

Bath*fp* has been used to simulate the performance of the test rig during both steady-state and dynamic operations. This has been done to validate each of the modelling tools which have been developed for the motor, pump and other hydraulic components.

The steady-state validation was carried out in order to check that the system simulation was capable of capturing the measured operating conditions, before the dynamic simulations examined the ability of the simulation to predict the rig behaviour during pump acceleration.

The steady-state validation work was conducted in two stages. The first looked at the rig behaviour using a full system simulation including the steady-state motor model. This simulation was capable of predicting the measured pump speed to less than 1% difference from the measured data, which resulted in predicted pump torque, flow rate and system pressures within 3.5% of the measured data, save for the valve outlet pressure which was within less than 10%.

The motor model was replaced by a direct input of the pump speed in order to separate validation of the hydraulic system model from the motor model. This improved the comparison of predicted and measured data by a small margin. Steady-state validation has been carried out at three pump speeds, and for each of these at three valve angles. In each case, the simulated data compared well to the predicted data, although it was shown that the accuracy reduced as the valve shut. The data were compared to both the measured dimensional and non-dimensional characteristics, and all points were shown to agree well.

For the dynamic validation, the rig was used to measure the pump behaviour during acceleration from rest to its maximum operating speed with the valve fully open. Five simulations were conducted. The first two examined the behaviour of the simulation using the dynamic motor model, and the latter three used the measured pump speed as the input. The motor model was shown to give good agreement between measured and simulated data when a ramp demand speed input was applied, although, as the nature of the actual ramp employed for the test data is unknown, it is difficult to assess how well the data compare.

Again, the motor speed was used as an input to the pump model in order to separate the effects of the motor model from the hydraulic system model. The three simulations assessed the rig behaviour using different combinations of models in order to ascertain if the dynamic rig behaviour could be considered quasi-steady-state, or if pump and pipe fluid inertances were important. Comparison of the measured and simulated data showed that the pipe inertance is of greatest importance, and that fluid inertia within the pump is insignificant in terms of the system response. It was clear that the steady-state pipe model was not sufficient to capture the behaviour of the rig, but that the

pump pressure rise, flow rate and torque all behave as quasi-steady-state during such a pump acceleration.

This validation of the component models has shown that, when combined to model a real system, they can be used to predict the system performance to a good degree of accuracy. The system pressure loss models developed from the measured data have been shown to be suitable for assessing the steady-state behaviour of the test rig. It is clear that for such a system, the pump inertia is not significant when compared to the inertia of the pipe, and that the steady-state pump model can be used to predict system behaviour during transient pump operations, provided that a suitable pipe model is used.

Chapter 7

System Modelling and Simulation

The component models developed in chapters 4 and 5, and validated in chapter 6 have been extended to examine the behaviour of the aircraft fuel system described in chapter 3. This allows the impact of the control schemes discussed in chapter 3 on the system performance to be analysed. This chapter describes the development of the fuel system definition from the general description given in chapter 3 to include a description of the physical fluid-mechanical network and pump definition for the trim to centre transfer and the subsequent Bath*fp* simulations. Validation of the models has been accomplished using the test rig and water as the working fluid. This validation process and the validity of the extension of the models to jet fuel and operating conditions at high altitude are discussed in the following chapter.

Current fuel system health monitoring principles are also discussed. Whereas these concepts tend to focus on health monitoring at the component or even functional level, they do not usually consider the behaviour of the system. It is proposed that a system simulation such as that presented here could form the basis of a health monitoring tool, which could be used in service to inform maintenance of components and preempt failures. The system could conceivably use minimal measurements of electrical inputs to predict system behaviour and compare the simulated performance against normal operation. This chapter presents these concepts in relation to the aircraft fuel system presented in chapter 3, and discusses their possible implementation.

7.1 Development of the generic aircraft fuel system definition

The fuel system for the generic aircraft described in chapter 3 has been defined in terms of the fluid-mechanical network and pump specification in order to model the system in Bath*fp*. The following section describes this definition method.

7.1.1 Fluid-mechanical network

The physical layout of the pipework is based on information from industry and several basic assumptions about the structure of the generic aircraft. Figure 7.1 is a plan drawing of the aircraft, showing the fuselage frames and wing ribs used to define the pipe path from the THS to the centre tank. From the information supplied from industry, the fuselage frame spacing and wing rib spacing were set. This allowed a definition of the pipework path, and the position of bends and couplings. The definition of the tanks is taken directly from those used for the AMPEC/CGFlight simulations in chapter 3.

It should be noted that this definition is not intended to represent an actual, finished design for a fuel system, or a particular real-world aircraft. It is to only be used for this analysis as an example of a representative system.

The trim to centre transfer pipe has been assumed to be $1.5''$ (38mm) in diameter, whereas the refuel gallery is $2''$ (51mm). This has been set as a result of simulations of the ground refuel, conducted as a part of the Active Valve project. The transfer is achieved by two centrifugal pumps in the trim tank, via two ball valves, as described in chapter 3. These are labelled valves N and M, and they and the trim to centre transfer route are highlighted in figure 7.2.

7.1.2 Transfer pump specification

The centrifugal pump modelling technique described in chapter 4 can be applied to an aircraft fuel system trim transfer pump. Clearly the characteristic definition used for the test rig modelling is inappropriate, so instead a characteristic definition has been derived using the specification given in table 7.1. Since little is known about typical

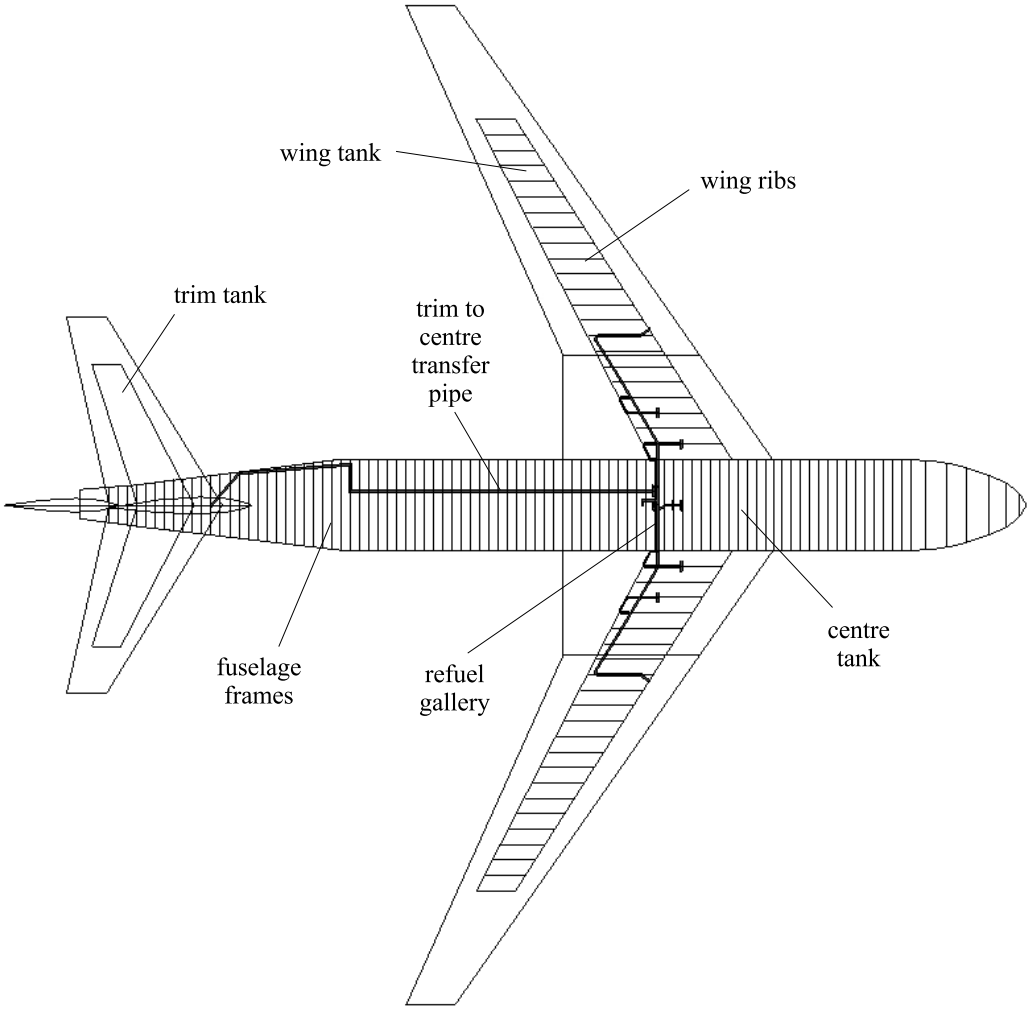

Figure 7.1: layout of transfer pipe network for fictitious aircraft definition

drive operating speeds, the maximum drive speed has been set to 3000rev/min, as would be expected for a two pole AC induction motor. The pressure requirements have been set according to general information from industrial partners, and the flow rate according to those recorded in the AMPEC/CGFlight simulations.

Whereas the definition of the test rig pump in chapter 4 used a known operating pressure value, p_1, here it has been defined with respect to the system flow rate using the value of the estimated system K factor, k_{system}. The value of this has been set from some initial Bath*fp* simulations of the fuel system, where the pipe pressure-flow characteristic was calculated. The fluid density has been set to that for Jet A-1 fuel

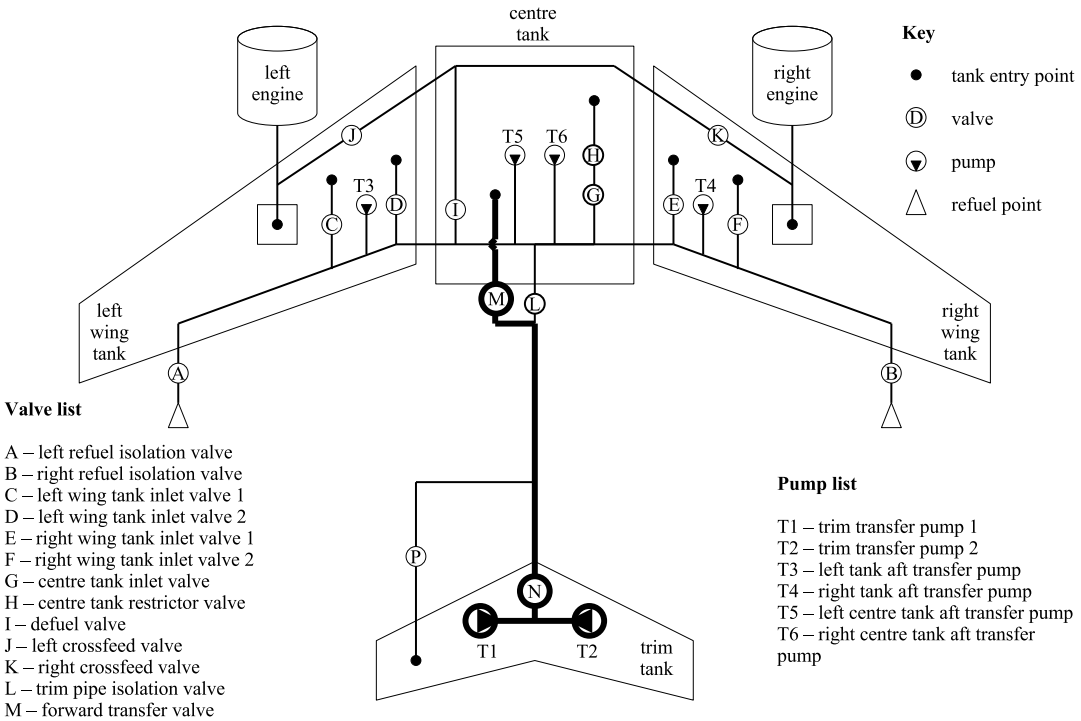

Figure 7.2: fuel system layout, with trim to centre transfer route emphasised

parameter	units	value
impeller radius	mm	150
p_0	bar	1
k_{system}	bar(L/min)^2	5.263×10^{-5}
q_1	L/min	54
T_0	Nm	0.07
η_{max}	%	80
n_1	rev/min	3000
ρ	kg/m^3	851.5

Table 7.1: aircraft fuel system transfer pump model inputs

at $-55°$C, as this is representative of the minimum expected fuel temperature during a long-haul flight at high altitude. Figures 7.3 through 7.5 show the non-dimensional pressure-flow, torque-hydraulic power and flow-efficiency curves of the pump.

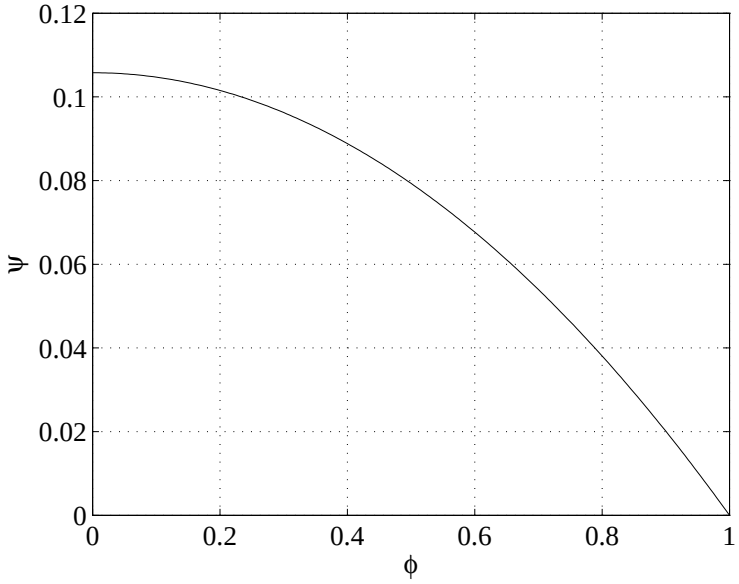

Figure 7.3: non-dimensionalised pressure-flow characteristic of trim to centre transfer pump

7.1.3 Extension of the pump model

In order to fully capture the behaviour of a fuel transfer pump accurately, the model developed in chapter 4 may need to be extended to include a dependence on altitude. The characteristics of fuel pumps are known to change significantly with altitude [10], due to changes in the fuel density and the vapour pressure. During a climb to altitude, the external temperature will reduce significantly and the atmospheric temperature will fall (see equations 3.4 and 3.5 in chapter 3). At some point, the atmospheric pressure will reach the vapour pressure of lighter fractions of the fuel, resulting in rapid vapour release, or boiling. Eventually, the vapour pressure will fall as light fractions of the fuel evaporate and vent to atmosphere, and the atmospheric and vapour pressures will reach an equilibrium point. This process is known as "weathering" of the fuel. During the model development and validation work, such behaviour could not be generated. The tank in the test rig is capable of withstanding a vacuum of 0.5bar below

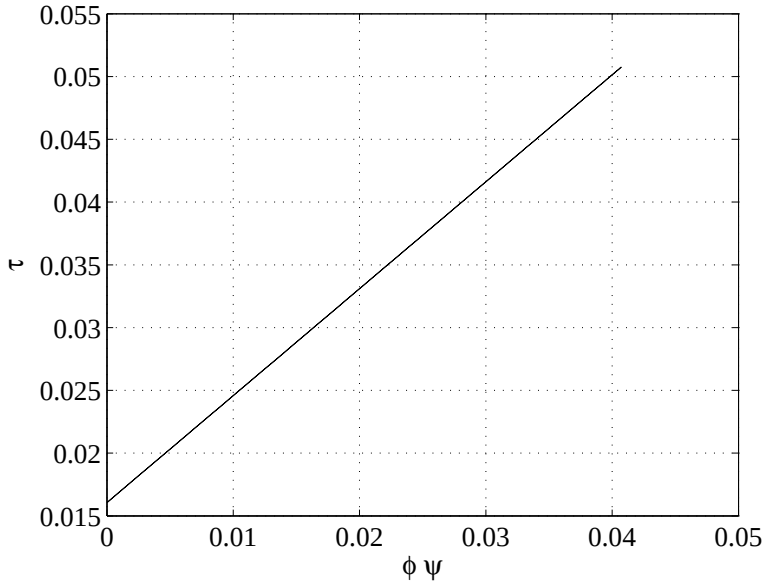

Figure 7.4: non-dimensionalised torque-hydraulic power characteristic of trim to centre transfer pump

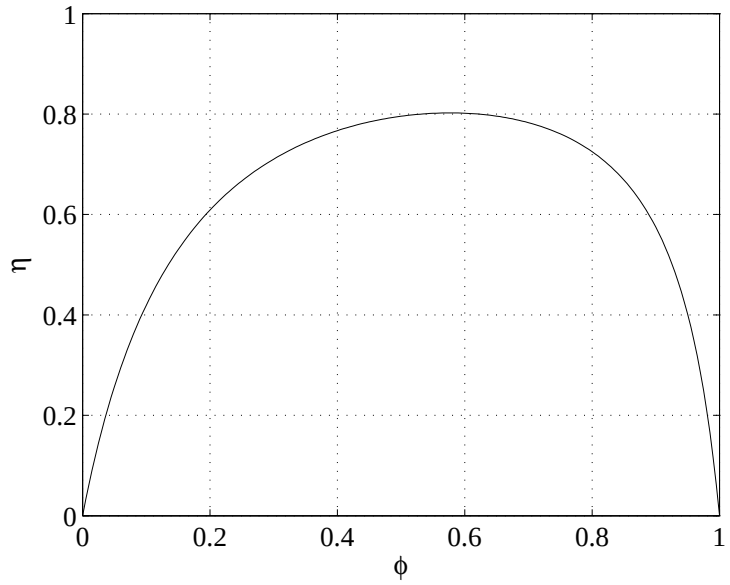

Figure 7.5: non-dimensionalised efficiency-flow characteristic of trim to centre transfer pump

atmospheric. It can be shown that conducting tests under these conditions would be equivalent of analysing the pump and system performance at around 26000ft (8000m) altitude. Information from industry suggests that over such a range there would be negligible change in the pressure-flow relationship. Since the modelling methods provide a means to change both the fuel density, atmospheric pressure and vapour pressure with time, it is quite possible that the simulations could capture the changes in the pump performance with altitude.

In the following section, the simulations which are presented are intended to predict the system behaviour during cruise, where the altitude and hence pump characteristic will be constant. It is therefore assumed that the characteristic defined in section 7.1.2 is suitable for the pump at the cruise altitude. If analysis was also to be conducted at lower altitudes, such as during the climb period, then the characteristic might need to be adjusted. It is proposed that this change in the characteristic could be included in the pump model by extending both the pressure-flow and hydraulic power-torque non-dimensional relationships to include a dependence on altitude, thus creating two three-dimensional characteristic maps. Figures 7.6 and 7.7 show an example of such maps, where the pressure-flow characteristic has been changed to result in a reduction in maximum flow rate, as is expected to occur, and the hydraulic power-torque characteristic increases linearly with altitude. It should be noted that the fuel system simulation software CGFlight takes no account of the variation of pump performance with altitude, but simply assumes a fixed flow rate for each transfer route.

Little information is known about how the hydraulic power-torque characteristic of a pump would change in reality. Such information could only be obtained through detailed testing on a particular fuel pump, if the techniques proposed here were to be put into use.

7.2 Bath*fp* simulations of trim to centre transfer

A Bath*fp* circuit has been constructed to analyse the performance of the trim to centre transfer system of the fictitious aircraft. It can be seen in figure 7.8. The circuit consists of a trim tank model, connected to two centrifugal pumps. These supply a single common pipe which is connected via two ball valves to the centre tank model. The pipe contains a change in height to represent the difference in elevation of the trim and centre tanks. The trim and centre tank models are connected to the aircraft

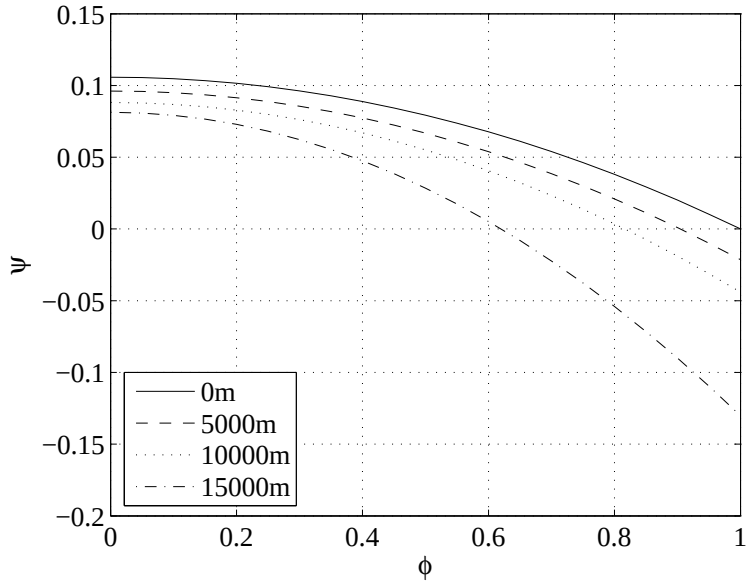

Figure 7.6: example of non-dimensional pressure-flow characteristic map allowing for changes with altitude

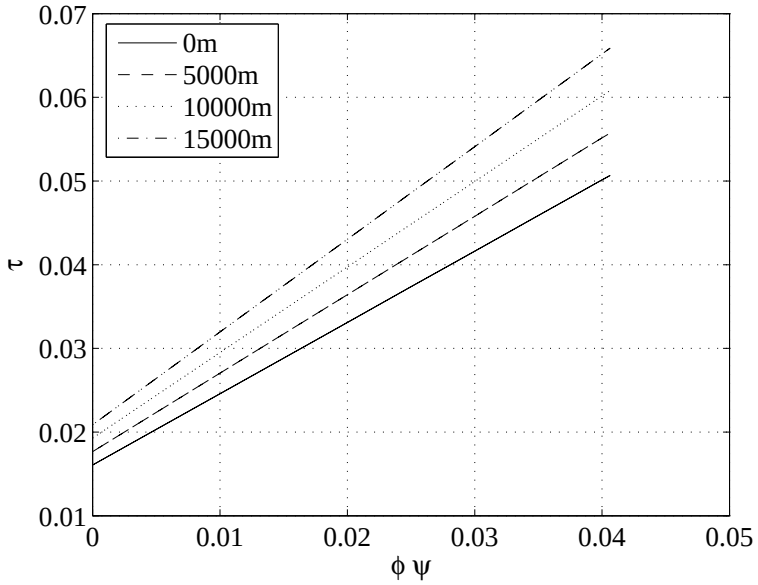

Figure 7.7: example of non-dimensional hydraulic power-torque characteristic map allowing for changes with altitude

model, which supplies the current altitude to the tank models. This also passes the engine fuel burn value to the centre tank model. The tank models return their current volume to the centre of gravity control model, which calculates the current centre of gravity, and thus decides the required pump and valves states. The demand signals are sent to each of the valve and pump models accordingly.

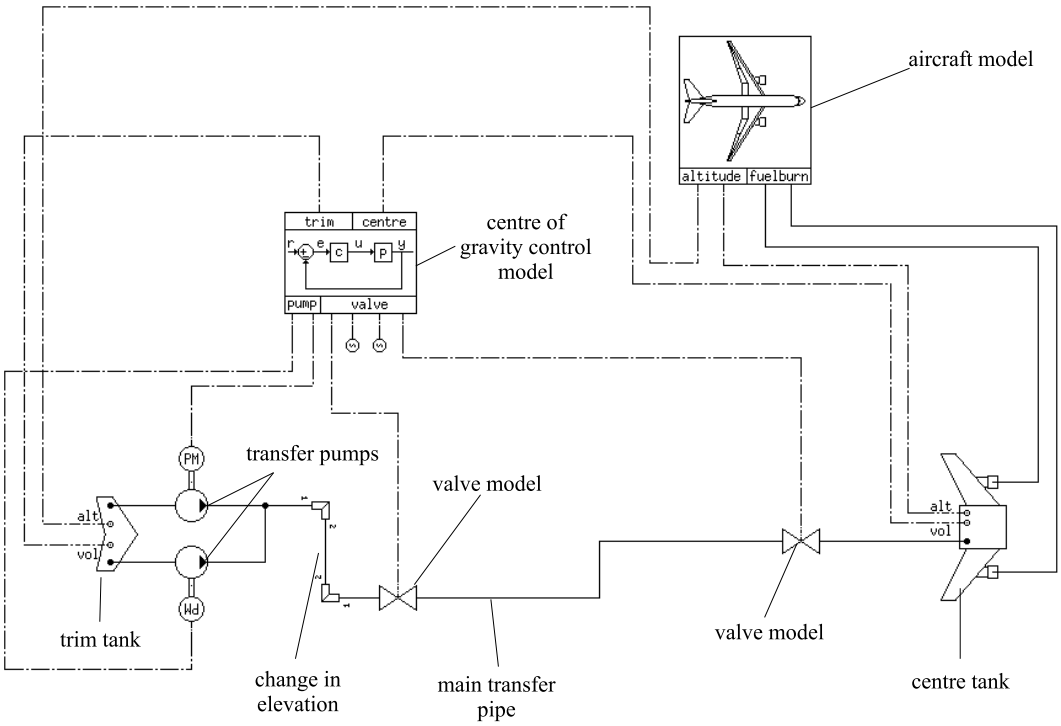

Figure 7.8: Bath*fp* circuit for trim to centre fuel transfer simulations

The pumps are modelled using the steady-state pump model developed in chapter 4, the valves using the same valve model as used in chapter 6 for validation. The pipes are modelled using a combination of the simple compressible volume model, steady-state pressure loss and volume models and the dynamic model used in chapter 6 for the system validation. The main, long section of pipe between valves N and L are modelled with the dynamic pipe model and all other pipes with the steady-state pressure loss and volume model. The pressure losses due to the couplings, bends and pipe friction are all defined using the pressure loss K factors described in chapter 4. The following sections describe each of the other models used to construct the circuit in figure 7.8 in detail.

7.2.1 The aircraft model

The aircraft model acts as a simple duty cycle model to output the engine fuel burn rate as a series of linear functions of time. It also outputs the altitude of the aircraft as a constant. Both of these signals are expected by the fuel tank models (see section 7.2.3).

7.2.2 The control system model

Two centre of gravity control models have been developed - the first to analyse the system performance using the existing on-off control method, and the second to analyse the system performance using the new, proposed variable fuel flow rate method using variable speed transfer pumps. These models effectively perform the same task as part of the fuel system management computer in that they calculate the current centre of gravity of the aircraft and then apply a control strategy to the pumps and valves. The two models use the same icon and require similar inputs from the user.

The required user inputs for each model are outlined in table 7.2. The model also requires an input of the volume of fuel in each of the trim and centre tanks. Throughout the simulation, the volume of fuel in the wing tanks is assumed to be constant, as for cruise only fuel from the trim and centre tanks is burned.

The models begin by calculating the mass of fuel in each tank, and hence the current centre of gravity position using a simple moment balance equation and the characteristic lengths input by the user. Here, the centre of gravity target has been simplified to be a constant, and for this the aft centre of gravity limit is used. It is conceivable that this could be replaced by a more complex function, like that used in the CGFlight simulations (see chapter 3), or even the proposed THS deflection angle. The error between the current centre of gravity and the rear limit is calculated.

In the on-off control model, this centre of gravity error is used to decide on the valve state. If the centre of gravity is rear of the limit, then the valves are opened to allow flow from the trim to the centre tank. The pumps are accelerated to their maximum speed at the beginning of the simulation, even if the valves are shut. This mimics current aircraft fuel system behaviour, where the pumps are run constantly during the flight (see the fuel system operation description in chapter 3). Once the centre of

parameter	units
both models:	
aircraft zero fuel weight	tn
zero fuel weight centre of gravity	m
wing tank centre of gravity	m
centre tank centre of gravity	m
trim tank centre of gravity	m
wing tank volume	L
MAC length	m
MAC leading edge position w.r.t datum	m
centre of gravity aft limit	%MAC
centre of gravity control band	%MAC
valve operation duration	s
pump operation duration	s
variable flow rate model only:	
proportional gain	
integral gain	

Table 7.2: aircraft fuel system centre of gravity control model inputs

gravity passes forward of the rear limit plus the control band, then the valves are shut again, meaning fuel is burned from the centre tank only, causing the centre of gravity to begin to move rearward again.

The second control model operates the pumps and valve in a different manner. The valves can either be open or shut at the beginning of the simulation, and the pumps can be running or not. If the valves are open, then the pumps are not running, and some fuel is transferred forward under gravity. If the valves are shut, then the pumps are initially running at full speed. The valves are opened once the centre of gravity moves to the rear limit. The pump control signal is set using the error signal from the centre of gravity calculation. A proportional plus integral (P+I) controller is implemented by setting the error signal, ϵ. The pump control signal, ω_{demand}, is then given by the equation:

$$\omega_{demand} = k_p\epsilon + \int k_i\epsilon \tag{7.1}$$

where ϵ is related to the centre of gravity error by:

$$\epsilon = \chi_{target} - \chi \tag{7.2}$$

The proportional and integral gains have been set by trial and error to give a suitable system response. In both models, the valves are controlled by setting a rate of change of closure, rather than by supplying a valve angle duty-cycle. This has required a small change to the valve model to expect an input of the valve closure as a percentage rather than an absolute valve angle.

7.2.3 The tank models

Two tank models have been developed to model the behaviour of the trim and centre fuel tanks. They differ only in their icons and the definition of their input parameters. The user must input the tank dimensions, the initial fill level as a percentage of maximum and the elevation of the tank outlet with respect to the level of the transfer pump. The model requires an input of altitude from the aircraft model and of flow rate from the transfer pipe, and returns the pressure in the tank according to the calculated atmospheric pressure and the head of the fuel.

The atmospheric pressure is calculated using the ISA calculations described in chapter 3 for the AMPEC analysis. The sum of the flow rate into the tank from the transfer pipe and the flow out to each of the engines, whose rate is defined by the aircraft model, is used to calculate the current fuel volume within the tank. The head of the fuel is then calculated from the user inputs of tank geometry. The tank is assumed for simplicity to be a cuboid, and it is assumed that the tank is always level (i.e. the aircraft is never subject to pitch or roll). No dynamic or surface effects such as fluid compressibility or sloshing are considered.

7.2.4 The motor model

Little information is available about current or future electric drives for aircraft fuel systems. The motor models developed in chapters 4 and 5 require details of electric parameters within the motor, and as such are not suitable for analysing the performance of the fuel system. Instead, a simple model of a motor which allowed for some account of dynamic behaviour and could operate at any speed was required. In order to achieve this, a first order lag model has been used, which allows for an acceleration to its full speed (defined by the pump model as 3000rev/min) in less than 5s. The model expects an input of demand speed in units rev/min and passes a value of shaft speed to the pump model. No account is taken of the torque required to accelerate the pump.

It is intended that further work as a part of the Electric Drives project could be undertaken to extend the Bath*fp* simulations to include the DC electric motor models described in chapters 4 and 5. Such work would require further detailed information about typical future fuel system drives.

7.2.5 Fuel properties

The majority of Western European and American commercial aircraft operate using Jet A-1 fuel. Bath*fp* requires an input of the fluid density, kinematic viscosity, bulk modulus and saturation pressure. These have been obtained from the Aviation Fuels Handbook [73]. The variation of the density, kinematic viscosity and vapour pressure with temperature, and the variation of bulk modulus with both temperature and operating pressure for Jet A-1 fuel are given in appendix C. The simulations have been conducted assuming a fuel temperature of $-55°$C. The fuel properties at this temperature are given in table 7.3.

7.2.6 Simulation scope

Three simulations have been conducted in order to compare the performance of the trim to centre transfer system using both the current on-off control method and the proposed variable flow rate method. All the simulations are identical, save for the control block. The simulations assume that the aircraft has reached its cruising altitude of 11000m (36000ft), and is flying straight and level. The trim tank and wing tanks

parameter	units	value
density	kg/m^3	857.5
kinematic viscosity	cSt	20.5
vapour pressure	bar	1.13×10^{-4}
bulk modulus (at 1bar)	bar	1.74×10^4

Table 7.3: fluid properties of Jet A-1 fuel at $-55°C$

are full at the beginning of the simulation, and the centre tank is depleted to the point where the centre of gravity is forward of the aft limit, but within the control band. The simulations last for a total of 1 hour, 23 minutes and 20 seconds (5000s). The variable flow rate case has been run twice; once with the valves shut at the start of the simulation, and once with them open.

The aim of the simulations is not to predict exactly how the fuel system would behave, but to indicate the difference in the implementation of the two control systems and how modelling can be used to examine the control required in order to achieve a constant centre of gravity position. The simulations are not intended to represent the actual behaviour of a real fuel system of an existing aircraft. In the case of the variable fuel flow rate, the control system has not been fully optimised, but the gains have been set to such a level as to represent acceptable system performance. The control system definition is not intended to represent an actual, finished design.

7.2.7 Simulation results

For simplicity, the simulations have been labelled case 1 through 3. Table 7.4 describes each of the cases.

The results of the three simulations are presented as centre of gravity fan plots in figure 7.9. These show the variation of the aircraft mass, as a ratio of maximum take-off weight (MTOW), with centre of gravity position, as a function of MAC relative to the target, and are comparable with those presented for the AMPEC/CGFlight analysis in chapter 3. The difference in the on-off and variable flow control cases is

case	description
1	on-off control
2	variable flow rate, valves open at the start
3	variable flow rate, valves shut at the start

Table 7.4: description of Bath*fp* simulations of the trim to centre transfer system

immediately clear. The on-off case shows the characteristic saw-tooth pattern, whereas it can be seen that the centre of gravity remains constant in the variable flow rate cases, once it has initially reached the target. The difference between cases 2 and 3 can be accounted for by the fact that fuel is initially transferred from trim to centre tank by gravity in case 2, whereas the valves are shut in case 3 until the centre of gravity reaches its target.

Figures 7.10 through 7.12 show the variations of pump speed, flow rate and pressure rise for each of the three cases. The data have been normalised by the values of the pump's design operating point in order to reduce the number of plots. Hence, $\omega_0 = 3000$rev/min, $q_0 = 54$L/min and $\delta p_0 = 0.61$bar. Since the design operating pressure is lower than the no-flow pressure, the normalised pressure can reach a peak value of around 1.65 in each of the cases. Once again, the differences in the three cases are clear. In case 1, with the pump running at full speed throughout the simulation and the valves opening and shutting periodically to control the flow, the pressure rise and flow rate switch between their respective maximum and minimum values. Cases 2 and 3 are similar, save for the point in time at which the pump speed is controlled using the `P+I` controller. In case 2, the pump is off at the beginning, but with the valves open and the height difference between the trim and centre tanks, fuel flows from trim to centre under gravity. However, this flow rate is less than is required to maintain the centre of gravity in a constant position. Once the centre of gravity reaches the target, the pumps are turned on. The required pump speed is much lower than its design speed, and as the flight continues the required flow rate increases, causing a small, gradual increase in the pump speed. Case 3 shows very similar behaviour to case 2, although here the pumps are turned on at full speed with the valves shut in the initial stages. Once the centre of gravity reaches its target, the valves are opened and the desired pump speed drops significantly in order to supply only a fraction of

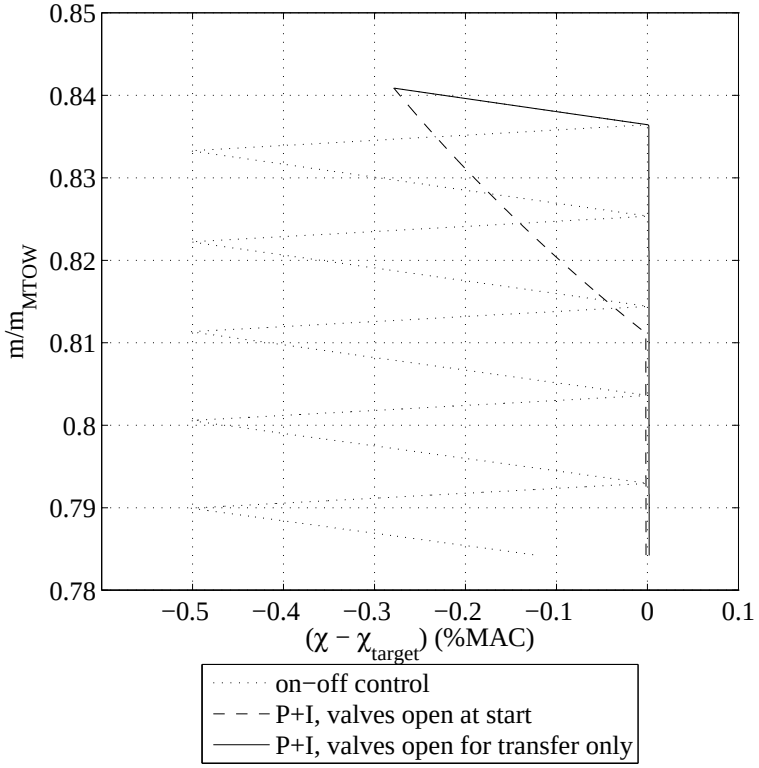

Figure 7.9: fan plots from Bath*fp* trim to centre fuel transfer simulations

the maximum possible flow rate.

Two other effects on the system behaviour as a result of the change in control strategy have been examined. Figure 7.13 shows the pressures in the pipe, measured at the outlet port of valve N and the inlet port of valve L (see figure 7.8), during a valve closure. This data has been taken from case 1. It is clear from the data that a linear valve closure in 2s is capable of producing a pressure wave within the system. The maximum pressure is around 1.43bar, which is 16% higher than the pressure at the pipe inlet during transfer, and 2% higher than the no-flow pressure. A further simulation has been conducted to examine the effect of reducing the valve closure time to 1s on the peak pressure seen in the pipe. Figure 7.14 shows this data. It can be seen that the peak pressure has increased to 2.41bar, which is equivalent to 230% higher than the pipe inlet pressure during transfer and 51% higher than the no-flow pressure.

The second aspect of the system behaviour which has been compared is the power

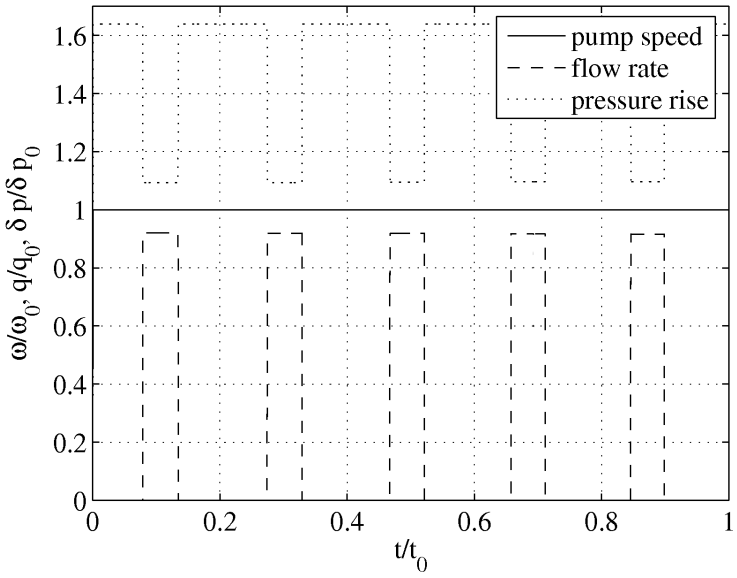

Figure 7.10: case 1: normalised pump speed, flow rate and pressure rise using existing on-off control

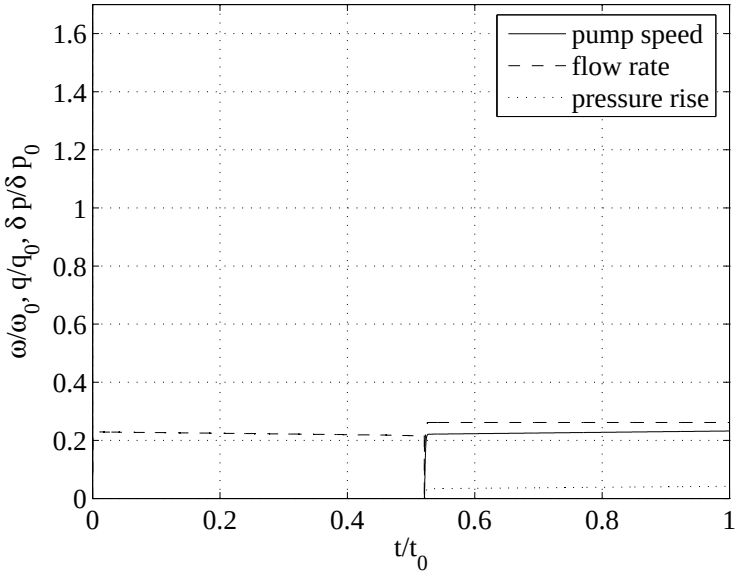

Figure 7.11: case 2: normalised pump speed, flow rate and pressure rise using existing on-off control

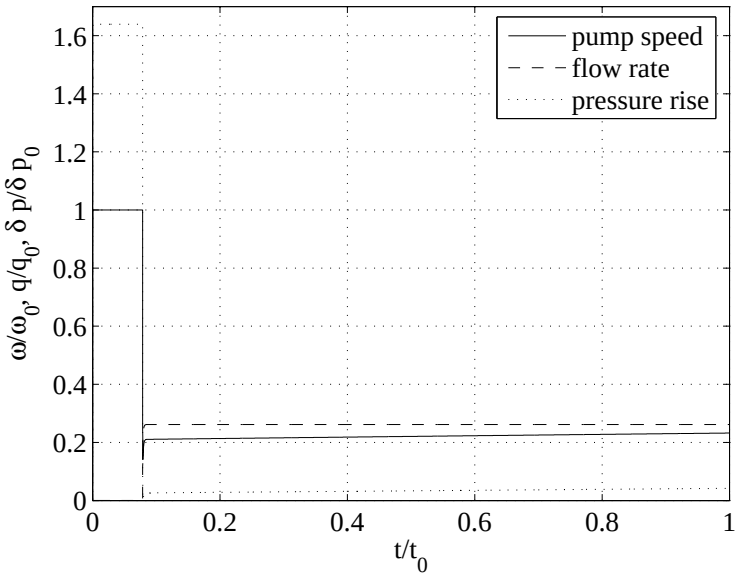

Figure 7.12: case 3: normalised pump speed, flow rate and pressure rise using on-off control

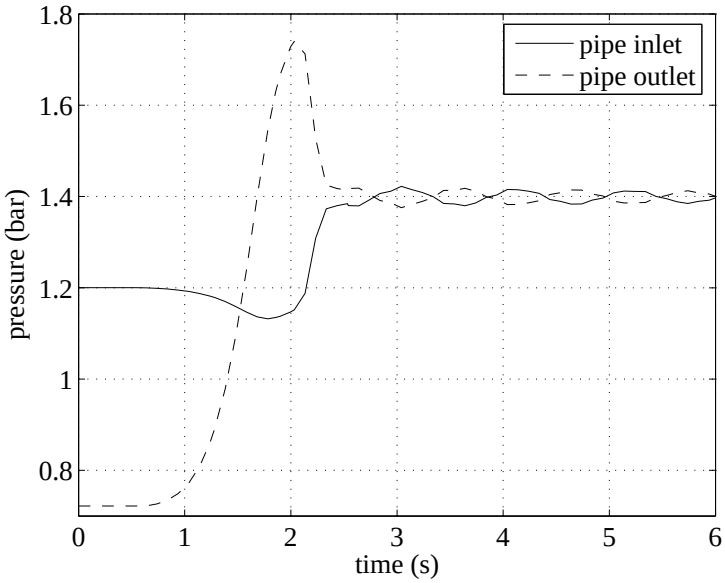

Figure 7.13: case 1: pipe inlet and outlet pressures during 2s valve closure

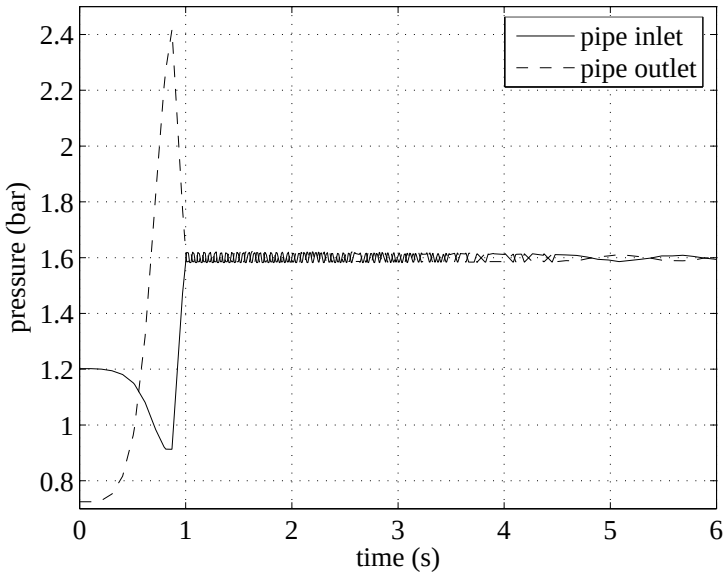

Figure 7.14: case 1: pipe inlet and outlet pressures during 1s valve closure

required to drive the pumps. By examining the pump flow rate, pressure rise and pump speed variation with time for each of the cases, the system behaviour becomes clear. Since the load torque of the pump is dependent on the pressure rise and flow rate, and power is the product of speed and torque, the power supplied to the fuel by the pumps can be calculated. If the motor model was included, then the input power to the motor would also be available. Both of these could be used to estimate the electrical power required to drive the pumps. In this case, where the motor performance is unknown, the power must be estimated from the pump data. The pump efficiency is output from the pump model, so this can be used to estimate the power delivered from the motors. Figure 7.15 shows a comparison of the pump efficiencies in each case. The calculation of the power requirements shows a very stark difference between case 1 and cases 2 and 3. During the on-off cycle of the valves, the power switches between 44W and 140W for the valve shut and valve open condition respectively. For the variable speed case, the operating power requirement of the pumps is between 1W and 2W, although in case 3, when the pumps are running at full speed against a shut valve in the initial stage of the simulation, the power requirement is 44W and in case 2 when the pumps are not running, the power requirement is zero.

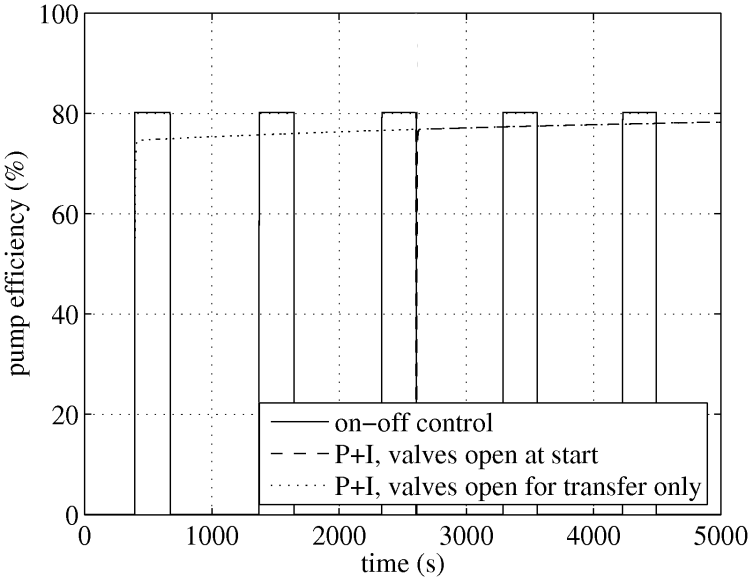

Figure 7.15: comparison of pump efficiency

7.2.8 Discussion

The results presented in section 7.2.7 show how the simulation of the trim to centre transfer system can be used to analyse the impact of changing the control method on the system performance. It is clear from the results that the pump definition given in section 7.1.2 delivers significantly more flow than is required in order to maintain a constant centre of gravity position. When the P+I controller is used, the pump operating speed drops to around 20% of its maximum value. Here, the effect of running a pump at such a low speed relative to its design speed has not been considered. This is clearly also connected with the behaviour of the drive, and could be the subject of further study as a part of the Electric Drives project.

The power reductions shown in section 7.2.7 appear extremely significant. However, they are clearly closely tied to the specification of the pump, especially the operating speed, pressure rise and flow rate. The results highlight that in general, if the pump speed is reduced, and hence the pressure rise and flow rate reduce in order to match the required flow rate to maintain the centre of gravity, then the power delivered to the fluid is reduced. Whilst this reduction in power consumption is small compared to the overall power generated for the aircraft systems, it is nevertheless significant.

One consequence of the system as described however, is that the fuel is no longer being mixed with any water present in the tank as currently happens when the pumps are operating against a shut valve.

By examining the pressures in the main transfer pipe, it is possible to see that reducing the number of valve cycles will reduce the number of times where pressure waves are generated in the pipe. The speed of valve closure can be variable, and these simulations have shown that a faster valve closure could generate pressures which are significantly greater than the typical operating pressures. Currently, the valves are shut in a reasonably short period to prevent fuel overshoot during the on-off control. Using a variable speed drive removes the need for using the valve for flow control, and as such the valve operation period could be extended. Doing so would reduce the surge pressure within the line, reducing the chance of high pressures damaging the pipe. Experimentation and modelling work on the Active Valve project have also shown that fast valve closures can produce significant cavitation downstream of the ball valve [71].

Here it has been assumed that, if such a control method were to be implemented in an aircraft, then the current system of using two pumps in parallel is still valid. Currently, two pumps are required for the trim to centre transfer route for redundancy, and they are sized in order to be able to supply the fuel from trim to centre at at least the same rate at which fuel is burned by the engines. The possibility exists to use two pumps, but not ones of the same specification. Instead, one pump could be used for normal transfer operation based on the simulated required normal transfer rate. The second pump could then be used as a back up pump, with a maximum flow rate to match that required for engine feed. It would only be required in an emergency, where fuel could not be supplied to the engines from elsewhere, or if the fuel needed to be suddenly transferred forwards. If the backup pump could be isolated from the transfer line by a separate ball valve, then the back up pump could be run constantly against a shut valve, thereby still circulating the fuel in order to mix water. The transfer pump speed could then be controlled by a simple P+I controller as described here. Figure 7.16 shows this schematically for the fuel system definition used in this analysis. T2 becomes the backup transfer pump, with T1 as the main transfer pump. Valve Q is introduced to remain shut unless required in an emergency to supply fuel directly to the engines.

If such a control system were implemented, then the requirement for a more advanced health monitoring or fault diagnostic system is increased. The following section discusses how such a system could be implemented.

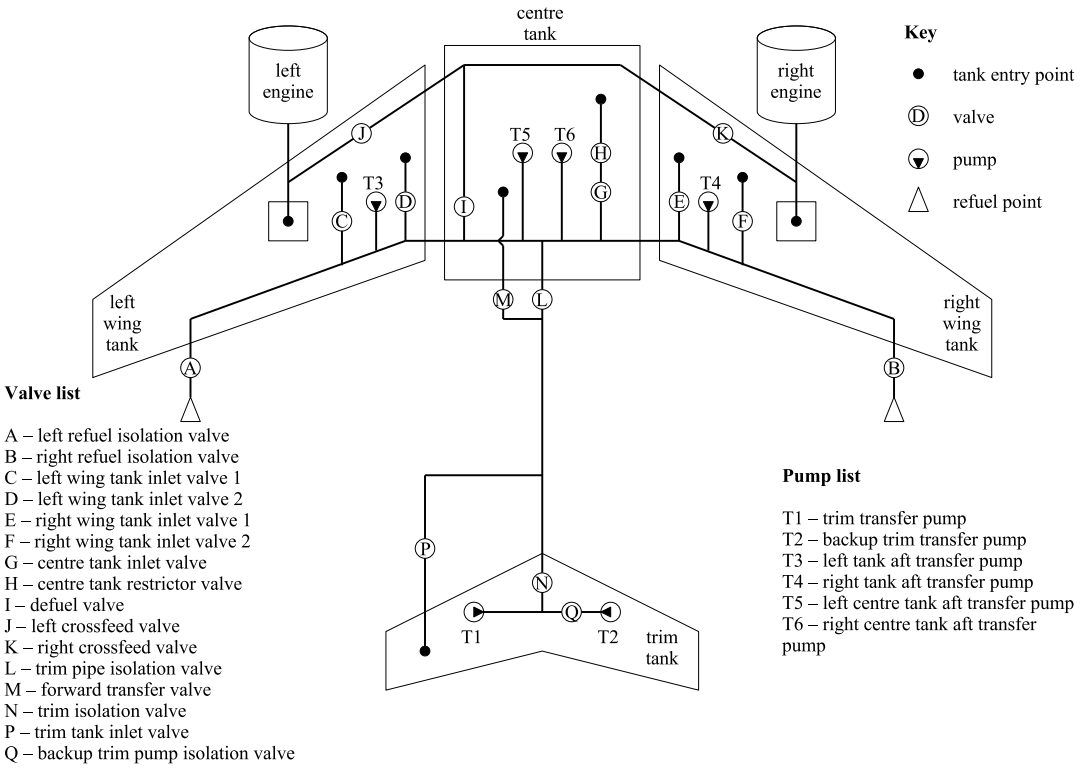

Figure 7.16: proposed fuel system layout, with normal and backup trim transfer pumps

7.3 Health monitoring concepts

7.3.1 Current fuel system health monitoring systems

Current aircraft fuel systems use rudimentary sensors and subsystem behaviour monitors to detect component failure. Component and subsystem behaviour is in general monitored using built-in test equipment, or "BITE", which is located within the computing resources of the fuel management system. This tends to focus on using simple, reliable indication of component behaviour to monitor the individual equipment, and a series of cross and range checks of resulting calculated subsystem parameters to monitor the subsystem behaviour.

Pumps generally use pressure sensors at outlet to detect if flow is passing through the component, although these operate on a minimum operating pressure principle, and as such only indicate that some flow is occurring and not how much. Valves tend to use

micro-switches on the motor shaft to indicate if the valve is open, shut, or somewhere in between. These simple equipment health indications are sent to the fuel system computing resources, along with the current demand signals to the equipment from the fuel management computer. They are resolved into an indication of the equipment's operational status, in terms of "on" or "off" for the pumps, and "open" or "shut" for the valves, and if the equipment is deemed to have failed. In order to meet data transmission redundancy and integrity targets, the signals are often transmitted by dissimilar dual-redundant communications systems, adding complexity to the system. At each stage, the health of the data transfer is monitored independently.

The individual equipment health status signals are often combined to give an indication of a subsystem or operational functionality of the fuel system. For example, if the fuel management were to command a trim to centre transfer during flight, but were to receive a "main trim pump failed" signal, then corrective action would be taken, and the back-up trim pump would be commanded on. Similarly, if a wing tank valve was indicated as failed shut during engine feed, then other valves would be commanded open to utilise the cross-feed function or the refuel gallery to supply fuel to the engine.

Currently, there is no trend for the use of system-wide health monitoring tools. Instead, the monitoring is focused on individual components and the various functionalities of the subsystems. It is proposed that, if the fuel system could be accurately simulated in real-time, then this could be compared to the actual system performance, and hence provide a full system view of the health of the fuel system. The following section briefly describes how system simulations could be applied to provide a system health monitoring application.

7.3.2 Proposed improved model-based health monitoring system

Condition monitoring applications for complex systems can broadly be split into three groups: knowledge-based, heuristic rule-based and training approaches [74]. The overall concepts of these approaches is described by Goodall and Li. [74], and two model-based methods, using Kalman filters and particle based-filters, are presented in detail with respect to railway vehicle condition monitoring. A similar approach is taken by Dewallef and Leonard [75], where a dual Kalman filter method is applied to the on-line condition monitoring of an aero-engine. Examples of heuristic and training systems can be found in Alcock and Shepherd [76], where Bayesian networks are used to incorporate observed data in real-time from an aero-engine to indicate its health, and in Caputo

and Pelagagge [77] where Artificial Neural Networks have been used to identify leaks within complex piping systems.

"Simulation in the loop" health monitoring systems have been used throughout the aerospace industry [76, 78, 79] to monitor the condition of aero-engines for maintainability. Such methods are of particular use where there is little available information from a minimal set of sensors about the system performance. It has been suggested that future aircraft fuel systems could benefit from such a health monitoring tool, especially if the variable fuel flow rate control methods outlined here and in chapter 3 were to be implemented. Here, the basic requirements of the measured data and performance metrics for an aircraft fuel system will be discussed, although detailed analysis of how the aforementioned methods could be employed is outside the scope of this study.

Clearly, the introduction of a closed-loop control system in order to optimise the centre of gravity position using variable speed pumps as described here would require a more sophisticated measurement and control system. In its most minimal form this system would require a measure of the fuel tank levels, the input demand to the transfer pumps and either a measurement of the centre of gravity if a target function or of the THS angle was defined as described in chapter 3. The basic input of speed could be applied to a simplified model in order to check the expected change in centre of gravity with time, and, if the measured behaviour began to seriously deviate from that modelled, then a fault would be flagged to the crew. A more complex system might make use of speed sensors on the pump shafts, position sensors on the valves and pressure and flow measurements. This could again be compared against the modelled performance, but in this case a much more clear picture of any failure could be built up.

Such examples indicate quite clearly that a balance must be sought when considering the implementation of a health monitoring system. Introducing many sensors into the system will increase complexity and cost, and, if not carefully implemented, could reduce the perceived system reliability if sensor failures were to lead to misdiagnosis of a fault. Too few sensors however, and the systems' usefulness is diminished. In the method presented by Gribble [78], a minimal set of measured data is taken from the engine. The model of the engine is then "tweaked" using a number of tuning parameters in order to match its current behaviour. Then, over time, the model is continually compared to the measured engine performance, an the tuning parameters adjusted accordingly. These tuning parameters can then be referred back to gain a measure of wear within the engine, and have been shown to be capable of predicting component wear and even failure. This procedure also means that more details of the

system performance can be known from the simulation. For example, where it might not be possible to measure gas temperatures at key points in the engine, the simulation can be used to estimate data at these points.

Figure 7.17 shows how such a system could be applied to the trim to centre transfer system. From the physical system, the tank volumes are measured. The centre of gravity and engine fuel burn rates can be calculated. These are passed to a controller, which supplies a pump and valve demand signal. This could be either the current on-off or proposed variable case. The engine fuel burn rate and control signals are supplied to the system simulation, which would then predict a centre of gravity position. The control signals are also applied to the physical system. The actual and simulated systems can then be compared. This comparison will depend greatly on what is to be measured in the real system. In its simplest form, this might be only the centre of gravity position. In a more complex system, pressures and flow rates within the system could also be compared.

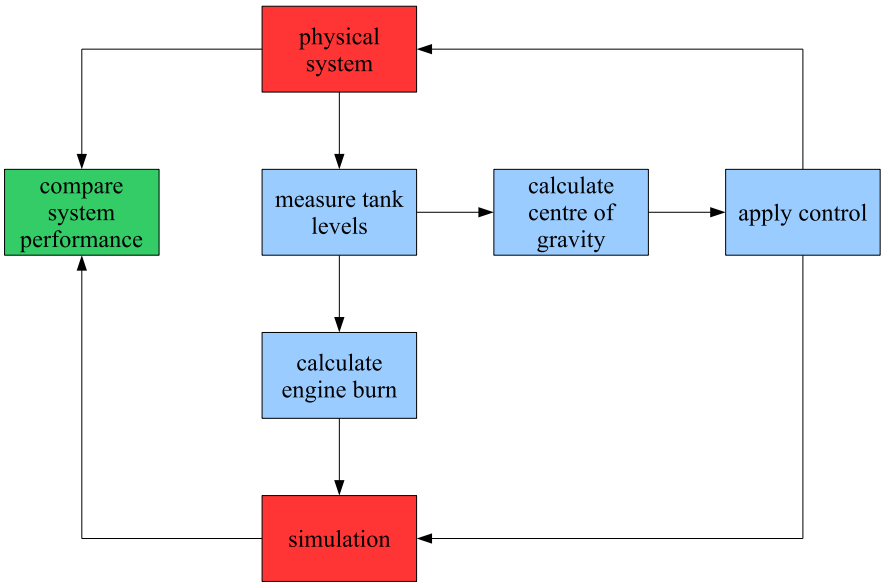

Figure 7.17: proposed health monitoring system block diagram

If only the centre of gravity is measured in the physical system, then the health monitoring system is limited. It can only be used to indicate that the system performance is not matching what is expected, but not why. If more details, such as pressure at the pump outlet or in the pipe or the valve angles, are known, then the system becomes capable of determining where a failure has occurred. For a simple, one route

transfer such as trim to centre, it is relatively simple to determine what sort of failure has occurred. However, as the system becomes more complex, and the centre to wing transfer route is included, failure identification becomes more difficult.

Consider the case were the valve angles and the pressure downstream of the pump are measured. The demand input speed to the motor is known from the controller, and, assuming that the behaviour of the motor is well modelled, the actual motor speeds are also known. The non-dimensional operating point of the pump will be known, and will not change provided the system characteristic changes. If the operating point does change suddenly, assuming that sensor failures can be detected through existing component level health monitoring, but no change in the valve angle is recorded, it is likely that a leak has developed in the pipe, and the transfer would need to be stopped. Any slight changes in the operating point over time may indicate wear in the pump or valve, or even blockages in the pipe. If a pump motor should fail, then a clear change should be noted in the operating point, and an increase in the demand signal to the other pump in order to maintain the correct transfer rate should be detected.

It is clear that, for a given system, it is possible to build up knowledge of how the system behaviour changes as a result of component failures. If the system is accurately modelled, then these failures can be detected by using minimal system measurements and a comparison against the simulated behaviour. The examples above are not intended to be exhaustive, but merely try to identify some of the concepts which could be applied where a more detailed model of an aircraft fuel system is available, and where more complex closed-loop control systems are employed. Indeed, considerable analysis would need to be conducted on a particular system design in order to fully anticipate typical failures, and prove through experimentation that they can be detected. This technique could provide a simple and cheap means to monitor the system health. Any means by which component maintenance can be preempted and reduce aircraft downtime or risk of serious failure is clearly of benefit to both aircraft designers and operators.

7.4 Use of hydraulic system models with AMPEC

In chapter 3, the limitations of the CGFlight/AMPEC simulations were outlined. Among these was the fact that the definition of the fuel system layout and tank moment files could not be changed to suit a different aircraft specification. It is proposed that

CGFlight could be replaced in such simulations by a simulation of the fluid-mechanical network, or that the AMPEC analysis could be conducted within an environment which can model the fluid-mechanical network accurately, hence removing this restriction. Here, it is assumed that the fluid-mechanical network would be modelled using Bath*fp*.

A number of extensions to the fuel system circuit described in section 7.2 would be required. If full analysis of the flight from take-off to landing was required, rather than solely cruise analysis, then the behaviour of the centre to wing tank transfers would be necessary. A Bath*fp* simulation of this has already been undertaken as a part of the Active Valve project, and a full definition of this transfer route is available. The simulation would also need to be extended to consider the exact shape of the fuel tanks, and the effect of aircraft pitch on their moment arms. This could either be provided through simplified tank definitions and a mathematical expression for the moment arm as a function of fill level and pitch, or using the current method of look up tables. In order to simplify the passing of data from one component to the other, it may be necessary to introduce common blocks to share information such as aircraft attitude and fuel tank volumes.

It is possible to implement Fortran code from within the Matlab/Simulink environment. Although, if the Bath*fp* simulation were to be inserted into AMPEC, care would need to be taken over the interface between the Matlab and Bath*fp* solvers. A more suitable solution may be to either reproduce the AMPEC functionality in Bath*fp*, by perhaps extending the aircraft model, or by implementing the simulation of the fuel system behaviour in Simulink using the Simhydraulics toolbox.

This would undoubtedly improve the usefulness of the simulations discussed in chapter 3, as they could be fully tailored to give a full description of a particular system, and would be of great use when designing the controller for the variable fuel flow rate case.

7.5 Closure

Bath*fp* has been used to simulate the behaviour of the aircraft fuel system trim to centre transfer route described in chapter 3. The definition of the fuel system has been extended to include a physical description of the pipe work, which includes fittings and bends whose pressure loss characteristics have been modelled using data from rig test

data. The transfer pump has also been defined using the modelling technique discussed in chapter 4, although using a different characteristic based on a suitable specification for such a system. No pump dynamics are considered in this analysis, as the model validation work concluded that the magnitude of the impedance of a long pipe line was significantly greater than that of a pump. The motor model has not been included, as too little information is available to describe a typical pump motor.

The centrifugal pump model has been validated at typical sea-level atmospheric conditions. It is known that the pressure-flow characteristics of a pump will change with altitude, due to changes in the inlet pressure and fluid characteristics, especially the vapour pressure. Relevant tests could not be conducted using the test rig, so the effect of altitude on the proposed non-dimensionalised modelling method could not be assessed. Instead, it was proposed that, if the model needed to include such behaviour, then it could be extended to use two three dimensional characteristics, one for the pressure-flow relationship, and one for the torque-hydraulic power relationship, which include variation with altitude. However, as the analysis conducted here on the trim to centre transfer was for a fixed altitude, the given characteristics were assumed to be accurate for these conditions.

Three cases were simulated. These examined the behaviour of the system using the current on-off control method, and two proposed variable fuel flow rate methods. These variable flow rate methods were achieved using a variable speed drive, whose speed was set using a P+I controller based on the error signal of the centre of gravity. A simple, constant centre of gravity target was applied, but more complex function such as the THS deflection angle method described in chapter 3 could just as easily be used. the first variable speed drive case examined the system behaviour when the trim to centre transfer valves were open at the start but the pumps were not running, allowing some fuel to be transferred forwards under gravity. The second case began with the valves shut, and the pumps running at full speed. The valves were opened when the centre of gravity reached the rear limit, and the pump speed was then adjusted accordingly.

In conjunction with the benefits of the variable fuel flow rate control case described in chapter 3, the simulations showed that the variable flow rate case results in a significantly smaller amount of power being transferred to the fuel, and hence a reduced power requirement. Since the motors were not modelled in this analysis, it is not possible to discern exactly what reduction in power would be possible. It was noted that the pump definition given here is perhaps not optimal, as the maximum possible fuel flow rate is significantly greater than that required to maintain a constant centre of

gravity. Instead, a new system was proposed, where one pump is used for fuel transfer under normal operations. This would be sized in order to provide a flow rate of similar magnitude to that required for a constant centre of gravity. A second pump could be used as a backup pump, capable of supplying the full flow rate if required. This could be isolated from the transfer pipe by a ball valve under normal operating conditions, and run constantly during flight with this valve shut in order to mix any water with the fuel in the trim tank.

The use of such a fuel system simulation as a part of a system health monitoring tool was discussed. Currently, the fuel system does not provide enough feed back on the system performance to discern what sort of failure has occurred, or if a failure is likely. It has been proposed that, if the system behaviour is well modelled, then, using the input signals to each of the pumps and a measurement of tank fuel volumes, the real system behaviour could be compared to a simulation of the system. Any significant deviation of the measured system performance from that predicted by the simulation would be indicative of a failure. If more information were available about the actual system behaviour, such as valve angles and pump shaft speeds, then this could be extended to diagnose faults, or even predict imminent component failures through wear. Such a system would require significant work in order to be able to accurately diagnose faults. It could easily be extended to cover the full fuel system, not just the trim to centre transfer.

The fuel system simulation could also be extended to replace CGFlight in the simulations in chapter 3. This would improve the accuracy of the simulations by allowing changes to the tank definitions.

Chapter 8

Conclusions

Current generation Airbus long-haul aircraft fuel systems use a fuel tank in the Trimmabel Horizontal Stabiliser (THS) to provide longitudinal control over the centre of gravity position. This is achieved by actively controlling the transfer of fuel between this tank and other tanks further forward, under the main fuselage or in the wings. The transfer pumps in the THS are run constantly throughout the flight, and flow control is achieved by opening and shutting the valves in the transfer line as appropriate. When the pumps are running against a shut valve, the recirculation of flow is useful for mixing any water which may be present in the tank with the fuel. The result of this system is an on-off control of the centre of gravity within a specified band.

Simulations have been developed to investigate the benefits of changing this control system to allow variable fuel flow rates in order to optimise the centre of gravity position. The perceived benefits of such a system were a reduction in fuel burn as a result in a reduction in the wing and THS loading during cruise, a reduction in the number of valve on-off cycles and hence a reduction in valve wear and a reduction in the amount of power required to run the pumps. These simulations extended an existing fuel system simulation to investigate the impact of the centre of gravity position on the mission fuel burn by means of a three-degree of freedom simulation of the aircraft during flight.

In order to assess the impact of the control system on the mission fuel burn, a generic near-future, long-range civil transport aircraft definition was derived. Using existing aircraft initial design tools, it was possible to derive definitions of the aircraft lift and drag characteristics, and separate the drag of the THS from that of the rest of the

aircraft. These parameters were used to assess the fuel burn of the aircraft over a long-haul mission profile which was representative of typical commercial flights. The simulations were conducted for four different control cases to assess the impact of the control strategy on the mission fuel burn.

The baseline case for the comparisons was the first case, where the aircraft was assumed to have no trim fuel tank. The fuel burn for the current scheme was compared against this baseline case for six different definitions of the THS lift and drag. The definition of the THS had a very significant impact on the absolute values of fuel burn. Therefore, in order to effectively compare the effect of the further changes to the control system on the fuel burn independently of the aircraft definition, it was decided to calculate the fuel burn changes with reference to the difference between the no trim case and the current control scheme. This removed the dependence of the results on either the aircraft definition or the THS definition. The effect of changing this control scheme to use a larger centre of gravity band was investigated, as was the use of the proposed variable low rate control case. For each of the six THS definitions, it was shown that increasing the centre of gravity control range increased the mission fuel burn by around 35% to 45% of the original benefit of using centre of gravity control compared to no trim tank, and introducing a variable fuel flow rate reduced the mission fuel burn by around 3% to 5%.

From the results of the simulations, it was clear that increasing the centre of gravity control band reduced the number of valve on-off cycles from 20 to 3, but with a significant fuel burn penalty. Using the variable fuel flow rate control reduced the number of valve cycles to 1, and reduced the fuel burn by a small margin. The reduction in fuel burn as a result of the variable flow rate control could not be seen as a reason on its own for introducing such a control method, especially as doing so would most likely lead to an increase in system cost, weight and complexity. However, the results must be seen in the light of the benefit in the reduction of valve wear as a consequence of the reduction in the number of on-off cycles. More simulations need to be conducted using a range of aircraft definitions, and the results would need to be validated from test flight data before any real, absolute estimate of the fuel burn reductions could be made. However, the results do indicate that using a variable fuel flow rate for the trim to centre fuel transfer is likely to provide significant benefit overall.

A further extension to the control system was suggested as a result of the simulations. The current system requires a measure of the centre of gravity, which must be compared against a target function. The simulation was altered to attempt to maintain a fixed

THS deflection angle of zero, as this was known to result in the minimum drag condition for this aircraft definition. The results of the simulations have shown that, in this case, such a control system had a very significant impact on the fuel burn, reducing it by as much as 283% of the benefit of the current control method over no trim tank. Whilst this increase appears large, it must be seen in the light of some of the limitations of the simulations. The definition of the target centre of gravity and the effect of the tank levels on it are fixed, and are based on a similar but not identical aircraft definition. Instead of demonstrating a definitive benefit of using the control based on THS angle over a centre of gravity target, the simulations have been conducted to highlight the usefulness of changing the nature of the input signal to the control. Currently, the input signal is the centre of gravity position, which is calculated from tank volumes and aircraft attitude, and is therefore subject to considerable inaccuracy. The new system proposes using the THS angle, which is easier to measure more accurately.

In order to investigate how the variable fuel flow rate control system used in the fuel burn simulations could be implemented, it was decided that a simulation of the behaviour of the trim to centre transfer route could be conducted. In order to achieve this, mathematical models of the components within the fuel system would need to be developed and validated. Models for electric drives, centrifugal pumps and various pipe fittings have been developed, and added to the existing component and pipe models in the Bath*fp* fluid power simulation package. A valve model has been developed separately as a part of a related project. A test rig has been built in order to validate the behaviour of the models.

The model development work was divided into two sections. The first was dedicated to developing models to describe the steady-state behaviour of centrifugal pumps, AC induction electric drives and various fittings within the pipes which are typical of aircraft fuel systems. In each case, the behaviour of the models has been determined from measured rig data, and then validated as a part of a system simulation of the test rig as a whole.

Two steady-state pump modelling techniques were identified in the literature, and their applicability to this analysis was assessed. The use of the steady-state, one-dimensional mean streamline analysis was rejected on the grounds that, whilst it is a useful design tool, it is not suitable for off-design point operation or variable speed driven pumps. Instead, a "black-box" type modelling technique was adopted. The behaviour of the pump was measured at a number of discrete operating speeds. Then, using non-dimensional parameters developed from those found in the literature and the

affinity laws, the full behaviour of the pump at any operating point or speed could be described by two curves. The modelling technique was applied to generate a centrifugal pump model in Bath*fp* which can predict the pump pressure rise, flow rate and torque at any operating condition. The steady-state characteristic was shown to be subject to change with time. This was attributed to differences in the motor and pump shaft alignment as a result of installing an in-line torque meter. The characteristic was shown to be accurate for a range of fluid temperatures.

The behaviour of the AC induction motor in the test rig has been described using an equivalent circuit model. Using electrical circuit parameters from both the motor manufacturer and separate tests as a part of the related Electric Drives project, the motor model has been shown to represent the measured behaviour well at its steady-state operating point, although some assumptions about the nature of the electrical supply were necessary.

Various fittings and components within the pipe work of the test rig have also been analysed. The pressure-flow characteristics of these have been modelled using a simplified square-law relationship, defined as a standard K factor. From these and measurements of pressure losses within the system, the relative roughness of the pipes has been calculated. The pipes were modelled using the existing Bath*fp* models, which use Darcy's equation using an estimate of pipe friction factor from Colebrooke's equation. The nature of the fluid within the test rig was also investigated, to ensure the addition of rust and bacterial inhibitor chemicals had not altered its properties. Tests revealed that the density of the fluid matched that of pure water, but the viscosity was around 3% greater. The measured properties were used for the test rig simulations.

Validation of the models was conducted by comparing the measured test rig system performance to that predicted from Bath*fp* simulations of the test rig. The system performance was analysed at three different valve angles, for four different operating speeds. This spot check of the system behaviour allowed for validation of the models across their full range of operating conditions. Using the motor model, the results of the simulations showed reasonable agreement with the measured data. The motor model was replaced with a direct input of the motor speed, in order to analyse the hydraulic system models independently of the motor model. This improved the fit of the data. By comparing the measured and simulated non-dimensional and dimensional pump behaviour, it was clear that the system simulations matched the measured behaviour well, although the results were best with the valve fully open. As the valve was shut, the pressure downstream of the valve and at the inlet of the pump showed significant

differences from the measured data. It was concluded that the K factor modelling technique used for the inlet line and system return line downstream of the valve was less accurate at low flow rates, and in highly cavitating conditions.

In developing the pump model, the torque was said to vary linearly with the hydraulic power. This fit was reasonable, and provided the most accurate way of determining the behaviour of the pump outside of the conditions which could be tested in the rig. However, from the validation work, it became clear that some local deviation of the measured data to this fit resulted in significant differences between the simulated and measured data. This fit to the torque data was capable of predicting a similar maximum efficiency to that supplied from the manufacturer, although limitations of the test rig meant that this could not be validated experimentally.

The dynamic behaviour of the components have also been investigated. For the hydraulic components, this includes consideration of dynamic effects such as fluid compressibility and inertia. The pump model has been extended to include a fluid inertia term, as a result of both rig tests and conclusions from other pump studies found in the literature. The secondary source test method was applied to the pump in order to determine its dynamic characteristic impedance. A new method of providing the secondary flow ripple was proposed. This involved using a short length of compressible hose attached to a branch line in the system. The hose was then laterally compressed by a mechanical shaker, providing a pressure and flow ripple. The method was shown to accurately predict the capacitive impedance of a dead-ended pipe over a reasonable frequency range. Subsequent tests on the pump revealed an impedance which was dominated by inductance, although this was clearly a simplification of the response. Further analysis revealed that this inertance value was dominated by the geometry of the reducing section downstream of the pump. The estimated pump and reducing section impedance was shown to be significantly lower in magnitude than the impedance of the pipe work, suggesting that any system model would not require the pump impedance to accurately model the behaviour.

A motor model which is capable of predicting its dynamic behaviour during accelerations has been developed. This extends the steady-state model to include a transformation of axes in order to make the fluxes and voltages independent of motor speed. The model behaviour has been compared against the measured motor performance from the test rig and the steady-state model for a number of discrete steady-state operating points, and agrees well.

Like the steady-state models, the validation has been conducted in the form of a system simulation of the test rig. The acceleration of the pump over 3 seconds has been analysed. The motor model response was shown to match the measured data well, although little information was available about the input signal to the motor from the frequency inverter. Again, in order to separate the hydraulic system model performance from the motor model, the measured speed of the pump was input directly to the simulation. Using the dynamic pump and pipe models resulted in a good agreement between the measured and simulated data. When the dynamic pump model was replaced by the steady-state model, the simulated performance was unchanged, showing that the pump inertance was indeed negligible compared to that of the pipe. The measured pump behaviour was shown to match the expected steady-state. It was therefore concluded that the pump acceleration could be considered quasi-steady-state, and that any system simulation of a fuel system with a long pipeline only requires a dynamic pipe model and a steady-state pump model.

A new method for measuring the dynamic response of a hydraulic component was developed. This requires the measurement of the natural frequency of a system containing the test component using an acoustic source and measurement. This response can be compared to an equivalent electric circuit of the system, and from this the inertance of the test component can be extracted. The method was compared against a CFD based method for a number of ball valves, and showed good agreement. It was proposed that this test method could be used to accurately measure component inertance, and was much simpler than setting up a secondary source test.

The aircraft fuel system definition for the trim to centre transfer route was extended to include definitions of the pumps and pipe work. These were used, along with the component models developed and validated using the test rig, to develop a Bath*fp* simulation of the system. These simulations were used to analyse the system behaviour for the current on-off control method as well as the proposed new variable flow rate system using variable speed drives for the transfer pumps.

The centrifugal pump model was applied to the transfer pump definition. The hydraulic performance of the pump is known to change with altitude due to changes in fluid properties, although no tests could be conducted to ascertain how this would affect the non-dimensional characteristics. Instead, it was proposed that, if future tests were to determine that the characteristic changes at altitude, then the characteristics could be extended to include a dependence on altitude, thereby creating two three-dimensional characteristic maps. The system simulations conducted here assumed a

constant altitude, and the pump definition used was assumed to be valid for this altitude.

By applying a simple proportional plus integral (P+I) controller to the pump drives, the flow rate was controlled to match the required flow rate. The error signal for the controller was based on the current centre of gravity position and a constant position demand. This demand signal could just as easily been a more complex function or even the THS deflection angle, as used in the fuel burn simulations. The benefits of this control system over the current on-off system were assessed in terms of the number of valve cycles, the pressure transient levels within the pipes as a result of valve closures, and of pump power consumption reduction. Fast valve closures are necessary in the on-off control case in order to minimise fuel transfer quantity overshoot. It was shown that fast valve closures could result in large pressure peaks during closure, and it was proposed that using the variable speed drives to control the flow removed the need for fast valve closures. The power requirements for the variable flow cases was shown to be significantly less than that for the on-off case. This however, was very dependent on the pump definition. In the simulations presented here, the pumps were capable of providing a high flow rate, and the pumps were run at around 20% of their full speed in order to control the centre of gravity.

A new system was proposed. One pump would be specified to be capable of transferring the expected amount of fuel to maintain the centre of gravity constant, and the second pump would be oversized and used only for emergency transfers. This second backup pump could be isolated from the system by a separate ball valve. Then, it could run throughout the flight providing mixing of the water and fuel in the tank. The transfer of the fuel would only be achieved by the first transfer pump.

It was proposed that the system simulation could form part of a system health monitoring tool. The system performance could be measured by a few key parameters. These parameters could be passed to the simulation. Then, the measured and simulated system response could be compared, and if any deviation in the two were noted, then a fault could be detected. The ability of the system to diagnose faults or even preempt failure by detecting long term changes in performance would require a larger number of measured parameters, but would be very useful in terms of increasing system reliability. It was also proposed that the system simulations could be interfaced with the aircraft three-degree of freedom simulations to improve the accuracy of the fuel burn results.

In conclusion, it has been shown that introducing variable fuel flow rate transfers into

the trim to centre transfer route of an aircraft fuel system could reduce both fuel burn and valve wear. This could be implemented by variable speed drives on the transfer pumps using a relatively simple control system. Other benefits include the reduction of pressure transient in the system due to fast valve operations and reduced power consumption of the transfer pumps.

The behaviour of centrifugal pumps in systems like aircraft fuel systems can, in the main, be described as quasi-steady-state, as the system behaviour will be dominated by inertance of fluid within long pipes. This assumption has been validated by applying the secondary source method to the pump. A new source for such tests has been developed, which is relatively simple to implement and has been shown to be suitable over a reasonable frequency range. Other component dynamic behaviour can be assessed using a new, simple acoustic test procedure.

Fuel system simulation can be useful in informing both system design and system control system design. Such simulations could be used to form the basis of a system health monitoring tool, which could be used to improve system reliability.

8.1 Recommendations for further work

The work reported in this thesis highlights a number of areas in which further work could be beneficial.

The aircraft fuel system simulations presented in chapter 3 demonstrated the principle of using a three degree of freedom aircraft model to predict the impact of control system changes on the fuel burn. However, due to limitations in the existing simulation, the definition of the fuel system and the aerodynamic model could not be matched exactly. With further input from the industrial partners, it is proposed that these definitions could be better aligned to investigate aircraft specific fuel burn reduction benefits. It is proposed that this could be extended to look at current and next generation aircraft to identify where relatively simple changes to the existing control could be implemented to reduce operating costs.

Centrifugal pump modelling and model validation was centred around the pump in the test rig, but not extended to look at aircraft fuel pumps due the limitations of the test rig and health and safety factors. Again, with further input from the industrial partners,

it is proposed that this modelling work could be extended to look at the application of the component and system models to actual aircraft fuel system components and aircraft fuel. This would help establish that the modelling assumptions regarding fluid properties were accurate, and strengthen the hypothesis that the models as developed are suitable for fuel system analysis. The acoustic inertance measurement method could be applied to other fuel system components, including pumps, as a means of informing dynamic modelling of such systems. It could provide a simpler alternative to the existing methods such as the secondary source technique.

Work continues on the topic of electrical power generation and electrical drives for aircraft fuel systems as a part of the electrical project. It is proposed that the hydraulic component models and fuel system simulations can be extended using improved electric drive models. Top level analysis of the impact of introducing variable speed drives for transfer pumps could be conducted to investigate cost or weight increases, as well as power reduction and the system and aircraft level benefits discussed in this thesis.

Finally, the proposed model-based health and condition monitoring concepts could be investigated further. A full literature review and detailed analysis of the application of different techniques could identify the best means of implementing such a system. Using the test rig and the system simulations developed as a part of this research, these principles could be demonstrated and validated for the simple hydraulic system. The design of the hydraulic system is such that it lends itself to modification, and so could be used to analyse the behaviour of a system containing parallel branches or multiple sinks. The analysis could then be extended to look at aircraft fuel system specific applications.

References

[1] C. Orme. The A310-300 Fuel System and Centre of Gravity Control. *FAST - Airbus Technical Digest*, Issue 7, Jan. 1987.

[2] S. P. Tomlinson and D. G. Tilley. Computer Modelling of Aircraft Hydraulic Systems Using Bathfp. *Proc Instn Mech Engrs*, 207:139–143, 1993.

[3] BS ISO/TR 3666:1998. Viscosity of Water, 1998.

[4] Joint Aviation Authorities. Joint Airworthiness Requirements JAR-25: Large Aeroplanes, 2007.

[5] International Civil Aviation Organisation. Manual of the ICAO standard atmosphere (extended to 80kilometres (262 500feet)), Doc 7488-CD, Third Edition, 1993.

[6] Stanford University Website. Aa241 - Aircraft Design: Synthesis and Analysis, Digital Textbook, http://adg.stanford.edu/aa241, first accessed July 2005, last accessed February 2008.

[7] Airbus Corporate Website. Airbus: Aircraft Families/A350 Family, A350-900XWB Specification, http://www.airbus.com/en/aircraftfamilies/a350/a350-900/specifications.html, first accessed July 2005, last accessed February 2008.

[8] M. Kingsley-Jones. Airbus's A350 vision takes shape - Flight takes an in-depth look at the new twinjet. *Flight International*, December, 2006.

[9] T. L. Skvarenina and W. E. DeWitt. *Electrical Power and Controls*. Prentice Hall, 2004.

[10] I. J. Karassik, W. C. Krutzsch, W. H. Fraser, and J. P. Messina. *Pump Handbook*. McGraw-Hill, 1986 (2nd Ed).

[11] D. S. Miller. *Internal Flow Systems*. BHRA, 2nd edition, 1990 (2nd Ed).

[12] G. Skawinski. *Active Valve and Pump Technology - Electric Drives (in preparation)*. PhD Thesis, University of Bath, 2009.

[13] S. L. Dixon. Centrifugal Pumps, Fans and Compressors. In *Fluid Mechanics and Thermodynamics of Turbomachinery Fourth Edition in SI/Metric Units*. Butterworth-Heinemann, 4th edition, 1998.

[14] A Whitfield and N. C. Baines. *Design of Radial Turbomachines*. Longman Scientific & Technical, 1990.

[15] H. W. Oh, E. S. Yoon, and M. K. Chung. An Optimum Set of Loss Models for Performance Prediction of Centrifugal Compressors. *Proceedings of the Institution of Mechanical Engineers*, 211(Part A):331–338, 1997.

[16] H. W. Oh and K-Y. Kim. Conceptual Design Optimisation of Mixed-Flow Pump Impellers Using Mean Streamline Analysis. *Proceedings of the Institution of Mechanical Engineers*, 215(Part A):133–138, 2001.

[17] J. P. Johnston and R. C. Dean. Losses in Vaneless Diffusers of Centrifugal Compressors and Pumps. *Transactions of the American Society of Mechanical Engineers, Journal of Engineering for Power*, 88:49–62, 1966.

[18] P. Thanapandi and R. Prasad. A Quasi-Steady Performance Prediction Model for Dynamic Characteristics of a Volute Pump. *Proceedings of the Institution of Mechanical Engineers*, 208(1):47–58, 1994.

[19] J. P. Veres. Centrifugal and Axial Pump Design and Off-Design Performance Prediction. Technical Memorandum 106745, NASA, 17-21/10/1994 1994.

[20] W Jansen and P. B. Sunderland. Off-Design Performance Prediction of Centrifugal Pumps. In *Winter Annual Meeting of the American Society of Mechanical Engineers*, volume 101 of *American Society of Mechanical Engineers, Fluids Engineering Division (Publication) FED*, pages 1–9, Dallas, TX, USA, 1990. ASME, New York, NY, USA.

[21] M. G. Khalafallah, M. A. Abolfadl, and H. M. Sadek. Performance Prediction of Centrifugal Pumps. *Journal of Engineering and Applied Science*, 45(6):989–1008, 1998.

[22] P. Thanapandi and R. Prasad. Performance Prediction and Loss Analysis of Low Specific Speed Submersible Pumps. *Proceedings of the Institution of Mechanical Engineers*, 204(Part A):243–252, 1990.

[23] R. H. Aungier. Mean Streamline Aerodynamic Performance Analysis of Centrifugal Compressors. *Transactions of the American Society of Mechanical Engineers, Journal of Turbomachinery*, 117:360–366, 1995.

[24] A. Stodola. *Steam and Gas Turbines*. McGraw-Hill, 1927.

[25] J. D. Stanitz. Some Theoretical Aerodynamic Investigations of Impellers in Radial and Mixed-flow Centrifugal Compressors. *Transactions of the American Society of Mechanical Engineers*, 74:473–497, 1952.

[26] F. J. Wiesner. A Review of Slip Factors for Centrifugal Impellers. *Transactions of the American Society of Mechanical Engineers, Journal of Engineering for Power*, 89:558–572, 1967.

[27] F. C. Visser, J. J. H. Brouwers, and R. Dbadie. Theoretical Analysis of Inertially Irrotational and Solenoidal Flow in Two-Dimensional Radial-Flow Pump and Turbine Impellers with Equiangular Blades. *Journal of Fluid Mechanics*, 269:107–142, 1994.

[28] K. S. Paeng and M. K. Chung. A New Slip Factor for Centrifugal Impellers. *Proceedings of the Institution of Mechanical Engineers*, 215(Part A):645–649, 2001.

[29] A. N. Sherstyuk and R. A. Erofeev. Determination of the Theoretical Head of a Centrifugal Pump or Compressor Stage. *Chemical and Petroleum Engineering (Khimicheskoe I Neftegazovoe Mashinostroenie)*, 37(3-4):154–157 (19–20), 2001.

[30] B. Donsky. Complete Pump Characteristics and Effects of Specific Speeds on Hydraulic Transients. *Transactions of the American Society of Mechanical Engineers, Journal of Basic Engineering*, 83:685, 1961.

[31] C. P. Kittredge. Hydraulic Transients in Centrifugal Pump Systems. *Transactions of the American Society of Mechanical Engineers*, 78:1807, 1956.

[32] Rizwan-Uddin. Steady-State Characteristics Based Model for Centrifugal Pump Transient Analysis. *Annals of Nuclear Energy*, 21(5):321–324, 1994.

[33] H. Tsukamoto and H. Ohashi. Transient Characteristics of a Centrifugal Pump During Starting Period. *Transactions of the American Society of Mechanical Engineers, Journal of Fluids Engineering*, 104:6–14, 1982.

[34] H. Tsukamoto, S. Matsunaga, H. Yoneda, and S. Hata. Transient Characteristics of a Centrifugal Pump During Stopping Period. *Transactions of the American Society of Mechanical Engineers, Journal of Fluids Engineering*, 108:392–399, 1986.

[35] P. C. Krause. *Analysis of Electric Machinery*. McGraw-Hill, 1987.

[36] F. M. White. *Fluid Mechanics*. McGraw-Hill International Editions, 4th edition, 1999.

[37] S. Saito. The Transient Characteristics of a Pump During Start Up. *Bulletin of the JSME*, 25:372–379, 1982.

[38] P. Thanapandi, T. Tsukamoto, and R. Prasad. Analytical Model for Transient Characteristics of Volute Pumps During Starting and Stopping Periods. *American Society of Mechanical Engineers, Fluids Engineering Division (Publication) FED, Numerical Solutions in Turbomachinery*, 227:167–171, 1995.

[39] T. C. Mohana Kumar and Y. V. N. Rao. Quasi Two-dimensional Analysis of a Flow Through a Centrifugal Pump Impeller. *American Society of Mechanical Engineers (Paper)*, (77-FE-29):7p, 1977.

[40] D. N. Johnston and J. E. Drew. Measurement of Positive Displacement Pump Flow Ripple and Impedance. *Proceedings of the Institution of Mechanical Engineers, Part I, Journal of Systems & Control Engineering*, 210(1):65–74, 1996.

[41] G. Rzentkowski and S. Zbroja. Experimental Characterisation of Centrifugal Pumps as an Acoustic Source at the Blade-Passing Frequency. *Journal of Fluids and Structures*, 14:529–558, 2000.

[42] D. Whitson. An Introduction to Fluid Borne Noise in the Marine Environment. *Journal of Noise and Vibration in Marine Applications*, 2005.

[43] K. A. Edge and D. N. Johnston. The "Secondary Source" Method for the Measurement of Pump Pressure Ripple Characteristics. Part 1: Description of Method. *Proceedings of the Institution of Mechanical Engineers, Part A: Power and Process Engineering*, 204(1):33–40, 1990.

[44] R. J. Whitson and I. M. Benson. Investigation of the Fluid Borne Noise Source Flow (Qs) and Source Impedance (Zs) Characteristics of a Single Stage Centrifugal Pump Using a Secondary Noise Source. In *1st International Symposium on Pump Noise and Vibrations*, pages 175–182, Clamart, France, 1993.

[45] C. A. F. De Jong, J. C. Kriesels, J. C. Bruggeman, and E. Van Bokhorst. Measurement of the Characteristics of a Centrifugal Pump as a Source of Pressure Pulsations. In *1st International Symposium on Pump Noise and Vibrations*, pages 167–174, Clamart, France, 1993.

[46] D. France and D. W. Bilyk. The Measurement of Pump Dynamic Impedance for Use in Piping System Dynamic Analysis. In *Proceedings of the first international symposium on pump noise and vibration*, Clamart, France, 1993.

[47] A. Stirnemann, J. Eberl, U. Bolleter, and S. Pace. Experimental Determination of the Dynamic Transfer Matrix for a Pump. *Transactions of the American Society of Mechanical Engineers, Journal of Fluids Engineering*, 109:218–225, 1987.

[48] K. A. Edge. The Theoretical Prediction of the Impedance of Positive Displacement Pumps. In *Seminar on Quieter oil hydraulics*, pages 95–103, London, UK, 1980.

[49] Y. Kawata, T. Takata, O. Yasuda, and T. Takeuchi. Measurement of the Transfer Matrix of a Prototype Multi-Stage Centrifugal Pump. *Institution of Mechanical Engineers*, 1988.

[50] M. J. R. Bardeleben and D. S. Weaver. Estimation of the Acoustic Scattering Matrix for a Centrifugal Pump. In *2002 ASME International Mechanical Engineering Congress and Exhibition*, volume 253 no. 2, pages 809–819, New Orleans, LA, USA, 2002.

[51] P. O. A. L. Davies. Practical Flow Duct Acoustics. *Journal of Sound and Vibration*, 124(1):91–115, 1988.

[52] D. N. Johnston. *Measurement and Prediction of the Fluid Borne Noise Characteristics of Hydraulic Components and Systems*. PhD Thesis, University of Bath, 1987.

[53] K. A. Edge and D. G. Tilley. The Use of Plane Wave Theory in the Modelling of Pressure Ripples in Hydraulic Systems. *Transactions of the Institution of Measurement and Control*, 5(4):171–178, 1983.

[54] K. A. Edge and D. N. Johnston. The "Secondary Source" Method for the Measurement of Pump Pressure Ripple Characteristics. Part 2: Experimental Results. *Proceedings of the Institution of Mechanical Engineers, Part A: Power and Process Engineering*, 204(1):41–46, 1990.

[55] D. N. Johnston and K. A. Edge. The Impedance Characteristics of Fluid Power Components: Restrictor and Flow Control Valves. *Proceedings of the Institution of Mechanical Engineers, Part I, Journal of Systems & Control Engineering*, 205(1):3–10, 1991.

[56] K. A. Edge and D. N. Johnston. The Impedance Characteristics of Fluid Power Components: Relief Valves and Accumulators. *Proceedings of the Institution*

of Mechanical Engineers, Part I, Journal of Systems & Control Engineering, 205(1):11–22, 1991.

[57] BS ISO 10767-1:1996. Hydraulic Fluid Power - Determination of Pressure Ripple Levels Generated in Systems and Components - Part 1: Precision Method for Pumps, 1996.

[58] H. E. Merritt. *Hydraulic Control Systems*. Wiley-Interscience, 1967.

[59] A. T. J. Hayward. How to Estimate the Bulk Modulus of Hydraulic Fluids. *Hydraulic Pneumatic Power*, 16(181):28–32,35–38,40, 1970.

[60] A. T. J. Hayward. How to Measure the Isothermal Compressibility of Liquids Accurately. *Journal of Physics D: Applied Physics*, 4:938–950, 1971.

[61] D. N. Johnston. Prediction of Fluid Inertance in Non Uniform Passageways. *Journal of Fluids Engineering, Transactions of the ASME*, 128(2):266–275, 2006.

[62] Boyd L. J., Roberts A. R., Collett A. P. S., Johnston D. N., Tilley D. G., and Edge K. A. Prediction of Hydraulic Inertance Using Acoustic Measurements and CFD Modelling. In *2006 ASME International Mechanical Engineering Congress and Exhibition*, Chicago, IL, USA, 2006.

[63] F. Yu, G. D. Baines, and B. J. Chalmers. Generalized Procedure for Transient Simulation of Electrical Machines and Circuits. *COMPEL - The International Journal for Computation and Mathematics in Electrical and Electronic Engineering*, 13(2):455–470, 1994.

[64] M. H. Salama and P. G. Holmes. Modelling and Dynamic Performance of Variable-Frequency-Fed Induction Motors. *IEE Proceedings-B*, 139(3):191–196, 1992.

[65] G. G. Richards. Reduced Order Model for Single and Double Cage Induction Motors During Startup. *IEEE Transactions on Energy Conversion*, 3(2):335–341, 1988.

[66] A. M. Monaghan. *Development of a Systematic Approach to Assist Power Transmission System Design*. MPhil Thesis, University of Bath, 1998.

[67] D. T. Blackstock. *Fundamentals of Physical Acoustics*. John Wiley & Sons, Inc., 2000.

[68] S. S. Rao. *Mechanical Vibrations (3rd edition)*. Addison-Wesley Publishing Company, 1995.

[69] A. P. S Collett. ME40069 Engineering Project: Measurement of Hydraulic Inertance within Fluid Components. Technical report, University of Bath, 2006.

[70] M. I. Soumelidis, D. N. Johnston, K. A. Edge, and D. G. Tilley. A Comparative Study of Modelling Techniques for Laminar Flow Transients in Hydraulic Pipelines. In *The Sixth JFPS International Symposium on Fluid Power*, Tsukuba, 2005.

[71] A. P. Roberts. *Active Valve and Pump Technology - Active Valves (in preparation).* PhD Thesis, University of Bath, 2008.

[72] A. M. Connor and D. G. Tilley. A Tabu Search Method for the Optimisation of Fluid Power Circuits. *Proceedings of the Institution of Mechanical Engineers, Part I, Journal of Systems & Control Engineering*, 212, 1998.

[73] Handbook of Aviation Fuel Properties, Third Edition, Coordinating Research Council, Atlanta GA, 2004.

[74] R. Goodall and P. Li. Model-Based Approaches for Condition Monitoring. In *IEE Colloquim (Digest), IEE Seminar - Railway Condition and Monitoring - Why What How*, Derby, UK, 2004.

[75] P. Dewallef and O. Leonard. On-Line Performance Monitoring and Engine Diagnostic Using Robust Kalman Filtering Techniques. In *American Society of Mechanical Engineers, International Gas Turbine Institute, Turbo Expo (Publication) IGTI*, Atlanta, GA, USA, 2003.

[76] A. Alcock and D. Shepherd. The Development of an Advanced Diagnostic/Prognostic System for the RB199 Aero-Engine. In *IEEE Aerospace Conference Proceedings, 2005*, Big Sky, MT, USA, 2005.

[77] A. C. Caputo and P. M. Pelagagge. Using Neural Networks to Monitor Piping Systems. *Process Safety Progress*, 22(2):119–128, 2003.

[78] J. J. Gribble. A Model Based Approach to Real-Time Aero-Engine Condition Monitoring. In *Aircraft Airborne Condition Monitoring*, volume 3-10203, pages 25–28, Gloucester, UK, 2003. IEE.

[79] A. Orsagh, D. Brown, M. Roemer, T. Dabney, and A. Hess. Prognostic Health Management for Avionics System Power Supplies. In *IEEE Aerospace Conference Proceedings, 2005*, Big Sky, MT, USA, 2005.

Appendix A

Test Rig Sensor data

parameter	units	value
pressure range	bar	0 to 10
proof pressure	bar	20
accuracy	% full scale	0.25
bandwidth	kHz	Unspecified

Table A.1: strain gauge pressure transducers (Gems Sensors, 2200AGB)

parameter	units	value
pressure range	bar	0 to 35
proof pressure	bar	70
accuracy	% full scale	0.25
bandwidth	kHz	up to 30

Table A.2: piezo-resistive pressure transducers (Entran, EPX-03-500P)

parameter	units	value
flow rate range	L/min	110 to 1100
linearity	% full scale	0.22
response time	ms	50 for 50% step change in flow

Table A.3: turbine flow meter (Logitech, NT48)

parameter	units	value
torque range	lbft	0 to 100
maximum torque	lbft	200
speed range	rev/min	0 to 6000
linearity	% full scale	0.11
bandwidth	kHz	unspecified

Table A.4: in-line torque meter, (Westland Aircraft Ltd. 200lbft)

parameter	units	value
temperature range	°C	−40 to +125
accuracy	% full scale	0.5
bandwidth	kHz	unspecified

Table A.5: thermocouples

parameter	units	value
number of analogue inputs		16
A/D throughput	kS/s	500
accuracy (gain=1, 500kHz)	% full scale	0.05
number of analogue outputs		4
output throughput	kS/s	500

Table A.6: data acquisition module (Data Translation USB DT9834)

Appendix B

Aircraft Definition for AMPEC Analysis

parameter	symbol	units	value
range	X_{max}	km	15000
taxi time	t_{taxi}	s	120
ICA	Y_{ICA}	m	11000
cruise Mach number	M_{cr}		0.85

Table B.1: mission parameters

parameter	symbol	units	value
take-off attitude	ϵ_{to}	$^\circ$	9
rotate speed	V_r	kts	149
MAC length	$\bar{c}$	m	9.35
MAC leading edge aft of datum	x_{MAC}	m	24.795
wing aerodynamic centre aft of datum	x_w	m	27.777
tailplane aerodynamic centre aft of datum	x_t	m	60
wing reference area	S_{ref}	m^2	464.5
tailplane wing reference area ratio	h		0.26

Table B.2: aircraft geometry

parameter	symbol	units	value
aircraft and wing moment coefficient	C_{mo}		-0.153
wing lift curve slope	A_{to}	$/^\circ$	0.0694
	A_c	$/^\circ$	0.0796
	A_l	$/^\circ$	0.0624
wing zero alpha lift	B_{to}		0.784
	B_c		0.144
	B_l		1.2
tailplane lift curve slope	C	$/^\circ$	0.0677
tailplane zero alpha lift	D		0
aircraft drag polar	$d_{a,1}$		4.3187×10^{-2}
	$d_{a,2}$		1.4211×10^{-3}
	$d_{a,3}$		1.0302×10^{-2}
tailplane drag polar	$d_{t,1}$		3.3221×10^{-3}
	$d_{t,2}$		1.0932×10^{-4}
	$d_{t,3}$		7.9244×10^{-4}

Table B.3: aerodynamic data

Appendix C

Jet A-1 Properties

The following properties of Jet A-1 aviation fuel have been obtained from [73].

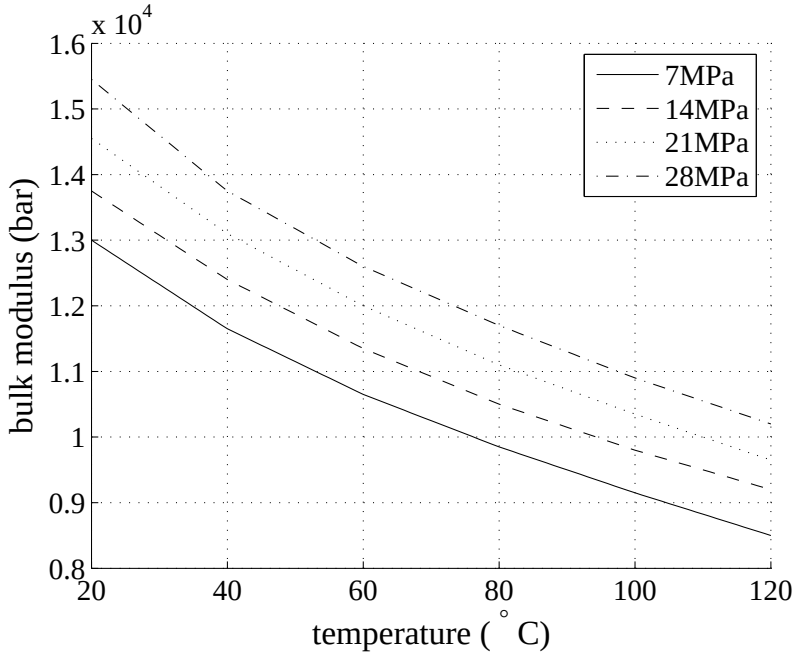

Figure C.1: variation of Jet A-1 bulk modulus with temperature for 4 system pressures

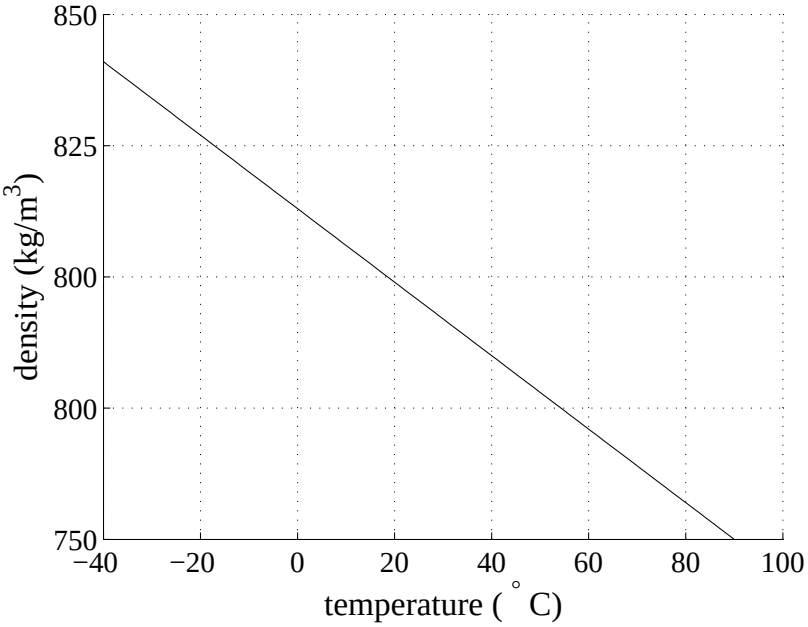

Figure C.2: variation of Jet A-1 density with temperature

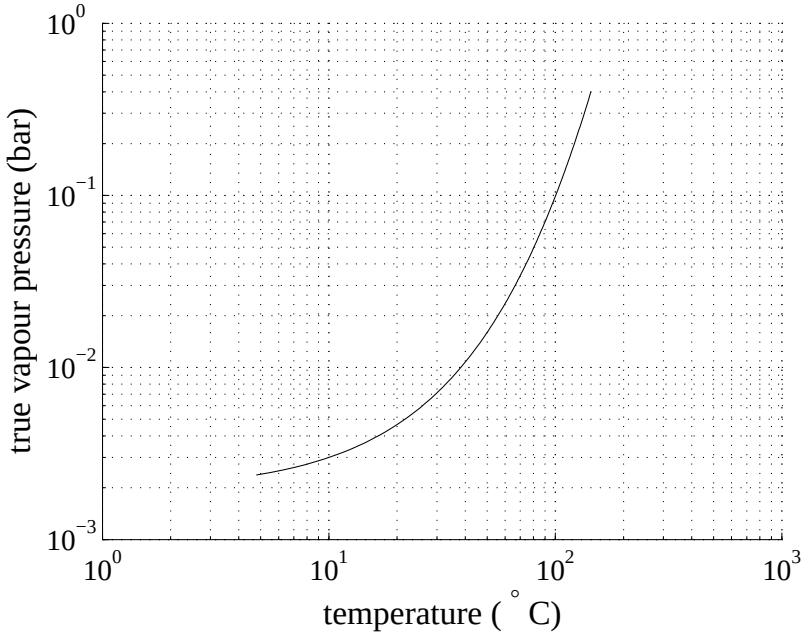

Figure C.3: variation of Jet A-1 vapour pressure with temperature

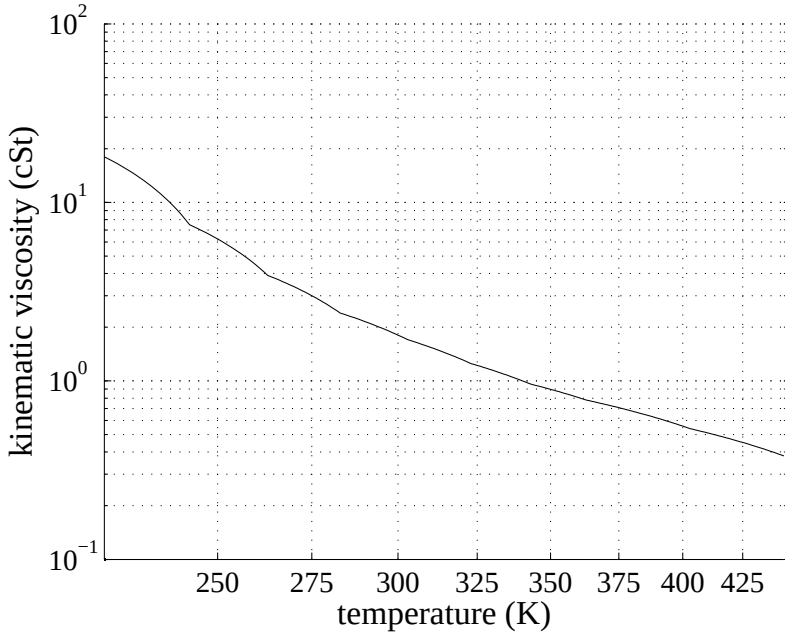

Figure C.4: variation of Jet A-1 kinematic viscosity with temperature